



THE HONG KONG
POLYTECHNIC UNIVERSITY

香港理工大學

Pao Yue-kong Library

包玉剛圖書館

Copyright Undertaking

This thesis is protected by copyright, with all rights reserved.

By reading and using the thesis, the reader understands and agrees to the following terms:

1. The reader will abide by the rules and legal ordinances governing copyright regarding the use of the thesis.
2. The reader will use the thesis for the purpose of research or private study only and not for distribution or further reproduction or any other purpose.
3. The reader agrees to indemnify and hold the University harmless from and against any loss, damage, cost, liability or expenses arising from copyright infringement or unauthorized usage.

IMPORTANT

If you have reasons to believe that any materials in this thesis are deemed not suitable to be distributed in this form, or a copyright owner having difficulty with the material being included in our database, please contact lbsys@polyu.edu.hk providing details. The Library will look into your claim and consider taking remedial action upon receipt of the written requests.

**EFFECT OF LOW-TEMPERATURE
AGING ON PHASE TRANSFORMATION
AND SUPERELASTICITY OF NITI
ALLOYS WITH DIFFERENT GRAIN
SIZES**

SUN BO

PhD

The Hong Kong Polytechnic University

This Programme is Jointly Offered by

The Hong Kong Polytechnic University and Tongji University

2019

The Hong Kong Polytechnic University

Department of Mechanical Engineering

Tongji University

School of Mechanical Engineering

**EFFECT OF LOW-TEMPERATURE AGING ON
PHASE TRANSFORMATION AND
SUPERELASTICITY OF NITI ALLOYS WITH
DIFFERENT GRAIN SIZES**

SUN BO

**A thesis submitted in partial fulfillment of
the requirements for the degree of
Doctor of Philosophy**

December, 2018

CERTIFICATE OF ORIGINALITY

I hereby declare that this thesis is my own work and that, to the best of my knowledge and belief, it reproduces no material previously published or written, nor material that has been accepted for the award of any other degree or diploma, except where due acknowledgement has been made in the text.

Sun Bo

Abstract

Nanocrystalline (NC) and Ultrafine grain (UFG) NiTi shape memory alloys possess superior functional and structural mechanical properties than the traditional coarse grain (CG) ones. The superelasticity adjustment of the NC and UFG NiTi alloys is a significant issue in this field. Although grain size alteration can be used to adjust their functional properties, the superior structural mechanical properties (e.g., high strength, high hardness, high fatigue resistance, and high corrosion resistance, etc.) brought about by the special NC and UFG grain sizes may be deteriorated. Thus, how to realize the functional property adjustment of NC and UFG NiTi alloys without losing the original fine grain size becomes a frontier research issue. It was recently found that the low-temperature aging (LTA) can introduce Ni_4Ti_3 nanoprecipitates into the matrix of Ni-riched NiTi shape memory alloys without changing their grain size, which is an effective solution to address this issue. Therefore, to understand the influence of LTA on the phase transformation and superelasticity of NiTi alloys regarding different grain sizes is a fundamental precondition for the superelasticity adjustment of NC and UFG NiTi alloys via LTA.

In this study, the effect of LTA on NC and CG NiTi alloys was comparatively investigated, and the feasibility of altering the phase transformation and superelasticity via LTA without changing grain size was verified. The different responses of NC and CG towards LTA were obtained.

To obtain the NiTi alloy with different grain sizes, the influence of direct electric resistance heat treatment on NiTi alloy with different grain sizes and aging states was studied. It was found that the nanograin size suppresses Ni₄Ti₃ precipitation during the direct electric resistance heat treatment. Based on the logistic function, grain size adjusting models were established by altering direct current magnitude or heating time, respectively. By using this method, NiTi alloys with grain sizes ranging from 34 to 8021 nm were rapidly obtained.

LTA at 573 K from 0 to 48 h was applied to the afore-obtained NiTi alloys, and its influence on their phase transformation characteristics was investigated. The variations of phase transformation sequence, temperature, enthalpy, thermal hysteresis, etc. with the alteration of grain size and the LTA time were obtained. The mechanisms of the different responses of the NiTi alloys with different grain sizes towards LTA were further investigated based on the microstructural evolutions and hardness variations. According to the experimental results, a B2→R phase transformation temperature model was established, which can calculate the B2→R phase transformation temperature at the given grain size and LTA time.

At which deformation stage that the unloading happens greatly affects the superelastic stress-strain path. To understand the effect of unloading at different deformation stage on superelasticity, the superelasticity that unloads at the maximum applied strain of 3% and 9% are respectively studied, which represents the unloading within and beyond the plateau deformation stage respectively. The variations of the loading and unloading plateau stress and strain, stress hysteresis,

residual strain, etc. with the alteration of grain size and the LTA time were obtained. Based on the microstructural evolution, hardness variation, and the corresponding phase transformation characteristics, the underlying mechanisms of the superelasticity variation were revealed. According to the experimental results, the function of the stress hysteresis increment and the post-plateau stress increment was proposed, and a stress hysteresis model considering the effect of grain size and LTA time was established.

A superelastic stress model considered the effect of grain size and LTA time was established based on Graesser model and the superelasticity experimental results. The parameters of the model, which can alter the shape of stress-strain curves, were treated as a function of grain size and LTA time so that the whole model can reflect the effect of these two factors. The model can be used to calculate the superelastic stress-strain curves of NiTi alloy at a certain condition (within the maximum applied strain from 3% to 9%, grain size from 34 to 8021 nm, and LTA time from 0 to 48 h at 573 K).

This study primarily investigated the influence of LTA on the phase transformation and superelasticity of the NiTi alloys with different grain sizes. It provides the experimental basis and theoretical reference to determine the processes and methods of the superelasticity adjustment of NC and UFG NiTi alloys by using LTA.

Keywords: NiTi, Low-temperature aging, Phase transformation, Superelasticity, Grain size, Nanocrystalline

Publications arising from the thesis

[1] Sun Bo, Fu M.W., Lin Jianping, Ning Yongquan. Effect of low-temperature aging treatment on thermally- and stress-induced phase transformations of nanocrystalline and coarse-grained NiTi wires. *Materials & Design*, 2017; Vol 131: 49-59.

[2] Sun Bo, Lin Jianping, Fu M.W.. Dependence of processing window and microstructural evolution on initial material state in direct electric resistance heat treatment of NiTi alloy. *Materials & Design*, 2018, Vol 139: 549-564.

[3] Sun Bo, Fu M.W., Lin Jianping, 2018. Effect of Low-temperature aging on thermally-induced B2 \leftrightarrow R phase transformation of NiTi alloy with nanocrystalline, ultrafine, and coarse grains, under preparation.

[4] Sun Bo, Lin Jianping, Fu M.W, 2018. Effect of Low-temperature aging on superelasticity of NiTi alloy with nanocrystalline, ultrafine, and coarse grains, under preparation.

Acknowledgements

This thesis is the result of encouragement, patience and support from many people who shaped my life and developed my research capability during the journey as a Ph.D. student.

I would like to express my sincere gratitude to my supervisors Prof. M.W. FU in The Hong Kong Polytechnic University (PolyU) and Prof. Jianping LIN at Tongji University for their kind advice, cheerful encouragement, and endless patience. This thesis was finished with their precious supervision. I would like to especially appreciate Prof. M.W. FU for his patient supervision and correction of my papers and the thesis word by word and sentence by sentence. I would like to thank for his trust and support on my explorative and relatively expensive experiments even at the time that I was a primary research student. I am also grateful to his kindness and generosity to support my prolonged study period in PolyU in both my studying and living.

In addition, I would like to thank Prof. Yongquan Ning, Dr. Jiaqi RAN, Dr. Jilai WANG, Dr. Fangfang LI, Dr. Haopeng YANG, and Dr. Wenting LI, etc. for providing the help and support in the course of my Ph.D. research.

Furthermore, I finished this thesis with the love and support from my family. Their sincere love has been my greatest strength and driving force to overcome the difficulties in my Ph.D. research and come out with the final research outcomes.

Table of Contents

CERTIFICATE OF ORIGINALITY	i
Abstract	ii
Publications arising from the thesis	vi
Acknowledgements	vii
Table of Contents	viii
Table of nomenclature and units	xiv
Schematic plot of superelastic indices	xvi
Chapter 1 Introduction	1
1.1 Background.....	1
1.2 Research overview.....	5
1.2.1 NiTi shape memory alloys and their functional properties.....	5
1.2.2 State-of-art of the influence of grain size on the properties of NiTi alloys	10
1.2.3 State-of-art of the influence of aging on the properties of NiTi alloys	16
1.2.4 State-of-art of the superelastic stress-strain models of NiTi alloys	24
1.3 Outline of the thesis.....	25
Chapter 2 Comparative study of the influence of low-temperature aging on the functional properties and microstructures of nanocrystalline and coarse-grained NiTi alloys.....	31
2.1 Introduction	31

2.2 Materials preparation and experimental procedure	31
2.2.1 Preparation of NC and CG NiTi alloys.....	31
2.2.2 Process of low-temperature aging.....	33
2.2.3 Microstructural observation and measurement of properties.....	35
2.3 Effect of LTA on the microstructures of NC and CG NiTi alloys	37
2.4 Effect of LTA on the hardness of NC and CG NiTi alloys	40
2.5 Effect of LTA on the phase transformation characteristics of NC and CG NiTi alloys	42
2.5.1 Effect of LTA on thermally-induced $B2 \leftrightarrow R$ transformation.....	43
2.5.2 Effect of LTA on thermally-induced $B2(R) \leftrightarrow B19'$ transformation....	45
2.6 Effect of LTA on the superelasticity of NC and CG NiTi alloys.....	47
2.6.1 Effect of LTA on stress-induced $B2 \rightarrow R$ transformation.....	48
2.6.2 Effect of LTA on stress-induced $B2(R) \leftrightarrow B19'$ transformation	50
2.6.3 Effect of LTA on superelasticity under different maximum strains	56
2.7 Summary.....	58
Chapter 3 Effect of direct electric resistance heat treatment on the properties and grain size of NiTi alloys.....	61
3.1 Introduction	61
3.2 Materials preparation and experimental procedure	62
3.2.1 Preparation of NiTi alloys with different initial states.....	62
3.2.2 The platform for DERHT.....	64
3.2.3 Experimental design of DERHT	68

3.3 Effect of DERHT on the phase transformation characteristics of NiTi alloys	69
3.4 Effect of DERHT on the superelasticity of NiTi alloys	74
3.5 Mechanisms of the influence of DERHT on NiTi alloys from the microstructural evolution perspective	80
3.5.1 Grain growth	80
3.5.2 Precipitation, growth, and dissolution of Ni ₄ Ti ₃	82
3.5.3 Nanograin size induced suppression of Ni ₄ Ti ₃ precipitation during DERHT	84
3.5.4 Corroborative evidence of the microstructural evolutions based on the variation of hardness	86
3.6 Grain size adjustment model based on DERHT	90
3.6.1 Grain size adjustment model based on the heating time of DERHT ...	90
3.6.2 Grain size adjustment model based on the current magnitude of DERHT	93
3.7 Summary.....	97
Chapter 4 Influence of low-temperature aging on phase transformation characteristics of NiTi alloys with different grain sizes	101
4.1 Introduction	101
4.2 LTA experimental design of the NiTi alloys with different grain sizes...	102
4.3 Effect of grain size on phase transformation characteristics before LTA	103
4.4 Effect of LTA on the phase transformation characteristics of the NiTi alloys with different grain sizes	107

4.4.1 Effect of LTA on phase transformation sequence and temperature...	109
4.4.2 Effect of LTA on B2 \leftrightarrow R transformation.....	111
4.4.3 Effect of LTA on B2(R) \leftrightarrow B19' transformation	118
4.5 Mechanisms for the influence of LTA on phase transformation.....	122
4.5.1 Effect of the preservation of grain size on phase transformation characteristics.....	122
4.5.2 Effect of LTA time on Ni ₄ Ti ₃ precipitation	123
4.5.3 Nanograin size induced suppression of Ni ₄ Ti ₃ precipitation during LTA	126
4.5.4 Corroborative evidence of the microstructural evolution based on the variation of hardness	132
4.6 B2 \rightarrow R transformation temperature model considering the effect of LTA time and grain size.....	133
4.7 Summary.....	137
Chapter 5 Influence of low-temperature aging on the superelasticity of NiTi alloys with different grain sizes.....	141
5.1 Introduction	141
5.2 Effect of grain size on superelasticity before LTA	142
5.2.1 Superelasticity under the maximum applied strain of 3% before LTA	142
5.2.2 Superelasticity under the maximum applied strain of 9% before LTA	143
5.2.3 Variations of superelastic indices with grain size before LTA.....	145

5.3 Effect of LTA on the superelasticity of the NiTi alloys with different grain sizes	148
5.3.1 Superelasticity under the maximum applied strain of 3% after LTA	148
5.3.2 Superelasticity under the maximum applied strain of 9% after LTA	150
5.3.3 Variations of superelasticity indices with LTA time and grain size ..	153
5.4 Mechanisms of the influence of LTA on superelasticity.....	163
5.5 Increase of the maximum loading stress and stress hysteresis	166
5.6 Stress hysteresis model considering the effect of LTA time and grain size	170
5.7 Summary.....	174
Chapter 6 Superelastic stress-strain model considering the effects of LTA and grain size	177
6.1 Introduction	177
6.2 Graesser model	177
6.2.1 Mathematical formulation of the Graesser model.....	178
6.2.2 Influence of the parameters of the Graesser model on superelastic stress-strain curves	180
6.2.3 Limitation of the Graesser model.....	182
6.3 The modified Graesser model	183
6.3.1 Mathematical formulation of the modified Graesser model	183
6.3.2 Parameters of the modified Graesser model	191

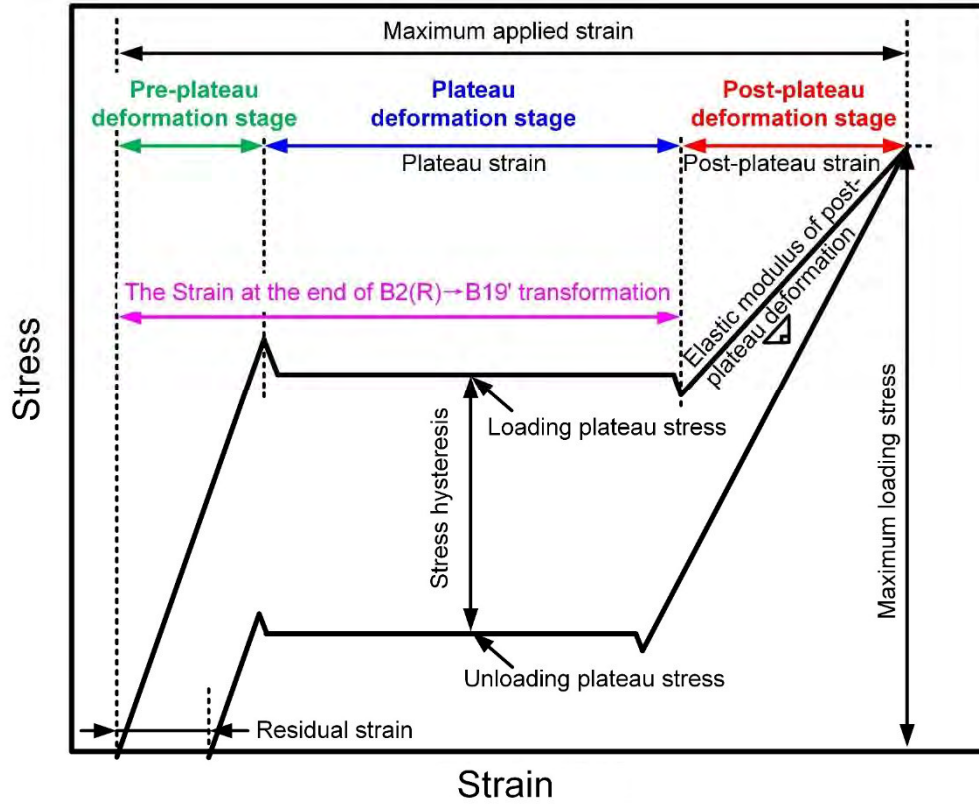
6.4 Superelastic stress-strain model considering the effects of LTA time and grain size.....	193
6.4.1 E_{req} function.....	194
6.4.2 E_{pre} function	196
6.4.3 Y function	197
6.4.4 ε_{mf} function.....	199
6.4.5 E_{post} function	200
6.4.6 E_{m} function.....	202
6.4.7 f_{T} function.....	204
6.4.8 $\varepsilon_{\text{risd}}$ function.....	207
6.5 Model validation and verification	212
6.5.1 Effectiveness validation	212
6.5.2 Accuracy verification.....	214
6.6 Summary.....	218
Chapter 7 Conclusions and suggestions for future research	220
7.1 Conclusions	220
7.2 Suggestions for future research	226
References.....	228

Table of nomenclature and units

Terminology	Abbreviation	Variable	Unit	Explanation
Low-temperature aging	LTA			Aging temperature smaller than 600 K
Nanocrystalline or nanograin	NC			Grain size ≤ 100 nm
Ultrafine grain	UFG			$100 \text{ nm} < \text{Grain size} \leq 1 \mu\text{m}$
Coarse grain	CG			Grain size $\geq 1 \mu\text{m}$
Nanograin after LTA	ANC			
Coarse grain after LTA	ACG			
Grain size	GS		nm or μm	
B2 austenite phase	B2 or A			High-temperature phase in NiTi alloys
R-phase	R			Intermediate phase in NiTi alloys
B19' martensite phase	B19' or M			Low-temperature phase in NiTi alloys
Ni ₄ Ti ₃ phase	Ni ₄ Ti ₃			Metastable precipitates in Ni-rich NiTi alloys
Two-way transformation	\leftrightarrow			A two-way transformation includes a forward transformation and a backward transformation
One-way transformation	\rightarrow or \leftarrow			\rightarrow represents forward transformation and \leftarrow represents backward transformation
Differential scanning calorimetry	DSC			
Transmission electron microscope	TEM			
Transformation enthalpy	ΔH	ΔH	J/g	The integration of transformation peaks
Transformation thermal hysteresis	TH	TH	K	The temperature difference between the forward and backward transformation
Loading plateau stress	σ_{lps}	σ_{lps}	MPa	Critical stress for activating B2(R) \rightarrow B19' transformation during superelasticity test
Unloading plateau stress	σ_{ulps}	σ_{ulps}	MPa	Critical stress for activating B19' \rightarrow B2(R) transformation during superelasticity test
Transformation stress hysteresis	$\sigma_{\text{hysteresis}}$	$\sigma_{\text{hysteresis}}$	MPa	The difference between loading and unloading plateau stress
Maximum loading stress	σ_{max}	σ_{max}	MPa	The maximum stress the superelastic stress reached before unloading.
Maximum applied strain	ϵ_{max}	ϵ_{max}		The maximum applied strain the superelastic deformation experienced.
Residual strain	ϵ_{risd}	ϵ_{risd}		See Fig. 6.6 for detail

Terminology	Abbreviation	Variable	Unit	Explanation
Pre-plateau deformation stage				Deformation stage before reaching B2(R)→B19' transformation plateau (see Fig. 6.6 for detail).
Plateau deformation stage				Deformation stage between the start and end of B2(R)→B19' transformation plateau deformation (see Fig. 6.6 for detail).
Plateau strain				The strain of plateau deformation stage
Post-plateau deformation stage				Deformation stage between the end of B2(R)→B19' transformation plateau deformation and the maximum applied strain (see Fig. 6.6 for detail).
Post-plateau strain				The strain of post-plateau deformation stage
The elastic modulus of B2 or R-phase	E_{pre}	E_{pre}	MPa	See Fig. 6.6 for detail.
The equivalent elastic modulus of B2↔R transformation related deformation	E_{rreq}	E_{rreq}	MPa	See Fig. 6.6 for detail.
The elastic modulus of post-plateau deformation	E_{post}	E_{post}	MPa	See Fig. 6.6 for detail.
Unloading elastic modulus of B19' phase	E_m	E_m	MPa	See Fig. 6.6 for detail.
The finish strain of B2(R)→B19' transformation	ϵ_{mf}	ϵ_{mf}		See Fig. 6.6 for detail.
The strain of B2→R related deformation	ϵ_{rrf}	ϵ_{rrf}		See Fig. 6.6 for detail.
Correlation coefficient	R			$R = \frac{\sum_{i=1}^n (E_i - \bar{E})(P_i - \bar{P})}{\sqrt{\sum_{i=1}^n (E_i - \bar{E})^2} \sqrt{\sum_{i=1}^n (P_i - \bar{P})^2}}$ See Eq. (3.5) for detail.
Average absolute relative error	AARE(%)			$AARE(\%) = \frac{1}{N} \sum_{i=1}^N \left \frac{E_i - P_i}{E_i} \right \times 100$ See Eq. (3.6) for detail.

Schematic plot of superelastic indices



Chapter 1 Introduction

1.1 Background

Owing to the superior superelasticity and shape memory effect, NiTi shape memory alloys (NiTi alloys for abbreviation) have been widely used in biomedical, aviation, MEMS, civil engineering fields, etc. [1], as shown in **Fig. 1.1**. The nature of the functional properties of NiTi alloys is the phase transformations among B2 austenite phase, B19' martensite phase, and the intermediate R-phase [2, 3]. The phase transformations can be induced by both the alterations of temperature and/or stress [4, 5], and can be affected by composition and microstructure [6-10]. Therefore, tailoring of the functional properties of NiTi alloys via alteration of composition and microstructure has always been the research focus [11].

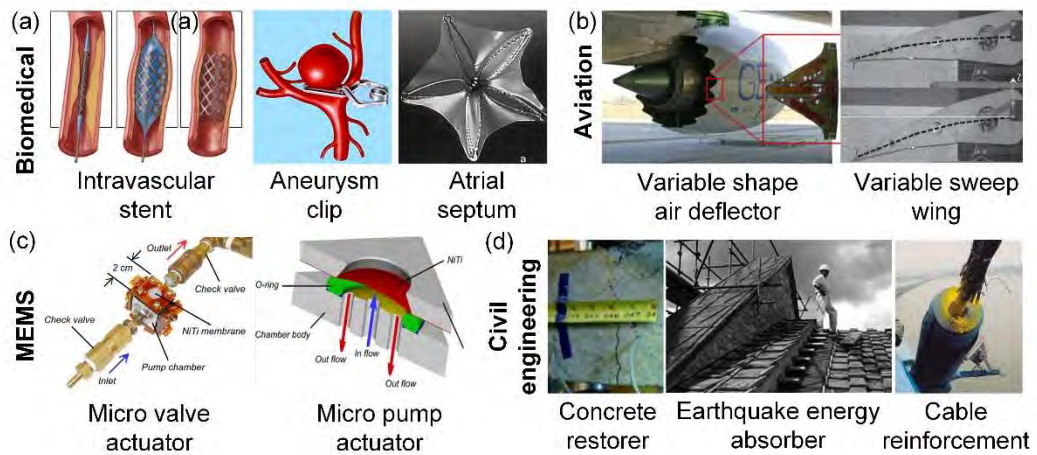


Fig. 1.1 The application of NiTi alloys in (a) biomedical [12-16]; (b) aviation [17-20]; (c) MEMS [2, 21-23]; (d) civil engineering [24-27] fields.

The NiTi alloys were firstly developed in the U.S. Naval Ordnance Laboratory in 1960s. After that, several methods for functional property adjustment were

developed, including adding alloying element [6, 7], altering Ni-Ti atomic ratio [8], introducing precipitates in Ni-rich NiTi matrix [9], introducing dislocation structure via plastic deformation [10], etc. However, the target of these methods was mainly the coarse-grained (CG) NiTi alloys (grain size $> 1 \mu\text{m}$) in the early research stage, as shown in **Fig. 1.2(a)**. It was until the late 1990s, the advent of nanocrystalline (NC, grain size $\leq 100 \text{ nm}$) and ultrafine-grained (UFG, $100 \text{ nm} < \text{grain size} \leq 1 \mu\text{m}$) NiTi alloys [28-30], as shown in **Fig. 1.2(b)** and (c), aroused the exploration of their phase transformations and functional properties in both academic and industrial fields.

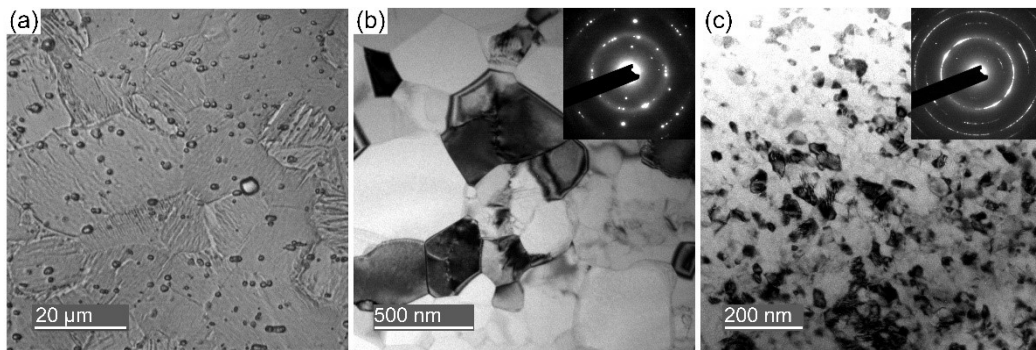


Fig. 1.2 Microstructure of NiTi alloys with different grain sizes: (a) coarse grains; (b) ultrafine grains; (c) nanocrystalline.

The NC and UFG NiTi alloys not only possess functional properties like the CG ones [31-33], but they also present higher strength (above 2 GPa) [34, 35], hardness (above 500 HV), elastic modulus (above 70 GPa) [35, 36], fatigue resistance [37, 38], corrosion resistance [39, 40], and lower cytotoxicity [40] than the CG ones. However, the advent of NC and UFG NiTi alloys brought out the challenges to their application. On one hand, the decreasing grain size from CG to UFG and even to NC scale affects the functional properties of the NiTi alloys [31, 32]. For instance, NC NiTi alloys possess special superelasticity (e.g., higher

plateau stress, higher recoverable strain, etc.) which is different from that of the CG ones [41]. On the other hand, the experiences and knowledge of the functional property adjustment of CG NiTi alloys are not completely applicable to NC and UFG NiTi alloys [42]. It is difficult to introduce additional dislocations to adjust the functional properties of NC NiTi alloys, because the nano-sized grains present a superior slip resistance [43]. Therefore, the recent researches are more focused on addressing two basic issues: 1) how does the NC and UFG grain size affect phase transformation and superelasticity of NiTi alloys? 2) how to further adjust phase transformation and superelasticity of the NiTi alloys if their grain size is fixed?

In tandem with this, many studies have been conducted to answer the first question, focusing on the effect of grain size on the phase transformation and superelasticity; to the second question, however, the solution is so far not very desirable. Some scholars suggested an idea to adjust the phase transformation and superelasticity by varying grain size [44-46], and the idea turns out to be effective as per the experimental results. However, this idea has inherent drawbacks: Though the functional properties can be varied when the grain size is changed, the other superior properties owned by the NC or UFG grain size can also be deteriorated such as the strength, hardness, fatigue and corrosion resistance, etc. That is to say, a trade-off between functional properties and other superior properties must be made when this method is employed. Therefore, how to address this dilemma becomes the frontier of this research field.

The current study proposed a method, by using aging, to alter the functional properties via simultaneously keeping the original grain size of NC, UFG, and CG NiTi alloys, i.e., it can alter the functional properties and simultaneously remain other superior properties owned by the original grain size. Thus, the aforementioned dilemma can be handled in this way.

In terms of aging, there are also two issues to solve, viz., 1) Before aging, by what means should the NiTi alloys with a certain grain size be obtained? and 2) under what conditions should the aging be conducted to alter the functional properties and simultaneously preserve the original grain size?

Regarding these two problems, some previous studies provided inspiration. During the procedure of obtaining NiTi alloys with different grain sizes, the undesired early aging should be avoided so that the NiTi matrix can be kept in Ni-rich state. As per the previous studies, this early aging can be effectively avoided by a short time heat treatment such as direct electrical resistance heat treatment (DERHT). With respect to the aging condition, the temperature and time should fulfill the requirements to cause precipitation while preserve the original grain size. This could be possible when the aging was conducted in low-temperature scale (aging temperature < 600 K [47]), which was named by J.I. Kim et al. [48] as “low-temperature aging (LTA)”. In addition, X.B. Wang et al. [49] applied the LTA of 523 K to NiTi alloys with the average grain size of 1.7 μm , and it turned out to be an effective way to alter the phase transformation and superelasticity of NiTi alloys, and the original grain size was kept. This proved that the LTA is an effective way

to alter the functional properties of CG NiTi alloys and simultaneously preserve the original grain size.

However, whether such LTA is also feasible for NC and UFG NiTi alloys remains unknown so far. Whether the influences of LTA on phase transformation and superelasticity of the NiTi alloys with different grain sizes are different is also not sure yet. Whether the microstructural evolutions of the NiTi alloys with different grain sizes are inherently different under LTA is also needed to be clarified. Addressing these issues is significant to realize the tailoring functional properties of NC, UFG, and CG NiTi alloys in the premise of preservation of the original grain size. Therefore, this study is to address the above issues respectively.

1.2 Research overview

1.2.1 NiTi shape memory alloys and their functional properties

NiTi shape memory alloys are near-equiatomic intermetallic compounds, whose main functional properties are superelasticity and shape memory effect [50]. Superelasticity means the shape can recover after unloading, with relative large recoverable strain, and the thermoelastic phase transformation happened during loading and unloading [51], as shown in **Fig. 1.3(a)**. Owing to the reversible martensitic transformation strain, NiTi alloys usually demonstrate a larger recoverable strain (as large as above 10%) than the pure elastic strain of common structural metals and alloys. Shape memory effect means that the plastic deformation of the materials can be recovered after they are heated to a certain temperature [50], as shown in **Fig. 1.3(b)**. This characteristic transfers heat to

kinetic energy, which is commonly used as the principle of actuators [52]. Among all types of shape memory alloys, NiTi alloys possess relatively higher strength and plasticity, ideal superelasticity and shape memory effect, higher service reliability, and better thermomechanical cyclic fatigue resistance [53].

In NiTi alloys, the thermoelastic martensitic transformation occurs between B2 austenite phase and B19' martensite phase, where B2 austenite phase is stable in higher temperature and B19' martensite phase is stable in lower temperature. Under a certain condition (introducing dislocations or precipitates, or reducing grain size), an intermediate R-phase can be involved between B2 and B19' phases [54]. Thus, the transformation sequence of NiTi alloys is $B2 \leftrightarrow (R) \leftrightarrow B19'$, as shown in **Fig. 1.3(c)** (B2 phase is of simple cubic lattice like CsCl, while B19' phase has monoclinic lattice, and R-phase has rhombohedral lattice). This phase transformation sequence can be thermally- and/or stress-induced, as shown in **Fig. 1.3(d)** and **(e)**.

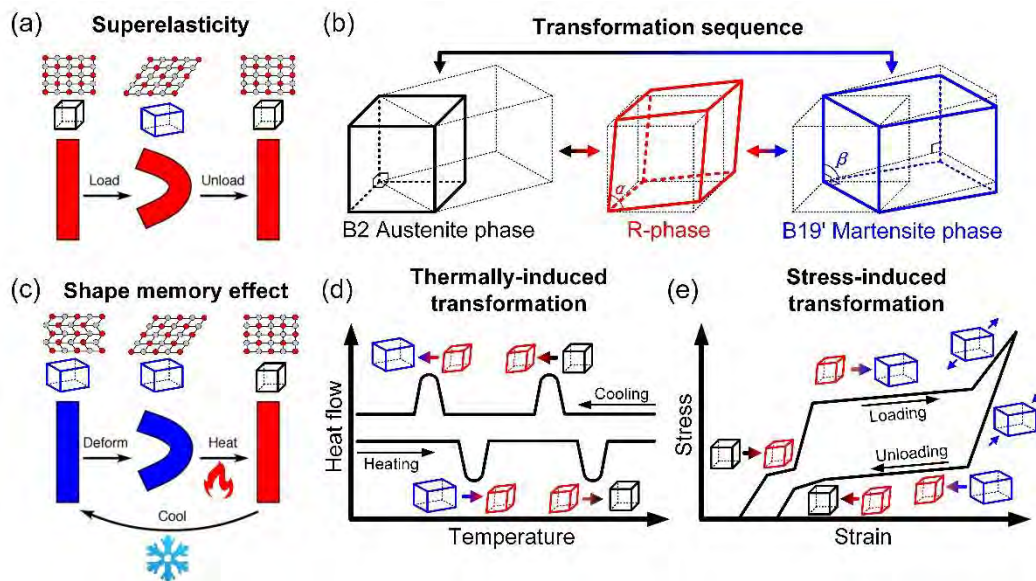


Fig. 1.3 Functional properties, lattice structure, and phase transformation of NiTi alloys: (a) superelasticity; (b) phase transformation sequence; (c) shape memory

effect; (d) thermally-induced phase transformation; (e) stress-induced phase transformation.

The functional properties of NiTi alloys are closely related to the service temperature [11]. As illustrated in **Fig. 1.4**, with the decrease of working temperature, the key temperatures of B2 \leftrightarrow B19' transformation sequentially arrive, which include M_d , A_f , A_s , M_s , and M_f . Among these key temperatures, M_d is the temperature at which B19' martensite can no longer be stress-induced; A_f is austenite-finish-temperature at which the B19' \rightarrow B2 transformation is finished; A_s is austenite-start-temperature at which the B19' \rightarrow B2 transformation starts; M_s is martensite-start-temperature at which the B2 \rightarrow B19' transformation starts; and M_f is martensite-finish-temperature at which the B2 \rightarrow B19' transformation is complete. The actual relationship among phase transformation, functional properties, and service temperature (T) is as follows:

- 1) When the service temperature is above M_d , stress can no longer induce B2 \rightarrow B19' transformation. NiTi alloys no longer possess functional properties.
- 2) When the service temperature is between M_d and A_f , NiTi alloys demonstrate superelasticity, the strain caused by the phase transformation can be completely recovered after unloading.
- 3) When the service temperature is between A_f and M_f , NiTi alloys show partly superelasticity and partly shape memory effect.
- 4) When the service temperature is below M_f , NiTi alloys show completely shape memory effect. The strain caused by the phase transformation can only be completely recovered after reheating to above A_f .

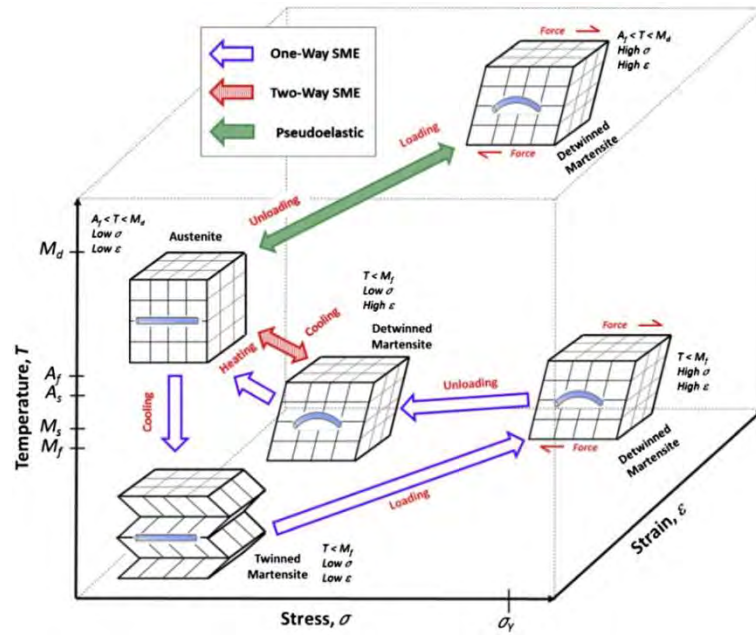


Fig. 1.4 Phase transformation and functional properties of NiTi alloys and the corresponding service temperatures [11].

It is worth noting that the above relationship is ideal, where only the $B2 \leftrightarrow B19'$ transformation is considered. Actually, other phenomena such as the dislocation activities, grain size variation, facilitation and suppression of phase transformations induced by Ni_4Ti_3 precipitates, etc. also influence the functional properties besides the key transformation temperatures.

Though NiTi alloys with different compositions and microstructures present different key transformation temperatures, the aforementioned relationships among the key transformation temperatures, service temperature, and functional properties are usually consistent. Thus, these key transformation temperatures, on one hand, restrict the service temperature range of a certain functional property, and, on the other hand, can be artificially altered to adjust the functional properties.

After years of research, scholars have found several key factors that influence the key transformation temperatures as follows:

- 1) Ni concentration [55]. The higher Ni concentration means the larger fraction of supersaturated Ni atoms, which impedes $B2 \rightarrow B19'$ transformation and correspondingly lowers the key transformation temperature.
- 2) Ternary elements [56]. Fe, Co, Cr, Mn, Mo, V, Nb, Cu, Pd, Hf, Zr, etc. can be used to replace Ni or Ti to form various solid solutions, so the key transformation temperatures can be altered.
- 3) Precipitates [57]. Ni-rich precipitates are able to be precipitated at 523~923 K, and the Ni_4Ti_3 , Ni_3Ti_2 , and Ni_3Ti can be sequentially dissolved out with aging time. The incoherent Ni_4Ti_3 , Ni_3Ti_2 , and Ni_3Ti can effectively reduce the Ni concentration of the NiTi matrix, and correspondingly elevate the key transformation temperatures. The coherent Ni_4Ti_3 can introduce elastic strain fields around the precipitates, which facilitate $B2 \leftrightarrow R$ transformation. The dense distribution of coherent Ni_4Ti_3 can impede the movement of $B2(R) \leftrightarrow B19'$ transformation frontier and also can elevate the dislocation slip resistance.
- 4) Dislocations [10]. The dislocations in the NiTi matrix can also impede the movement of $B2(R) \leftrightarrow B19'$ transformation frontier. The elastic strain fields around the dislocations can also facilitate $B2 \leftrightarrow R$ transformation.
- 5) Grain size [32, 58, 59]. In recent years, scholars have found that NC and UFG grain size can facilitate $B2 \leftrightarrow R$ transformation, impede and even completely suppress $B2(R) \leftrightarrow B19'$ transformation.

It can be summarized from the aforementioned key factors that appropriately introducing point defects (e.g., substitutional solute atoms), line defects (e.g. dislocations), and face defects (e.g., grain and phase boundaries) can remarkably alter the phase transformation characteristics and functional properties. This points out the principle of the functional property adjustment of NiTi alloys.

1.2.2 State-of-art of the influence of grain size on the properties of NiTi alloys

The studies of the influence of grain size on the properties of NiTi can be traced back to 2002 [34, 60, 61], which have gradually become research hotspot in recent years. The experimental results show that NC and UFG grain size of metallic materials lead to various advantages such as higher yield and ultimate strength [62], partitioned Hall-Petch relation [63, 64], moderate ductility [65], higher fatigue resistance [66], optimized toughness [67], and potential superplasticity [68] compared with the common CG ones. With respect to NiTi alloys, the influence of grain size on the functional properties is additionally concerned. The related studies have focused on the preparation of NC and UFG NiTi alloys, the microstructure identification, and the effect of NC and UFG grain size on the phase transformation characteristics, functional properties, and structural mechanical properties.

1.2.2.1 Preparation and microstructural identification of NC and UFG NiTi alloys

The preparation of NC and UFG NiTi alloys can be classified into “bottom-up” [69] and “top-down” [70, 71] methods. The “bottom-up” method mainly indicates

powder metallurgy [72, 73], which includes but not limited to magnetron sputtering technology [28], melt spinning technology [74-76], mechanical alloying technology [77, 78], high-energy ball milling process [79, 80], etc. The “top-down” method mainly includes severe plastic deformation plus post-deformation annealing [81-83] and surface nanocrystallization [84]. The “bottom-up” method is more fit for the preparation of porous or film NiTi alloys, while the “top-down” method is suitable for the preparation of dense and block NiTi alloys [85]. The NiTi alloys used in this study are NiTi wires, which are fabricated by the method of severe plastic deformation plus post-deformation annealing. Thus, this method is briefly introduced as follows.

The severe plastic deformation includes high pressure torsion (HPT) [86-88], equal channel angular extrusion (ECAE) [53, 89], cold rolling [90-94], cold drawing [35, 95, 96], groove rolling [97], local canning compression [98], etc. The obtained microstructures and defects of the NC and UFG via the above methods closely depend on the process. The main factors are as follows:

- 1) The initial state before the severe plastic deformation. Usually, solution treatment is used to eliminate work hardening and dissolve the previous precipitates.
- 2) Deformation degree. As the deformation degree increases, the NiTi alloys experience stress-induced martensitic transformation, detwinning of martensite phase, dislocation slip, severe shear deformation, and amorphization [98]. The degree of amorphization increases with the deformation degree [90], and the amorphous phase and grain debris distribute alternately [86, 87]. As the fraction of amorphous phase increases, the required

thermal energy for nanocrystallization decreases and the nanocrystallization temperature also decreases [91]. Under a small deformation degree, the nanocrystallization is led by grain growth; under large deformation degree, the nanocrystallization is accomplished via both crystal nucleation and grain growth [99]. Under the same post-deformation annealing condition, with the increasing deformation degree, the fraction of nanograin increases, the fraction of nanosubgrain decreases [93, 100], and the superelastic loading plateau stress increases [90]. The excessive deformation degree can cause more defects in the NiTi matrix and more cracks in the edges of samples, and the thermomechanical cyclic fatigue resistance will be impaired [92, 101-103].

- 3) Temperature and time of post-deformation annealing. The temperature affects nanocrystallization degree and grain size [104, 105]. Below the nanocrystallization temperature, the amorphous phase and grain debris are only recovered. Above the nanocrystallization temperature, the nanocrystallization happens and the grain size increases with annealing temperature and time. The optimized nanocrystallization temperature of amorphous NiTi was about 673 K [104, 106]. It is worth noting that excessive annealing time can lead to undesired precipitation [107].
- 4) The combination with the other deformation processes. Yann Facchinello et al. [108, 109] and A. Kreitzberg et al. [110, 111] studied the combination of cold rolling, intermediate annealing, and hot rolling. It is found that this process can reduce the process-induced defects and elevate the thermomechanical cyclic fatigue resistance. VV Stolyarov et al. [112] and R.F. Zhu et al. [113, 114] studied the effect of electroplastic rolling on the properties of the obtained nanocrystalline NiTi alloys. The results turn out that electroplastic rolling can

elevate the rolling deformation degree and produce nanocrystalline NiTi alloys directly without post-deformation annealing.

The microstructure of NC and UFG can be identified by transmission electron microscope (TEM) and selected area electron diffraction (SAED). S.D. Prokoshkin et al. [93, 100, 105, 115], V. Brailovski et al. [92], and K.E. Inaekyan et al. [116] identified various microstructures produced by different severe plastic deformation degree plus post-deformation annealing. The results show that the NiTi matrix is changed from nanosubgrain-dominant to nanocrystalline-dominant with the plastic strain increasing from 0.25 to 3. The nanosubgrains are usually of NC grain size and exists within the same ultrafine grain with low-angle grain boundary among each of them. The nanocrystalline is usually of NC grain size and individually exists in the NiTi matrix. SAED patterns are also used in these studies for microstructure identification.

1.2.2.2 Effect of NC and UFG grain size on the properties of NiTi alloys

After the advent of NC and UFG NiTi alloys, studies on the effect of grain size on the properties of NiTi alloys have become popular. These studies mainly focus on phase transformation characteristics, functional properties, and structural mechanical properties.

With respect to phase transformation characteristics, V.G. Pushin et al. [60, 61, 117, 118] found that thermally-induced B2→B19' transformation in NC NiTi alloys is in the form of "single crystal-to-single crystal", and the B19' twinned variant pairs were not observed. However, in UFG NiTi alloys, B19' martensite

phase in the form of twinned variant pairs was observed. T. Waitz et al. [31, 59, 119-123] further found that, as the grain size decreases into NC scale, the phase transformation sequence transfers from $B2 \rightarrow B19'$ to $B2 \leftrightarrow R \leftrightarrow B19'$. They also reported that, within NC grains, $B19'$ phase is of (001) compound twins, and the $R \leftrightarrow B19'$ transformation is completely suppressed when the grain size is less than 60 nm. After that, Gyu-Bong Cho et al. [124], Haitian Zhang et al. [125], and Xiaobin Shi et al. [58, 126] found that, with the decreasing grain size, $B2 \leftrightarrow R$ transformation temperature increases, $R \rightarrow B19'$ transformation temperature decreases, and $R \leftrightarrow B19'$ transformation thermal hysteresis increases. Thus it can be seen that, with the grain size decreasing from CG to UFG and further to NC scale, the twin type, the phase transformation sequence and temperature are all changed.

With respect to the functional properties, scholars mainly focus on the effect of grain size on superelasticity. This is not only because the superelasticity is the predominant functional property of NiTi alloys, but this is also due to the fact that NC NiTi alloys usually demonstrate superelasticity rather than shape memory effect [41]. The research teams of Q.P. Sun and Ahadi Aslan contributed plenty of works in this area [45, 127-129]. They found that the superelasticity stress-strain relationship of NiTi alloys with different grain sizes show different sensitivity to strain rate. Grain size affects stress hysteresis, and the temperature variation decreases with grain size during the superelastic loading-unloading process. Haitian Zhang et al. [125] found that plateau stresses increase with the decreasing grain size and also reported the thermally-suppressed $R \leftrightarrow B19'$ can be stress-induced. K.A. Polyakova-Vachiyan et al. [130] found that plateau strain varied

with grain size. S.D. Prokoshkin et al. [107] pointed out that nanocrystalline presented higher dislocation slip resistance than nanosubgrain even when the grain sizes are similar. Yao Xiao et al. [44] studied the NiTi alloys with the grain size less than 30 nm and found that the deformation is homogeneous when the grain size is below 14 nm, while it becomes Lüders-like deformation when the grain size is above 14 nm. They also indicate that the superelasticity of NC NiTi alloys can be adjusted by varying grain size. T. Tadaki et al. [131] found that NiTi alloys after cold rolling show linear superelasticity with small stress hysteresis, and the matrix is in a laminated structure with the width of about 200 nm. Y.F. Zheng et al. [132] found that NiTi alloys after cold drawing also present linear superelasticity, and the (001) compound twins replace the type II <001> twins. K. Tsuchiya et al. [35] owed this linear superelasticity to the combination of nanoscale $B2 \leftrightarrow B19'$ transformation and the elastic deformation of the amorphous phase.

With respect to the structural mechanical properties, A.V. Sergueeva et al. [34] found that NC NiTi alloys show the ultimate tensile strength of 2650 MPa and ductility of about 5%. They also pointed out that NC NiTi alloys possess superplasticity when the deformation temperature reaches 0.4-0.5 of the melt point. Q.S. Mei et al. [36] reported that the measured elastic modulus increases with the decreasing grain size, and they owed this to the suppression of $B2(R) \rightarrow B19'$ induced by the decreasing NC grain size. Ruslan Valiev et al. [133] found that the stress-induced $B2(R) \rightarrow B19'$ transformation elevates the ductility of NiTi alloys, and the ductility is decreased when the deformation temperature elevates to above M_d . Hao Yin et al. [37] reported that low-cycle fatigue resistance increased when

the grain size decreased from 80 to 10 nm. Aafonina V.S. et al. [134] pointed out that NC and UFG NiTi alloys possess higher strength and thermomechanical cyclic stability than the CG ones, which are more suitable for superelastic applications.

In summary, NC and UFG NiTi alloys not only demonstrate different phase transformation characteristics and functional properties from CG ones, but they also show higher strength, fatigue resistance, and thermomechanical cyclic stability than the CG ones. This further indicates that not only the phase transformation characteristics and functional properties change with the varying grain size, but the structural mechanical properties are also varied. Therefore, simply by the method of varying grain size, the functional property adjustment will be compromised by the variation of structural mechanical properties, which reflects the inherent limitation of the method.

1.2.3 State-of-art of the influence of aging on the properties of NiTi alloys

Studies concerning the influence of aging on the properties of NiTi alloys can be traced back to 1984 when M. Nishida et al. [135-137] introduced precipitates in a Ni-riched NiTi alloy by aging. The precipitates are regarded as $\text{Ni}_{14}\text{Ti}_{11}$ [136] at first and are clarified as Ni_4Ti_3 later by experimental evidence [138].

In the following decades, the studies of the influence of aging had been limited in CG NiTi alloys before the advent of NC and UFG NiTi alloys. Scholars learnt a

lot about the effect of aging on the properties of CG NiTi alloys and the underlying mechanisms, and the corresponding processes were also understood. The knowledge and experiences were gradually accumulated towards this issue [9, 139-141]. Within this period, the concept of low-temperature aging (LTA) (aging temperature was less than 600 K) was firstly proposed by J.I. Kim et al. [47, 48]. As per the experimental results, LTA leads to the nanoprecipitation of Ni_4Ti_3 which greatly affects the properties of CG NiTi alloys. Xiebin Wang et al. [49] carried out LTA of 523 K to NiTi alloys with the average grain size of 1.7 μm , which proves that the LTA can effectively alter the properties of the CG NiTi alloys. After the advent of NC and UFG NiTi alloys [28], most scholars focus on the influence of grain size. It is not until 2010 when a few studies began to concern the aging of NC and UFG NiTi alloys [142]. However, these researches were conducted under non-LTA conditions (aging temperature larger than 600 K) so that the obtained Ni_4Ti_3 particles are of larger size. There is little research on the effect of LTA on NC and UFG NiTi alloys.

It is noteworthy that Ti-rich NiTi alloys can precipitate Ti_2Ni after aging, which can elevate Ni concentration of the NiTi matrix. However, the functional properties of the Ti-rich NiTi alloys are less sensitive than the Ni-rich ones regarding the Ni concentration [8]. Therefore, in practice, aging is used more commonly in Ni-rich NiTi alloys to adjust the functional properties. The present work thus adopts a Ni_{50.8 at.%}-Ti alloy for the study of LTA.

1.2.3.1 Influence of aging on CG NiTi alloys

Since 1984, aging has become an important method to adjust the functional properties of CG NiTi alloys. The principle is that aging can precipitate Ni-rich particles from Ni-riched NiTi matrix, as indicated by the Ni-Ti phase diagram [50] shown in **Fig. 1.5(a)**. there are three kinds of precipitates in Ni-riched NiTi alloys, i.e., Ni_3Ti , Ni_3Ti_2 , and Ni_4Ti_3 . Ni_3Ti is equilibrium phase, whilst Ni_3Ti_2 and Ni_4Ti_3 are non-equilibrium phases. The precipitation sequence is usually $\text{Ni}_4\text{Ti}_3 \rightarrow \text{Ni}_3\text{Ti}_2 \rightarrow \text{Ni}_3\text{Ti}$ depending on aging temperature and time, as shown in **Fig. 1.5(b)**.

Among the three precipitates, Ni_3Ti_2 and Ni_3Ti require higher aging temperature (e.g., at 873 K) and longer aging time (e.g., after 10 h) for precipitation. They are both incoherent precipitates with size ranging from hundred nanometers to even several micrometers. They usually distribute separately with few amounts, and have little influence on the functional properties of NiTi alloys. Ni_4Ti_3 , however, is able to be precipitated even at a lower aging temperature (e.g., at 473 K) and a shorter aging time (e.g., within 0.5 h). The size of Ni_4Ti_3 is ranging from several nanometers to hundreds of nanometers, and the Ni_4Ti_3 precipitates with small size are coherent with NiTi matrix. The precipitates are usually of the large number and dispersedly distributed in the matrix.

Ni_4Ti_3 affects the functional properties of NiTi alloys from two aspects: 1) numerous and the dispersed distribution of Ni_4Ti_3 remarkably reduces the Ni concentration of the NiTi matrix [143]; 2) coherent Ni_4Ti_3 introduces elastic strain field at the adjacent NiTi matrix [144]. Besides, Ni_4Ti_3 is of higher hardness than

NiTi matrix [145], and the dispersedly distributed Ni_4Ti_3 also impedes the dislocation activity in NiTi matrix, which effectively influences both the functional properties and the structural mechanical properties of NiTi alloys. Therefore, the alteration of Ni_4Ti_3 precipitates can effectively adjust phase transformation characteristics, functional properties, and structural mechanical properties of CG NiTi alloys.

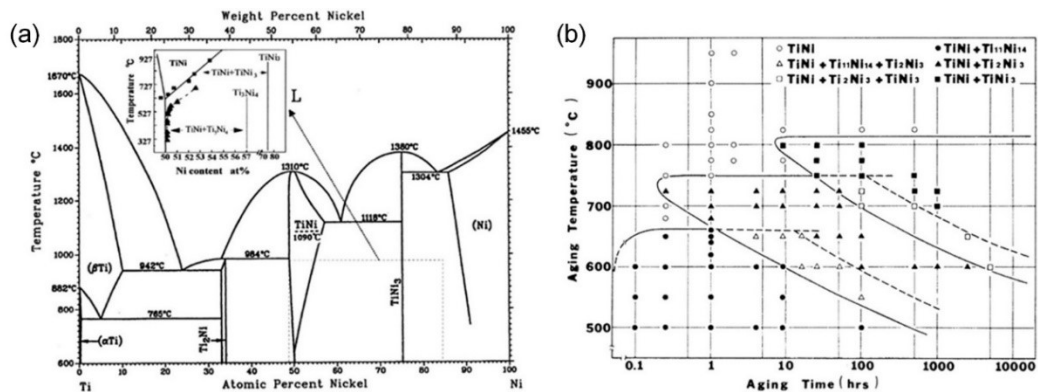


Fig. 1.5 Influence of aging on NiTi alloys: (a) phase diagram and (b) schematic illustration of aging temperature-aging time-aging product relationship [57].

Among numerous studies on the aging-induced functional property adjustment of CG NiTi alloys, K. Otsuka et al. [146] found that Ni_4Ti_3 precipitates can transfer transformation sequence from $\text{B2} \leftrightarrow \text{B19}'$ to $\text{B2} \leftrightarrow \text{R} \leftrightarrow \text{B19}'$, and it can also alter the $\text{B2} \leftrightarrow \text{R} \leftrightarrow \text{B19}'$ transformation temperatures. Wim Tirry et al. [144, 147] experimentally observed the elastic strain fields and Ni-depletion zones around the Ni_4Ti_3 precipitates and pointed out that these phenomena are the reasons for the change of phase transformation characteristics led by the precipitates. D.Y. Cong et al. [148] implemented the aging of 773 K to a solution-treated NiTi alloy and investigated the effect of precipitates size on the mechanical properties of CG NiTi

alloys. The results show that $R \leftrightarrow B19'$ transformation temperatures increase with the increasing fraction and size of Ni_4Ti_3 precipitates, but the $B2 \leftrightarrow R$ transformation temperatures are slightly elevated. Kamel Kazemi-Choobi et al. [149] found that higher aging temperature after cold working leads to lower plateau stress and larger residual strain. B. Karbakhsh Ravari et al. [150, 151] investigated the effect of aging of 773 K-1 h on NiTi alloys with different compositions. They reported that multiple phase transformation happen after the aging while the transformation sequences depend on the composition of the NiTi alloys. Jafar Khalil-Allafi et al. [9] owed the discrepancy of transformation sequence to the inhomogeneous distribution of Ni_4Ti_3 from grain inners to grain boundaries.

It can be seen from the above studies that aging leads to the precipitation of Ni_4Ti_3 in Ni-riched CG NiTi alloys, and its influences are as follows: 1) transformation sequence is transferred from $B2 \leftrightarrow B19'$ to $B2 \leftrightarrow R \leftrightarrow B19'$; 2) multiple transformation may appeared after aging; 3) $R \leftrightarrow B19'$ transformation temperature and thermal hysteresis increase with the precipitation of Ni_4Ti_3 ; 4) $B2 \leftrightarrow R$ transformation temperature slightly increase with the precipitation of Ni_4Ti_3 , and the $B2 \leftrightarrow R$ transformation thermal hysteresis is hardly affected; 5) aging leads to precipitation strengthening on the NiTi matrix.

1.2.3.2 Influence of aging on NC and UFG NiTi alloys

Though there are many studies on the aging of CG NiTi alloys, those on the aging of NC and UFG NiTi alloys are only a few. V. Abbasi-Chianeh et al. [152] carried out the aging of 723 K on the NiTi alloys with the plastic strain of 0.4 and 0.6. The

results show that, after aging, the NiTi alloy with 0.4 plastic strain becomes the recovered microstructure containing Ni₄Ti₃ precipitates, and that with 0.6 plastic strain becomes NC microstructure without Ni₄Ti₃ precipitates. E.P. Ryklina et al. [153] applied the aging of 703-723 K to CG NiTi alloys with 0.3 and 1.5 plastic strain. The results indicate that the functional properties of UFG and CG NiTi alloys are able to be altered by varying aging time, while those of NC NiTi alloys are barely influenced. E. Prokofiev et al. [142, 154] adopted the aging of 673 K to representative NC and UFG NiTi alloys, and the Ni₄Ti₃ precipitates were not observed in NC NiTi alloys.

The above studies indicate that, even under the same aging conditions, NC and UFG NiTi alloys response differently from CG NiTi alloys. Aging can introduce Ni₄Ti₃ precipitates in CG NiTi alloys with experimental evidence. However, whether it can also precipitate Ni₄Ti₃ in NC and UFG NiTi alloys are still not sure. The studies about the aging of NC and UFG NiTi alloys are generally in the preliminary stage and lack the comprehensive analyses from the aspects of microstructure, phase transformation, and superelasticity. Furthermore, the influence of low-temperature aging on NiTi alloys with different grain sizes (ranging from NC to UFG and further to CG) is not clear and calls for further study.

1.2.3.3 Influence of low-temperature aging on NiTi alloys

In 2002, J.I. Kim et al. [48, 155] proposed the concept of LTA, and they carried out LTA on CG NiTi alloys. The results show that LTA of 373 K is inadequate to precipitate Ni₄Ti₃; LTA of 473 K leads to the precipitation of Ni₄Ti₃ after 100 h, and the size of Ni₄Ti₃ increases to 5 nm after 3000 h; LTA of 573 K introduces

Ni_4Ti_3 particles after 0.3 h, and the size of Ni_4Ti_3 increases to 40 nm after 3000 h. The results further indicate that, when the size of Ni_4Ti_3 is below 15 nm, the increasing density of Ni_4Ti_3 can lead to the increase of dislocation slip resistance; when the size of Ni_4Ti_3 further increases to above 15 nm, the space among precipitates increases and the dislocation slip resistance decreases. Besides, during LTA, the Ni_4Ti_3 nucleation is easier than its growth, so the number of Ni_4Ti_3 increases with the LTA time while the size of Ni_4Ti_3 increases slowly. The functional properties thus benefit from these densely distributed Ni_4Ti_3 nanoprecipitates. J.I. Kim et al. [155] also pointed out that $\text{B2} \leftrightarrow \text{R}$ transformation temperature increases with aging time under the LTA of 473 K. This is different from the results under the non-LTA conditions [148], which indicates LTA is more effective to vary $\text{B2} \leftrightarrow \text{R}$ transformation temperature than the non-LTA. By comparing the results from Yumei Zhou et al. [156] and Genlian Fan et al. [157], it can be seen that LTA is inadequate for the long-range diffusion of Ni atom, while the non-LTA is adequate for the long-range diffusion. Shuyong Jiang et al. [158] studied the effect of LTA and non-LTA on CG NiTi alloys. The results show that the densely distributed coherent Ni_4Ti_3 precipitates effectively impede dislocation slip, while the dispersedly distributed incoherent Ni_4Ti_3 precipitates are less effective.

Based on these researches, Xiebin Wang et al. [49] studied the effect of LTA (at 523 K, within 1-500 h) on the phase transformation and superelasticity of CG NiTi alloys (average grain size of 1.7 μm). The results show that LTA at 523 K and within 24-100 h suppressed $\text{R} \leftrightarrow \text{B19}'$ transformation, and the plastic deformation

during loading-unloading is suppressed by the Ni_4Ti_3 nanoprecipitates. They also reported that LTA facilitates $\text{B2} \leftrightarrow \text{R}$ transformation [159].

It can be summarized from the above studies that 1) LTA leads to the nanoprecipitation of Ni_4Ti_3 (with size from several nanometers to tens of nanometers), and the Ni_4Ti_3 precipitates induced by LTA are of smaller size and distribute more densely than those induced by non-LTA; 2) the Ni_4Ti_3 nanoprecipitates can remarkably alter the phase transformation characteristics, functional properties, and structural mechanical properties of NiTi alloys, which is different from those led by the non-LTA; 3) even in micrograin-sized NiTi alloys, LTA can introduce Ni_4Ti_3 nanoprecipitates and consequently alter the properties of the NiTi alloys. This indicates that LTA has the ability to realize the functional property adjustment for the grain-refined NiTi alloys, which points out the direction of the functional property adjustment of NC and UFG NiTi alloys, i.e., by using LTA.

However, it also can be seen from the above researches that 1) the studies of aging on NC and UFG NiTi alloys are mainly at non-LTA condition, while the effect of LTA on UC and UFG NiTi alloys is seldom concerned; 2) the studies of LTA have been mainly focused on CG NiTi alloys so far, while those focus on NC and UFG NiTi alloys are very few. Therefore, it is significant to study the influence of LTA on the properties of NiTi alloys with different grain sizes (including NC, UFG, and CG), which will provide references and facilitate the understanding of the above issues.

1.2.4 State-of-art of the superelastic stress-strain models of NiTi alloys

The superelastic stress-strain model of NiTi alloys possesses significant value for engineering application. It is used to calculate the loading-unloading stress-strain relations and of great importance for the materials selection and functional simulation of superelasticity devices. During decades of development, the models have been systematically studied and can be mainly classified as macroscopic phenomenological models and microscopic mechanical models [160-162].

The macroscopic phenomenological models are mainly based on macro experimental results and approximately describe the macroscopic deformation behavior. These models are mostly based on the thermomechanical framework, where martensite fraction is generally treated as the function of stress and temperature. The representative ones include Tanaka-Liang-Brinson models [163-165], B. Raniecki model [166], R. Abeyaratne model [167], Auricchio model [168, 169], Graesser model [170], etc.

The microscopic mechanical models are mainly based on the lattice variations of B2 \leftrightarrow B19' transformation, which describe the relationship between deformation and phase transformation of NiTi alloys from the lattice strain of different B19' martensite variants. They are more suitable for the calculation of deformation strain and the phase-mixture state. The representative ones include Patoor model [171], Falk model [172], Peultier model [173], Chao Yu models [174-180], etc.

As the effect of grain size on the properties of NiTi alloys becomes research hotspot, the stress-strain models regarding this issue also emerge in recent years. Q.P. Sun et al. [127, 181] established the stress-strain model considering the effects of grain size and the thickness of grain boundaries. Based on the fraction of B19' martensite phase and gradient-dependent plasticity theory, L. Qiao et al. [161, 182] established the stress-strain model considering the constraint effect of grain boundaries. Chao Yu et al. [178, 179] regarded the NiTi alloys as the mixture of grain inner and grain boundaries and established the microscopic mechanical stress-strain model considering the effect of grain size.

Among the superelastic stress-strain models which consider the effect of grain size, it can hardly find a stress-strain model which considers both the effect of grain size and LTA on the superelasticity of NiTi alloys. However, this type of model is significant for the LTA induced functional property adjustment of NiTi alloys with different grain sizes. It thus deserves further investigation. For clarification, the term "stress-strain model" in this study describes the relation between effective stress and effective strain but not the stress and strain tensors.

1.3 Outline of the thesis

It can be seen from the research overview that the functional property adjustment has always been the key issue of the NiTi alloys. However, this adjustment is challenged by the advent of NC and UFG NiTi alloys, because the knowledge and experiences that are fit for CG NiTi alloys are no longer completely suitable for the NC and UFG ones. Though the functional properties of NC and UFG NiTi

alloys can be directly altered by varying grain size, the superior structural mechanical properties induced by the grain-refine strengthening can also be deteriorated. Therefore, both industrial and academic fields are eager for a functional property adjustment method for NC and UFG NiTi alloys in the premise of the preservation of original grain size.

The LTA is an effective solution for this issue. On one hand, LTA can lead to nanoprecipitation in NiTi matrix, and, on the other hand, LTA can avoid undesired grain growth as happened during non-LTA which is beneficial for the preservation of the original grain size and the relative superior properties of NC and UFG NiTi alloys.

Though the aging of NC and UFG NiTi alloys has received some concerns so far, the studies are still mainly in the preliminary stage. The aging was mainly carried out under non-LTA conditions, while the LTA is seldom studied. Since the concept of the LTA of NiTi alloys was proposed in 2004, the relative studies are mainly confined to CG NiTi alloys, and the studies on the LTA of NC and UFG NiTi alloys are very few.

Therefore, to study the influence of LTA on the phase transformation and superelasticity of NiTi alloys with different grain sizes (including NC, UFG, and CG) becomes the research frontiers of these two branches, which has both scientific and engineering significance.

This study focused on the influence of LTA on the phase transformation and superelasticity of NiTi alloys with various grain sizes (ranging from NC to CG scale). The Ni_{50.8 at.%}-Ti is studied as the representative Ni-rich NiTi alloys. The phase transformation, as the basis of functional properties, is studied from the aspects of transformation sequence, temperature, thermal hysteresis, enthalpy, etc. The superelasticity, as the representative functional properties of NC, UFG, and CG NiTi alloys, is studied from the aspects of loading and unloading plateau stress, plateau strain, stress hysteresis, post-plateau modulus, residual strain, etc. In addition, microstructural evolution (including grain size, phase constituent, precipitates, etc.) and the hardness variation of the NiTi alloys with various grain sizes subjected to different LTA are further studied to analyse the underlying mechanism of the influence of LTA. In the end, models of phase transformation temperature, stress hysteresis, and superelastic stress-strain relation considering the influence of LTA and grain size are established. The details of each chapter are described as follows, where the technical route and the logic of different chapters is showed in **Fig. 1.6**.

Chapter 1 provides a brief research overview of the influence of grain size and aging on the properties of NiTi alloys. The significance of the study of the influence of LTA on phase transformation and superelasticity of NiTi alloys with different grain sizes is pointed out, and the main research contents are listed.

Chapter 2 describes the different responses of NC and CG NiTi alloys to LTA. The feasibility of the LTA-induced functional property adjustment is identified.

The key indices of microstructures, phase transformation characteristics, and superelasticity to be studied in the following chapters are determined.

Chapter 3 presents the effect of DERHT on the properties of NiTi alloys with different grain sizes and aging states. The effects of short time LTA via DERHT (0-600 s) on NiTi alloys are also demonstrated. The underlying mechanisms of the influence of DERHT are analyzed based on the microstructural evolution and hardness variation. In the end, the grain size adjustment models based on DERHT are given, and NiTi alloys with grain size from 34 to 8021 nm are consequently obtained for the studies in the following chapters.

Chapter 4 demonstrates the effect of LTA (at 573 K, under 0-48 h) on phase transformation characteristics of NiTi alloys with different grain sizes (34-8021 nm). The changes in transformation sequence, temperature, thermal hysteresis, enthalpy, etc. are studied. The evolutions of $B2 \leftrightarrow R$ and $B2(R) \leftrightarrow B19'$ transformation temperatures with grain size and LTA time are provided, and the underlying mechanisms are studied based on the microstructural evolution and hardness variation. In the end, $B2 \leftrightarrow R$ transformation temperature model considering the effect of LTA time and grain size is proposed.

Chapter 5 articulates the effect of LTA (at 573 K, under 0-48 h) on superelasticity of NiTi alloys with different grain sizes (34-8021 nm). Superelasticity at the maximum strain of 3% and 9% are comparatively studied based on the analyses of loading and unloading plateau stress, plateau strain, stress hysteresis, residual strain, etc. The mechanisms of the influence of LTA on superelasticity are studied

based on the microstructural evolution, hardness variation, and the variations of phase transformation characteristics. In the end, the stress hysteresis model considering the effect of LTA time and grain size is suggested.

Chapter 6 suggests a modified Graesser superelastic stress-strain model based on the experimental results from the previous chapters. The model reflects the influence of LTA time and grain size on superelasticity.

Chapter 7 concludes this thesis and provides summaries of the present researches. In addition, future work is also introduced.

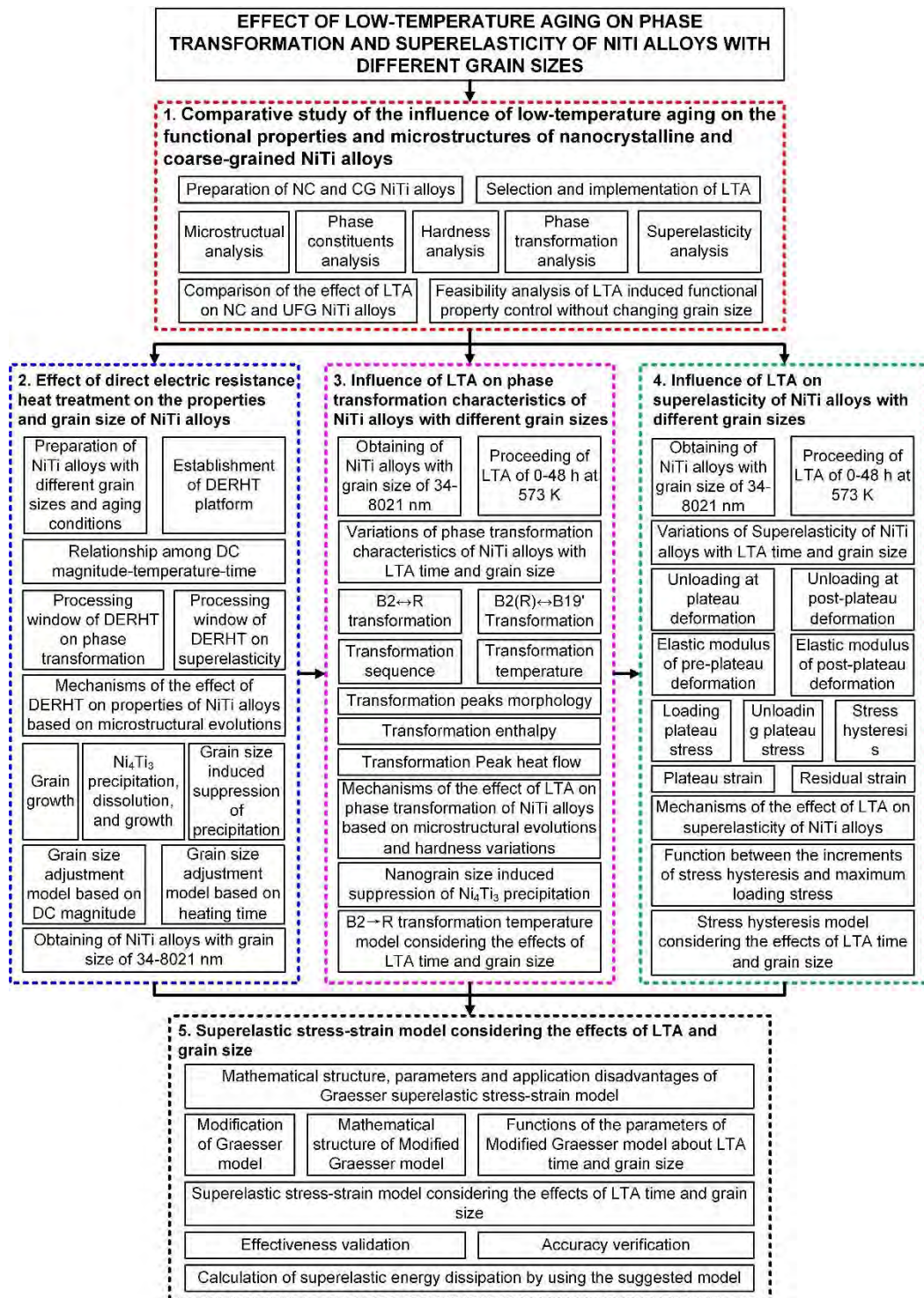


Fig. 1.6 Schematic illustration of the technical route and logic of different chapters

Chapter 2 Comparative study of the influence of low-temperature aging on the functional properties and microstructures of nanocrystalline and coarse-grained NiTi alloys

2.1 Introduction

The NiTi alloys with representative NC and CG grain sizes are comparatively studied in this chapter. The responses of these two alloys to the same LTA parameters are comparatively investigated regarding microstructures, phase transformation characteristics, and superelastic indices. The reasons for the discrepancies are preliminarily probed. The feasibility of the LTA-induced functional property adjustment is determined, and the research issues of the following chapters are pointed out.

2.2 Materials preparation and experimental procedure

2.2.1 Preparation of NC and CG NiTi alloys

The representative NC and CG NiTi alloys were prepared for the study. The NC NiTi alloy was nanocrystalline provided by (Peiertech Co. In.), which was in the

wire shape and with a diameter of 1 ± 0.01 mm. The composition of the as-received NiTi alloy is as shown in **Table 2.1**. The NiTi alloy consists of numerous nanograins and a few nano-subgrains, as shown in **Fig. 2.1**. The as-received NC alloy was fabricated through severe plastic deformation plus post-deformation annealing, and the process procedure is as shown in **Fig. 2.2**. Before receiving, the material had been sequentially subjected to solution treatment of 1073 K-30 min, cold drawing with the plastic strain of 1.02, and post-deformation annealing of 673 K-10 min. The CG NiTi alloy was prepared from the NC NiTi alloy, which was solution treated at 1123 K-2 h and cooled by the flowing cold argon in the furnace. The process and obtained microstructure are shown in **Fig. 2.3**.

Table 2.1 The composition of the as-received NiTi alloy (wt.%)

Ni	C	O	N	H	Co	Cu	Cr	Nb	Fe	Ti
55.9	0.016	0.037	0.0025	0.0005	<0.01	<0.01	<0.01	<0.02	<0.02	Bal.

*Ni 55.9 wt.%-Ti was equivalent to Ni 50.8 at.%-Ti

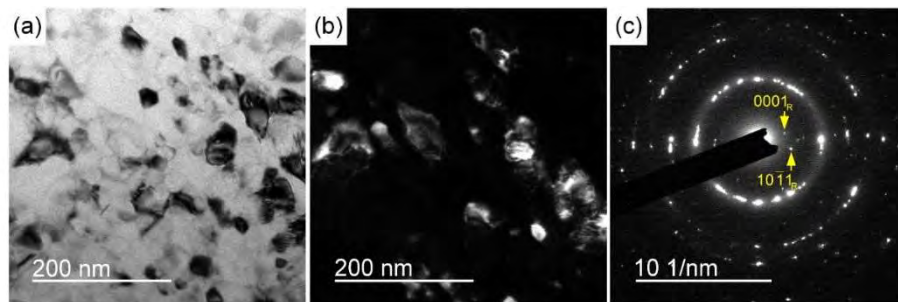


Fig. 2.1 Microstructure and phase constitution of the as-received NC NiTi alloys:

- (a) the TEM bright-field micrograph; (b) the corresponding TEM dark-field micrograph of (a); (c) the corresponding SAED pattern of (a).

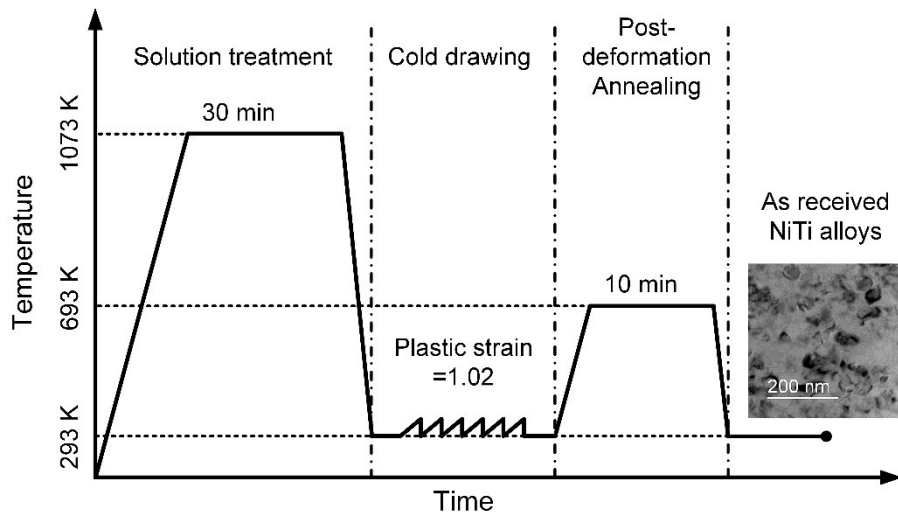


Fig. 2.2 Schematic illustration of the process of the as-received NC NiTi alloy.

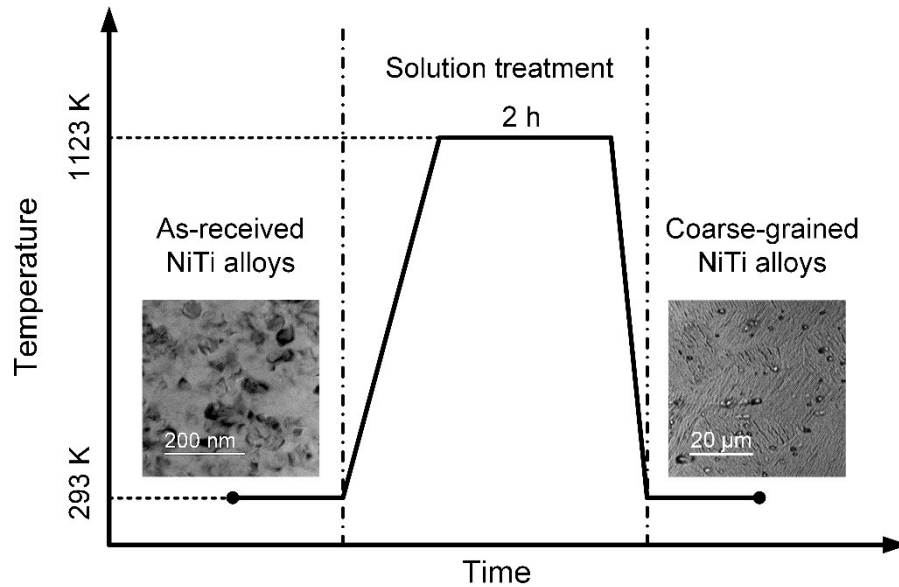


Fig. 2.3 Schematic illustration of the process of the CG NiTi alloy.

2.2.2 Process of low-temperature aging

As reviewed in the 1st chapter, short-range diffusion of Ni atoms is able to be induced by LTA, while the long-range diffusion of Ni is suppressed, which leads to the nanoprecipitation of Ni₄Ti₃ [48]. The present studies summarized the aforementioned studies regarding LTA and considered both the effective

precipitation and the preservation of the original grain size of NC NiTi alloys. The LTA condition of 573 K-2 h was determined after referring the following references: 1) the Ni₄Ti₃ nanoprecipitates can be precipitated if the aging temperature is above 473 K [155]; 2) the LTA of 573 K-2 h can induce Ni₄Ti₃ nanoprecipitation in CG NiTi alloys; 3) the recrystallization and grain growth temperatures of the NiTi alloys with cold plastic strain of 0.5-2.0 were above 593 K [93, 120], thus the LTA of 573 K can avoid undesired grain growth of NC NiTi alloys. This LTA process facilitates the independent study of the effect of LTA and the effect of grain size on the properties of the NiTi alloys.

The LTA was carried out in a vacuum furnace and protected by 99.99% pure argon. The temperature accuracy is within ± 1 K. The samples after LTA was cooled by the flowing cold argon. The aged NC NiTi alloys are abbreviated as ANC NiTi alloys, and the aged CG NiTi alloys are abbreviated as ACG NiTi alloys. The abbreviations and the corresponding processing histories are demonstrated in **Table 2.2**.

Table 2.2 Abbreviations and corresponding processing histories of the NiTi alloys

Abbreviations of samples	Thermomechanical processing histories				
	Solution treatment	Cold drawing	Post-deformation annealing	Solution treatment	Low-temperature aging
NC	1073 K-30 min	$\varepsilon = 1.02$	693 K-10 min	--	--
ANC	1073 K-30 min	$\varepsilon = 1.02$	693 K-10 min	--	573 K-2 h
CG	1073 K-30 min	$\varepsilon = 1.02$	693 K-10 min	1123 K-2 h	--
ACG	1073 K-30 min	$\varepsilon = 1.02$	693 K-10 min	1123 K-2 h	573 K-2 h

2.2.3 Microstructural observation and measurement of properties

Optical microscope (Nikon-Epiphot 200) and TEM (JEOL JEM-2100F) was used for microstructural observation of NC, CG, ANC, and ACG NiTi alloys. The samples for optical microscope observation were sequentially ground by abrasive papers of #600, #1200, #2000 and polished by Al₂O₃ of 0.1 and 0.03 μm respectively. The samples were then etched with an etchant (5% HF, 10% HNO₃, and 85% H₂O) by 15 s. The samples for TEM observation were sequentially ground by abrasive papers of #600, #1200, #2000 to 30 μm, and ion milled (Gatan 691 PIPS). The TEM operation voltage was 200 kV. The phase constituents of the samples were determined by SAED. The grain size of the optical micrograph was calculated by the linear intercept method [183]. The grain size of TEM micrograph was calculated from the software of Gatan DigitalMicrograph[®]. The grain size of each sample was calculated from above 200 independent grains. The hardness of each sample was tested via a hardness tester (FM-7E). The load was set to 200 g·force and 10 indents were used to calculate the average hardness and error bars.

Differential scanning calorimeter (TA Q 200) (DSC) was used to investigate the phase transformation characteristics of the NiTi alloys. To obtain the complete transformation cycle, the samples were firstly heated to 373 K and soaked for 3 min for austenization. They were then cooled to 183 K by 10 K min⁻¹ and soaked at 183 K for another 3 min through which the exothermic peaks were recorded. Finally, they were reheated to 373 K by 10 K min⁻¹ through which the endothermic peaks were recorded. The tangent method [184] was used to obtain the transformation start and end temperatures. The peak temperatures were also

recorded and the thermal hysteresis of each phase transformation was calculated from the difference of peak temperatures. The enthalpy was calculated by integrating each transformation peak. The abbreviations and notations of the above transformation indices are shown in **Fig. 2.4**.

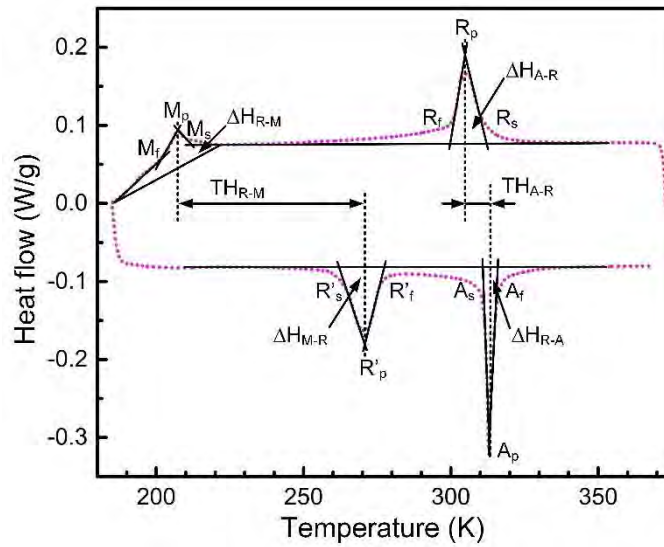


Fig. 2.4 Abbreviations and notations of the transformation temperatures, thermal hysteresis and enthalpy.

The superelasticity was tested on a universal material testing machine (Instron 5565) at room temperature (295 K). The dimension of the samples for the loading-unloading tensile test is as shown in **Fig. 2.5**. The strain rate was set to 1×10^{-3} and kept constant during the tensile test. Engineering stress and strain are used in this study (abbreviated as stress and strain, respectively). The samples were loaded from the strain of 0% to 9% and then unloaded to 0 MPa. Each test was carried out by three times for the repeatability. To further compare the superelasticity at different maximum strains of the different NiTi alloys, maximum strains of 3%, 5%, 7%, 8%, and 13% were additionally used for the superelasticity tests. The typical superelastic indices, such as loading plateau stress, unloading plateau stress,

plateau strain, stress hysteresis, residual strain, and the maximum loading stress, were investigated of which the definitions are as shown in the figure “schematic plot of superelastic indices” at the beginning of this dissertation.

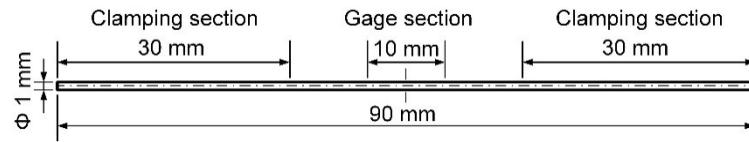


Fig. 2.5 Schematic illustration of the samples for loading-unloading tensile test.

2.3 Effect of LTA on the microstructures of NC and CG

NiTi alloys

The microstructure of the NC sample, as shown in **Fig. 2.6(a)**, mainly consists of nanograins, while Ni_4Ti_3 precipitates, B19' martensite phase, dislocations are not observed. As per the process history of NC, the strain of 1.02 is able to amorphize the solution treated NiTi matrix, and nanocrystalline debris and amorphous phase can be generated [98, 100]. The nanocrystalline matrix was then obtained from the post-deformation annealing of 693 K-10 min. The SAED pattern is shown in **Fig. 2.6(b)**, which indicates that the NC samples mainly consist of B2 austenite phase and a small part of R-phase. The Ni_4Ti_3 and B19' diffraction patterns are not found, which is consistent with the results of TEM morphology. The grain size distribution frequency of NC samples is shown in **Fig. 2.6(c)**, which indicates that the average grain size of NC samples is 34.2 nm and mainly distributes from 10 to 60 nm.

The microstructure of ANC samples is shown in **Fig. 2.6(d)** where the nanocrystalline microstructure is preserved. The Ni_4Ti_3 precipitates, B19' martensite phase, and dislocations are also not observed. The SAED pattern of ANC samples is shown in **Fig. 2.6(e)** where the phase constituents are also B2 austenite phase and R-phase, while R-phase fraction is larger than that of NC samples. The diffraction patterns of Ni_4Ti_3 and B19' are not observed, which is consistent with the TEM micrograph. The grain size distribution frequency is shown in **Fig. 2.6(f)**, which indicates that the average grain size is 34.9 nm. The grain size distribution is similar to that of the NC sample.

The microstructure of CG is shown in **Fig. 2.6(g)** and (i) where the solution treatment of 1123 K-2 h leads to the grain growth from nanograins to coarse grains. The Ni_4Ti_3 precipitates, B19' martensite phase, and dislocations are not observed in the CG sample. The SAED pattern is shown in **Fig. 2.6(h)**, which only shows B2 austenite phase and thus consistent with the TEM results. This indicates that the phase constituents of NC and CG samples are different. The former contains B2 austenite phase and R-phase, while the latter only presents B2 austenite phase. The average grain size of CG samples is 20.6 μm .

The microstructure of ACG samples is shown in **Fig. 2.6(j)** and (l). The densely distributed Ni_4Ti_3 precipitates are found, of which the length is 7-15 nm and the gap between precipitates is 5-15 nm. The B19' martensite phase and dislocations are not observed. The SAED pattern is shown in **Fig. 2.6(k)**, which presents the B2 phase, R-phase, and Ni_4Ti_3 phase, while the B19' phase is not found. This is consistent with the TEM results of the ACG sample. This indicates that the LTA

leads to the change of phase constituents from pure B2 phase into the mixture of B2 phase, R-phase, and Ni_4Ti_3 . The average grain size of the ACG sample is 21.9 μm , which is similar to that of the CG sample.

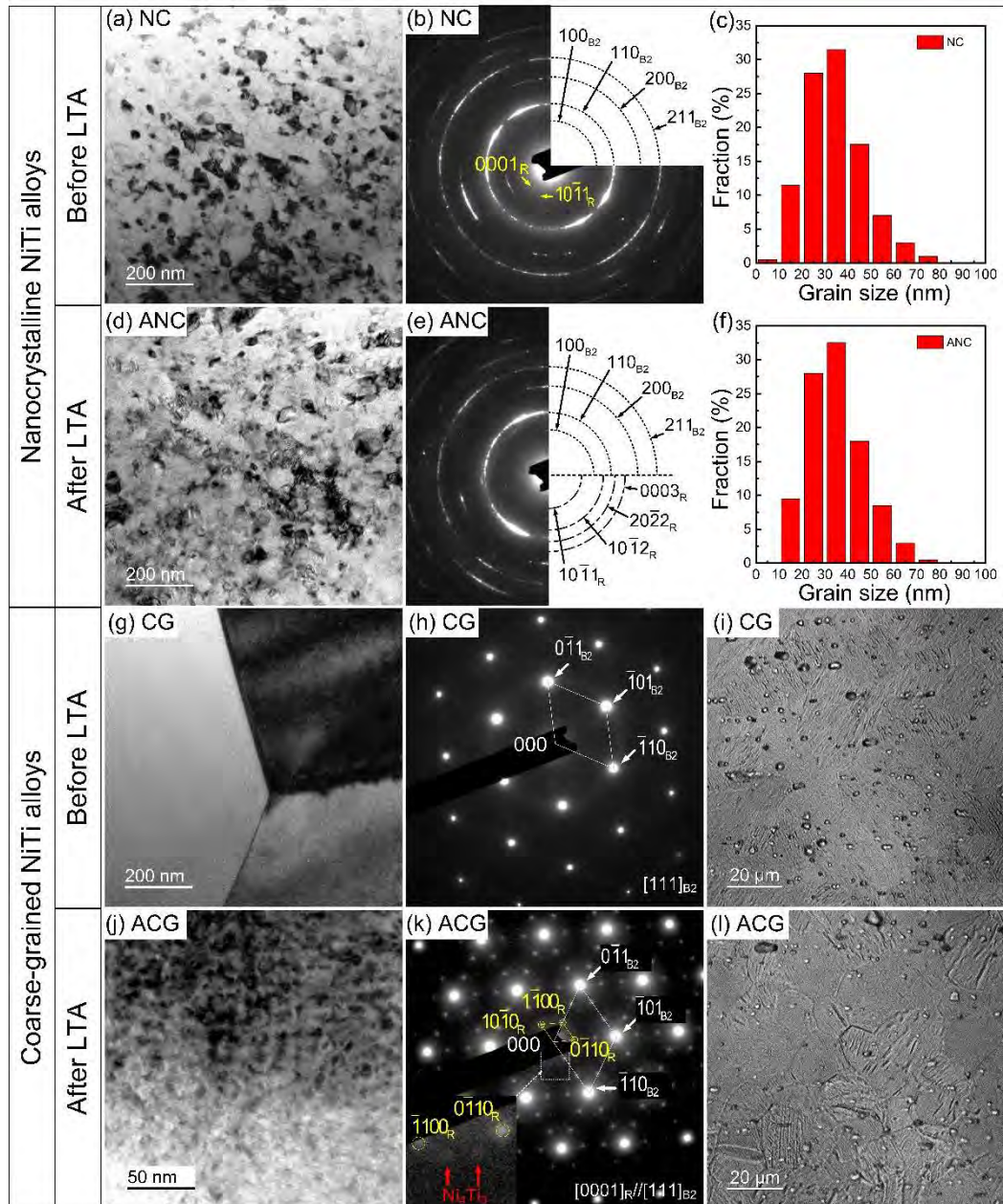


Fig. 2.6 Microstructures of the NiTi alloys: (a) TEM micrograph of NC sample; (b) SAED pattern of (a); (c) grain size distribution frequency of NC sample; (d) TEM micrograph of ANC sample; (e) SAED pattern of (d); (f) grain size distribution frequency of ANC sample; (g) TEM micrograph of CG sample; (h) SAED pattern of (g); (i) TEM micrograph of CG sample; (j) TEM micrograph of ACG sample; (k) SAED pattern of (j); (l) TEM micrograph of ACG sample.

SAED pattern of (g); (i) optical micrograph of CG sample; (j) TEM micrograph of ACG sample; (k) SAED pattern of (j); (l) optical micrograph of ACG sample.

Based on the above results, it can be seen that 1) both of the nanograin size and coarse grain size are able to be preserved after LTA; 2) LTA increases R-phase fraction of NC sample, and it leads to the appearance of R-phase in CG sample; 3) after LTA, Ni_4Ti_3 is not observed in ANC samples, while it is observed in ACG samples.

2.4 Effect of LTA on the hardness of NC and CG NiTi alloys

The comparison of the hardness of the NiTi alloys is as shown in **Fig. 2.7**. Before LTA, due to grain refinement strengthening and Hall-Petch relationship [63, 64], the hardness of the NC samples is higher than that of the CG samples. After LTA, the hardness of the ACG samples increases obviously from that of CG samples, which indicates the precipitation strengthening of Ni_4Ti_3 . This is consistent with the results of the previous study [48], which reflects the high dislocation slip resistance of the nanoprecipitates. However, the ANC samples present similar hardness to NC samples, which means that LTA barely leads to precipitation strengthening in nanograins.

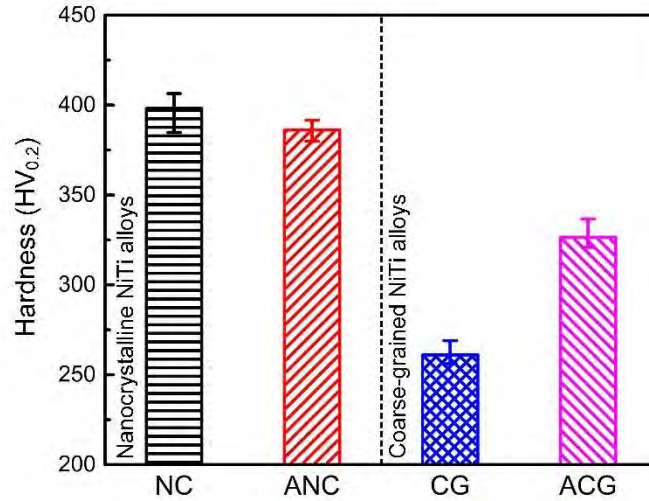


Fig. 2.7 hardnesses of the NiTi alloys.

It can thus be concluded that LTA leads to different effects on the hardness of NC and CG samples. It causes obvious precipitation strengthening in CG samples but does not in NC samples, as shown in **Fig. 2.8**. According to the TEM and SAED results, this difference can be explained as follows. The LTA of 573 K-2 h did not precipitate Ni_4Ti_3 and consequently did not introduce precipitation strengthening. The previous studies [142, 152] found that the nanograin size suppressed the Ni_4Ti_3 precipitation during non-LTA. In this study, the phenomenon happened during LTA. Whether the LTA induced precipitation is suppressed by the nanograin size will be further investigated in the following chapters.

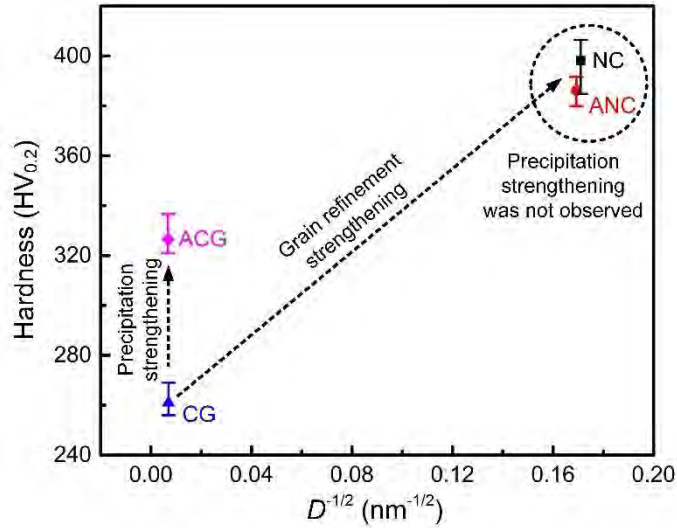


Fig. 2.8 LTA leads to precipitation strengthening in CG NiTi alloys but not in NC NiTi alloys (D is average grain size).

2.5 Effect of LTA on the phase transformation characteristics of NC and CG NiTi alloys

The DSC curves of the NiTi alloys are shown in **Fig. 2.9**, and the corresponding thermal hysteresis and enthalpy are shown in **Table 2.3** where the subscript A, R, and M represent B2 austenite phase, R-phase, and B19' martensite phase, respectively. Among the phase transformations of $B2 \leftrightarrow R$, $B2 \leftrightarrow B19'$, and $R \leftrightarrow B19'$, $B2 \leftrightarrow R$ transformation possesses the smallest thermal hysteresis (about 5-8 K), while $B2 \leftrightarrow B19'$ and $R \leftrightarrow B19'$ transformation possess larger thermal hysteresis (about 20-70 K) [185]. Based on this, the transformation types and sequences are determined, as noted in **Fig. 2.9**.

As can be seen from **Fig. 2.9** and **Table 2.3**, within a complete DSC cycle, ANC samples present only $B2 \leftrightarrow R$ transformation, which shows the same

transformation sequence with NC samples. The CG samples present $B2 \leftrightarrow B19'$ transformation, while the ACG samples present $B2 \leftrightarrow R \leftrightarrow B19'$ transformation.

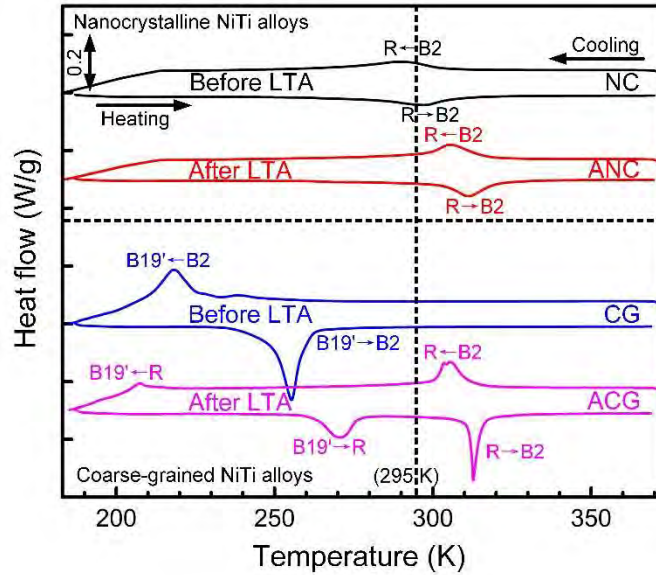


Fig. 2.9 DSC curves of the NiTi alloys.

Table 2.3 Thermal hysteresis (TH) and enthalpy (ΔH) of the NiTi alloys

Abbreviations of samples	TH (K)				ΔH (J/g)				
	TH _{AR}	TH _{RM}	TH _{AM}	ΔH_{AR}	ΔH_{RA}	ΔH_{RM}	ΔH_{MR}	ΔH_{AM}	ΔH_{MA}
NC	7.6	--	--	5.41	4.87	--	--	--	--
ANC	6.4	--	--	5.70	5.51	--	--	--	--
CG	--	--	37.1	--	--	--	--	15.72*	13.50
ACG	7.4	63.3	--	5.96	5.83	3.88*	4.17	--	--

*: Due to the heat flow limitation of the DSC curves at low-temperature section, the marked data were influenced by systematic errors.

2.5.1 Effect of LTA on thermally-induced $B2 \leftrightarrow R$ transformation

As shown in **Fig. 2.9**, NC samples present relatively flattened $B2 \leftrightarrow R$ transformation peaks. The room temperature (295 K) lies in the middle of the transformation peaks, which explains the small volume fraction of R-phase shown in the TEM and SAED observation. According to the previous study [126], these $B2 \leftrightarrow R$ transformation peaks are introduced by the nanograin size.

Compared with NC samples, ANC samples present larger B2 \leftrightarrow R transformation enthalpy, which indicates the increase of the volume fraction of transformable material. The transformation peaks become more concentrated, which indicates that the transformation happens more synchronously. This further indicates that, though the grain size is not varied after LTA, the defects in the nanocrystalline lattice decrease during the LTA. The ANC samples present higher B2 \leftrightarrow R transformation temperatures than the NC samples, which explains the more volume fraction of R-phase of ANC samples as observed in the TEM. It is known from the previous studies that the reasons for the increasing B2 \leftrightarrow R transformation temperatures include a decrease of grain size [126], an increase of dislocations [10] and Ni₄Ti₃ precipitation [186], and a decrease of Ni concentration [187] in NiTi matrix. With respect to the ANC samples of this study, LTA neither decreases the grain size nor increases dislocations, and Ni₄Ti₃ is also not observed. The decrease of Ni concentration could thus be the reason, which will be further studied in the following chapters.

The CG samples show no B2 \leftrightarrow R transformation peak because the solution treated coarse-grained NiTi alloys contain no precipitates or dislocations. After LTA, ACG samples present obvious B2 \leftrightarrow R transformation peaks, which is caused by the precipitation of Ni₄Ti₃. As indicated from the previous study [144], coherent Ni₄Ti₃ precipitates are able to introduce elastic strain field in the adjacent NiTi matrix, which arouses the B2 \leftrightarrow R transformation.

The B2 \leftrightarrow R transformation temperatures of ACG and ANC are almost the same, while the enthalpy of the ACG samples is larger than ANC samples. This is because ANC samples possess higher volume fraction of grain boundaries and consequently lower volume fraction of transformable NiTi matrix than ACG samples. In addition, the B2 \leftrightarrow R transformation temperatures of ACG samples are not affected by grain size, but those of the ANC samples are affected by the nanograin size. Therefore, the nanograins with different grain sizes in ANC samples further flatten the B2 \leftrightarrow R transformation peaks.

2.5.2 Effect of LTA on thermally-induced B2(R) \leftrightarrow B19' transformation

As shown in **Fig. 2.9**, even cooled to 183 K, the NC samples do not show R \rightarrow B19' transformation, and the B19' \rightarrow R transformation also does not appear during reheating. This indicates that the thermally-induced R \rightarrow B19' transformation is suppressed in the NC samples. It is commonly known that the lattice shear happens during B2(R) \leftrightarrow B19' transformation, and the thermally-induced B2(R) \leftrightarrow B19' transformation preserves the macro shape of the NiTi alloys. It thus requires that the position and shape of each grain generally keep unchanged during the phase transformation. Therefore, the transformation lattice shear has to be compensated by the self-accommodation deformation within each grain. With respect to CG NiTi alloys, the self-accommodation deformation is accomplished by the twinning of B19' martensite phase along the habit planes and grain boundaries. This self-accommodation deformation reduces the elastic strain energy of the transformation lattice shear but increases the interfacial energy of the habit planes

and grain boundaries. Therefore, the decreasing temperature can lead to $B2(R) \leftrightarrow B19'$ transformation in CG NiTi alloys. With respect to NC NiTi alloys, however, the grain boundaries present constraint effect on the grain inner due to the small nanograin size. The twinning along the habit planes within each grain becomes difficult. Thus, the transformation lattice shear has to be accommodated by $(100)_{B19'}$ compound twins where the intervals between the twin variant interfaces are only several atoms [120]. The elastic strain energy and interfacial energy increased by this twinning mode are higher than those increased by $\{011\}$ type I twinning and $\langle 011 \rangle$ type II twinning of CG NiTi alloys [50]. Therefore, it required a higher driving force, i.e., lower temperature, to thermally-induce $B2(R) \leftrightarrow B19'$ transformation [120] in nanocrystalline samples. According to the study of Waitz.T et al. [120], if the grain size is smaller than 60 nm, the thermally-induced $R \rightarrow B19'$ transformation can be completely suppressed even at 77 K. In this study, most grains of NC samples are smaller than 60 nm. The $R \rightarrow B19'$ transformation is consequently suppressed. With respect to the ANC samples, the $R \rightarrow B19'$ transformation keeps being suppressed after LTA, which is due to the preservation of the nanograin size.

The CG samples present $B2 \leftrightarrow B19'$ transformation, which is typical in solution treated CG NiTi alloys. This indicates that the $B2 \leftrightarrow B19'$ transformation is complete within a complete DSC cycle. After LTA, the ACG samples showed a lower $R \rightarrow B19'$ transformation temperature than the $B2 \rightarrow B19'$ transformation temperature of the CG samples, and a higher $B19' \rightarrow R$ transformation temperature than the $B19' \rightarrow B2$ transformation temperature of the CG samples, which means that the $R \leftrightarrow B19'$ transformation thermal hysteresis of the ACG samples is higher

than the $B2 \leftrightarrow B19'$ transformation thermal hysteresis of the CG samples. This is because the Ni_4Ti_3 nanoprecipitation increases the volume fraction of interfaces in the NiTi matrix, which consequently increases the energy dissipation of the transformation frontier propagation. In the CG samples, Ni_4Ti_3 precipitates do not exist, which presents the lower energy dissipation of the transformation frontier propagation and consequently the lower thermal hysteresis.

It can be summarized from the above results that LTA transfers the transformation sequence of CG NiTi samples from $B2 \leftrightarrow B19'$ to $B2 \leftrightarrow R \leftrightarrow B19'$. The precipitation of Ni_4Ti_3 increases the thermal hysteresis of $B2(R) \leftrightarrow B19'$ transformation. LTA preserves the suppression of $R \rightarrow B19'$ transformation induced by nanograin size due to the preservation of the nanograin size.

2.6 Effect of LTA on the superelasticity of NC and CG

NiTi alloys

The superelastic stress-strain curves of the NiTi alloys are shown in **Fig. 2.10** where the maximum strain is 9%. All the samples present typical superelasticity, while they each owns distinctive stress-strain paths. As shown in the child window of **Fig. 2.10**, the elastic modulus of the NiTi alloys before plateau deformation stage are different. In addition, as shown in **Fig. 2.10**, different NiTi alloys show different superelasticity indices, such as the loading plateau stress, unloading plateau stress, plateau strain, stress hysteresis, and residual strain, etc. The stress-induced $B2 \rightarrow R$ transformation and the stress-induced $B2(R) \leftrightarrow B19'$

transformation (as the superelasticity concerned in this study) were also different among the alloys.

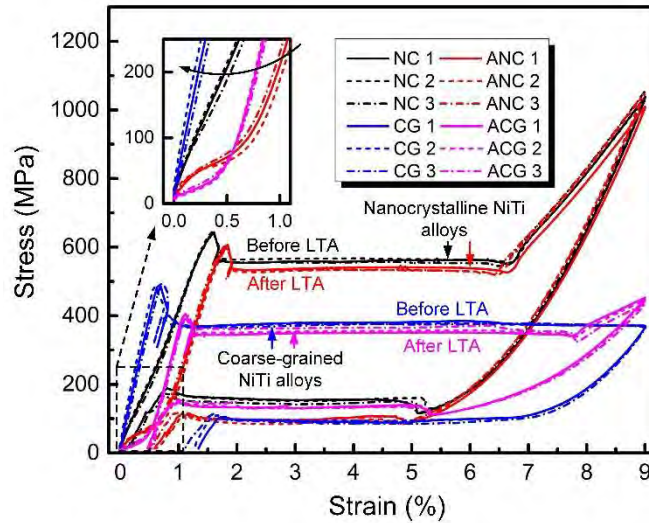


Fig. 2.10 Superelastic stress-strain curves of the NiTi alloys (the maximum strain of 9%).

2.6.1 Effect of LTA on stress-induced B2→R transformation

The relationship of the elastic modulus of the NiTi alloys and the applied stress is shown in **Fig. 2.11**. The modulus of the CG samples is larger than 70 GPa. Since the elastic modulus of B2 austenite phase is about 70 GPa [188], the CG samples are mainly subjected to the elastic deformation of B2 austenite phase. On the other hand, the modulus of the NC, ANC, and ACG samples firstly decrease and then increase before reaching the maximum values. The maximum values of the modulus of NC, ANC, and ACG samples are smaller than 70 GPa. This indicates that the NC, ANC, and ACG samples not only experience the elastic deformation of B2 austenite phase, but they are also subjected to B2↔R transformation related deformations (such as stress-induced B2→R transformation, reorientation of R-

phase, and the elastic deformation R-phase, etc.). The reduced elastic modulus in the NC, ANC, and ACG samples reflect the stress-induced B2→R transformation and the reorientation of R-phase [50], which forms the B2→R transformation plateau and consequently lowers the elastic modulus. The subsequent increase of elastic modulus reflect the elastic deformation of R-phase [188].

It is worth noting that, as shown in **Fig. 2.9**, ANC and ACG samples present similar B2→R transformation temperature, which indicates that ANC and ACG samples need similar driving force for the thermally-induced B2→R transformation. However, the ANC samples present higher B2→R transformation plateau than the ACG samples, as shown in **Fig. 2.10**. This indicates that ANC samples require higher driving force for the stress-induced B2→R transformation than ACG samples. According to the study [189], dislocations are more effective to impede the movement of B2↔R transformation frontier than the precipitates, and it is known that grain boundaries contain numerous dislocations and present higher interfacial energy than the dislocations. Therefore, the ANC samples with high grain boundary volume fraction show higher resistance to the stress-induced B2→R transformation than the ACG samples.

It can be summarized from the above results that, after LTA, both nanocrystalline and coarse-grained NiTi alloys present stress-induced B2→R transformation and/or R-phase reorientation. Though the B2→R transformation temperatures of ANC and ACG samples are similar, higher stress is required in ANC samples to activate the B2↔R transformation than that of the ACG samples.

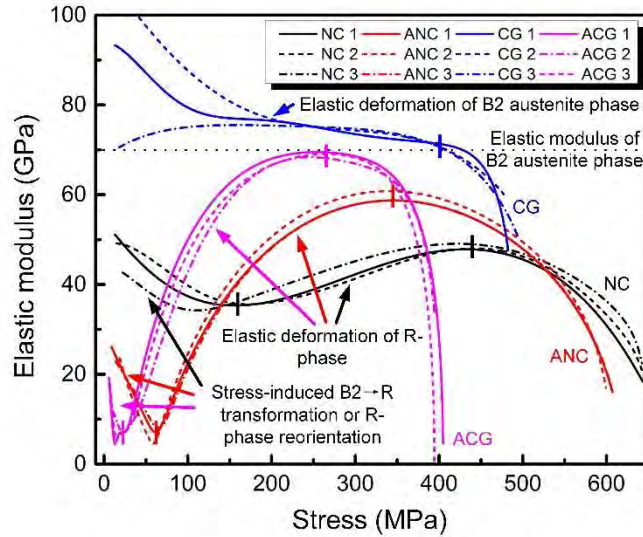


Fig. 2.11 Relationship of the elastic modulus and the applied stress of the NiTi alloys.

2.6.2 Effect of LTA on stress-induced $B2(R) \leftrightarrow B19'$ transformation

Numerous applications of NiTi alloys that involve superelasticity are based on stress-induced $B2(R) \leftrightarrow B19'$ transformation [11]. The superelasticity to be studied in this study is also based on the stress-induced $B2(R) \leftrightarrow B19'$ transformation. This section comparatively analyzes the superelasticity indices of the NiTi alloys, as shown in **Fig. 2.12**.

The loading plateau stress is the required stress for activating the $B2(R) \rightarrow B19'$ transformation. The four NiTi alloys experience complete unloading plateau deformation stage, which indicates that the $B19'$ phase is completely transformed to B2 or R-phase after unloading. As shown in **Fig. 2.12(a)**, the NC samples show higher loading plateau stress than the CG samples. This indicates that nanograin size can impede the stress-induced $R \rightarrow B19'$ transformation. The NC samples

present complete loading plateau, which indicates that the stress-induced R→B19' transformation is not suppressed. This is different from the thermally-induced R→B19' transformation of the NC samples which is completely suppressed by the nanograin size even when the temperature drops to 183 K. According to the previous study [44], stress-induced R→B19' transformation happen even when the grain size drops to 14 nm, which is smaller than the critical grain size for the thermally-induced R→B19' transformation (60 nm [121]). Though the thermally-induced R→B19' transformation of the NC and ANC samples is suppressed, the stress-induced R→B19' transformation still happen because the grain size is larger than 14 nm (the critical grain size for the stress-induced R→B19' transformation), i.e., the NC and ANC samples still present superelasticity.

After LTA, the loading plateau stress of the ANC and ACG samples decreases. With respect to the ACG samples, the elastic strain field facilitates the stress-induced R↔B19' transformation, thus the required external stress decreases. In terms of the ANC samples, the defects of the nanograins decreases, thus the required external stress also decreases.

The unloading plateau stress and stress hysteresis are shown in **Fig. 2.12(b)** and (c). NC samples present larger stress hysteresis than the CG samples, which indicates that nanocrystalline NiTi alloys dissipate more energy than coarse-grained NiTi alloys during superelastic deformation. The reasons are as follows:

- 1) Nanocrystalline NiTi alloys possess higher grain boundary volume fraction, and the grain boundaries also attend the superelastic deformation, which increases the energy dissipation of stress-induced R↔B19' transformations.

- 2) The NC samples finish the plateau deformation stage and reach to the post-plateau deformation stage. The post-plateau deformation contains the elastic deformation of B19' phase, further transformation of residual B2 and R-phase, reorientation of B19' phase, the elastic deformation of grain boundaries, and dislocation slip induced plastic deformation [190]. This deformation process further increases the stress hysteresis of the NC samples. It is noteworthy that, even the maximum stress reaches to about 1000 MPa, the stress-strain curve still nearly returns to the origin. This indicates that the NC samples still possess superelasticity even after they are subjected to the post-plateau deformation stage.
- 3) The CG samples are in the solution state and present low resistance to dislocation slip. With the maximum strain of 9%, the CG samples unload within plateau deformation stage. The effect of post-plateau deformation can thus be excluded. During unloading, though the unloading plateau is complete, the residual strain of 1.2% still exists, which is due to dislocation slip. The increasing dislocations increase the energy dissipation during superelastic deformation [192]. According to the results of this study, under the maximum strain of 9%, though the stress hysteresis of the CG samples is elevated by the increasing dislocations, such effect is not as remarkable as those induced by the high grain boundary volume fraction and the post-plateau deformation of the NC samples.

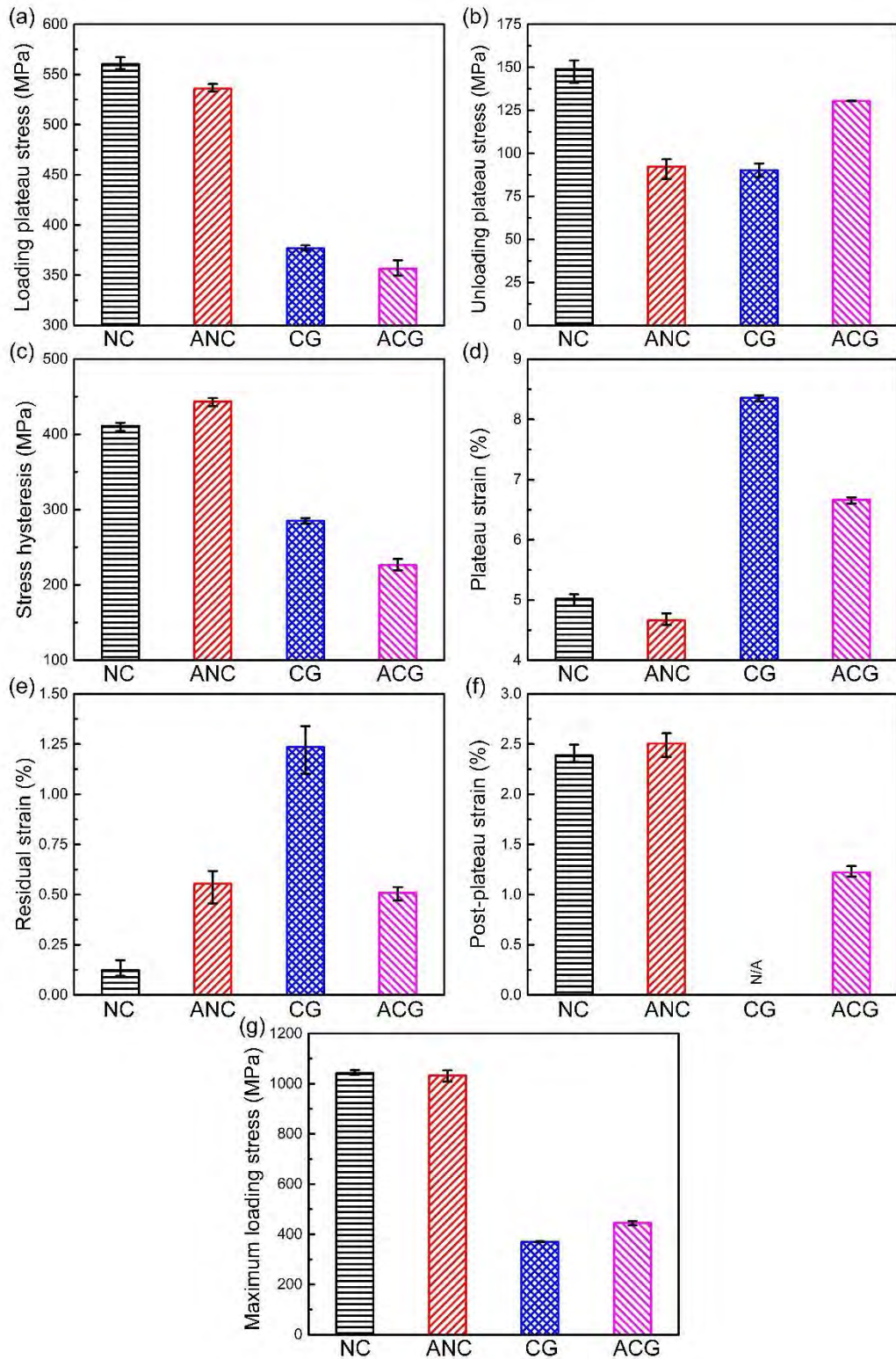


Fig. 2.12 Superelasticity indices of the NiTi alloys: (a) loading plateau stress; (b) unloading plateau stress; (c) stress hysteresis; (d) plateau strain; (e) residual strain; (f) post-plateau strain; and (g) the maximum loading stress.

After LTA, the stress hysteresis of the ANC samples increases, while that of the ACG samples decreases. With respect to the ANC samples, the nanograin size is preserved, and the energy dissipated by nanograin boundaries is similar to that of the NC samples. The ANC samples present larger post-plateau strain than the NC samples, as shown in **Fig. 2.12(f)**, which thus leads to higher energy dissipation and larger stress hysteresis. The ACG samples experience post-plateau deformation stage under the maximum strain of 9%, which increases the stress hysteresis. Though both the Ni_4Ti_3 precipitates and post-plateau deformation increase the energy dissipation during transformation, the experimental results show that they are less effective than the decrease of stress hysteresis induced by the suppression of dislocation slip caused by the Ni_4Ti_3 precipitation.

With respect to plateau strain, as shown in **Fig. 2.12(d)**, the ANC samples present a little smaller plateau strain than the NC samples. The change of texture can be a reason. The texture of NiTi alloys after a cold drawing is generally $\langle 111 \rangle_{\text{B}2}$, which presents relative large plateau strain [49]. LTA can weaken this texture and consequently decrease the plateau strain. The decreasing transformable NiTi matrix within grains may be another reason. The ANC samples can exist a small portion of grains with large grain size, which can precipitate Ni_4Ti_3 after LTA and consequently decrease the plateau strain. The ACG samples present much smaller plateau strain than the CG samples, which is due to the Ni_4Ti_3 precipitation that decreases the transformable NiTi matrix fraction. The Ni_4Ti_3 precipitates can change $\text{R} \rightarrow \text{B}19'$ transformation orientation of a portion of the NiTi matrix [191], which also reduces the plateau strain.

With respect to residual strain, as shown in **Fig. 2.12(e)**, the ANC samples present larger residual strain than the NC samples, while the ACG samples show smaller residual strain than the CG samples. For the ANC samples, the increase of residual strain is due to the incomplete R→B2 transformation. As shown in **Fig. 2.9**, the R→B2 transformation temperature of the ANC samples is higher than the superelastic testing temperature (295 K). Therefore, the ANC samples consist of reoriented R-phase after unloading, and the B2→R transformation strain and reorientation strain of R-phase were thus unable to be recovered, which leads to the increase of residual strain. For the ACG samples, though the dislocation slip is suppressed by the Ni₄Ti₃ precipitates, the residual strain still consists of the strain of R-phase reorientation. The CG samples did not contain R-phase, thus the residual strain is only induced by dislocation slips. According to the experimental results, the residual strain induced by dislocation slipping in the CG samples is much larger than that induced by the R-phase reorientation and B2→R transformation strain in the ACG samples.

In addition, for the ACG samples, the densely distributed Ni₄Ti₃ nanoprecipitates impede R→B19' transformation, but they reduce the critical stress for activating stress-induced R→B19' transformation. The former is due to the elevation of self-accommodation deformation resistance induced by the Ni₄Ti₃ nanoprecipitates during thermally-induced R→B19' transformation. The latter is due to the fact that the elastic strain field around the nanoprecipitates is able to facilitate the R→B19' transformation. Though similar phenomena also happen in previous studies [47, 192, 193], they did not draw enough attention. It thus indicates that the superelasticity of NiTi alloys cannot be simply deduced from phase transformation

temperature. On the contrary, the features of microstructure should also be considered.

2.6.3 Effect of LTA on superelasticity under different maximum strains

The superelastic stress-strain curves of the NiTi alloys under maximum strains of 3%, 5%, 7%, 8%, and 9% are shown in **Fig. 2.13**. The evolutions of stress hysteresis and residual strain with the different maximum strains are shown in **Fig.**

2.14.

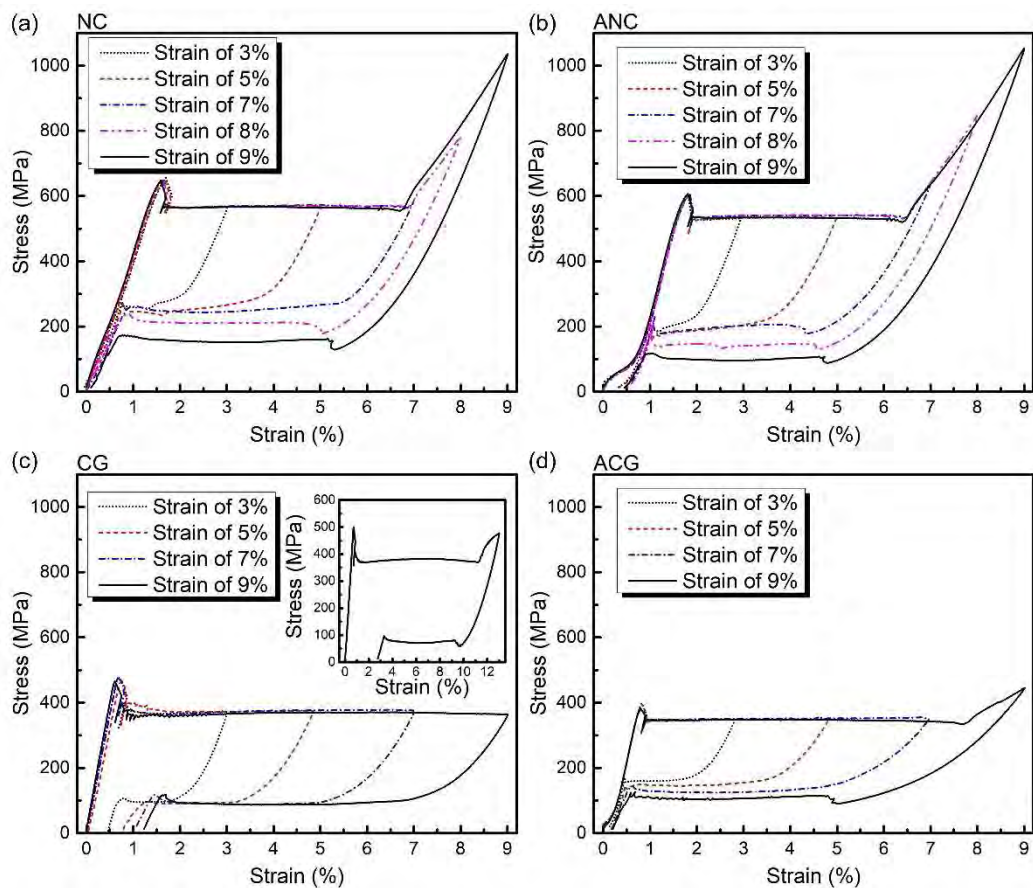


Fig. 2.13 Superelastic stress-strain curves of the NiTi alloys under different maximum strains: (a) the NC samples; (b) the ANC samples; (c) the CG samples; and (d) the ACG samples.

With the increasing maximum strain, the NiTi alloys respectively enter the post-plateau deformation stage. The maximum loading stress and stress hysteresis consequently increase. Due to the characteristics of Lüders-like deformation [194, 195], the stress hysteresis within the plateau deformation stage is nearly unchanged. The post-plateau deformation belongs to homogenous deformation. It can increase the energy dissipation of the whole NiTi sample during superelastic deformation, and the stress hysteresis increases with the post-plateau deformation.

The residual strain of the NC, ANC, and ACG samples increases slightly with the increasing maximum strain, while that of the CG samples increases drastically with the increasing maximum strain. This is because the dislocation slips are suppressed either by the nanograin size or by the Ni_4Ti_3 nanoprecipitates of the NC, ANC, and ACG samples. By contrast, the CG samples present much lower dislocation-slip resistance and consequently show the largest residual strain.

LTA presents opposite effects on stress hysteresis and residual strain between nanocrystalline and coarse-grained NiTi alloys, as shown in **Fig. 2.14**. These differences do not only exist under the maximum strain of 9%, but they also exist within the maximum strain range of 3%-9%. The specific reasons have been discussed in section 2.6.2 which are not to be repeated here.

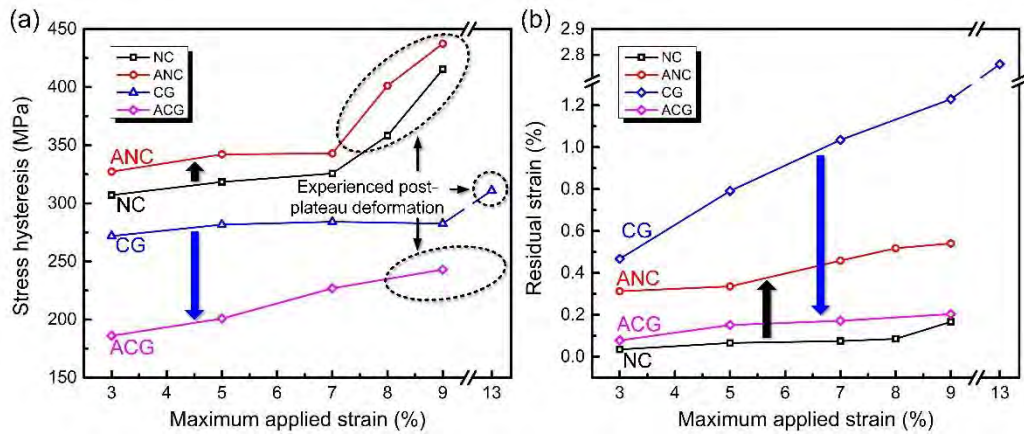


Fig. 2.14 Evolution of (a) the stress hysteresis and (b) the residual strain with different maximum strains of the NiTi alloys.

2.7 Summary

This chapter comparative studies the effect of LTA (573 K-2 h) on the representative nanocrystalline and coarse-grained NiTi alloys regarding microstructures, phase transformation characteristics, and superelasticity. The following concluding remarks can thus be drawn:

- (1) The LTA at 573 K successfully avoids further grain growth of the NC and CG NiTi alloys. The phase transformation characteristics and superelasticity can also be altered. This indicates that the LTA is fit for adjusting functional properties of NiTi alloys without varying the original grain size. LTA shows different influences on NC and CG NiTi alloys, which includes precipitation behavior, phase transformation characteristics, and superelasticity. These issues are going to be further studied in the following chapters.

- (2) The LTA of 573 K-2 h preserves the suppression of thermally-induced $B2 \rightarrow B19'$ transformation induced by the nanograin size. It also elevates $B2 \leftrightarrow R$ transformation temperature. This indicates that the $B2 \leftrightarrow R$ transformation temperature of nanocrystalline NiTi alloys can be adjusted by LTA. No matter it is nanocrystalline and coarse-grained NiTi alloys, the appearance of thermally-induced $B2 \rightarrow R$ transformation indicates the $B2 \leftrightarrow R$ transformation related deformation during superelastic deformation. Even the $B2 \rightarrow R$ transformation temperature is similar, nanocrystalline NiTi alloys require higher stress for activating the stress-induced $B2 \rightarrow R$ transformation. The above findings of $B2 \leftrightarrow R$ transformation may facilitate the design and application of the NiTi functional parts based on $B2 \leftrightarrow R$ transformation.
- (3) After LTA, $R \leftrightarrow B19'$ transformation stress hysteresis of NC NiTi alloys increases, while that of CG NiTi alloys decreases. The former is due to the higher grain boundary volume fraction and the additional post-plateau deformation, while the latter is due to the suppression of dislocation slip induced by the Ni_4Ti_3 nanoprecipitates.
- (4) After LTA, the residual strain of NC NiTi alloys increases, while that of CG NiTi alloys decreases. The former is due to the elevation of $R \rightarrow B2$ transformation temperature, and the R-phase reorientation strain is consequently preserved after unloading. The latter is due to the suppression of dislocation slip induced by the Ni_4Ti_3 nanoprecipitates.

(5) For nanocrystalline NiTi alloys, though the thermally-induced R→B19' transformation is suppressed, the stress-induced R→B19' transformation still proceeds, i.e., they still present superelasticity. For coarse-grained NiTi alloys, thermal hysteresis increases after LTA, while stress hysteresis decreases. The increase of thermal hysteresis is caused by the increasing resistance of the self-accommodation deformation induced by the densely distributed Ni₄Ti₃ nanoprecipitates. The decrease of stress hysteresis is because the suppression of dislocation slip induced by the Ni₄Ti₃ nanoprecipitates. This indicates that the superelasticity of NiTi alloys should not be simply deduced from transformation temperatures. The effect of microstructural features should also be considered.

Chapter 3 Effect of direct electric resistance heat treatment on the properties and grain size of NiTi alloys

3.1 Introduction

To effectively obtain NC, UFG, and CG NiTi alloys without the interference of undesired early aging is the premise of this study. The grain size adjustment of NiTi alloys is usually achieved by severe plastic deformation plus annealing in a furnace. Several scholars have obtained NiTi alloys with different grain sizes by this method [90, 92, 107, 196, 197]. Among these studies, the NC and UFG NiTi alloys are obtained from post-deformation annealing of tens of minutes or several hours at 573-873 K. However, based on the NiTi phase diagram as shown in **Fig. 1.5**, this temperature range and time can also introduce aging effect besides the variation of grain size. This means the undesired Ni_4Ti_3 precipitates may exist in the NiTi alloys before LTA, which is detrimental to the LTA induced functional property adjustment.

Direct electric resistance heat treatment (DERHT) [198] is able to rapidly change the microstructure NiTi alloys via internal Joule heating [199] and consequently vary the functional properties of NiTi alloys [198] within the time of seconds. Due to the short heating time, DERHT is able to avoid Ni_4Ti_3 precipitation, which is

beneficial for the subsequent LTA induced functional property adjustment of NiTi alloys.

Therefore, this chapter firstly investigates the effect of DERHT on the properties and microstructures of NiTi alloys with different grain sizes and aging conditions. Then, DERHT is used for the grain size adjustment in this study. The NiTi alloys with the average grain size of 34-8021 nm are obtained via DERHT, which are prepared for the studies of the following chapters.

3.2 Materials preparation and experimental procedure

3.2.1 Preparation of NiTi alloys with different initial states

The NC, ANC, CG, and ACG NiTi alloys obtained in chapter 2 were used as the representative NiTi alloys with different initial states of this chapter, which represented the NiTi alloys of different grain sizes and aging conditions. The comparisons of microstructure, phase constituent, phase transformation, superelasticity, and hardness of the four types of NiTi alloys are shown in **Fig. 3.1**. The detailed comparative study of these four types of NiTi alloys have been conducted in chapter 2, thus they are not to be repeated here.

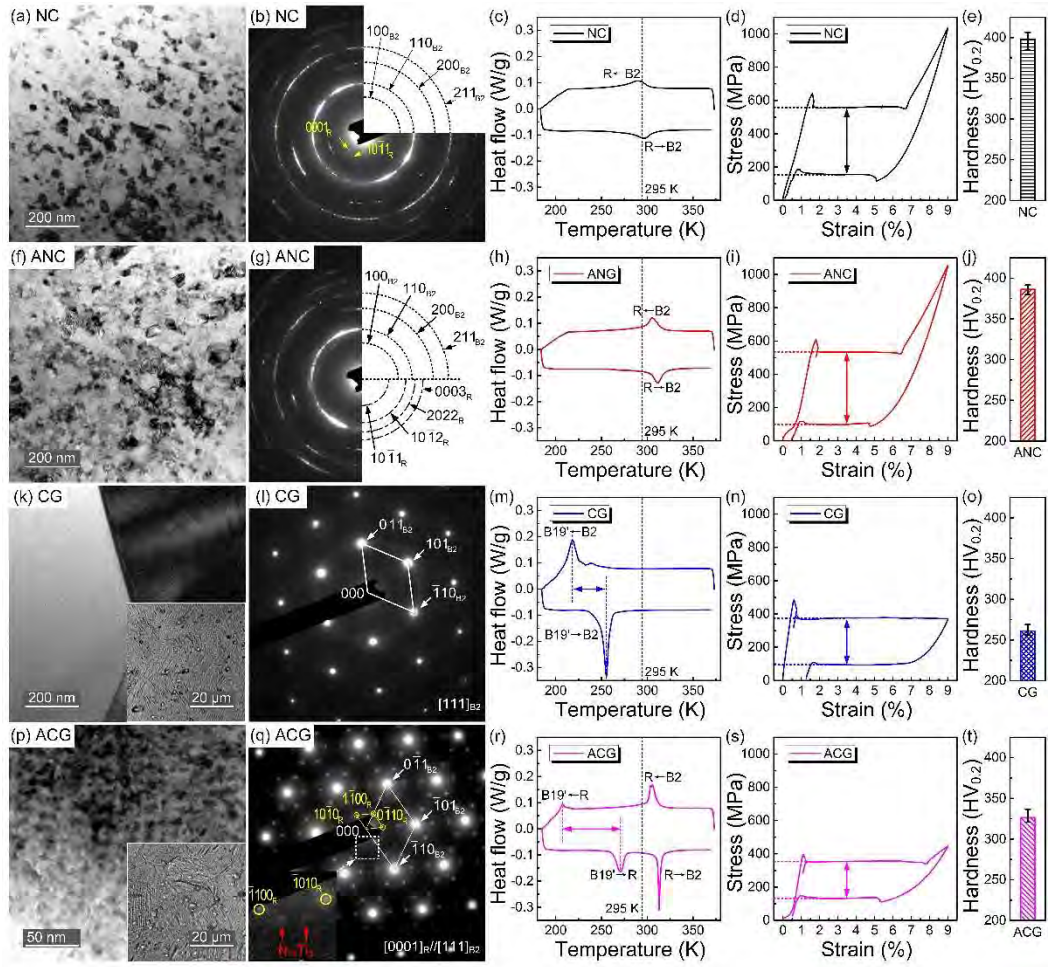


Fig. 3.1 Comparisons of the microstructure, phase constituents, phase transformation characteristics, superelasticity, and hardness of the four types of NiTi alloys: (a) TEM micrograph of the NC samples; (b) SAED pattern of (a); (c) DSC curve of the NC samples; (d) superelasticity of the NC samples; (e) hardness of the NC samples; (f) TEM micrograph of the ANC samples; (g) SAED pattern of (f); (h) DSC curve of the ANC samples; (i) superelasticity of the ANC samples; (j) hardness of ANC samples; (k) TEM and optical micrographs of the CG samples; (l) SAED pattern of (k); (m) DSC curve of the CG samples; (n) superelasticity of the CG samples; (o) hardness of the CG samples; (p) TEM and optical micrographs of the ACG samples; (q) SAED

pattern of (p); (r) DSC curve of the ACG samples; (s) superelasticity of the ACG samples; and (t) hardness of the ACG samples.

The samples for DERHT of the four NiTi alloys are shown in **Fig. 3.2**. The length of each sample was 120 mm. The positions, at 15 mm of each end, were used for connecting with electrodes. After DERHT, each end with 15 mm was cut off and the remaining NiTi sample with 90 mm in length was used for superelasticity tests. The configuration of superelasticity tests is as introduced in section 2.2.4.

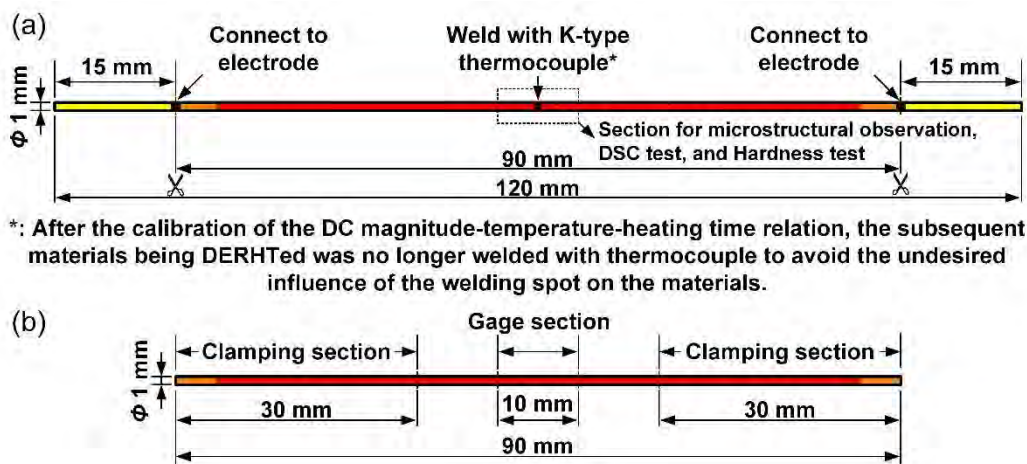


Fig. 3.2 Schematic illustration of (a) the samples for DERHT and (b) the samples for superelasticity tests.

3.2.2 The platform for DERHT

This study set up a platform for the DERHT of the NiTi alloy. The physical map and the corresponding schematic diagram of the platform are shown in **Fig. 3.3**. The platform consists of a power supply which can output constant direct current, an amperemeter for measuring the direct current (DC) magnitude of the circuit, a voltmeter (Voltmeter₁) for measuring the voltage of the NiTi samples, another voltmeter (Voltmeter₂) for measuring the output voltage of the power supply, an

K-type thermocouple for measuring the temperature of the NiTi samples, and a temperature recorder for the thermocouple of which the sampling frequency is 1 Hz. The diameter of the thermocouple is 0.62 mm which was welded on the surface in the middle position of the NiTi samples. The current magnitude was set to be constant during DERHT. The DERHT was implemented at room temperature and in a lab room with still air.

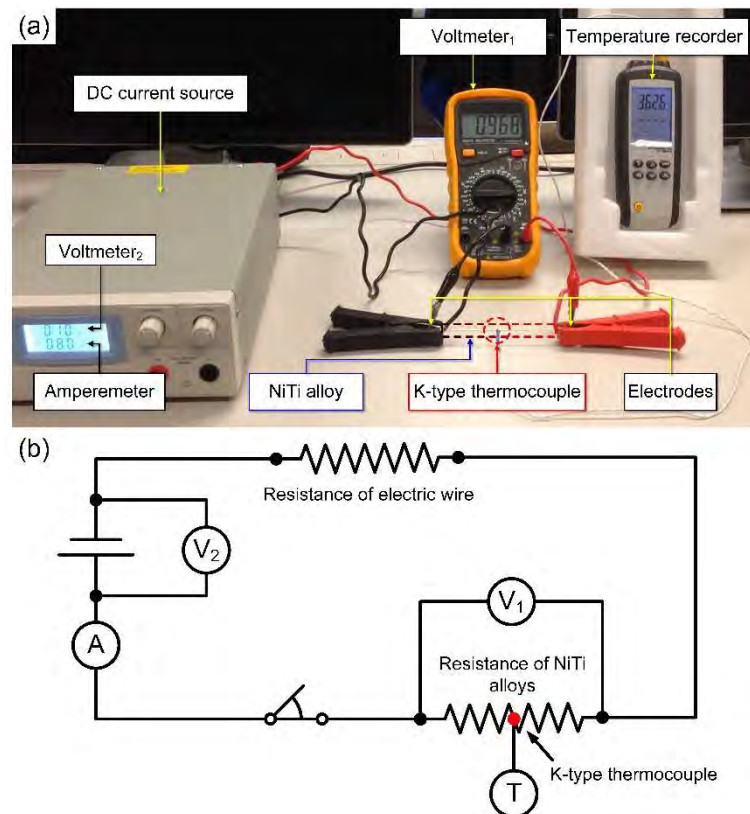


Fig. 3.3 Schematic illustration of the platform for DERHT: (a) physical map; and (b) schematic diagram.

The obtained relationship among direct current magnitude, heating time, and measured temperature are shown in **Fig. 3.4**. Based on the experimental results, it can be obtained that 1) the temperatures of the NiTi alloys elevate in 0-30 s and reach stable after 30 s regardless of current magnitude, which is generally

consistent with the study [200] where the temperature is saturated at 25 s; 2) the temperature increasing rates reach to the maximum in 5-15 A; 3) the saturated temperature increases with the current magnitude and presents nearly linear relationship, as shown in **Fig. 3.4** (c), and the correlation coefficient R is 0.99982. The obtained linear relationship between the saturated temperature and the current magnitude is as shown by Eq. (3.1):

$$T_c = 172.7 + 52.5 \cdot I \quad I \in [5, 15] \quad (3.1)$$

where T_c is the measured temperature (K), I is the current magnitude. Under 5 A, the saturated temperature is 435.5 K. The saturated temperature increases by about 52.5 K when the current magnitude increases by 1 A.

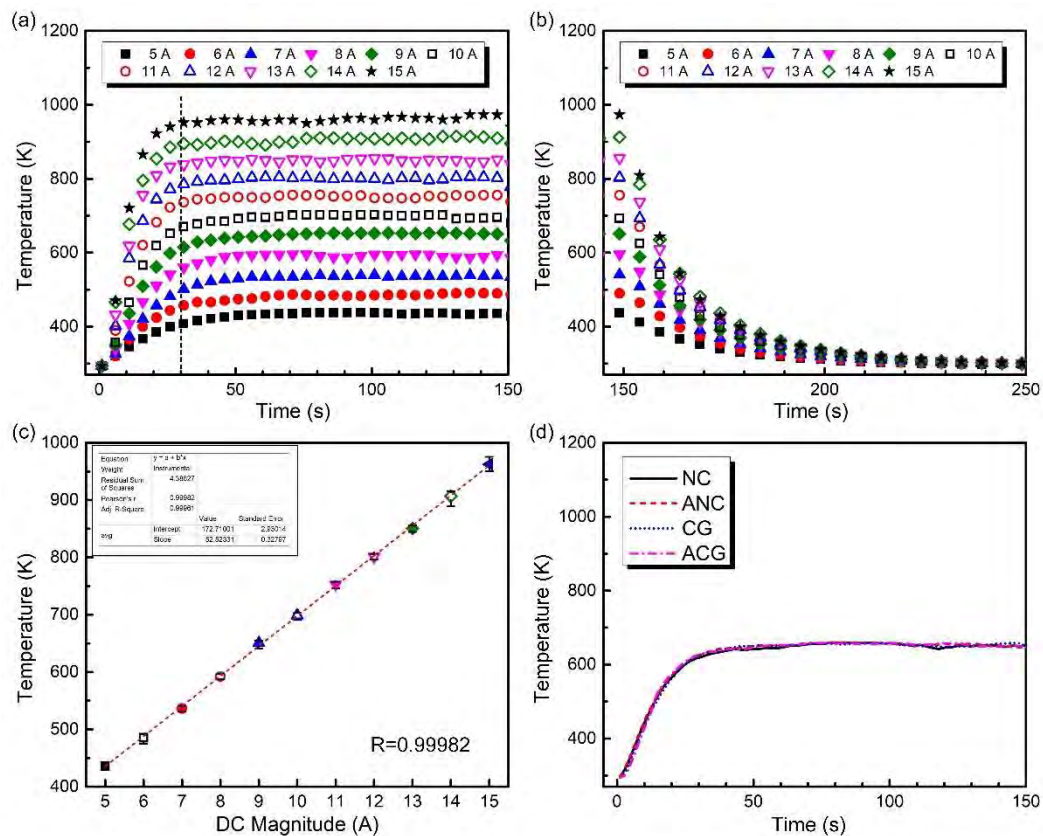


Fig. 3.4 Relationships among the measured temperature, heating time, and direct current magnitude of the DERHT: (a) heating and soaking stages of the DERHT; (b) cooling stage of the DERHT; (c) relationship of the measured temperature at

soaking stage and the direct current magnitude; and (d) relationship of the measured temperature and heating time of the different NiTi alloys at 9 A.

The comparison of the measured temperature-heating time relationship of the four alloys is shown in **Fig. 3.4** (d). The temperature elevation paths of the different NiTi alloys are nearly the same. Theoretically, smaller grain size leads to higher electrical resistance. The results of this study indicate that the NiTi alloy with grain size 34 nm presents similar temperature elevation paths with coarse-grained samples. R. Delville et al. [201] measured the electrical resistance of the nanocrystalline NiTi alloys with similar grain size as the NC and ANC samples of this study, and the results show that their electrical resistance was similar to coarse-grained ones.

In addition, due to the small diameter of the samples (1 mm), the internal temperature of the samples is slightly higher than that at the surface due to the surface convection and radiation with the still air. The previous studies [200, 202] indicate that the shorter sample length and larger contact area with electrodes increase the heat loss along the axial direction and enlarged the temperature gradient. To reduce the gradient along the axial direction, this study adopts the heating section of 90 mm in length, which is much longer than those in the previous studies (20 mm [202] or 30 mm [200]). The contact area with electrodes, of 0.5 mm in width, was adopted to reduce the heat loss through the electrodes, which is smaller than those in the previous studies (10 mm [200, 202]). The sample reached to saturated temperatures through the balance of the internal Joule heat input and heat loss at the surface. Therefore, during DERHT, the temperature distribution at the middle section of the samples can be regarded as homogeneous.

This middle section was of 10 mm in length and used to investigate microstructure, phase transformation characteristics, superelasticity, and hardness, as shown in **Fig. 3.2(b)**.

3.2.3 Experimental design of DERHT

For the four types of NiTi alloys, two representative current magnitudes (8 A and 12 A) were adopted according to **Fig. 3.4** and Eq. (3.1). The current magnitude of 8 A corresponds to 592 K of the samples which is close to the temperature of LTA of this study (573 K). 8 A is thus selected to investigate the effect of DERHT induced short-time LTA on the properties of the NiTi alloys. 12 A is corresponding to the heating temperature of 801 K which is higher than 693 K (the recrystallization temperature of the as-received nanocrystalline NiTi alloys). Therefore, at 12 A, the corresponding heating temperature can effectively lead to grain growth. Too larger DC magnitude may lead to rapid grain growth within one or several seconds, which is difficult for the precise grain size adjustment; too smaller DC magnitude corresponds to the lower heating temperature, which may lead to less effectiveness of grain growth. Thus, 12 A is one of the feasible DC magnitude for grain size adjustment and is thus selected to investigate the grain growth induced by DERHT.

The heating time of 0-600 s was selected to investigate short-time influence of DERHT on the properties of the NiTi alloys. Based on the experimental results, to obtain the processing windows of the DERHT on the different NiTi alloys, different heating times were adopted for different NiTi alloys. Some additionally levels of DERHT time are to further understand the rapid variations of phase

transformation and superelasticity. The detailed experimental design of the DERHT is as shown in **Table 3.1**.

Table 3.1 Experimental design of the DERHT on the different NiTi alloys

Abbreviations of samples	DC magnitude (A)	Heating time (s)											
		0	5	7	8	9	10	15	25	50	100	300	600
NC	12	•	•					•	•	•	•	•	•
	8	•								•	•	•	•
ANC	12	•	•					•	•	•	•	•	•
	8	•								•	•	•	•
CG	12	•						•	•	•	•		•
	8	•								•	•	•	•
ACG	12	•	•	•	•	•		•	•	•	•	•	•
	8	•								•	•	•	•

3.3 Effect of DERHT on the phase transformation characteristics of NiTi alloys

The DSC curves of the four types of NiTi alloys under DERHT of 12 A and 8 A within 0-600 s are shown in **Fig. 3.5**. The corresponding thermal hysteresis and transformation enthalpy are shown in **Table 3.2-3.5**.

The NC samples keep B2 \leftrightarrow R transformation sequence and temperatures nearly unchanged under 12 A in 0-10 s. The transformation temperatures decrease in 10-15 s, and the transformation sequence changes from B2 \leftrightarrow R to B2 \leftrightarrow B19' in 15-20 s. The B2 \leftrightarrow B19' transformation sequence keeps unchanged but the transformation temperatures increase in 20-600 s. With the increasing heating time, the transformation peaks become more concentrated, the transformation enthalpy increases, and the thermal hysteresis decreases. Under 8 A in 0-600 s, B2 \leftrightarrow R transformation keeps unchanged. The transformation temperatures decrease

slightly in 0-100 s but then slightly increase in 100-600 s. With the increasing heating time, transformation enthalpy increases and thermal hysteresis decreases.

The ANC samples present the decrease of $B2 \leftrightarrow R$ transformation temperatures under 12 A in 0-10 s. Then, the ANC samples show a similar change of phase transformation characteristics to that of the NC samples. Under 8 A, the $B2 \leftrightarrow R$ transformation temperatures decrease in 0-100 s and then slightly increase in 100-600 s. The transformation enthalpy increases with the increasing heating time.

The CG samples keep $B2 \leftrightarrow B19'$ transformation unchanged under 12 A. The transformation temperature slightly increases in 0-10 s and keeps stable in 10-600 s. The thermal hysteresis rapidly decreases in 0-10 s and then keeps stable in 10-600 s. Under 8 A, the transformation sequence changes from $B2 \leftrightarrow B19'$ to $B2 \rightarrow R \rightarrow B19'/B19' \rightarrow B2$ in 0-50 s and further changes to $B2 \leftrightarrow R \leftrightarrow B19'$ in 50-600 s. The transformation temperatures, the thermal hysteresis of $R \leftrightarrow B19'$ transformation, and the $B2 \leftrightarrow R$ transformation enthalpy increase with the increasing heating time.

The ACG samples change the transformation sequence from $B2 \leftrightarrow R \leftrightarrow B19'$ to $B2 \rightarrow R \rightarrow B19'/B19' \rightarrow B2$ under 12 A in 0-10 s and further to $B2 \leftrightarrow B19'$ in 10-600 s. In 0-10 s, the $B2 \leftrightarrow R$ transformation temperatures gradually decrease and the transformation peaks gradually flatten. The $R \rightarrow B19'$ transformation temperature increases while the $B19' \rightarrow R$ transformation temperature decreases, which leads to the decrease of thermal hysteresis of $R \leftrightarrow B19'$ transformation. In 10-600 s, $B2 \leftrightarrow B19'$ transformation sequence is preserved and the transformation

temperature, thermal hysteresis, and transformation enthalpy generally keeps unchanged. Under 8 A, the $B2 \leftrightarrow R \leftrightarrow B19'$ transformation sequence keeps unchanged. In 0-50 s, $B2 \rightarrow R$, $B19' \rightarrow R$, and $R \rightarrow B2$ transformation temperatures decrease, while $R \rightarrow B19'$ transformation temperature increase. The $R \leftrightarrow B19'$ transformation thermal hysteresis also decreases. In 50-600 s, all the transformation temperatures increase with heating time. The thermal hysteresis and transformation enthalpy generally keep unchanged.

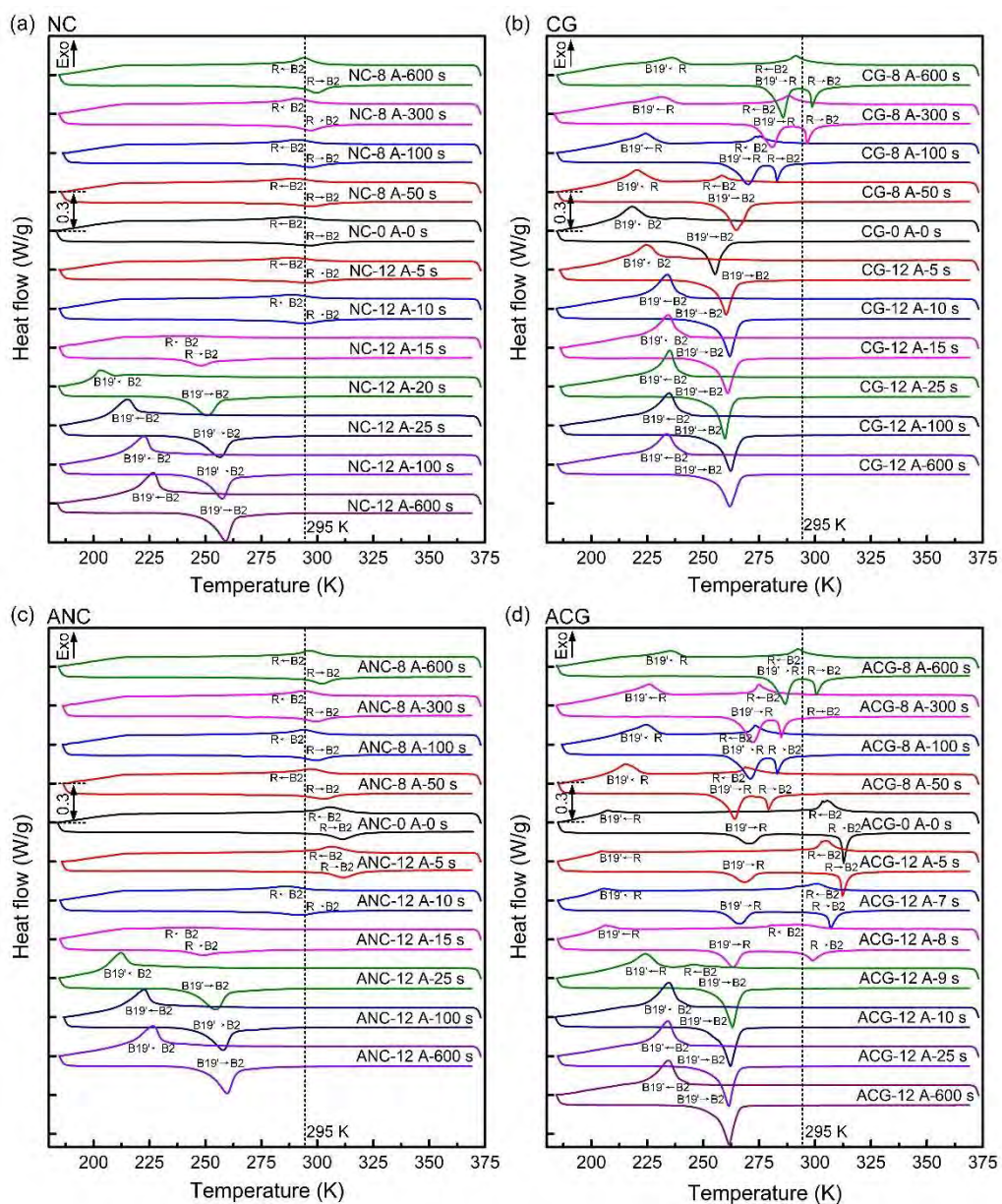


Fig. 3.5 DSC curves of the NiTi alloys before and after DERHT: (a) the NC samples; (b) the CG samples; (c) the ANC samples; and (d) the ACG samples.

Table 3.2 Thermal hysteresis and transformation enthalpy of the NC samples

Abbreviations of samples	TH (K)			ΔH (J/g)					
	TH _{AR}	TH _{RM}	TH _{AM}	ΔH_{AR}	ΔH_{RA}	ΔH_{RM}	ΔH_{MR}	ΔH_{AM}	ΔH_{MA}
NC-0 A-0 s	7.60	--	--	5.40	4.86	--	--	--	--
NC-12 A-5 s	7.95	--	--	5.21	4.54	--	--	--	--
NC-12 A-10 s	6.98	--	--	5.38	4.83	--	--	--	--
NC-12 A-15 s	8.36	--	--	1.77*	6.62	--	--	--	--
NC-12 A-20 s	--	--	47.98	--	--	--	--	13.38*	12.79
NC-12 A-25 s	--	--	41.24	--	--	--	--	15.08*	13.76
NC-12 A-100 s	--	--	34.94	--	--	--	--	16.24*	13.84
NC-12 A-600 s	--	--	32.43	--	--	--	--	16.76*	14.49
NC-8 A-50 s	9.38	--	--	5.55	4.83	--	--	--	--
NC-8 A-100 s	7.45	--	--	5.44	5.02	--	--	--	--
NC-8 A-300 s	7.01	--	--	5.81	5.42	--	--	--	--
NC-8 A-600 s	6.31	--	--	6.33	5.78	--	--	--	--

*: Due to the heat flow limitation of the DSC curves at the low-temperature section, the marked data were influenced by systematic errors. A: B2 austenite phase, M: B19' martensite phase, R: R-phase.

Table 3.3 Thermal hysteresis and transformation enthalpy of the ANC samples

Abbreviations of samples	TH (K)			ΔH (J/g)					
	TH _{AR}	TH _{RM}	TH _{AM}	ΔH_{AR}	ΔH_{RA}	ΔH_{RM}	ΔH_{MR}	ΔH_{AM}	ΔH_{MA}
ANC-0 A-0 s	6.40	--	--	5.7	5.51	--	--	--	--
ANC-12 A-5 s	6.27	--	--	7.28	5.73	--	--	--	--
ANC-12 A-10 s	7.83	--	--	5.50	5.00	--	--	--	--
ANC-12 A-15 s	7.15	--	--	1.98*	5.48	--	--	--	--
ANC-12 A-25 s	--	--	42.43	--	--	--	--	14.32*	13.53
ANC-12 A-100 s	--	--	35.58	--	--	--	--	15.12*	13.20
ANC-12 A-600 s	--	--	33.26	--	--	--	--	18.97*	15.53
ANC-8 A-50 s	6.83	--	--	5.46	5.27	--	--	--	--
ANC-8 A-100 s	6.31	--	--	5.99	5.30	--	--	--	--
ANC-8 A-300 s	6.76	--	--	6.04	5.53	--	--	--	--
ANC-8 A-600 s	6.06	--	--	6.38	5.92	--	--	--	--

*: Due to the heat flow limitation of the DSC curves at the low-temperature section, the marked data were influenced by systematic errors. A: B2 austenite phase, M: B19' martensite phase, R: R-phase.

Table 3.4 Thermal hysteresis and transformation enthalpy of the CG samples

Abbreviations of samples	TH (K)			ΔH (J/g)					
	TH _{AR}	TH _{RM}	TH _{AM}	ΔH_{AR}	ΔH_{RA}	ΔH_{RM}	ΔH_{MR}	ΔH_{AM}	ΔH_{MA}
CG-0 A-0 s	--	--	37.10	--	--	--	--	15.72*	13.50
CG-12 A-5 s	--	--	35.70	--	--	--	--	15.48*	13.82
CG-12 A-10 s	--	--	27.87	--	--	--	--	15.55*	14.78
CG-12 A-15 s	--	--	26.72	--	--	--	--	15.34*	14.31
CG-12 A-25 s	--	--	24.65	--	--	--	--	15.38*	14.19
CG-12 A-100 s	--	--	27.49	--	--	--	--	16.67*	14.47
CG-12 A-600 s	--	--	28.01	--	--	--	--	16.61*	13.70
CG-8 A-50 s	6.41	--	44.58	3.37	--	16.76*	--	--	14.49
CG-8 A-100 s	7.79	45.84	--	4.48	3.97	11.90*	10.22	--	--
CG-8 A-300 s	8.20	49.69	--	5.27	4.72	10.22*	9.74	--	--
CG-8 A-600 s	7.23	49.85	--	5.63	5.05	11.62*	10.74	--	--

*: Due to the heat flow limitation of the DSC curves at the low-temperature section, the marked data were influenced by systematic errors. A: B2 austenite phase, M: B19' martensite phase, R: R-phase.

Table 3.5 Thermal hysteresis and transformation enthalpy of the ACG samples

Abbreviations of samples	TH (K)				ΔH (J/g)				
	TH _{A-R}	TH _{R-M}	TH _{A-M}	ΔH_{A-R}	ΔH_{R-A}	ΔH_{R-M}	ΔH_{M-R}	ΔH_{A-M}	ΔH_{M-A}
ACG-0 A-0 s	7.40	63.30	--	6.59	6.86	5.82*	4.17	--	--
ACG-12 A-5 s	7.41	64.22	--	7.47	6.49	2.99*	5.40	--	--
ACG-12 A-7 s	6.36	61.09	--	6.76	5.82	3.48*	6.63	--	--
ACG-12 A-8 s	6.91	57.28	--	6.31	5.34	4.85*	7.45	--	--
ACG-12 A-9 s	17.97	--	39.11	1.96*	--	14.40*	--	--	14.42
ACG-12 A-10 s	--	--	27.48	--	--	--	--	18.17*	14.63
ACG-12 A-25 s	--	--	27.41	--	--	--	--	16.26*	14.64
ACG-12 A-600 s	--	--	27.19	--	--	--	--	18.44*	14.82
ACG-8 A-50 s	10.17	49.22	--	4.57	4.11	8.85*	9.80	--	--
ACG-8 A-100 s	9.79	46.89	--	4.79	4.03	10.97*	10.51	--	--
ACG-8 A-300 s	9.75	46.40	--	4.81	4.21	10.87*	10.58	--	--
ACG-8 A-600 s	8.09	51.36	--	5.09	4.84	7.36*	9.83	--	--

*: Due to the heat flow limitation of the DSC curves at the low-temperature section, the marked data were influenced by systematic errors. A: B2 austenite phase, M: B19' martensite phase, R: R-phase.

The variations of the transformation temperatures with the heating time of the NiTi alloys are shown in **Fig. 3.6**. The processing windows of DERHT regarding the transformation temperature adjustment under 12 A and 8 A are respectively shown in **Fig. 3.6**. As can be seen from the figure, NiTi alloys with different grain sizes present different responses to the same DERHT. Nanocrystalline NiTi alloys are more sensitive under 12 A, while coarse-grained NiTi alloys are more sensitive under 8 A.

NiTi alloys before and after aging also present different responses to the same DERHT. The ACG samples are sensitive to 12 A, and both transformation sequence and temperatures rapidly change in 0-10 s. By contrast, the CG samples are not sensitive to 12 A.

The above results indicate that NiTi alloys with different grain sizes and aging states present different phase transformation characteristics after DERHT, and the DERHT processing windows for these NiTi alloys are also different.

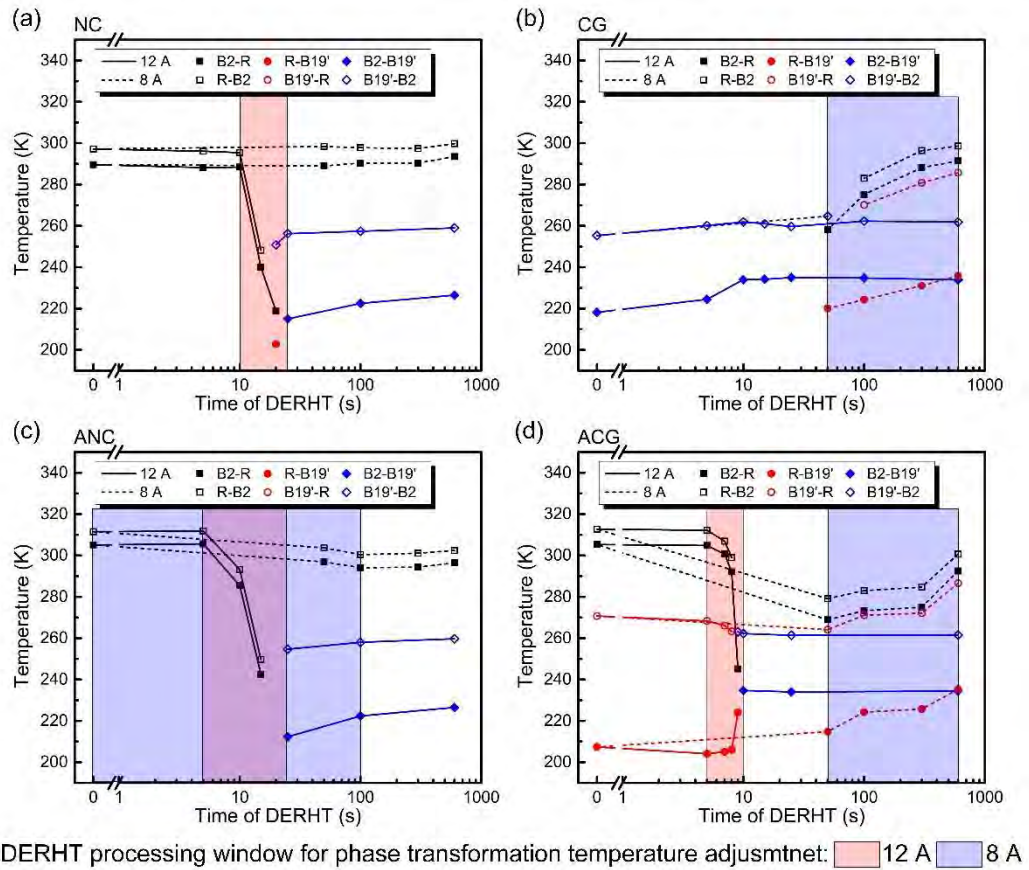


Fig. 3.6 Phase transformation temperatures of the NiTi alloys after DERHT and the corresponding processing windows: (a) the NC samples; (b) the CG samples; (c) the ANC samples; and (d) the ACG samples.

3.4 Effect of DERHT on the superelasticity of NiTi alloys

The variations of superelastic stress-strain curves of the NiTi alloys under 12 A are shown in **Fig. 3.7**. 12 A remarkably changes the superelasticity of nanocrystalline samples, while it shows little effect on coarse-grained samples. For the NC samples, in 0-25 s, the loading plateau stress, stress hysteresis, post-plateau strain, and the maximum loading stress decrease, while the plateau strain and residual strain increase. In 25-600 s, the superelasticity presents little change. For ANC samples, in 0-10 s, the loading and unloading plateau stress slightly increase,

while the strains induced by B2 \leftrightarrow R transformation or R-phase reorientation decrease, which leads to the decreasing residual strain. In 10-600 s, the variation of superelasticity is similar to the NC samples. For the CG samples, the loading plateau stress and plateau strain are unchanged. In 0-10 s, stress hysteresis and residual strain increase. In 10-600 s, the residual strain increases slightly. For the ACG samples, in 0-10 s, plateau strain increases, while the strains induced by B2 \leftrightarrow R transformation or R-phase reorientation decrease. The stress hysteresis increases rapidly in 9-10 s. In 10-600 s, the variation of superelasticity is similar to that of the CG samples.

The variations of superelastic stress-strain curves of the NiTi alloys under 8 A are shown in **Fig. 3.8**. 8 A shows little effect on the nanocrystalline NiTi alloys while remarkably it affects the coarse-grained NiTi alloys. For the NC samples, superelasticity presents little change in 0-300 s. In 300-600 s, loading and unloading plateau stress and plateau strain decrease slightly, while stress hysteresis increases slightly. For the ANC samples, in 0-100 s, the unloading plateau stress and plateau strain increase. In 100-600 s, it presents similar variation of superelasticity as the NC samples. For the CG samples, the loading and unloading plateau stress and plateau strain decrease with the heating time in 0-600 s. Stress hysteresis and residual strain decrease in 0-100 s while increase in 100-600 s. In 300-600 s, plateau strain decreases while the post-plateau strain increases. For the ACG samples, loading and unloading plateau stress decrease, while stress hysteresis increases with heating time in 0-600 s. Plateau strain increases in 0-50 s but decreases in 50-600 s. Residual strain decreases in 0-100 s but increases in 100-600 s.

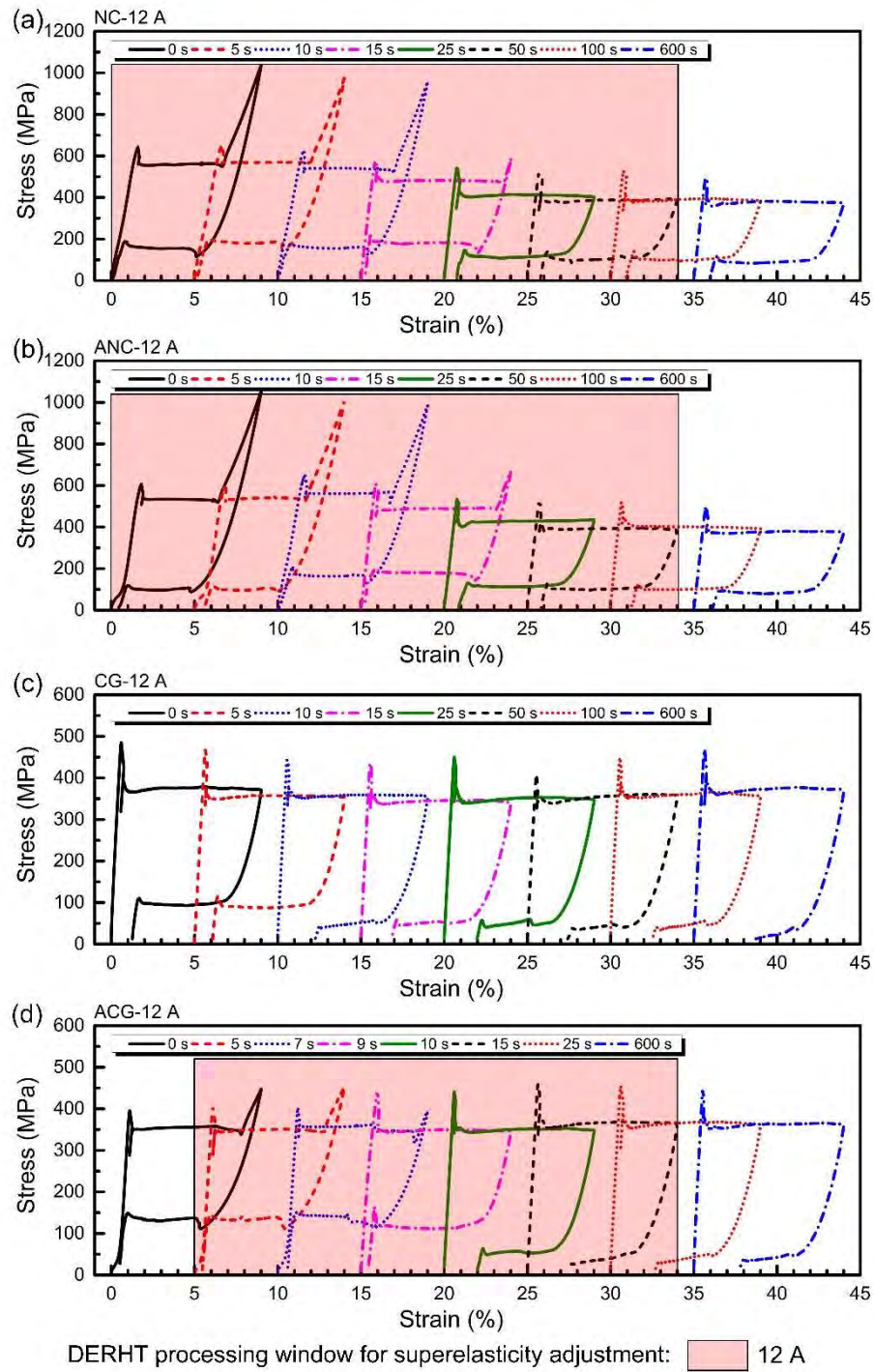


Fig. 3.7 Superelasticity curves of the NiTi alloys after DERHT of 12 A and the corresponding processing windows: (a) the NC samples; (b) the ANC samples; (c) the CG samples; and (d) the ACG samples.

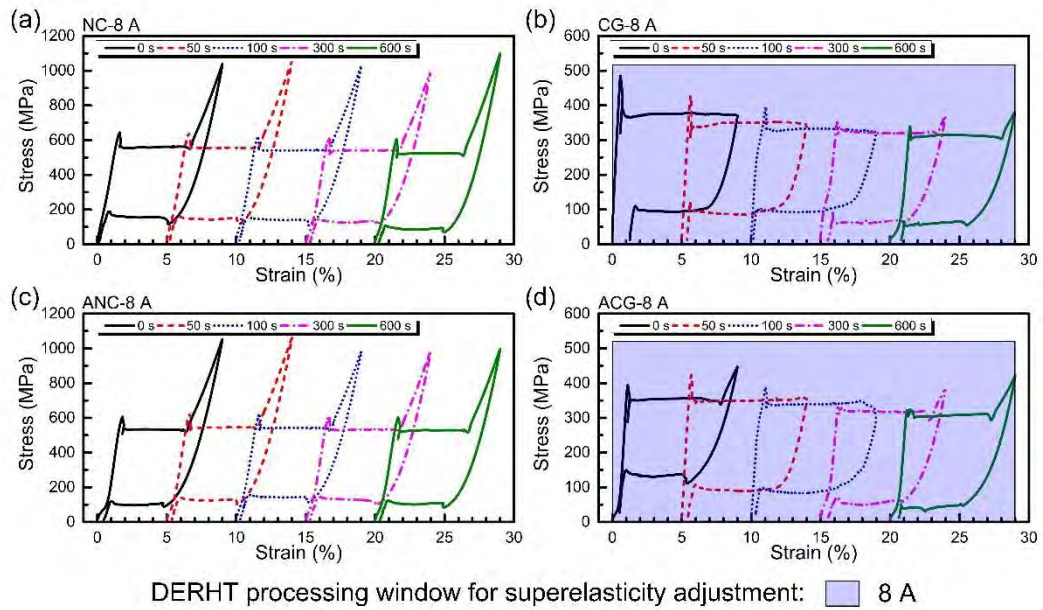


Fig. 3.8 Superelasticity curves of the NiTi alloys after DERHT of 8 A and the corresponding processing windows: (a) the NC samples; (b) the ANC samples; (c) the CG samples; and (d) the ACG samples.

The variations of superelasticity indices of the NiTi alloys with DERHT heating time are shown in **Fig. 3.9**. **Fig. 3.9(a)** presents the variations of loading plateau stress. The loading plateau stress of the nanocrystalline NiTi alloys rapidly decreases under 12 A in 10-50 s, while that of the coarse-grained NiTi alloys slowly decreases under 8 A in 0-600 s. **Fig. 3.9(b)** presents the variations of unloading plateau stress. The unloading plateau stress of the NC, CG, and ACG samples decreases with the increasing heating time, while that of the ANC samples firstly increases and then decreases no matter under 12 A or 8 A. Under 12 A, the unloading plateau stress of nanocrystalline NiTi alloys decreases rapidly in 10-50 s, while that of coarse-grained NiTi alloys decreases rapidly in 5-10 s. Under 8 A, the unloading plateau stress of all the NiTi alloys decreases remarkably in 100-600 s.

Fig. 3.9(c) presents the variations of stress hysteresis. Under 12 A, in 5-15 s, the stress hysteresis of the nanocrystalline NiTi alloys rapidly decreases, while that of the coarse-grained NiTi alloys rapidly increases. In the following 15-600 s, the stress hysteresis of all the NiTi alloys is generally unchanged. Under 8 A, the stress hysteresis of all the NiTi alloys is also hardly changed.

Fig. 3.9(d) presents the variation of plateau strain. Under 12 A, in 5-25 s, the plateau strain of the NC, ANC, and ACG samples fast increases to above 8% then keeps unchanged. Under 8 A, the plateau strains of the NC and ANC samples are generally unchanged. That of the ACG samples rapidly increases in 0-50 s and then decreases in 50-600 s as similar to the CG samples.

Fig. 3.9(e) presents the variation of residual strain. Under 12 A, the residual strain of the NC and ACG samples rapidly increases in 5-25 s and then keeps stable in the following 25-600 s. The residual strain of the CG samples increases with heating time. That of the ANC samples decreases in 5-10 s and then varies as similar to the NC samples in 10-600 s. Under 8 A, the residual strain of the NC and ANC samples generally keeps stable, while that of the CG and ACG samples decreases in 0-100 s and then gradually increases in 100-600 s.

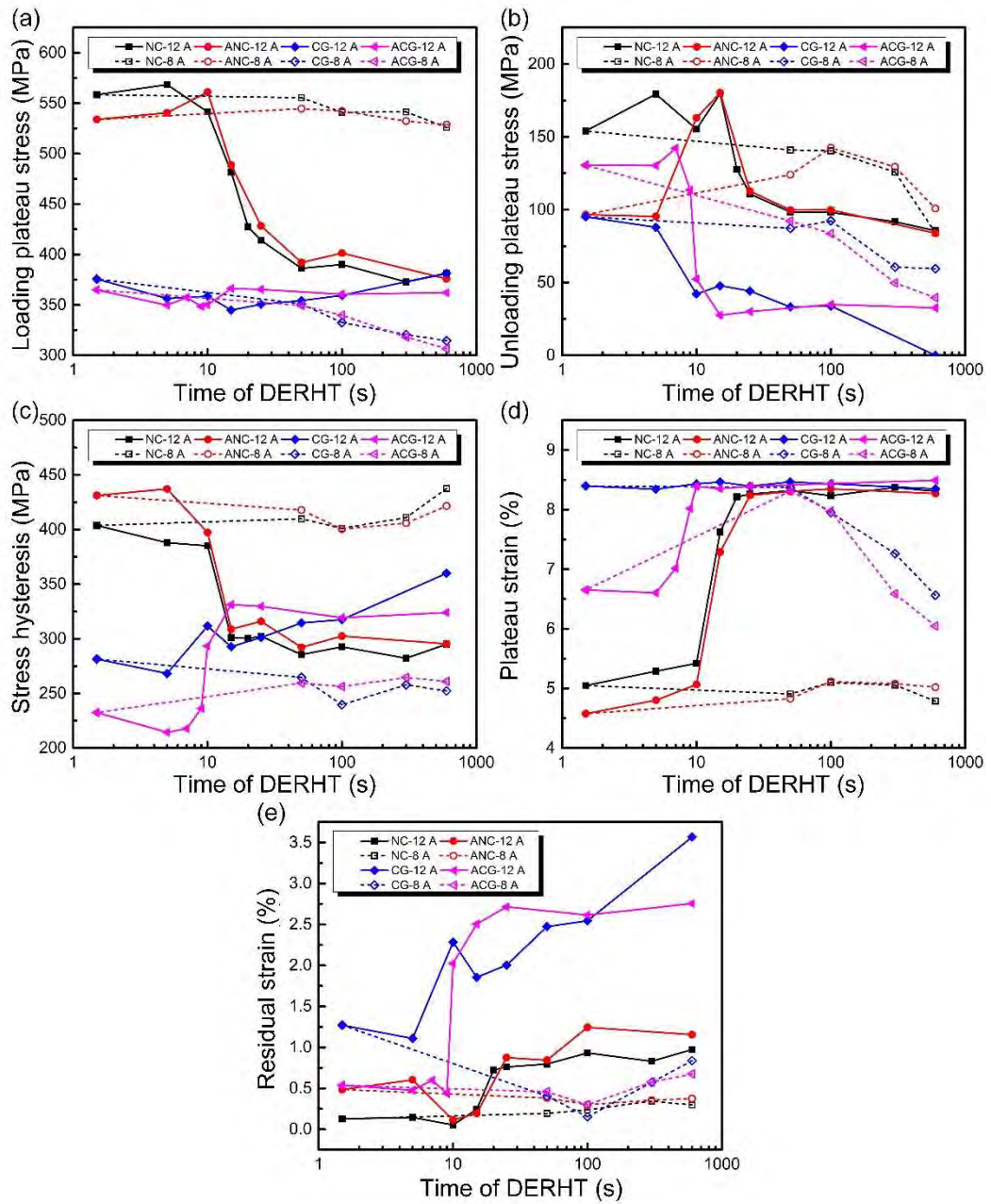


Fig. 3.9 Variations of the superelasticity indices with DERHT heating time: (a) loading plateau stress; (b) unloading plateau stress; (c) stress hysteresis; (d) plateau strain; and (e) residual strain.

Based on the above results, it can be seen that the NiTi alloys with different grain sizes and aging states present different variations of superelasticity under DERHT. The corresponding DERHT processing windows are also different. It is

noteworthy that, to a certain type of NiTi alloys, the DERHT processing windows for phase transformation temperature adjustment and superelasticity adjustment are generally consistent. It is the microstructural evolutions induced by DERHT that are the underlying mechanisms for the above variations, which are to be studied in the next section.

3.5 Mechanisms of the influence of DERHT on NiTi alloys from the microstructural evolution perspective

3.5.1 Grain growth

The microstructural evolution of NC samples under DERHT is shown in **Fig. 3.10**. Under 12 A, the grain size of the NC samples remarkably increases. In 10-25 s, the nanograins are rapidly enlarged to ultrafine grains and further to coarse grains. In 25-600 s, the grain size gradually increases within the coarse-grained scale. Under 8 A, however, the grain size keeps unchanged even when the heating time reaches to 600 s. The ANC samples present similar grain size variations as the NC samples under DERHT. The effect of DERHT on the grain size variation of the CG samples is shown in **Fig. 3.11**. It indicates that either 12 A or 8 A cannot effectively change the grain size of the CG samples. The grain size variations of the ACG samples are as similar as the CG samples where DERHT of 12 A or 8 A hardly affects their grain size.

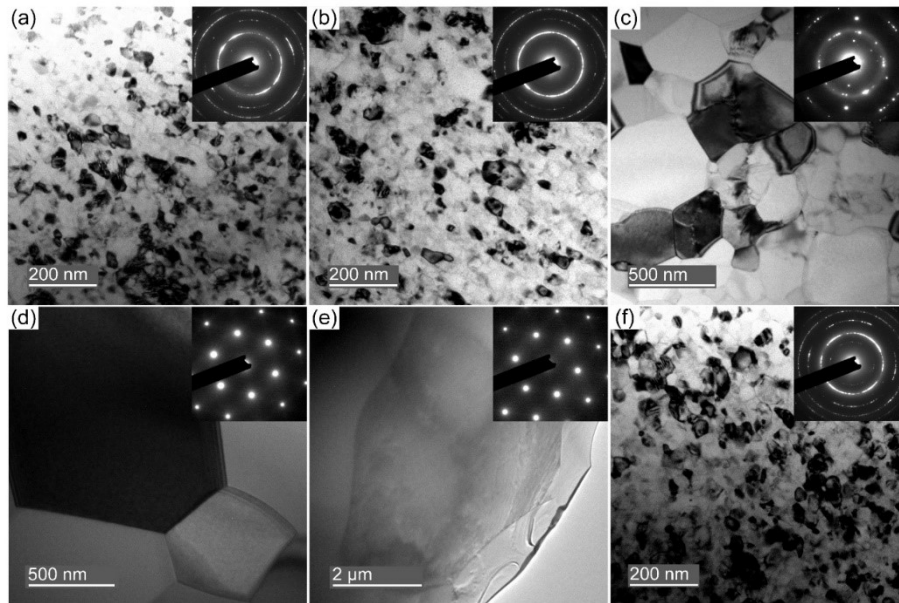


Fig. 3.10 Microstructural evolution of the NC samples under DERHT: (a) NC-0 A-0 s; (b) NC-12 A-10 s; (c) NC-12 A-15 s; (d) NC-12 A-25 s; (e) NC-12 A-600 s; and (f) NC-8 A-600 s.

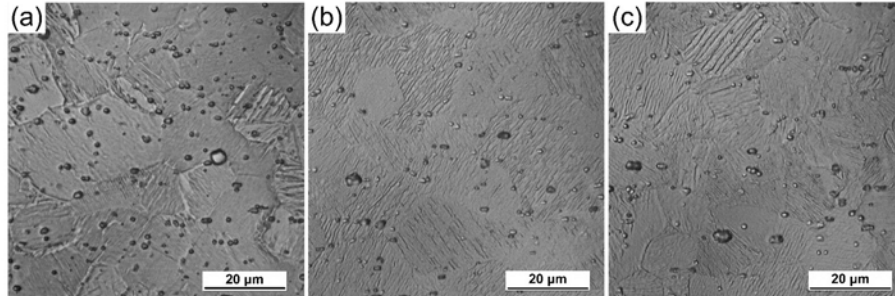


Fig. 3.11 Variation of the grain size of the CG samples under DERHT: (a) CG-0 A-0 s; (b) CG-12 A-600 s; (c) CG-8 A-600 s.

It can be seen from **Fig. 3.4(a)**, **Fig. 3.10** and **Fig. 3.11** that, if the DERHT heating temperature is higher than the post-deformation annealing temperatures that produced the initial grain size (e.g., 693 K for the NC samples of this study), the grain size is to be further enlarged. If the DERHT heating temperature is lower than the post-deformation annealing temperatures that produce the initial grain size

(e.g., 1123 K for the CG samples), the grain size is to be preserved. The saturated temperature of 8 A (592 K) is lower than the post-deformation annealing temperatures of both the NC and CG samples. Their grain sizes thus keep unchanged. The rapid grain growth of the NC samples provides a method for grain size adjustment of NiTi alloys, which is to be introduced in section 3.6 of this chapter.

3.5.2 Precipitation, growth, and dissolution of Ni₄Ti₃

According to the microstructures of the NC samples after DERHT, Ni₄Ti₃ precipitates are not found either under 12 A or 8 A. However, they are obviously observed in the CG samples, as shown in **Fig. 3.12**. Under 12 A, even after the DERHT of 600 s, the microstructure is still preserved as pure B2 austenite phase. Under 8 A, however, the Ni₄Ti₃ nanoprecipitates with the size of 15-25 nm and the gap of 15-30 nm are clearly observed in the NiTi matrix after the DERHT of 600 s. The SAED pattern verifies the existence of Ni₄Ti₃ and R-phase.

The microstructural evolution of the ACG samples under DERHT is shown in **Fig. 3.13**. Under 12 A, The Ni₄Ti₃ precipitates and R-phase that contained in the ACG samples are disappeared after the DERHT of 10 s, and the microstructure becomes pure B2 austenite phase. This indicates that, under 12 A, the previously formed Ni₄Ti₃ nanoprecipitates in the NiTi matrix are rapidly dissolved in 10 s. Under 8 A, after 600 s, the Ni₄Ti₃ precipitates are obviously grown in size but decrease in density, which present the size of 15-25 nm and the gap of 15-30 nm. These precipitates are similar to those in the CG samples after DERHT of 8 A-600 s.

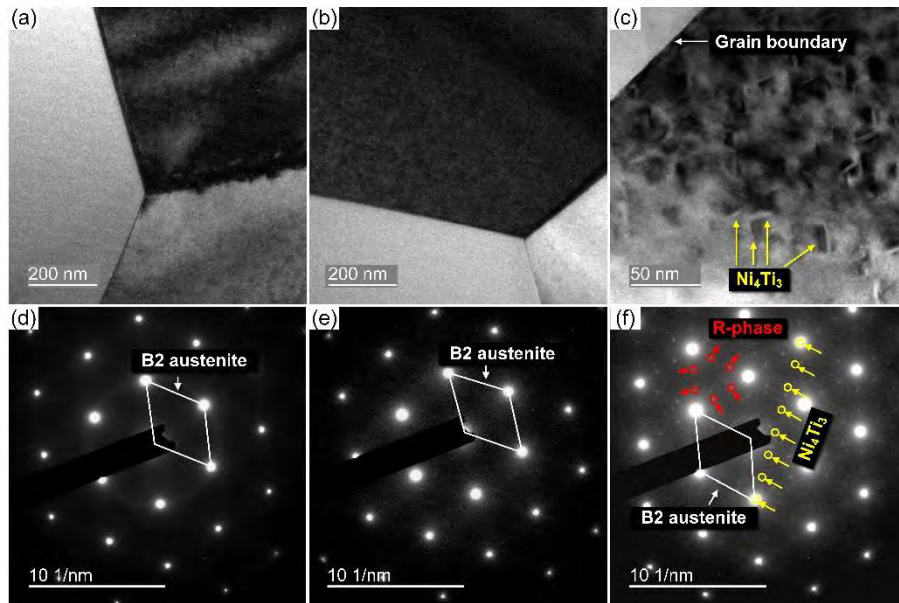


Fig. 3.12 Microstructural evolution of the CG samples induced by DERHT: (a) CG-0 A-0 s; (b) CG-12 A-600 s; (c) CG-8 A-600 s; (d) SAED pattern of (a); (e) SAED pattern of (b); and (f) SAED pattern of (c).

It can be seen from the effect of DERHT on grain size and precipitates that the higher current magnitude can rapidly enlarge nanocrystalline grain size, while the lower current magnitude can hardly affect the grain size even after the DERHT of 600 s. For the non-aged coarse-grained NiTi alloys, the higher current magnitude presents little effect on the microstructure, while the lower current magnitude can effectively introduce Ni_4Ti_3 precipitates. For the aged coarse-grained NiTi alloys, the higher current magnitude can rapidly dissolve the previously formed Ni_4Ti_3 nanoprecipitates in 10 s, while the lower current magnitude can lead to the growth of Ni_4Ti_3 precipitates.

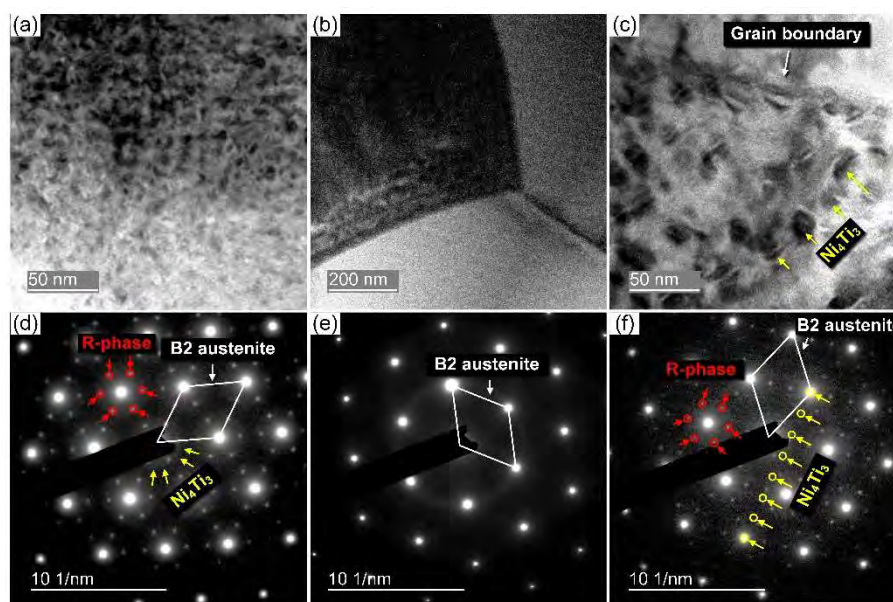


Fig. 3.13 Microstructural evolution of the ACG samples induced by DERHT: (a) ACG-0 A-0 s; (b) ACG-12 A-10 s; (c) ACG-8 A-600 s; (d) SAED pattern of (a); (e) SAED pattern of (b); and (f) SAED pattern of (c).

3.5.3 Nanograin size induced suppression of Ni_4Ti_3 precipitation during DERHT

There is a noteworthy phenomenon in the above results: the DERHT of 8 A-600 s presents different influences on the NC and CG samples regarding the Ni_4Ti_3 precipitation, which is comparatively demonstrated in **Fig. 3.14**. After the DERHT of 8 A-600 s, the NC samples still show nanocrystalline microstructure within which the Ni_4Ti_3 precipitates are not observed. The SAED pattern of the NC sample also presents B2 austenite phase, which has no trace of Ni_4Ti_3 . However, in the CG samples, the Ni_4Ti_3 precipitates are obviously observed after the DERHT of 8 A-600 s. The precipitates are of 15-25 nm in size and 15-30 nm in gap. The SAED pattern also verifies their existence and their coherency with the NiTi matrix.

The above comparison reveals two facts: 1) Under 8 A, even in short heating time (600 s), the DERHT is adequate to introduce Ni_4Ti_3 nanoprecipitates with 15-25 nm in size and 15-30 nm in gap in the coarse-grained NiTi alloys; 2) Nanograin size introduces obvious suppression of Ni_4Ti_3 precipitation, which results in the consequence that the Ni_4Ti_3 are not precipitated in the nanocrystalline NiTi matrix.

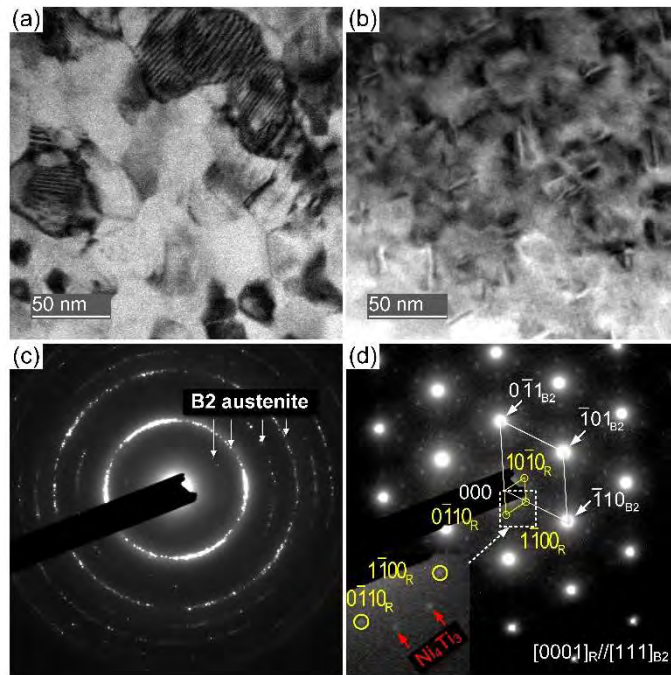


Fig. 3.14 Nanograin size induced suppression of Ni_4Ti_3 precipitation during DERHT: (a) NC-8 A-600 s, in which nanograin size was preserved and Ni_4Ti_3 precipitates were not observed; (b) CG-8 A-600 s, in which Ni_4Ti_3 precipitates with size of 15-25 nm and gap of 15-30 nm were obviously observed; (c) the SAED pattern of (a) which presented pure B2 austenite phase; and (d) the SAED pattern of (b) which presented B2 austenite phase, R-phase, and Ni_4Ti_3 phase.

3.5.4 Corroborative evidence of the microstructural evolutions based on the variation of hardness

The variations of grain size and Ni₄Ti₃ precipitates can lead to the variation of hardness. The hardness variations of the four NiTi alloys after the DERHT of 12 A and 8 A are shown in **Fig. 3.15**. For the NC and ANC samples, under 12 A, the hardness rapidly decreases in 5-25 s, which is consistent with the time interval of grain growth. This indicates that the drop of hardness is induced by grain growth. Under 8 A, the hardness only slightly decreases in 0-600 s, which indicates that the preservation of grain size and the decreasing defects of the nanocrystalline NiTi matrix.

For the CG samples, under 12 A, the hardness decreases slightly in 0-10 s and then keeps stable. This is because the CG samples are cooled by the cold argon in the furnace of which the cooling speed is less than water quenching. The Ni-rich Guinier-Preston (G.P.) zones [203] or spinodal decomposition [48] may be introduced in the NiTi matrix in such a situation. Though the G.P. zones and spinodal decomposition are difficult to be observed in TEM, they are able to elevate the hardness a little. However, this elevation effect is limited, which is much less effective than that induced by Ni₄Ti₃ nanoprecipitates as showed by the hardness of the ACG samples. Under 12 A, the G.P. zones or spinodal decomposition are fast dissolved in the NiTi matrix only in 10 s, and the hardness is consequently dropped and then keeps stable in the following 10-600 s. Under 8 A, the hardness obviously increases with heating time, which reflects the effect of precipitation strengthening.

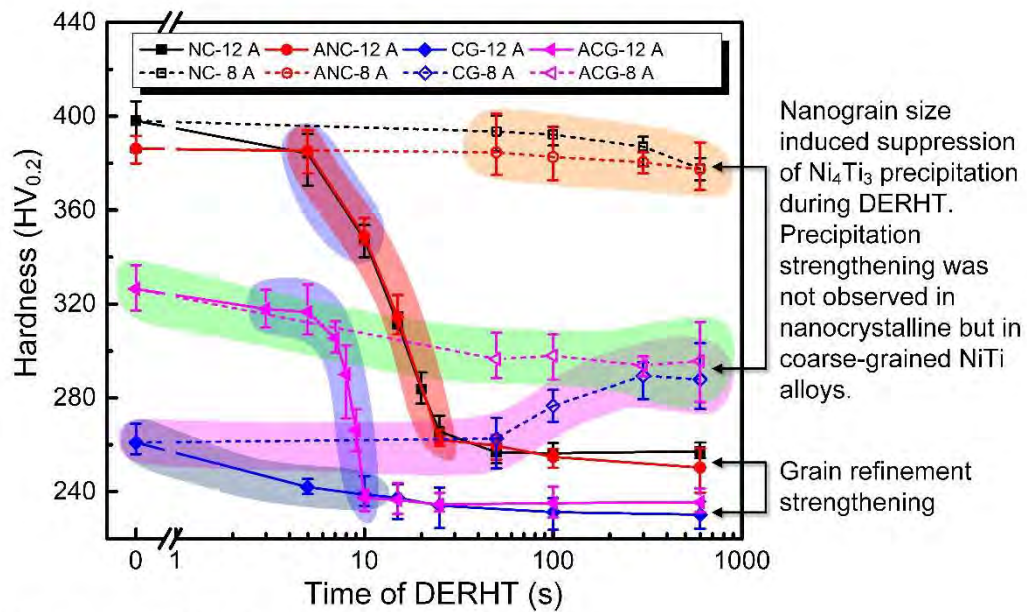
For the ACG samples, under 12 A, the hardness drops quickly in 5-10 s, which reflects the dissolution of Ni_4Ti_3 . In the following 10-600 s, the hardness keeps stable as similar to that of the CG samples. This indicates that the ACG samples keeps in solution state after the dissolution of Ni_4Ti_3 . Under 8 A, the hardness drops gradually with the increasing heating time. This indicates that the enlarged Ni_4Ti_3 precipitates (15-25 nm in size and 15-30 nm in gap) are less effective than the original Ni_4Ti_3 precipitates (7-15 nm in size and 5-15 nm in gap) regarding their strengthening effect on NiTi matrix. As pointed out by J.I. Kim et al. [48], finer Ni_4Ti_3 nanoprecipitates present higher resistance to dislocation slip. The hardness at 8 A is higher than that of 12 A, which indicates that the enlarged Ni_4Ti_3 precipitates also present a strengthening effect on the NiTi matrix compared with the solution state.

It is noteworthy that, under the DERHT of 8 A, the hardness of the nanocrystalline samples is not elevated, which indicates no precipitation strengthening. This works as a corroborative evidence for the above conclusion that nanograin size induces suppression of Ni_4Ti_3 precipitation during DERHT.

On the other hand, though the hardness of the NC and ANC samples drastically decreases under 12 A, it is still higher than those of the CG samples. This reflects the grain-refine strengthening effect because the grain size of the NC and ANC samples after the DERHT is 6.2 μm , while that of the CG samples is 21 μm .

The effect of DERHT on the microstructures of the different NiTi alloys can be summarized as follows: 1) higher current magnitude causes grain growth; 2) lower

current magnitude induces Ni_4Ti_3 precipitation and growth; 3) higher current causes dissolution of Ni_4Ti_3 ; and 4) nanograin size suppresses the Ni_4Ti_3 precipitation during DERHT.



Microstructural evolution:

- Ni_4Ti_3 precipitation
- Ni_4Ti_3 growth
- Ni_4Ti_3 Dissolution
- Grain growth
- Dissolution of G.P. Zone and other defects
- Further decrease of dislocations and other defects, and grain equiaxialization

Fig. 3.15 The corroborative evidence for the microstructural evolutions based on hardness variation

The above different microstructural evolutions are the underlying mechanisms for the different variations of phase transformation characteristics and superelasticity of the different types of NiTi alloys. The corresponding relationships are as follows:

- 1) Under 12 A, in 10-25 s, the disappearance of $\text{B2} \leftrightarrow \text{R}$ transformation, the emergence of $\text{B2} \leftrightarrow \text{B19}'$ transformation, the decrease of the loading plateau stress and stress hysteresis, and the increase of plateau strain and residual strain

in the NC and ANC samples, are all due to the grain growth. With the increasing grain size, the grain size induced activation of $B2 \leftrightarrow R$ transformation gradually weakens, and the suppression of $B2 \leftrightarrow B19'$ transformation also weakens. In the meanwhile, the volume fraction of the transformable material increases, but the energy dissipation during $R \leftrightarrow B19'$ transformation and the resistance to dislocation slip decreases.

2) Under 8 A, in 0-600 s, the CG and ACG samples show $B2 \leftrightarrow R$ transformation and the $B2 \leftrightarrow R$ and $R \leftrightarrow B19'$ transformation temperatures increase. The thermal hysteresis of $R \leftrightarrow B19'$ transformation is higher than that of $B2 \leftrightarrow B19'$ transformation. The loading plateau stress decreases. These phenomena are caused by the precipitation and growth of Ni_4Ti_3 . As the precipitation of the coherent Ni_4Ti_3 , $B2 \leftrightarrow R$ transformation is facilitated, and the energy dissipation of $R \leftrightarrow B19'$ transformation increases. The elastic strain field around the coherent precipitates facilitates the stress-induced $R \leftrightarrow B19'$ transformation. Besides, the Ni depletion in the NiTi matrix caused by the precipitation also decreases the required stress for activating $R \leftrightarrow B19'$ transformation.

3) Under 12 A, in 5-10 s, $B2 \leftrightarrow R$ transformation disappears in the ACG samples, while $B2 \leftrightarrow B19'$ transformation replaces $R \leftrightarrow B19'$ transformation. In the meantime, the loading plateau stress, residual strain, and stress hysteresis increase. These phenomena are due to the dissolution of Ni_4Ti_3 . As Ni_4Ti_3 dissolved, the facilitation of $B2 \leftrightarrow R$ transformation and the suppression of $B2 \leftrightarrow B19'$ transformation are both removed. Meanwhile, the volume fraction

of the transformable material increases, the dislocation slip resistance decreases, and the energy dissipation increases due to the increasing dislocation activities.

- 4) Under 8 A, in 0-600 s, the phase transformation characteristics and superelasticity of the NC and ANC samples generally keep unchanged, which reflects the nanograin size induced suppression of Ni₄Ti₃ precipitation during DERHT.

3.6 Grain size adjustment model based on DERHT

As can be seen from the results of section 3.5, the higher current magnitude can effectively alter the grain size of the nanocrystalline NiTi alloys with different heating time, e.g., the grain size of the NC samples can be increased to coarse-grained scale under 12 A in 0-600 s. In the meanwhile, by comparing the effect of DERHT of 12 A and 8 A on grain size, it also indicates that altering the current magnitude can also adjust the grain size. Therefore, this section suggests two grain size adjustment models based on DERHT from the perspectives of altering the heating time and altering the current magnitude, respectively.

3.6.1 Grain size adjustment model based on the heating time of DERHT

As seen in **Fig. 3.10**, the NiTi alloys with the diameter of 1 mm and the initial grain size of 34 nm experience grain growth under the DERHT of 12 A (current density of 15.28 A·mm²). The relationship between grain size and heating time is

shown in **Fig. 3.16**. For the convenience of modeling, the grain size in the DERHT of 1 s is assumed unchanged, i.e., the grain size after the DERHT of 1 s is assumed as same as that before the DERHT. As shown in **Fig. 3.16**, the grain size increases to 6.2 μm from 34 nm in 0-600 s under 12 A. The figure also indicates that the grain size rapidly increases in 10-50 s.

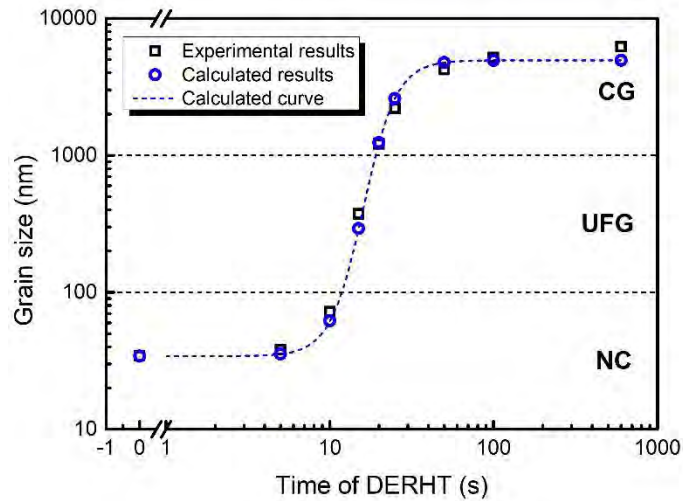


Fig. 3.16 The relationship of grain size and the heating time under DERHT of 12 A ($15.28 \text{ A}\cdot\text{mm}^2$)

Based on the variations of grain size with DERHT heating time, the model of grain size adjustment can be obtained. Under certain current magnitude, the samples respectively experience slow grain growth, rapid grain growth, and grain size saturated stages, of which the grain size presents “S” shape relation with heating time. The logistic function [204] is commonly used in the engineering field to depict the process from growth to saturation, which is appropriate for describing the aforementioned grain size variations. Therefore, the logistic function is adopted as the basis of the grain size adjustment model. The equation of logistic function is as follows:

$$f(x) = \frac{k}{1 + \exp(a - bx)} \quad (3.2)$$

where x is the independent variable, a , b , and k are constants. Based on experimental results, the original grain size of the NC samples is 34.2 nm, thus a constant term was added after this function to represent the initial grain size before DERHT. The Eq. (3.2) was turned to:

$$f(x) = \frac{k}{1 + \exp(a - bx)} + c \quad (3.3)$$

where c was the constant term representing the initial grain size. based on the grain size growth data of the NC samples under 12 A. The Eq. (3.3) is calibrated as:

$$\log_{10} D \Big|_{\substack{I_{\text{DERHT}}=12 \text{ A} \\ D_0=34 \text{ nm}}} = \frac{2.15}{1 + \exp(9.84 - 8.30 \cdot \log_{10} t_{\text{DERHT}})} + \log_{10} D_0 \Big|_{D_0=34 \text{ nm}} \quad (3.4)$$

$t_{\text{DERHT}} \in [1, 600] \text{ (s)}$

where D is grain size (nm), D_0 is the initial grain size, I_{DERHT} is direct current magnitude (A), t_{DERHT} is the heating time (s).

The correlation between the calculated values and experimental values of the grain size is shown in **Fig. 3.17**. The correlation coefficient R is 0.99891, and the average absolute relative error (AARE(%)) is 6.77%. The equations to obtain the R and AARE(%) are shown in Eq. (3.5) and (3.6).

$$R = \frac{\sum_{i=1}^n (E_i - \bar{E})(P_i - \bar{P})}{\sqrt{\sum_{i=1}^n (E_i - \bar{E})^2} \sqrt{\sum_{i=1}^n (P_i - \bar{P})^2}} \quad (3.5)$$

$$\text{AARE}(\%) = \frac{1}{N} \sum_{i=1}^N \left| \frac{E_i - P_i}{E_i} \right| \times 100 \quad (3.6)$$

where E_i is the experimental result, \bar{E} is the average value of the experimental results, P_i is the calculated result, \bar{P} is the average value of the calculated

results, and N is the number of data points. When the R is more close to 1, and the AARE(%) is more close to 0, the model is more accurate.

The result indicates that the model can calculate the grain size of the nanocrystalline NiTi alloys under the DERHT of 12 A (15.28 A·mm²). It can further be deduced that, as long as the temperature of the DERHT is higher than the post-deformation annealing temperature for the initial grain size, the DERHT induced grain growth should also show “S” shape variation with heating time. Then, the relationship can also be calibrated by the model.

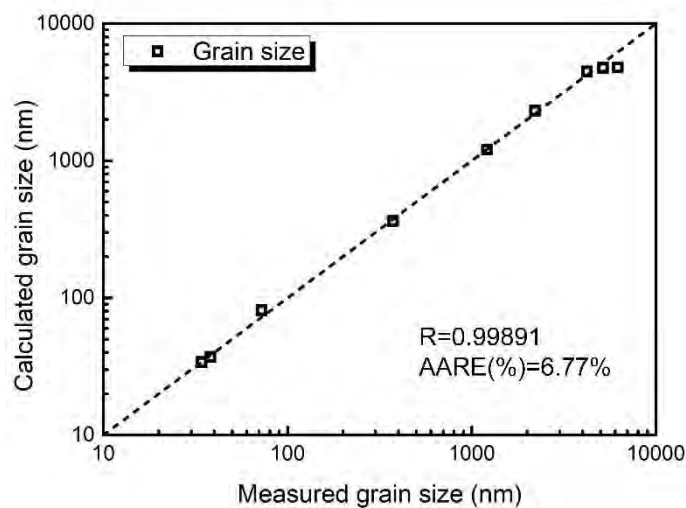


Fig. 3.17 The correlation between the calculated results and experimental results of grain size under DERHT of 12 A (15.28 A·mm²)

3.6.2 Grain size adjustment model based on the current magnitude of DERHT

As can be seen in the experimental results of this study, for the NiTi alloys with grain size of 34 nm and 1 mm in diameter, the DERHT of 12 A can effectively increase the grain size to 2190 nm in only 25 s, which can also effectively avoid

undesired Ni_4Ti_3 precipitation. However, the DERHT of 8 A cannot lead to further grain growth from 34 nm even after 600 s. This indicates that the grain size can be adjusted by altering the current magnitude when the heating time keeps constant.

Therefore, this chapter applied the DERHT of 9-14 A in 25 s to the NiTi alloy with 34 nm in grain size and 1 mm in diameter. The obtained microstructures are respectively shown in **Fig. 3.18**. The grain size remarkably increases with applied current magnitude. It can be seen from the TEM micrographs and SAED patterns that the NiTi matrix consists of B2 austenite phase and a small part of R-phase. The obtained grain sizes and the corresponding DERHT processing parameters are shown in **Table 3.6**, and the variation of grain size with applied current magnitude is shown in **Fig. 3.19**. The grain size increases with the current magnitude from NC to UFG and further to CG scale. In 0-9.5 A, the grain size increases slowly within NC scale; in 9.5-12 A, the grain size rapidly increases from NC to CG scale; in 12-14 A, the grain size increases slowly in CG scale.

Table 3.6 The obtained grain size and the corresponding DERHT parameters.

Average grain size before DERHT (nm)	DC magnitude (A)	Time of DERHT (s)	Average grain size after DERHT (nm)
34	0	0	34
34	9	25	40
34	9.5	25	51
34	10	25	105
34	10.5	25	217
34	11	25	523
34	11.5	25	1106
34	12	25	2190
34	13	25	4972
34	14	25	8021

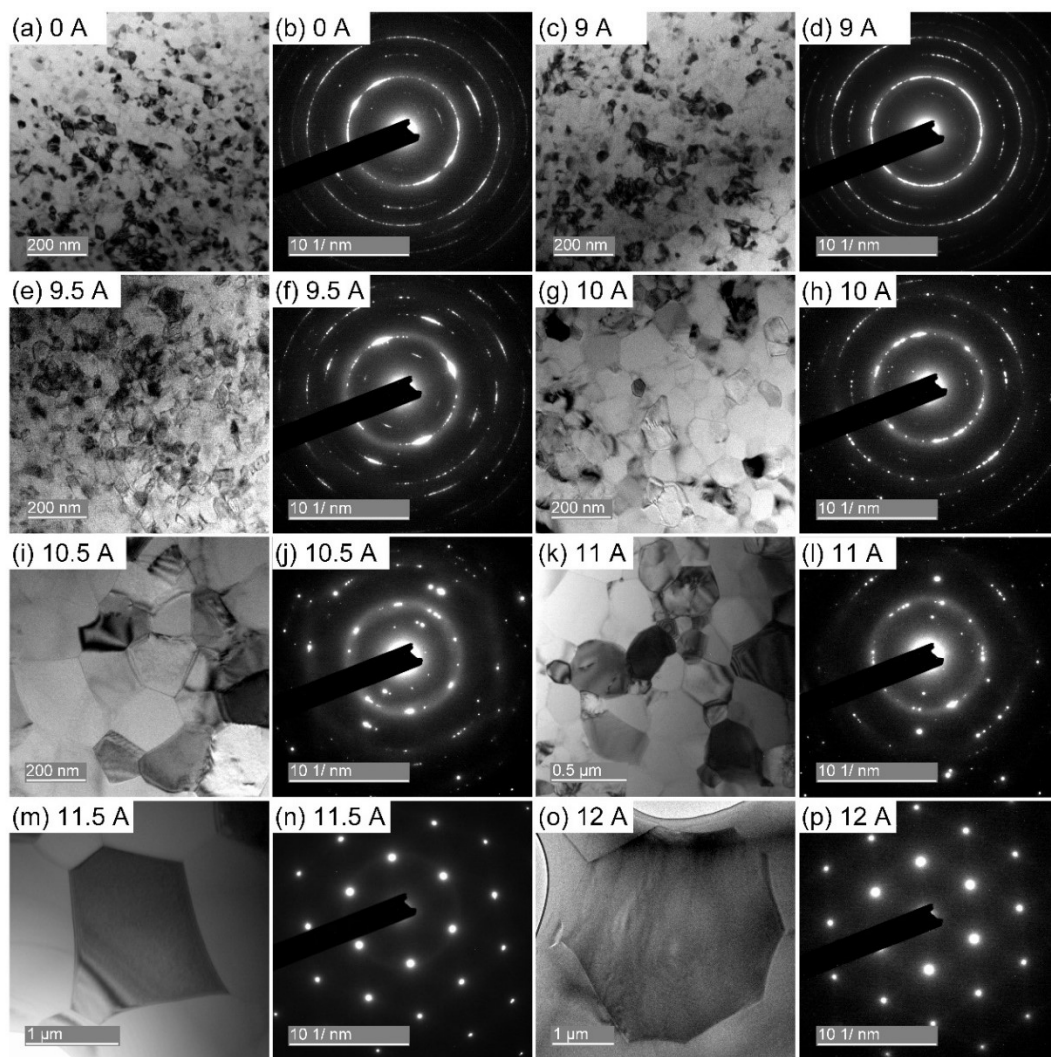


Fig. 3.18 The microstructures and corresponding SAED patterns after the DERHT of 25 s from the NiTi alloy with initial grain size of 34 nm under current

magnitude of: (a)-(b) 0 A; (c)-(d) 9 A; (e)-(f) 9.5 A; (g)-(h) 10 A; (i)-(j) 10.5 A; (k)-(l) 11 A; (m)-(n) 11.5 A; and (o)-(p) 12 A.

As seen in **Fig. 3.19**, the relationship of the current magnitude and grain size also presents “S” shape, thus the logistic function [204] of Eq. (3.3) can also be used to construct the grain size adjustment model, which is as follows:

$$\log_{10} D \Big|_{\substack{I_{\text{DERHT}}=25 \text{ s} \\ D_0=34 \text{ nm}}} = \frac{2.35}{1 + \exp(15.16 - 1.37 \cdot \log_{10} I_{\text{DERHT}})} + \log_{10} D_0 \Big|_{D_0=34 \text{ nm}} \quad (3.7)$$

$$I_{\text{DERHT}} \in [9, 14] \text{ (A)}$$

The comparison of the calculated results and experimental results of grain size are also shown in **Fig. 3.19**, and the correlation of them is shown in **Fig. 3.20**. As can be seen from the figures, the calculated and experimental results are consistent, and the correlation coefficient R is 0.99850 and the AARE(%) is 7.31%, which indicates that the model can be used to calculate the grain sizes that are adjusted by the DERHT of 25 s with 9-14 A.

By using this method, the NiTi alloys with grain size of 34-8021 nm (including NC, UFG, and CG grain size scales) without Ni₄Ti₃ precipitates are obtained by using this model via DERHT, which are prepared for the study of the subsequent chapters.

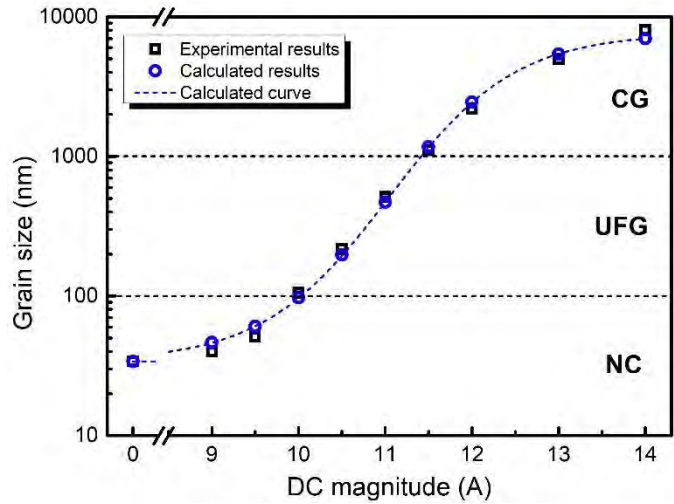


Fig. 3.19 Relationship between grain size and the current magnitude under DERHT of 25 s, which also presented the comparison of the calculated values and experimental values of the grain sizes

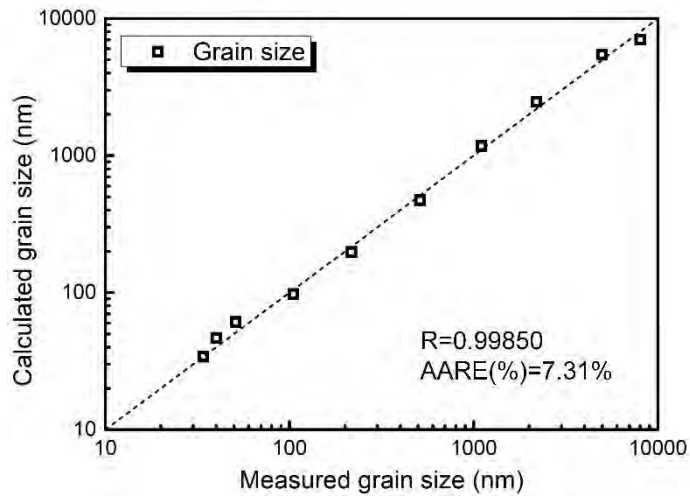


Fig. 3.20 Correlation between the calculated results and the experimental results of grain size under the DERHT of 25 s with different current magnitude.

3.7 Summary

This chapter studies the influence of DERHT on the microstructures, phase transformation characteristics, and superelasticity of the NiTi alloys (with

different grain sizes and aging states). The grain size adjustment models based on DERHT are obtained, which are used to prepare the NiTi alloys with grain size of 34-8021 nm without Ni₄Ti₃ precipitates. The following concluding remarks can thus be drawn:

- (1) The DERHT of 5-15 A can elevate the temperature of the NiTi alloys with 1 mm in diameter from room temperature to 435-960 K. Within the experimental current magnitude range, the temperatures were saturated at 30 s, which was irrelevant to current magnitude. When the current magnitude increased per 1 K, the saturated temperature increased about 52.5 K.
- (2) The DERHT of 12 A effectively increased the grain size of the NiTi alloys with the initial grain size of 34 nm: the grain size increased from 34 nm to about 2 μm in 0-25 s, and it further increased to 6.2 μm in the following 25-600 s. However, 12 A hardly affected the grain size of the coarse-grained NiTi alloys with the initial grain size of about 20 μm.
- (3) The DERHT of 12 A rapidly dissolved the previously formed Ni₄Ti₃ nanoprecipitates by LTA. This can be used as a method to eliminate the LTA induced nanoprecipitation in NiTi alloys.
- (4) By using the DERHT of 8 A in 0-600 s, Ni₄Ti₃ nanoprecipitates with 15-25 nm in size and 15-30 nm in gap are precipitated in the coarse-grained NiTi matrix with the grain size of about 20 μm. The DERHT of 8 A also leads to Ni₄Ti₃ growth from 7-15 nm in size and 5-15 nm in gap to 15-25 nm in size

and 15-30 nm in gap. However, 8 A is unable to precipitate Ni_4Ti_3 in the nanocrystalline NiTi alloys, which indicates that nanograin size suppresses Ni_4Ti_3 precipitation during DERHT.

(5) With respect to the phase transformation characteristics, under 12 A, $\text{B2} \leftrightarrow \text{R}$ transformation of the NC samples is turned to $\text{B2} \leftrightarrow \text{B19}'$ transformation in 10-25 s, which is due to the DERHT induced grain growth. Under 8 A, in 0-100 s, $\text{B2} \leftrightarrow \text{B19}'$ transformation of the CG samples is turned to $\text{B2} \leftrightarrow \text{R} \leftrightarrow \text{B19}'$ transformation, which is caused by the DERHT induced precipitation of Ni_4Ti_3 and Ni depletion in the NiTi matrix. Under 12 A, in 0-10 s, $\text{B2} \leftrightarrow \text{R} \leftrightarrow \text{B19}'$ transformation of the ACG samples is turned to $\text{B2} \leftrightarrow \text{B19}'$ transformation, which is because of the DERHT induced dissolution of Ni_4Ti_3 nanoprecipitates. Under 8 A, $\text{B2} \leftrightarrow \text{R}$ and $\text{B19}' \rightarrow \text{R}$ transformation temperatures of the ACG samples increase in 50-600 s, which is due to the DERHT induced Ni_4Ti_3 growth.

(6) With respect to the superelasticity, under 12 A, in 10-25 s, the loading and unloading plateau stress and stress hysteresis decrease, while plateau strain and residual strain increase. These variations are respectively because the DERHT weakens the nanograin size induced suppression of stress-induced martensitic transformation, lowers the transformation energy dissipation by reducing grain boundary volume fraction, increases the transformable NiTi matrix fraction, and reduces dislocation slip resistance by grain growth. Under 8 A, in 0-600 s, the coarse-grained NiTi alloys present the decrease of loading and unloading plateau stress, plateau strain, and residual strain. This is due to

the DERHT induced Ni_4Ti_3 precipitation and growth, which induces Ni depletion in the NiTi matrix and consequently lowers the required stress for activating the stress-induced transformation. Besides, the Ni_4Ti_3 precipitation reduces the transformable NiTi matrix fraction and increases the dislocation slip resistance of the NiTi matrix. Under 12 A, the ACG samples present the same superelasticity after 10 s, which is due to the DERHT induced dissolution of Ni_4Ti_3 .

- (7) Based on the grain growth induced by DERHT, the grain size adjustment models from the perspectives of the heating time and current magnitude are respectively obtained. The former can be used to calculate the grain size variation under DERHT of 12 A within 1-600 s. The latter can be used to calculate the grain size variation under DERHT of 25 s within 9-14 A. Both grain size adjustment models can increase the grain size of the NiTi alloys from 34 nm to coarse-grained scale. The NiTi alloys with grain size of 34-8021 nm are obtained based on the latter method via DERHT, which are prepared for the studies of the subsequent chapters.

Chapter 4 Influence of low-temperature aging on phase transformation characteristics of NiTi alloys with different grain sizes

4.1 Introduction

The superelasticity of NiTi is inherently due to the $B2 \leftrightarrow (R) \leftrightarrow B19'$ phase transformation, thus the study of the phase transformation characteristics is the basis of the study of superelasticity. As seen from the results in chapter 2 that LTA of 2 h presents different influences on phase transformation characteristics on NC and CG NiTi alloys. Based on the results of chapter 3, the NC and CG NiTi alloys respond differently to the DERHT induced short-time LTA of 0-600 s in terms of phase transformation characteristics. Therefore, the influence of LTA on phase transformation characteristics of the NiTi alloys with different grain sizes (ranging from NC to CG) deserves to study.

This chapter studies 1) the effect of LTA at 573 K in 0-48 h on the phase transformation characteristics of the NiTi alloys with grain size of 34-8021 nm; 2) the variations of phase transformation sequence, temperature, enthalpy, and thermal hysteresis with the increase of grain size and LTA time; 3) the underlying mechanisms of the variations of transformation characteristics from the

microstructural evolution aspect; and 4) the B2→R transformation temperature model considering the effects of LTA time and grain size, which may provide references for the design and adjustment of the NiTi functional devices.

4.2 LTA experimental design of the NiTi alloys with different grain sizes

According to the grain size adjustment model obtained in the last chapter, the NiTi alloys with grain size of 34, 40, 51, 105, 217, 523, 1106, 2190, 4972, and 8021 nm were obtained via DERHT. The grain sizes covers NC, UFG, and CG scales. The NiTi alloys were subjected to the LTA of 0, 2, 4, 8, 24, and 48 h at 573 K. The experimental design is shown in **Table 4.1** where 60 independent combinations of grain size and LTA time were obtained. The phase transformation characteristics, hardness, and representative microstructures of these samples were respectively measured and observed based on the experimental procedures as introduced in chapter 2.

Table 4.1 The LTA experimental design for the NiTi alloys with different grain sizes

Grain size (nm)	LTA temperature (K)	LTA time (h)					
		0	2	4	8	24	48
34	573	•	•	•	•	•	•
40	573	•	•	•	•	•	•
51	573	•	•	•	•	•	•
105	573	•	•	•	•	•	•
217	573	•	•	•	•	•	•
523	573	•	•	•	•	•	•
1106	573	•	•	•	•	•	•
2190	573	•	•	•	•	•	•
4972	573	•	•	•	•	•	•
8021	573	•	•	•	•	•	•

4.3 Effect of grain size on phase transformation characteristics before LTA

As reported in the previous studies [58, 59, 125, 126, 205], even though the NiTi alloys have not been subjected to LTA, the grain size can still affect the phase transformation characteristic. Therefore, before studying the influence of LTA on the phase transformation characteristics of the NiTi alloys with different grain sizes, it is necessary to preliminarily understand the effect of grain size itself on the phase transformation characteristics of the NiTi alloys.

Before LTA, DSC curves of the NiTi alloy with different grain sizes are shown in **Fig. 4.1**. The variations of phase transformation temperatures with grain size are shown in **Fig. 4.2**. The thermal hysteresis and transformation enthalpy are shown in **Table 4.2**. In the figures and table, A_f is the finish transformation temperature for $B19' \rightarrow B2$ or $R \rightarrow B2$ transformations, and applying loading-unloading deformation above this temperature can theoretically obtain complete superelasticity [206].

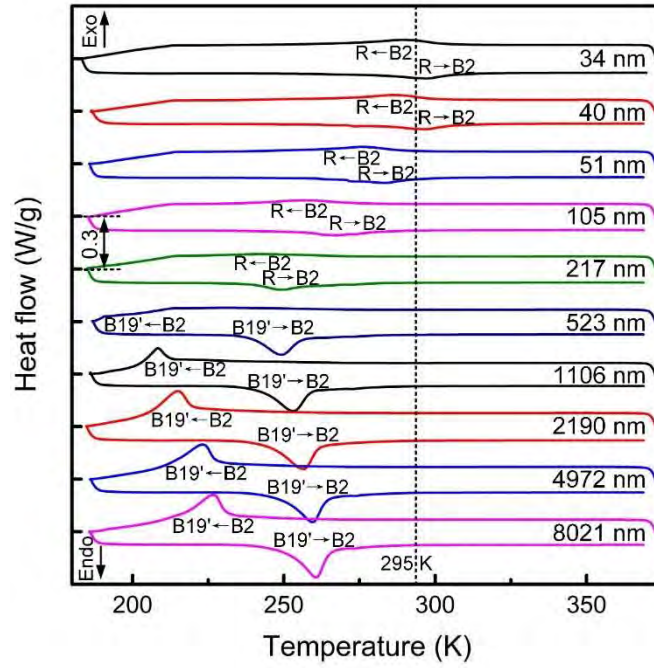


Fig. 4.1 DSC curves of the NiTi alloys with different grain sizes before LTA.

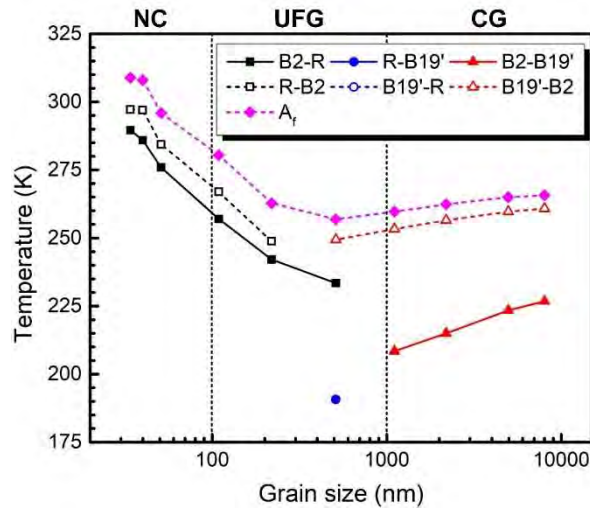


Fig. 4.2 Variations of phase transformation temperatures with grain size before LTA.

Table 4.2 Thermal hysteresis and transformation enthalpy of the NiTi alloys with different grain sizes before LTA

Grain size (nm)	TH (K)			ΔH (J/g)					
	TH _{AR}	TH _{RM}	TH _{AM}	ΔH_{AR}	ΔH_{RA}	ΔH_{RM}	ΔH_{MR}	ΔH_{AM}	ΔH_{MA}
34	7.6	--	--	5.40	4.86	--	--	--	--
40	11.07	--	--	5.39	5.24	--	--	--	--
51	8.48	--	--	4.68	4.76	--	--	--	--
105	9.89	--	--	3.31	4.15	--	--	--	--
217	6.72	--	--	2.00*	5.57	--	--	--	--
523	15.9*	--	58.61	0.98*	--	0.59*	--	--	10.59
1106	--	--	44.85	--	--	--	--	13.17*	12.5
2190	--	--	41.44	--	--	--	--	14.67*	13.86
4972	--	--	36.3	--	--	--	--	14.91*	13.52
8021	--	--	34.05	--	--	--	--	14.94*	14.13

*: Due to the heat flow limitation of the DSC curves at the low-temperature section, the marked data were influenced by systematic errors. A: B2 austenite phase, M: B19' martensite phase, R: R-phase.

As shown in the figures and table, the transformation sequence, temperature, thermal hysteresis, and enthalpy are greatly affected by grain size. When the grain size increases within NC scale, the transformation sequence keeps unchanged. The R \leftrightarrow B19' transformation is not observed within the DSC temperature range (183-373 K), which indicates that the B2 \leftrightarrow R transformation keeps activated while the R \leftrightarrow B19' transformation keeps suppressed by the nanograin size in NC scale. B2 \leftrightarrow R transformation temperature decreases with the increasing grain size, which indicates that the facilitation of the B2 \leftrightarrow R transformation induced by the nanograin size is weakened. Transformation enthalpy is not changed, which indicates that the material volume fraction of B2 \leftrightarrow R transformation is of little change.

For the grain size within UFG scale, with the increasing grain size, the transformation sequence increases from B2 \leftrightarrow R to B2 \rightarrow R \rightarrow B19'/B19' \rightarrow B2 and further to B19' \leftrightarrow B2. The B2 \leftrightarrow R transformation disappears, while the B19' \leftrightarrow B2 transformation appears. This indicates that the grain size induces facilitation of B2 \leftrightarrow R transformation and the suppression of B19' \leftrightarrow B2 weakens with the

increasing grain size. When the grain size increases from 105 nm to 1106 nm, the $B2 \rightarrow R$ transformation peaks gradually flatten till disappeared as indicated by the transformation enthalpy. The $R \rightarrow B2$ transformation peak is replaced by the $B19' \rightarrow B2$ transformation, and the $B19' \rightarrow B2$ transformation enthalpy increases. This indicates that the material volume fraction of $B2 \leftrightarrow R$ transformation decreases while that of $B2 \leftrightarrow B19'$ transformation increases with the increasing grain size in UFG scale.

For the grain size increasing to CG scale, the $B2 \rightarrow R$ transformation completely vanishes and the transformation sequence is $B2 \leftrightarrow B19'$, and the transformation temperature increases with grain size. This indicates that the micro-sized CG grain size is unable to facilitate $B2 \leftrightarrow R$ but can impede $B2 \leftrightarrow B19'$ transformation, i.e., the increasing grain size can increase $B2 \leftrightarrow B19'$ temperatures. As the grain size increases in CG scale, the $B2 \leftrightarrow B19'$ transformation enthalpy gradually increases while the thermal hysteresis gradually decreases. This indicates that the decreasing grain boundary volume fraction increases the volume fraction of transformable material, which decreases the energy dissipation of the phase transformation frontiers passing through grain boundaries.

It can be seen from the above results, grain size itself greatly affects the phase transformation characteristics before LTA. With the increase of grain size, the grain size induced facilitation of $B2 \leftrightarrow R$ transformation and suppression of $B2(R) \leftrightarrow B19'$ are weakened, which leads to the decrease of $B2 \leftrightarrow R$ transformation temperatures and the increase of $B2(R) \leftrightarrow B19'$ transformation temperatures. This

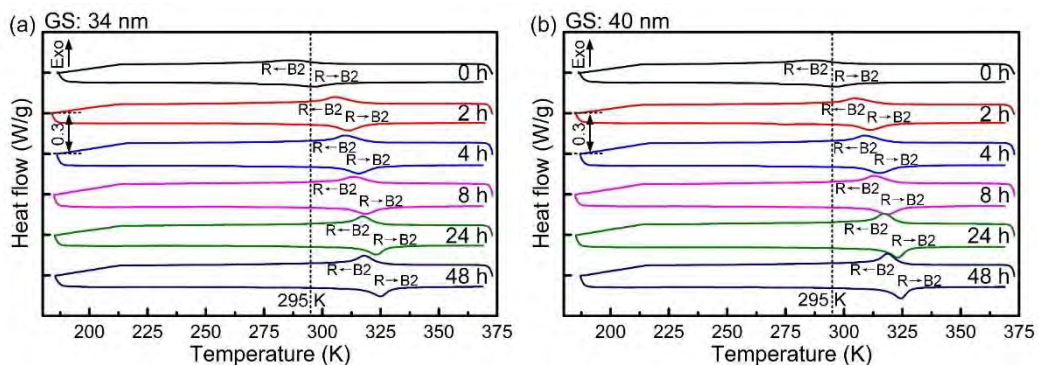
finally causes the first decrease and then increase of the A_f transformation temperature, and the minimum value is reached when the grain size is at 523 nm.

4.4 Effect of LTA on the phase transformation

characteristics of the NiTi alloys with different grain

sizes

The variations of DSC curves of the NiTi alloys with LTA time and grain size are shown in Fig. 4.3. It can be seen in the figure that 1) the variations of phase transformation sequence and temperature are prominent under the LTA of 2 h; 2) $B2 \leftrightarrow R$ transformation appears after LTA regardless of grain sizes; 3) as the LTA time increases from 2 h to 48 h, $B2 \leftrightarrow R$ transformation temperature increases, transformation enthalpy increases, and the peak intensity also increases; 4) after LTA, $R \leftrightarrow B19'$ transformation keeps in suppression when grain size is smaller than 1106 nm; 5) after LTA, NiTi alloys with grain size of 2190-8021 nm still present $R \leftrightarrow B19'$ transformation of which the temperature increases with LTA time.



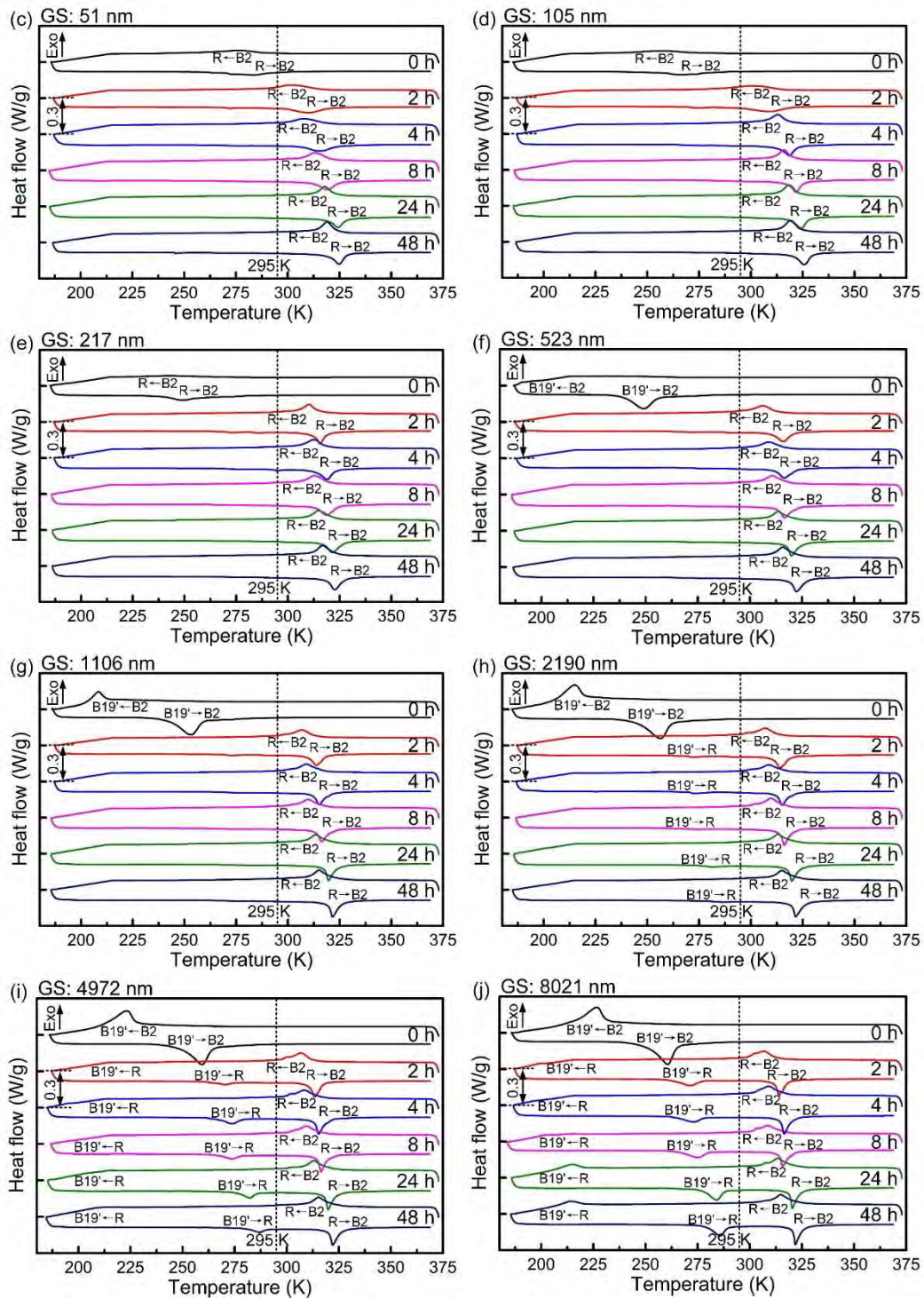


Fig. 4.3 Variations of DSC curves with LTA time of the NiTi alloys with grain size of: (a) 34 nm; (b) 40 nm; (c) 51 nm; (d) 105 nm; (e) 217 nm; (f) 523 nm; (g) 1106 nm; (h) 2190 nm; (i) 4972 nm; and (j) 8021 nm

Based on the above variations of phase transformation characteristics, this chapter studies the effect of LTA of 2 h on transformation sequence and temperatures, the effect of LTA of 2-48 h on $B2 \leftrightarrow R$ transformation, and the effect of LTA of 2-48 h on $B2(R) \leftrightarrow B19'$ transformation. The variations of transformation sequence, temperature, enthalpy, thermal hysteresis, and peak intensity with the increasing LTA time and grain size are concerned.

4.4.1 Effect of LTA on phase transformation sequence and temperature

The variations of phase transformation sequence and temperature with grain size after the LTA of 2 h are shown in **Fig. 4.4**. The thermal hysteresis and transformation enthalpy are shown in **Table 4.3**. As shown in the figure and table, within NC scale, the LTA of 2 h elevates $B2 \leftrightarrow R$ transformation temperature. This elevation is more prominent with the increasing grain size.

Within UFG scale, the LTA of 2 h elevates the $B2 \leftrightarrow R$ transformation temperature for the NiTi alloys with grain size of 105 and 217 nm. For the NiTi alloy with grain size of 523 nm, the transformation sequence is turned from $B2 \rightarrow R \rightarrow B19'/B19' \rightarrow B2$ to $B2 \leftrightarrow R$, while the $R \rightarrow B19'$ transformation is suppressed after the LTA of 2 h. The $B2 \rightarrow R$ transformation temperature increased from 249.4 K to 316.1 K, i.e., increases by 66.7 K, which increases most among the NiTi alloys.

Within CG scale, for the NiTi alloys with grain size of 1106 and 2190 nm, the LTA of 2 h changes the transformation sequence from $B2 \leftrightarrow B19'$ to $B2 \leftrightarrow R$, while

the R \leftrightarrow B19' transformation is suppressed. For the NiTi alloys with grain size of 4972 nm and 8021 nm, phase transformation sequence is turned from B2 \leftrightarrow B19' to B2 \leftrightarrow R \leftrightarrow B19' after the LTA of 2 h, and R \leftrightarrow B19' transformation temperature increases with grain size. By comparing to **Table 4.2**, it can be known that thermal hysteresis of R \leftrightarrow B19' transformation after LTA is larger than that of B2 \leftrightarrow B19' transformation before LTA.

The above results indicate that the LTA of 2 h greatly affects the phase transformation characteristics of the NiTi alloys with different grain sizes, and the influences are dependent on grain size.

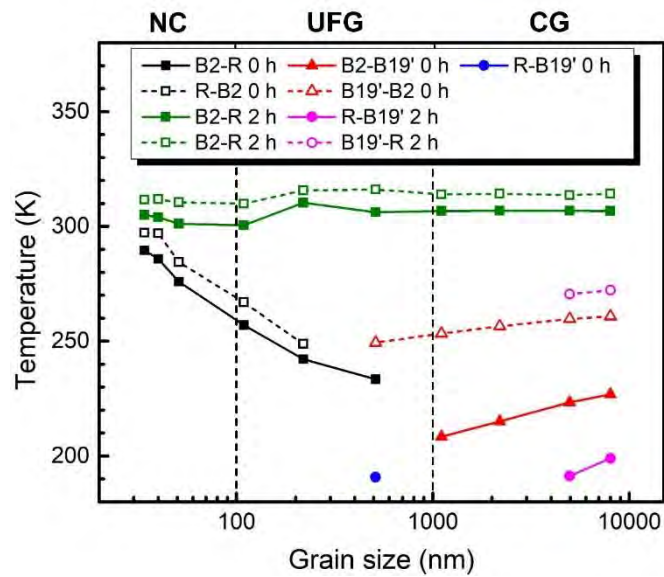


Fig. 4.4 Variations of the transformation sequence and temperature with grain size after the LTA of 2 h

Table 4.3 Thermal hysteresis and transformation enthalpy after the LTA of 2 h of the NiTi alloys with different grain sizes

Grain size (nm)	LTA time (h)	TH (K)			ΔH (J/g)					
		TH _{AR}	TH _{RM}	TH _{AM}	ΔH_{AR}	ΔH_{RA}	ΔH_{RM}	ΔH_{MR}	ΔH_{AM}	ΔH_{MA}
34	2	6.59	--	--	7.32	6.27	--	--	--	--
40	2	7.79	--	--	7.23	6.36	--	--	--	--
51	2	9.33	--	--	7.36	6.67	--	--	--	--
105	2	9.38	--	--	7.56	6.86	--	--	--	--
217	2	5.34	--	--	8.47	7.71	--	--	--	--
523	2	9.96	--	--	8.28	7.98	--	--	--	--
1106	2	7.24	--	--	8.13	7.93	--	--	--	--
2190	2	7.35	--	--	8.45	8.52	--	--	--	--
4972	2	6.79	79.20	--	8.59	7.71	--	2.02*	--	--
8021	2	7.49	73.24	--	7.78	6.96	--	4.52*	--	--

*: Due to the heat flow limitation of the DSC curves at the low-temperature section, the marked data were influenced by systematic errors. A: B2 austenite phase, M: B19' martensite phase, R: R-phase.

4.4.2 Effect of LTA on B2 \leftrightarrow R transformation

4.4.2.1 Effect of LTA on B2 \leftrightarrow R peak shape

The variations of B2 \leftrightarrow R transformation peaks with LTA of 2-48 h are shown in **Fig. 4.5**. Under each grain size, the B2 \rightarrow R and R \rightarrow B2 transformation temperature, enthalpy, and peak intensity increase with LTA time, and the transformation peaks become more concentrated. Within grain size of 34-105 nm, the transformation peaks gradually concentrate with LTA time. Within grain size of 217-8021 nm, the transformation peaks become concentrated rapidly after the LTA of 2 h. Within grain size of 1106-8021 nm, the R \rightarrow B2 transformation peaks are more concentrated than those of the B2 \rightarrow R transformation. It is noteworthy that the B2 \rightarrow R transformation peaks are concentrated within grain size of 34-523 nm, while they become split within grain size of 1106-8021 nm. X.B. Wang et al [186] points out that Ni₄Ti₃ precipitation become inhomogeneous along the direction between grain boundary and grain inner with the increasing grain size. Therefore, based on the experimental results of this study, the LTA can hardly lead to the

The factors inducing the B2↔R transformation include nanograin size [58], coherent Ni₄Ti₃ [159], and dislocations in the matrix [10]. Before LTA, the NiTi alloy of 34 nm have experienced recrystallization from the cold drawing state, and the NiTi alloys with grain size of 40-8021 nm have experienced grain growth from 34 nm. Because they have not been subjected to aging and plastic deformation before LTA, there are no Ni₄Ti₃ precipitates and dislocations in the grains. Therefore, the B2↔R transformation emerges in NiTi alloys within grain size of 34-217 nm is due to nanograin size. With the increasing average grain size, the nanograin volume fraction decreases, which decreases the material volume fraction of B2↔R transformation and consequently decreases the B2↔R transformation enthalpy.

After LTA, for the NC samples, the nanograin sizes are preserved, thus they still facilitate B2↔R transformation. The minority ultrafine grains in the samples precipitate Ni₄Ti₃, which slightly increases the B2↔R transformation enthalpy. in the meanwhile, the defects in the matrix further decrease and the residual amorphous phase further turns to nanograins after LTA, which further increases the B2↔R transformable material volume fraction and consequently the B2↔R transformation enthalpy.

Within the grain size of 523-8021 nm, LTA induced Ni₄Ti₃ precipitation leads to B2↔R transformation, and the transformation enthalpy is larger than that of NiTi alloys with grain size of 34-217 nm. This indicates the volume fraction of transformable material of UFG and CG NiTi alloys is larger than that of the NC

NiTi alloys, which is due to the lower grain boundary volume fraction of the formers.

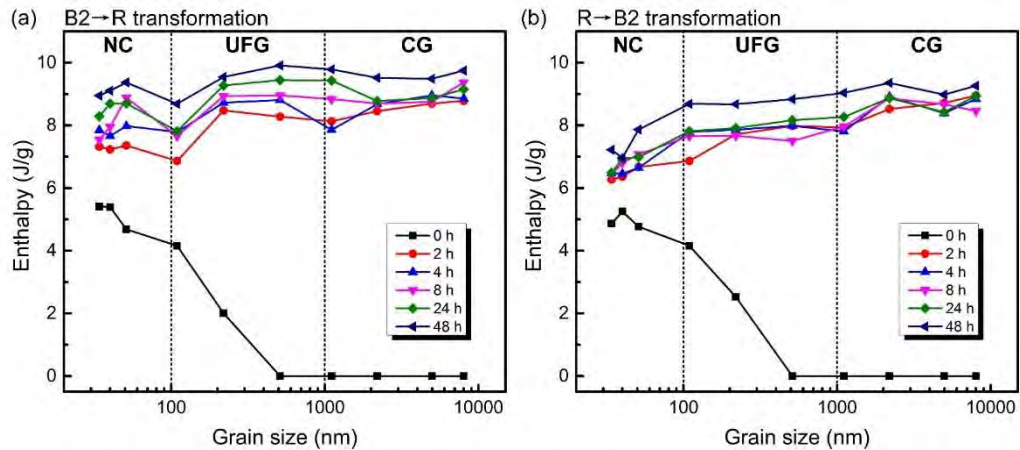


Fig. 4.6 Variations of B2↔R transformation enthalpy with grain size and LTA time: (a) B2→R transformation; (b) R→B2 transformation.

4.4.2.3 Effect of LTA on B2↔R transformation peak intensity

The transformation peak intensity means the height of transformation peak. Under the same transformation enthalpy, the higher the transformation peak intensity it is, and the more concentrated the peak it is. Under the same peak concentration degree, the lower the transformation peak intensity it is, and the smaller the transformation enthalpy it is. **Fig. 4.7** shows the variations of phase transformation intensity with grain size and LTA time.

Before LTA, the peak intensity of B2↔R transformation is smaller, this is because B2↔R transformation mostly happens in NC NiTi alloys and the transformation enthalpy is relatively small. The peak intensity decreases with grain size, which reaches to 0 W/g when the grain size increases to 523 nm. This is because the grain

size induced facilitation of $B2 \leftrightarrow R$ transformation gradually decreases, as shown in region I of **Fig. 4.7(a)** and (b).

After LTA, $B2 \leftrightarrow R$ transformation peak intensity generally increases with LTA time regardless of grain size. On one hand, the increasing transformation enthalpy after LTA leads to the increase of transformation peak intensity. On the other hand, by taking $R \rightarrow B2$ transformation as an example, the transformation peak intensity of the CG NiTi alloys increases more than that of the NC and UFG NiTi alloys, as shown in **Fig. 4.7(b)**. However, the transformation enthalpies of the three types of NiTi alloys present less changed compared with the variations of transformation peak intensity, as shown in **Fig. 4.6(b)**. Therefore, it can be deduced that the CG NiTi alloys present more concentrated transformation peaks than the UFG and NC NiTi alloys. Besides, the increase of $B2 \rightarrow R$ transformation peak intensity is less than that of $R \rightarrow B2$ transformation in the UFG and CG NiTi alloys, which is due to the split of $B2 \rightarrow R$ transformation peaks.

Because the LTA preserves the grain size, the influence of nanograin size on $B2 \leftrightarrow R$ transformation temperature is maintained in the NC NiTi alloys. Since the grain size of the NC NiTi alloys is inhomogeneous, the $B2 \leftrightarrow R$ transformation peaks of the NC NiTi alloys are more shallow than those of the UFG and CG samples, which presents lower peak intensity, as shown in region II of **Fig. 4.7(a)** and (b). By contrast, in the NiTi alloys with grain size larger than 523 nm, the grain size hardly affects $B2 \leftrightarrow R$ transformation, thus the $B2 \leftrightarrow R$ transformation is only influenced by Ni_4Ti_3 precipitates. Therefore, their transformation peaks

become more concentrated than those of grain size less than 217 nm, as shown in region III of Fig. 4.7(a) and (b).

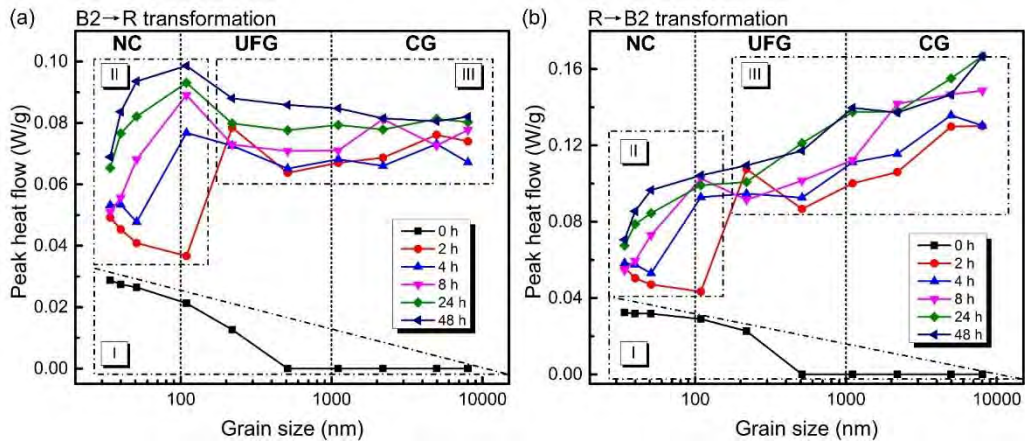


Fig. 4.7 Variations of transformation peak intensity with grain size and LTA time: (a) B2→R transformation; (b) R→B2 transformation.

4.4.2.4 Effect of LTA on B2↔R transformation temperature

Fig. 4.8 demonstrates the variations of B2↔R transformation temperatures with grain size and LTA time. The B2→R and R→B2 transformation temperatures present similar variations. Under the same grain size, the B2↔R transformation increases with LTA time. Under the same LTA time, B2↔R transformation varies differently depending on the grain size.

For the NC NiTi alloys, under the LTA of 2h, B2↔R transformation temperatures decrease with the increasing grain size, which is similar with those before LTA. When the LTA time further increases to 8 h, B2↔R transformation temperature first decreases and then increases. When the LTA time further increases to 48 h, B2↔R transformation temperature increases with grain size. In the meanwhile, after the LTA of 2 h, the NC NiTi alloys present lower B2↔R transformation

temperatures than the UFG and CG NiTi alloys. After the LTA of 48 h, the NC NiTi alloys present the highest $B2 \leftrightarrow R$ transformation temperature.

For the UFG NiTi alloys, after the LTA of 2 h, $B2 \rightarrow R$ transformation temperature increases with the grain size from 105 nm to 217 nm while decreases with the grain size from 217 nm to 1106 nm. After the LTA of 4-48 h, $B2 \leftrightarrow R$ transformation temperature decreases with the increasing grain size.

For the CG NiTi alloys, $B2 \leftrightarrow R$ transformation temperatures increase with LTA time while generally unchange with grain size. The LTA of 2 h activates $B2 \leftrightarrow R$ transformation. Further elevating the LTA time from 2 h to 48 h, the elevation of $B2 \leftrightarrow R$ transformation temperature is less than those in the NC and UFG samples.

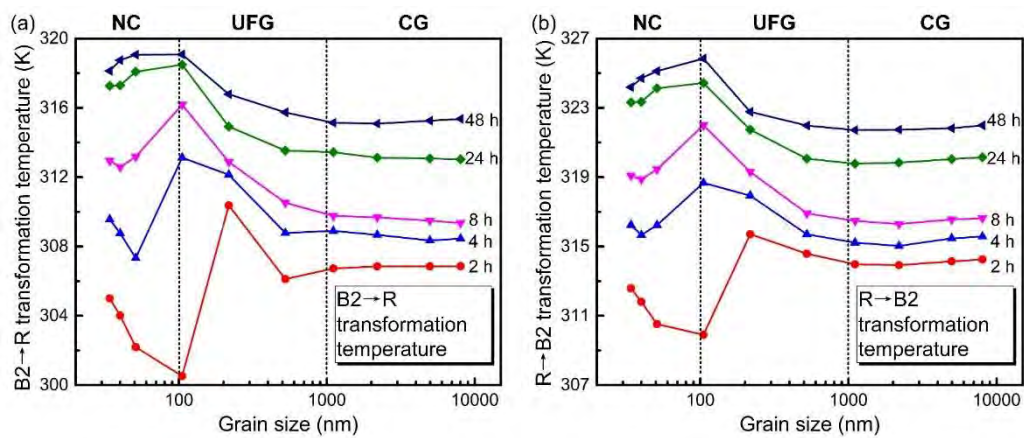


Fig. 4.8 Variations of the $B2 \leftrightarrow R$ transformation temperature with grain size and LTA time: (a) $B2 \rightarrow R$ transformation; (b) $R \rightarrow B2$ transformation.

The optimum smaller range depends on the actual requirements. For instance, if the highest $B2 \rightarrow R$ transformation temperature is desired, LTA time of 48 h with

grain size of about 100 nm is recommended; if the required $B2 \rightarrow R$ transformation temperature is larger than 314 K, LTA times larger than 4 h are recommended.

It was worth noting that, the NiTi alloys with grain size of 105 nm present highest $B2 \rightarrow R$ transformation temperature elevation. Before LTA, the $B2 \rightarrow R$ transformation temperature is 257.1 K. After the LTA of 2-48 h, the transformation temperature increases to 43.4-62.0 K. Since the NiTi actuators based on $B2 \leftrightarrow R$ transformation are sensitive to the transformation temperature [207, 208], these findings may facilitate the functional property adjustment of the NiTi alloy applications.

As can be summarized from the above results, LTA can not only elevate the $B2 \leftrightarrow R$ transformation temperatures of CG NiTi alloys [155, 159, 187], but it can also present $B2 \leftrightarrow R$ transformation temperature of NC and UFG NiTi alloys. Furthermore, the elevation of $B2 \leftrightarrow R$ transformation temperatures in UFG and NC NiTi alloys is strongly affected by grain size, while it is hardly affected by the grain size of CG NiTi alloys. These findings are of significance for the LTA induced $B2 \leftrightarrow R$ transformation temperature adjustment of NC and UFG NiTi alloys.

4.4.3 Effect of LTA on $B2(R) \leftrightarrow B19'$ transformation

$B2(R) \leftrightarrow B19'$ transformation is the basis of superelasticity. Compared with $B2 \leftrightarrow R$ transformation, the functional properties based on $B2(R) \leftrightarrow B19'$ transformation are used more widely in practical applications [11]. Within the temperature range of the DSC tests (183-373 K), $B2(R) \leftrightarrow B19'$ transformation is suppressed in the

NiTi alloys with grain size of 34-1106 nm. After LTA, B2(R) \leftrightarrow B19' transformation only presents in the NiTi alloys with grain size of 2190-8021 nm. Therefore, the B2(R) \leftrightarrow B19' transformation of the NiTi alloys with grain size of 2190, 4972, and 8021 nm are studied in this section. The variation of transformation peaks with LTA time and grain size are shown in **Fig. 4.9**.

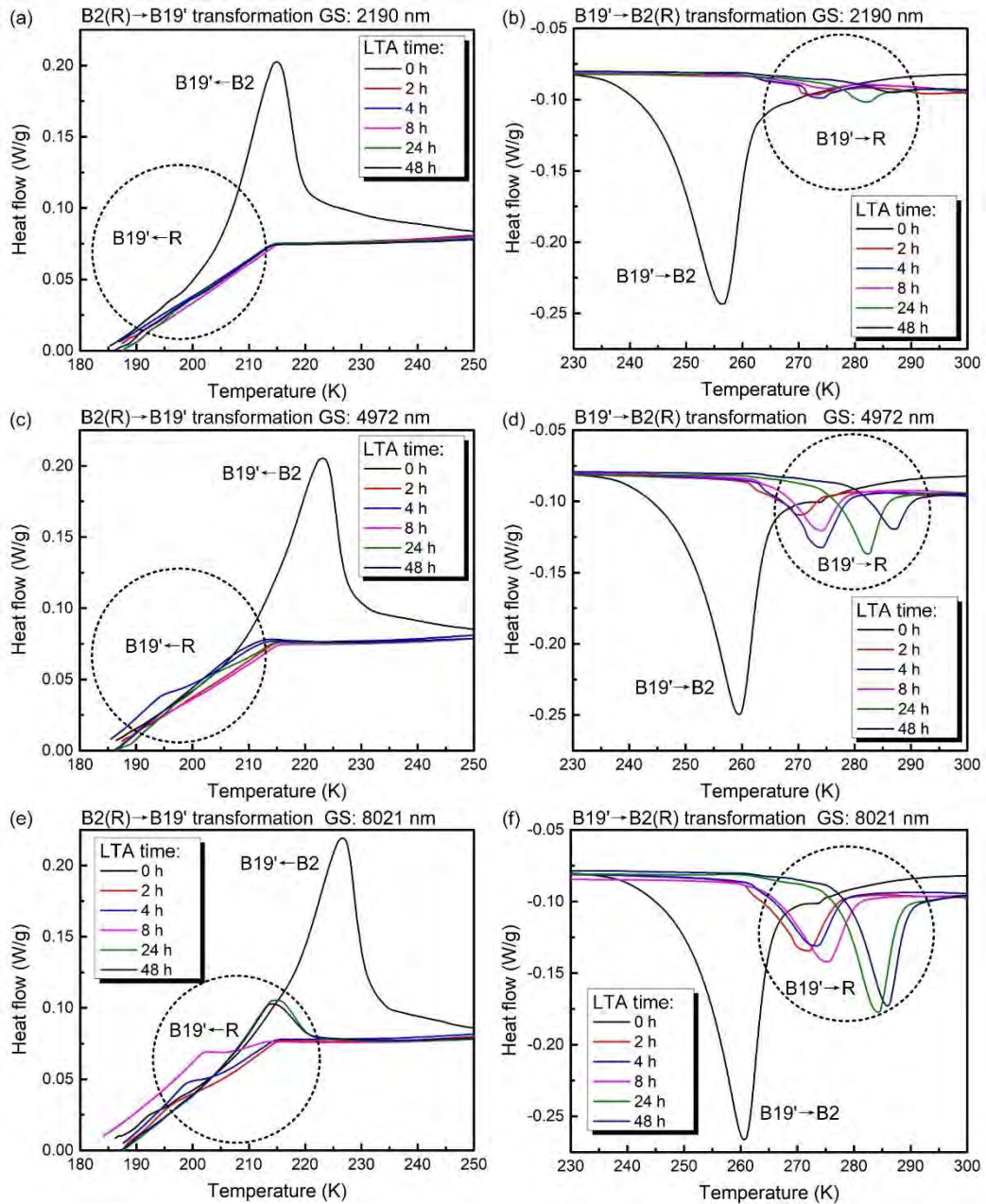


Fig. 4.9 Variations of B2(R) \leftrightarrow B19' transformation peaks with grain size and LTA time: (a) B2(R) \rightarrow B19' transformation peaks of grain size of 2190 nm; (b)

B19'→B2(R) transformation peaks of grain size 2190 nm; (c) B2(R)→B19' transformation peaks of grain size of 4972 nm; (d) B19'→B2(R) transformation peaks of grain size 4972 nm; (e) B2(R)→B19' transformation peaks of grain size of 8021 nm; and (f) B19'→B2(R) transformation peaks of grain size 8021 nm.

Before LTA, as shown in **Fig. 4.2**, B2(R)↔B19' transformation exists in the NiTi alloys with grain size of 523-8021 nm. In addition, even the grain size is in CG scale, the micro-scale grain size also impedes B2(R)→B19' transformation.

After LTA, as shown in **Fig. 4.3**, only the NiTi alloys with grain size of 2190-8021 nm present R↔B19' transformation. R→B19' transformation temperature becomes lower and B19'→R transformation temperature becomes higher, which leads to the increase of thermal hysteresis. Consequently, R→B19' transformation of the NiTi alloys with grain size of 523 and 1106 nm could not be activated even when the temperature decreases to 183 K. That is to say, the R→B19' transformation of the NiTi alloys with grain size of 523 and 1106 nm is suppressed after LTA.

For the NiTi alloys with grain size of 2190, 4970, and 8021 nm. For their higher B2→B19' transformation temperature than that of the NiTi alloys with grain size of 523 and 1106 nm, though the transformation is also impeded after LTA, decreasing temperature to 183 K still can drive the R→B19' transformation. Thus the B19'→R transformation peaks are observed during the heating procedure of the DSC test, as shown in **Fig. 4.9**. With the increasing grain size, the decreasing temperature to 183 K drives more material volume fraction of R→B19'

transformation. The $R \rightarrow B19'$ and $B19' \rightarrow R$ transformation peaks thus become larger.

The variations of $B2(R) \leftrightarrow B19'$ transformation temperatures with LTA time and grain size are shown in **Fig. 4.10**. The LTA of 2 h can effectively decrease $R \rightarrow B19'$ transformation temperature and increase $B19' \rightarrow R$ transformation. Besides, further increasing the LTA time to 48 h, $R \rightarrow B19'$ and $B19' \rightarrow R$ transformation temperatures further increases. Under the same LTA time, $R \rightarrow B19'$ transformation temperatures of different grain sizes are different from each other, while the $B19' \rightarrow R$ transformation temperatures are almost the same. X.B. Shi et al. [58] attributed this phenomenon to the different facilitation and suppression of the $R \rightarrow B19'$ and $B19' \rightarrow R$ transformation led by the elastic strain energy and dissipation energy.

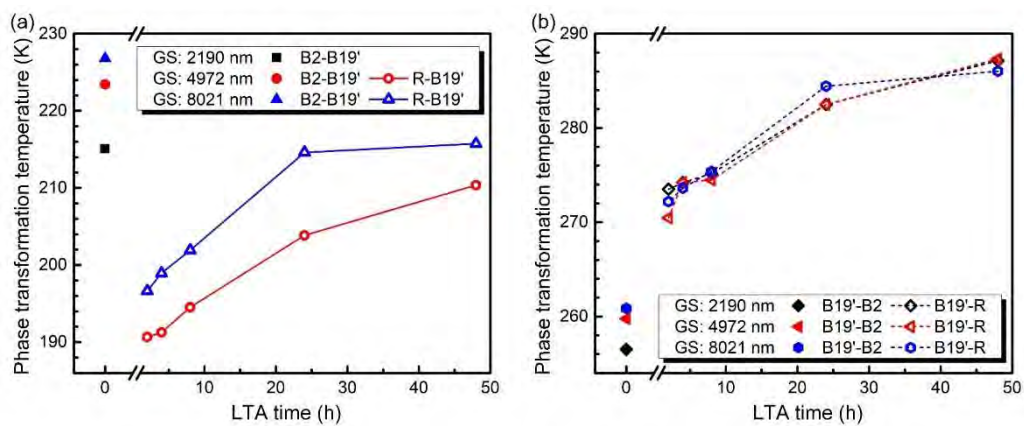


Fig. 4.10 Variations of $B2(R) \leftrightarrow B19'$ transformation temperature with LTA time and grain size: (a) $B2(R) \rightarrow B19'$ transformation; and (b) $B19' \rightarrow B2(R)$ transformation.

As can be summarized above, LTA effectively alters the $B2(R) \leftrightarrow B19'$ transformation temperatures of a part of UFG and CG NiTi alloys, and the

suppression of $B2(R) \leftrightarrow B19'$ transformation induced by nanograin size in NC NiTi alloys is not deteriorated. These findings can facilitate LTA induced $B2(R) \leftrightarrow B19'$ transformation temperature adjustment of NiTi alloys with different grain sizes, which may also be beneficial for the design and phase transformation characteristics adjustment of the NiTi functional devices based on $B2(R) \leftrightarrow B19'$ transformations.

4.5 Mechanisms for the influence of LTA on phase transformation

In this section, the influence of LTA on phase transformation characteristics of the NiTi alloys with different grain sizes are explained from the following perspectives: the effect of the preservation of grain size on phase transformation characteristics, the effect of LTA time on Ni_4Ti_3 precipitation, and the nanograin size induced suppression of Ni_4Ti_3 precipitation during LTA. These explanations are further corroborated by the variation of hardness.

4.5.1 Effect of the preservation of grain size on phase transformation characteristics

According to the results of chapter 2, the LTA of 573 K preserves the nanograin size even at 34 nm. The influences of nanograin size on $B2 \leftrightarrow R$ and $B2(R) \leftrightarrow B19'$ phase transformation are thus maintained during LTA. For the NC NiTi alloys, the nanograin size induced suppression of $B2(R) \rightarrow B19'$ transformation always exists during LTA. The $B2(R) \rightarrow B19'$ transformation peaks are thus not observed before and after LTA. For the UFG and CG NiTi alloys, after LTA, the influences of grain

size and LTA are superposed, which makes the B2(R)→B19' transformation disappear in the NiTi alloys with the grain size of 523 and 1106 nm and increases the B2(R)→B19' transformation temperatures with the grain size increasing from 2190 to 8021 nm.

4.5.2 Effect of LTA time on Ni₄Ti₃ precipitation

For individually investigating the LTA time on Ni₄Ti₃ precipitation, the NiTi alloys with grain size of 8021 nm subjected to different LTA time are investigated. The variations of microstructures are shown in **Fig. 4.11**. Before LTA, the NiTi matrix presents pure B2 austenite phase, which is consistent with the DSC results. After the LTA of 2 h, the densely distributed Ni₄Ti₃ nanoprecipitates with size of 7-15 nm and gap of 5-15 nm are observed. Further increasing LTA time to 8 h and 48 h, the size of the nanoprecipitates is not further increased, which keeps as 7-15 nm. J.I. Kim et al. [48] applied the LTA of 573 K-100 h to solution treated CG NiTi alloys and observed Ni₄Ti₃ nanoprecipitates with size of about 10 nm. The size of Ni₄Ti₃ nanoprecipitates observed in this study is consistent with that reported in the study of J.I. Kim et al. [48]. On the other hand, the diffraction patterns of Ni₄Ti₃ become brighter with the increasing LTA time, which indicates that the amount of the nanoprecipitates increases, i.e., the density of the nanoprecipitates increases. Besides, these nanoprecipitates keeps in coherency with the B2 austenite phase.

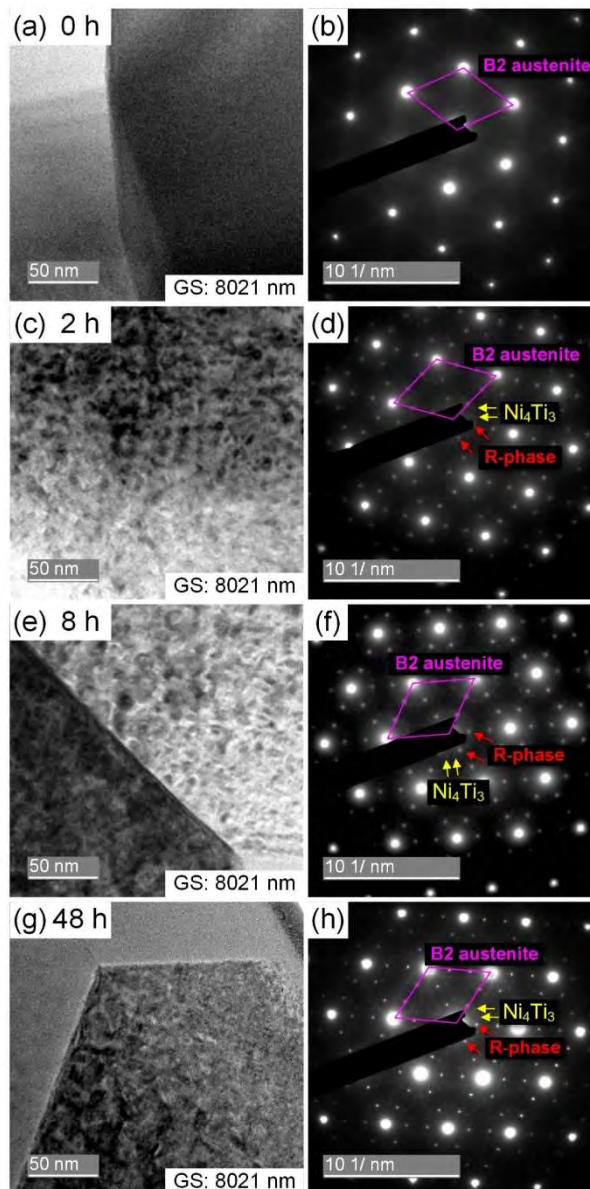


Fig. 4.11 Variations of the microstructures of the NiTi alloys with grain size of 8021 nm with LTA time: (a) before LTA, no precipitates are observed in the NiTi matrix; (b) the SAED pattern presents only B2 austenite phase; (c) after the LTA of 2 h, precipitates with size of 7-15 nm and gap of 5-15 nm are observed; (d) the SAED pattern indicates that they are coherent Ni_4Ti_3 nanoprecipitates; (e) after the LTA of 8 h, the size of the nanoprecipitates is not changed so much; (f) the SAED pattern shows bright Ni_4Ti_3 diffraction; (g) after the LTA of 48 h, the

size of the nanoprecipitates is generally preserved; and (h) the SAED pattern further shows brighter Ni_4Ti_3 diffraction.

The above microstructural variations explain the increase of $\text{B2} \leftrightarrow \text{R}$ transformation temperature in the CG NiTi alloys. The grain size of the CG NiTi alloys is not able to facilitate $\text{B2} \leftrightarrow \text{R}$ transformation, and the LTA is unable to introduce additional dislocations. Thus the factors of grain size and dislocation that facilitate $\text{B2} \leftrightarrow \text{R}$ transformation can be excluded. The precipitation of Ni_4Ti_3 leads to the depletion of Ni in the NiTi matrix and introduces elastic strain fields around the precipitates, which are the reasons for the elevation of $\text{B2} \leftrightarrow \text{R}$ transformation temperature.

The above results also disclose the reasons why $\text{R} \rightarrow \text{B19}'$ and $\text{B19}' \rightarrow \text{R}$ transformations are impeded after LTA and why $\text{R} \leftrightarrow \text{B19}'$ transformation temperatures increase with LTA time in the CG NiTi alloys. The thermally-induced $\text{R} \rightarrow \text{B19}'$ and $\text{B19}' \rightarrow \text{R}$ transformation in the CG NiTi alloys are realized by self-accommodation deformation in the grain inners [50], while the densely distributed Ni_4Ti_3 nanoprecipitates can impede such self-accommodation deformation [209]. Therefore, $\text{R} \rightarrow \text{B19}'$ and $\text{B19}' \rightarrow \text{R}$ transformations could happen only by increasing the supercooling. With the increasing LTA time, the density of Ni_4Ti_3 precipitates increases, which leads to further Ni depletion in the matrix and consequently causes the increase of $\text{R} \leftrightarrow \text{B19}'$ transformation temperatures.

4.5.3 Nanograin size induced suppression of Ni₄Ti₃ precipitation during LTA

The LTA of 2-48 h can dissolve out Ni₄Ti₃ nanoprecipitates in the CG NiTi alloys. Whether it can also precipitate similar Ni₄Ti₃ within in the UFG and NC NiTi alloys is studied in this section.

Fig. 4.12 presents the TEM microstructures and the corresponding SAED patterns of the NiTi alloys with grain size of 34, 105, and 2190 nm. For the NiTi alloys with the average grain size of 34 nm, as shown in **Fig. 4.12(a)-(c)**, the LTA effectively preserves the nanograin size, which reflects the advantage of LTA in the preservation of the original nanograin size. In the dominant nanograins of the NiTi matrix, no Ni₄Ti₃ is observed no matter in bright-field, dark-field micrographs, or in the SAED pattern, which is very different from the results in the CG NiTi alloys as discussed in the last section. On the other hand, due to the inhomogeneous grain size of the NiTi alloys [59, 197], a few ultrafine grains may still exist in the NC NiTi alloys even if the average grain size was 34 nm. As representatively shown by the dash-line circled grain in **Fig. 4.12(a)** and **(b)**, the grain is isolated in the NC NiTi matrix, with grain size of about 150 nm. In the grain, the morphology of Ni₄Ti₃ precipitates is obviously observed, which is different from those nanograins. It is worth noting that, the SAED pattern show no diffraction pattern of Ni₄Ti₃. This is due to the low volume fraction of Ni₄Ti₃ in this microstructure which is much less than those of B2 austenite phase and R-phase. The corresponding diffraction pattern of Ni₄Ti₃ is thus too dim to be obviously observed.

For the NiTi alloys with the average grain size of 105 nm, as shown in **Fig. 4.12(d)**-**(f)**, the ultrafine grains in the matrix generally present obviously the morphology of Ni₄Ti₃ precipitates after the LTA of 48 h. A representative ultrafine grain with grain size about 150 nm clearly shown the morphology of nanoprecipitates, as shown in **Fig. 4.12(e)**. The corresponding SAED pattern of this grain proves the existence of coherent Ni₄Ti₃ nanoprecipitates. Thus, it can be deduced that LTA at 573 K could lead to the Ni₄Ti₃ nanoprecipitation in the NiTi ultrafine grains with grain size larger than 150 nm, and the size of the Ni₄Ti₃ nanoprecipitates was about 10 nm.

For the NiTi alloys with the average grain size of 2190 nm, the precipitation behavior is as similar as that in the NiTi alloys with grain size of 8021 nm, i.e., the LTA of 48 h precipitates Ni₄Ti₃ with size of 7-15 nm and gap of 5-15 nm. Therefore, it further proves that the coarse grain size does not suppress the Ni₄Ti₃ precipitation led by LTA.

It can be summarized from these results that nanograin size is able to induce suppression of Ni₄Ti₃ precipitation during LTA. With the increasing grain size, a critical grain size (less than 150 nm) exists, which suppresses the Ni₄Ti₃ precipitation if the grain size of the NiTi alloys is smaller than this critical value. By contrast, if the grain size of the NiTi alloys is larger than this critical value, Ni₄Ti₃ precipitation can still proceed.

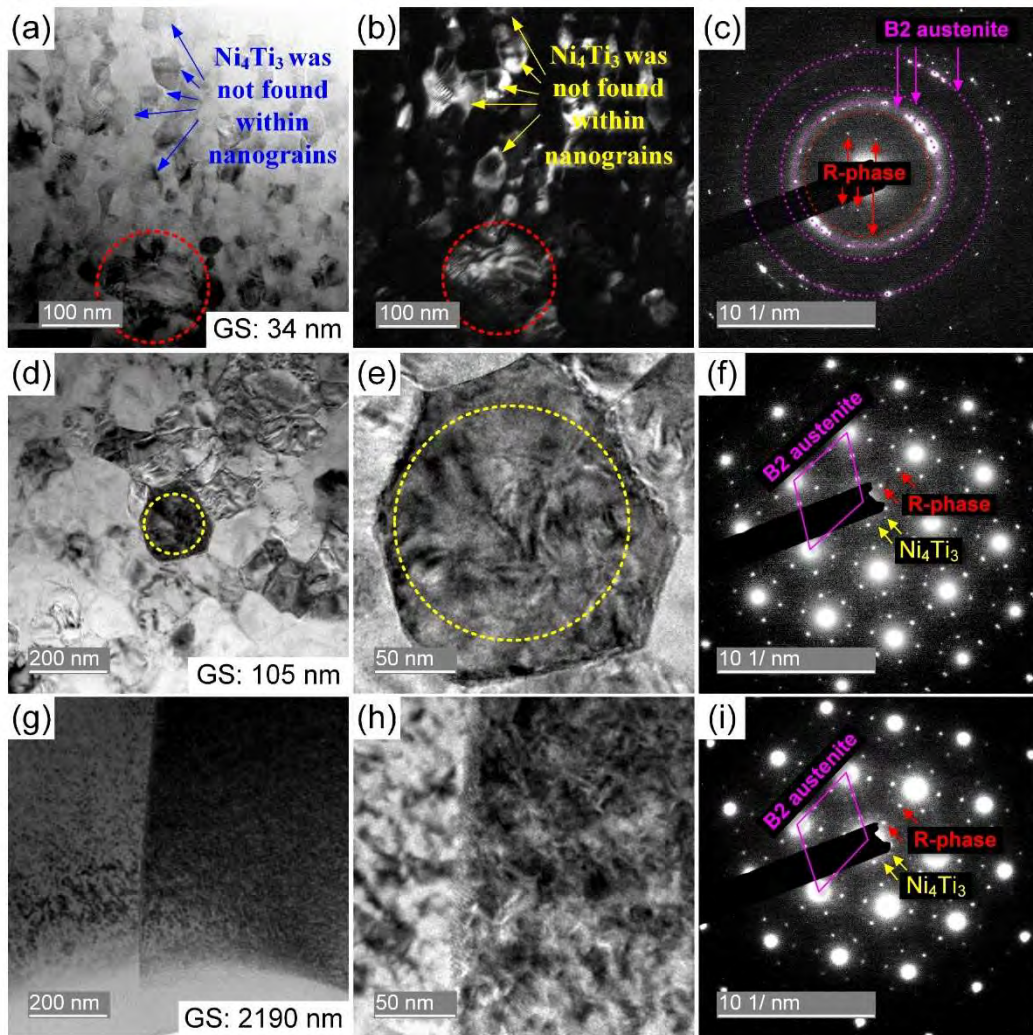


Fig. 4.12 Effect of grain size on precipitation: (a) the bright-field TEM micrograph of NiTi alloy with the average grain size of 34 nm after LTA of 48 h, in which the precipitates are not observed in the nanograins but observed in the isolated UFG grain as circled by dash line of which the grain size was about 150 nm; (b) the dark-field TEM micrograph of (a) of which the results are consistent with (a); (c) the SAED pattern of (a) and (b), which presents B2 phase and R-phase, while Ni_4Ti_3 diffractions are hardly observed; (d) the TEM micrograph of NiTi alloys with the average grain size of 105 nm after the LTA of 48 h and the grain circled by dash line is with grain size of about 150 nm; (e) the magnified micrograph of the circled grain in which the morphology of Ni_4Ti_3 are clearly

observed; (f) the SAED pattern of the circled grain in (e), which clearly shows the diffractions of B2 phase, R-phase, and Ni_4Ti_3 phase; (g) the TEM micrograph of the NiTi alloy with the average grain size of 2190 nm after the LTA of 48 h; (h) the magnified micrograph in grain boundary region around where nanoprecipitates also exist; and (i) the SAED pattern of (g) which proves the existence of B2 phase, R-phase, and coherent Ni_4Ti_3 phase.

The aforementioned effect of nanograin size on Ni_4Ti_3 precipitation explains the discrepancies of the influences of LTA on phase transformation characteristics of the NiTi alloys with different grain sizes. Combining with the results shown in **Fig. 4.8**, it can be seen that the $\text{B2} \leftrightarrow \text{R}$ transformation temperatures are affected by both grain size and LTA. Therefore, if it is assumed that the effect of LTA is not affected by grain size, the $\text{B2} \leftrightarrow \text{R}$ transformation temperatures of each LTA time should be a monotonic downward curve with grain size, which should be as similar as those before LTA, as shown in **Fig. 4.2**. However, the actual $\text{B2} \leftrightarrow \text{R}$ transformation temperatures of the NC NiTi alloys are lower than those assumed, and there is a critical grain size, i.e., around 105 nm, makes the variations of $\text{B2} \leftrightarrow \text{R}$ transformation temperatures with grain size not monotonic. When the grain size is larger than this critical value, $\text{B2} \leftrightarrow \text{R}$ transformation temperatures decrease with the increasing grain size, which is mainly due to the effect of grain size on $\text{B2} \leftrightarrow \text{R}$ transformation. When the grain size is smaller than this critical value, LTA is only able to induce Ni_4Ti_3 precipitates within the small portion of ultrafine grains in the NC NiTi matrix, while it is unable to precipitate Ni_4Ti_3 in the dominant nanograins. This finally leads to the result that $\text{B2} \leftrightarrow \text{R}$ transformation temperatures do not elevate as much as assumed.

It is as early as in chapter 3 that the nanograin size is found suppressing the Ni_4Ti_3 precipitation, where the LTA was carried out by short-time DERHT. It can thus be known that, combined with the results of this chapter, nanograin size induces suppression of Ni_4Ti_3 precipitation during LTA, no matter in short-time (0-600 s) or long-time (2-48 h).

The studies about this phenomenon are very limited, and only a few studies pointed out similar phenomena at non-LTA conditions. For instances, Egor A. Prokofiev et al. [142] applied the aging of 673 K to the NiTi alloys of NC, UFG, and CG grain sizes. They found that Ni_4Ti_3 precipitates with size of 70-140 nm exist in the CG samples, Ni_4Ti_3 precipitates with size of 50-90 nm exist in the UFG samples, and no Ni_4Ti_3 precipitates are found in the NC samples. Abbasi-Chianeh et al. carried out aging of 723 K-0.75 h to the NiTi alloys with the severe plastic strain of 0.4 and 0.6. They found that the NiTi alloys with the strain of 0.4 present CG microstructure and contained Ni_4Ti_3 precipitates, while the NiTi alloys with the strain of 0.6 present NC microstructure and did not contain Ni_4Ti_3 precipitates. Besides grain size, Jiang et al [210] applied the aging of 873 K-1 h to the severe deformed NiTi alloys. They found that the interfaces produced from the severe deformation with intervals of tens of nanometers also suppress Ni_4Ti_3 precipitation. The findings of this study proves that such suppression was not only happened under non-LTA conditions, but it also happens under the LTA condition. Although LTA produces Ni_4Ti_3 with size of 7-15 nm in the UFG and CG NiTi alloys, the nanograin size can suppress their precipitation in the NC NiTi alloys.

Based on the results of chapter 2, 3, and the present chapter, regarding the nanograin size induced suppression of Ni_4Ti_3 precipitation during LTA. The mechanisms leading to such phenomenon are analyzed as follows: 1) the study of Waitz.T et. al. [123] proves the nanograin size provided higher resistance of lattice deformation, and it is known that the coherent Ni_4Ti_3 inevitably induces elastic strain in the lattice [144]. Therefore, it is more difficult to precipitate Ni_4Ti_3 in the nanograin inner than in the coarse grain inner. 2) the formation of Ni_4Ti_3 precipitates requires Ni atom diffusion and aggregation [50]. In coarse grains, the impediments within the grain inner are little, thus it is easy for the Ni atom to aggregate and form Ni_4Ti_3 ; in nanograins, however, due to the high volume fraction of grain boundaries and the high vacancy volume fraction in grain boundaries [211], the Ni atom tends to move along grain boundaries after they diffused to grain boundaries rather than to diffuse across the grain boundaries. 3) per the study of K. Lu et. al. [212], the grain boundary segregation happens during LTA in nanocrystalline materials with saturated solute atoms. The NiTi alloy studied in the present study is nanocrystalline one and the Ni atom was saturated in the matrix, thus the LTA can lead the segregation of Ni in the grain boundaries, which consequently leads to the difficulty for the precipitation of Ni_4Ti_3 within the nanograins. In summary, per the results of this study, the nanograin size induces suppression of Ni_4Ti_3 precipitation during LTA is led by one or multiple aforementioned mechanisms, which calls for more advanced experimental methods and apparatus for further study.

4.5.4 Corroborative evidence of the microstructural evolution based on the variation of hardness

The Variations of hardness with LTA time and grain size are shown in **Fig. 4.13**. Before LTA, the hardness of the NiTi alloys decreases with the increasing grain size which presents typical Hall-Petch relation [213]. After LTA, within grain size range of 217-8021 nm, the LTA of 2 h remarkably elevates hardness, which is due to precipitation strengthening. Further increasing LTA time, the hardness shows no obvious elevation, which indicates that, though the density of the Ni_4Ti_3 precipitates increased, the elevation of dislocation slip resistance is barely further improved. By contrast, within grain size range of 34-105 nm, LTA does not lead to precipitation strengthening, which is consistent with the TEM results. Therefore, the variation of hardness corroborates the aforementioned conclusion that nanograin size induces suppression of Ni_4Ti_3 precipitation during LTA.

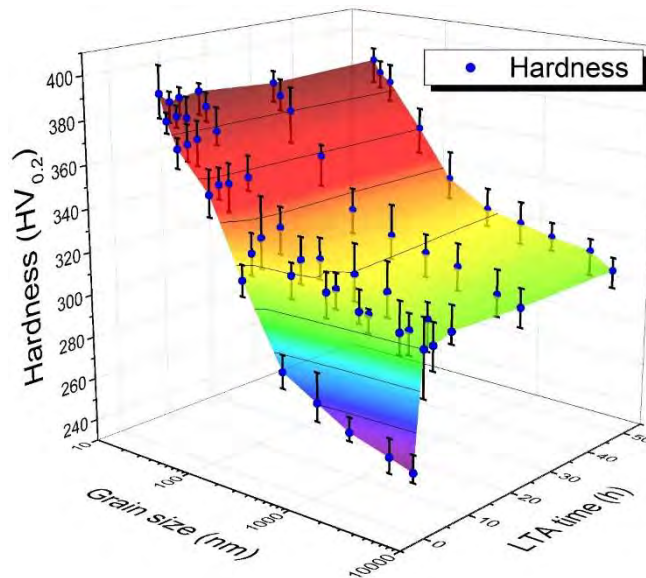


Fig. 4.13 Variations of hardness with LTA time and grain size.

4.6 B2→R transformation temperature model considering the effect of LTA time and grain size

To determine of B2→R transformation temperature is the basis of the design of NiTi functional devices based on B2↔R transformation. According to the experimental results, the B2↔R transformation temperature varies with not only the grain size but also the LTA time. This variation challenges the design and applications, when LTA is used as the transformation temperature adjustment method. Thus, the B2→R transformation temperature model that consider the two factors is required.

As per the experimental results, the B2→R transformation temperatures were 50 data points in total regarding different grain sizes (34-8021 nm) and LTA time (2-48 h). The data points are divided, by random, into the modeling dataset (38 data points in total) and the verification dataset (12 data points). The detailed division is shown in **Table 4.4**.

Table 4.4 Division of modeling dataset and verification dataset

LTA time (h)	Grain size (nm)									
	34	40	51	105	217	523	1106	2190	4972	8021
2	○	○	○	(1)	○	○	○	○	○	(2)
4	○	○	(3)	○	○	(4)	○	○	○	○
8	(5)	○	○	○	(6)	○	○	(7)	○	○
24	○	(8)	○	○	○	○	(9)	○	○	(10)
48	○	○	(11)	○	○	○	○	○	(12)	○

○ Modeling dataset; (1)~(12) Verification dataset

Firstly, at each LTA time, the variations of B2→R transformation temperature presented “s” shape with the increasing grain size. Therefore, according to the superposition principle [214], the basic functions shown in **Fig. 4.14(a)-(c)** can be

used for superposition to establish the function of the B2→R transformation temperature about grain size at certain LTA time. The obtained function is shown in Eq. (4.1) and the function graph is shown in **Fig. 4.14(d)**.

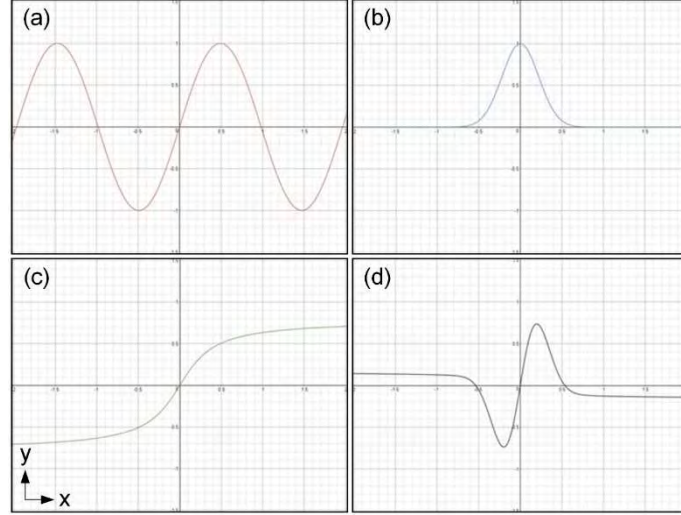


Fig. 4.14 B2→R transformation temperature as a function of grain size, at certain LTA time: basic function graphs of (a) $a \cdot \sin(c(x - b))$; (b) $\exp(-(c(x - b))^2)$; (c) $a \cdot \arctan(c(x - b))$; and (d) the established function graph of $a \cdot$

$$\sin(c \cdot (x - b)) \left\{ \exp \left[-(c \cdot (x - b))^2 \right] \right\} - d \cdot \arctan(c \cdot (x - b)) + g$$

$$T_{AR} \Big|_{t_{LTA}} = a \cdot \sin(c \cdot (\log_{10} D - b)) \left\{ \exp \left[-(c \cdot (\log_{10} D - b))^2 \right] \right\} - d \cdot \arctan(c(\log_{10} D - b)) + g \quad D \in [34, 8021] \text{ (nm)} \quad (4.1)$$

where T_{AR} represents the B2→R transformation temperature, t_{LTA} represents the LTA time, D represents grain size, a , b , c , d , and g are the parameters of Eq. (4.1) which are also the function of t_{LTA} . At certain LTA time, the values of a , b , c , d , and g are of certain values.

Based on the modeling dataset, the B2→R transformation temperature function at each LTA time (2-48 h) are respectively obtained according to Eq. (4.1), which are respectively shown in Eq. (4.2)-(4.6).

$$T_{AR}|_{t_{LTA}=2h} = 13.11 \cdot \sin(3.13(\log_{10} D - 2.14)) \left\{ \exp\left[-(3.13(\log_{10} D - 2.14))^2\right] \right\} + 0.88 \cdot \arctan(3.13(\log_{10} D - 2.14)) + 305.16 \quad D \in [34, 8021] \text{ (nm)} \quad (4.2)$$

$$T_{AR}|_{t_{LTA}=4h} = 10.98 \cdot \sin(2.76(\log_{10} D - 1.93)) \left\{ \exp\left[-(2.76(\log_{10} D - 1.93))^2\right] \right\} - 1.72 \cdot \arctan(2.76(\log_{10} D - 1.93)) + 310.64 \quad D \in [34, 8021] \text{ (nm)} \quad (4.3)$$

$$T_{AR}|_{t_{LTA}=8h} = 9.18 \cdot \sin(2.53(\log_{10} D - 1.81)) \left\{ \exp\left[-(2.53(\log_{10} D - 1.81))^2\right] \right\} - 3.32 \cdot \arctan(2.53(\log_{10} D - 1.81)) + 314.27 \quad D \in [34, 8021] \text{ (nm)} \quad (4.4)$$

$$T_{AR}|_{t_{LTA}=24h} = 6.87 \cdot \sin(2.33(\log_{10} D - 1.71)) \left\{ \exp\left[-(2.33(\log_{10} D - 1.71))^2\right] \right\} - 3.80 \cdot \arctan(2.33(\log_{10} D - 1.71)) + 317.68 \quad D \in [34, 8021] \text{ (nm)} \quad (4.5)$$

$$T_{AR}|_{t_{LTA}=48h} = 5.70 \cdot \sin(2.26(\log_{10} D - 1.68)) \left\{ \exp\left[-(2.26(\log_{10} D - 1.68))^2\right] \right\} - 2.81 \cdot \arctan(2.26(\log_{10} D - 1.68)) + 318.93 \quad D \in [34, 8021] \text{ (nm)} \quad (4.6)$$

Based on the obtained values of a , b , c , d , and g at different LTA time, the functions of a , b , c , d , and g about t_{LTA} are established as shown in Eq. (4.7).

$$\begin{cases} a = a_1 \cdot \exp(-a_2 \cdot -\log_{10} t_{LTA}) + a_3 = 16.33 \cdot \exp(-0.56 \cdot \log_{10} t_{LTA}) - 0.69 \\ b = b_1 \cdot \exp(-b_2 \cdot \log_{10} t_{LTA}) + b_3 = 0.84 \cdot \exp(-1.75 \cdot \log_{10} t_{LTA}) + 1.64 \\ c = c_1 \cdot \exp(-c_2 \cdot \log_{10} t_{LTA}) + c_3 = 1.58 \cdot \exp(-1.56 \cdot \log_{10} t_{LTA}) + 2.15 \\ d = d_1 + d_2 \cdot \log_{10} t_{LTA} + d_3 \cdot \log_{10}^2 t_{LTA} = -4.49 + 13.66 \cdot \log_{10} t_{LTA} - 5.54 \cdot \log_{10}^2 t_{LTA} \\ g = -g_1 \cdot \exp(-g_2 \cdot \log_{10} t_{LTA}) + g_3 = -24.50 \cdot \exp(-1.37 \cdot \log_{10} t_{LTA}) + 321.38 \end{cases} \quad t_{LTA} \in [2, 48] \text{ (h)} \quad (4.7)$$

The B2→R transformation temperature model considering the effects of LTA time and grain size is thus obtained, which is represented by Eq. (4.1) and (4.7). The parameters of the model are shown in **Table 4.5**. The surface of the obtained T_{AR} function is shown in **Fig. 4.15(a)**. The model can be used to calculate the B2→R transformation temperature at different grain sizes and LTA time. The correlation

relationship of the calculated values and the experimental values of the verification dataset is shown in **Fig. 4.15(b)**. The correlation coefficient R was 0.99875, and the AARE(%) was 0.09%.

The comparison of the experimental values and the calculated values of the verification dataset is shown in **Fig. 4.16**. Among the 12 data points, the maximum absolute error was 0.53 K, and the maximum relative error was 0.17%. Therefore, this model can be used to calculate B2→R transformation temperature within grain size of 34-8021 nm and LTA time of 2-48 h.

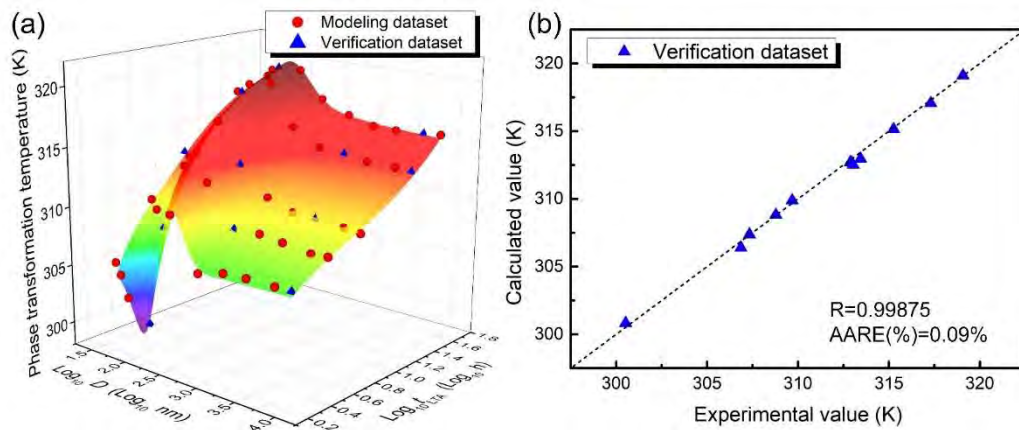


Fig. 4.15 The obtained T_{AR} model: (a) modeling dataset, verification dataset, and the surface of the obtained T_{AR} function; (b) the correlation between the calculated values and the experimental values of the verification dataset.

Table 4.5 The values of the parameters of the T_{AR} model

Parameter	Value	Parameter	Value
a_1	16.33	c_3	2.15
a_2	0.55	d_1	-4.49
a_3	-0.69	d_2	13.66
b_1	0.84	d_3	-5.54
b_2	1.75	g_1	24.50
b_3	1.64	g_2	1.37
c_1	1.58	g_3	321.38
c_2	1.56		

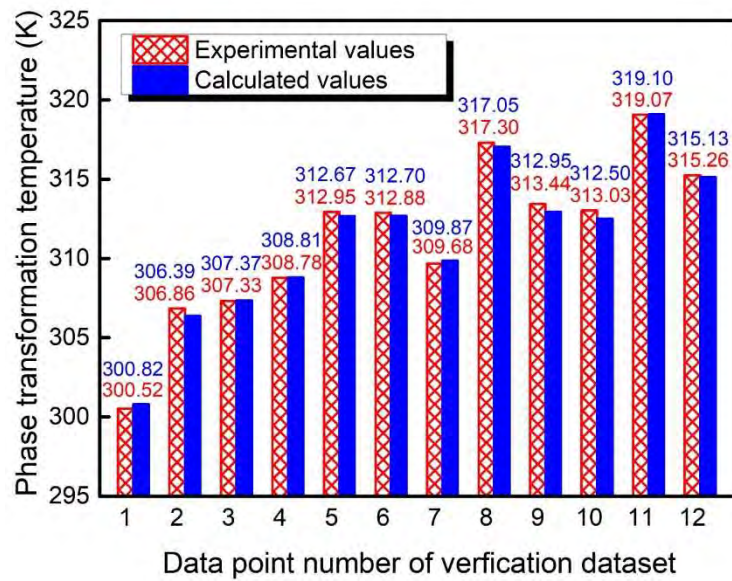


Fig. 4.16 Comparison of the experimental values and the calculated values of the verification dataset of B2→R transformation temperature

4.7 Summary

This chapter studies the effect of LTA at 573 K in 0-48 h on the phase transformation characteristics of NiTi alloys with grain size of 34-8021 nm. The following concluding remarks can thus be drawn:

- (1) Before LTA, grain size itself affects the phase transformation characteristics of the NiTi alloys. Within grain size of 34-217 nm, B2↔R transformation is

activated, $R \leftrightarrow B19'$ transformation is suppressed, and $B2 \leftrightarrow R$ transformation temperature decreases with the increasing grain size. Within grain size of 523-8021 nm, $B2 \leftrightarrow R$ transformation disappears, $B2 \leftrightarrow B19'$ transformation is activated, and $B2 \leftrightarrow B19'$ transformation temperature increases with grain size.

(2) After the LTA of 2 h, within grain size of 34-217 nm, $B2 \leftrightarrow R$ transformation is preserved. $B2 \leftrightarrow R$ transformation temperatures are elevated compared with those before LTA and decreases with the increasing grain size. $R \leftrightarrow B19'$ transformation keeps suppressed. Within grain size of 523-8021 nm, $B2 \leftrightarrow R$ transformation is elevated, and $B2 \leftrightarrow R$ transformation temperature decreases with increasing grain size. The $R \leftrightarrow B19'$ transformation is impeded, which represents suppression within grain size of 523-1106 nm and represents the decrease of transformation temperature decrease and the increase of thermal hysteresis within grain size of 2190-8021 nm.

(3) With the increasing LTA time from 2 h to 48 h, $B2 \leftrightarrow R$ transformation temperature increases regardless of grain size. Under the same LTA time, $B2 \leftrightarrow R$ transformation temperatures elevation induced by the LTA are different with different grain sizes. In the NC NiTi alloys, the elevation amplitudes of $B2 \leftrightarrow R$ transformation temperature increase with grain size. In the UFG NiTi alloys, $B2 \leftrightarrow R$ transformation temperature decreases with the increasing grain size. In the CG NiTi alloys, $B2 \leftrightarrow R$ transformation temperature is generally unchanged with the increasing grain size. The NiTi alloys with grain size of 105 nm present the highest elevation of $B2 \leftrightarrow R$ transformation temperature, which is as much 62.0 K at the LTA of 48 h. With

respect to $R \leftrightarrow B19'$ transformation, it is suppressed within grain size of 34-1106 nm, and its temperature increases with LTA time within grain size of 2190-8021 nm.

- (4) Grain size affects Ni_4Ti_3 precipitation. In the CG NiTi alloys, the LTA of 2 h precipitates Ni_4Ti_3 with grain size of 7-15 nm and gap of 5-15 nm. Further increasing LTA time from 2 h to 48 h, the size of the Ni_4Ti_3 precipitates is unchanged while their density increases. In the NiTi matrix of average grain size of 34 nm, Ni_4Ti_3 is not observed in the dominant nanograins, even though the LTA time reaches 48 h. By contrast, Ni_4Ti_3 is clearly observed in ultrafine grains with grain size about 150 nm, which presents similar size of precipitates as those found in the CG NiTi alloys. Therefore, there is a critical grain size, less than 150 nm, can affect the suppression of Ni_4Ti_3 : when grain size is larger than this critical value, Ni_4Ti_3 precipitation will proceed; when grain size is smaller than this critical value, Ni_4Ti_3 precipitation will be suppressed.
- (5) The underlying mechanisms for the LTA presenting different effects on the phase transformation characteristics of the NiTi alloys with different grain sizes are as follows: 1) LTA preserves the original grain size, which maintains the effect of grain size on phase transformation during LTA; 2) LTA induces densely distributed Ni_4Ti_3 nanoprecipitates with size of 7-15 nm in UFG and CG matrix, of which the size of precipitates does not increase but the density increases with the LTA time; 3) nanograin size suppresses the Ni_4Ti_3 precipitation during LTA.

- (6) The B2→R transformation temperature model considering the effects of LTA time and grain size is provided, which can be used to calculate B2→R transformation temperature of the NiTi alloys with grain size of 34-8021 nm and LTA time of 2-48. The model may provide a reference for the design of NiTi functional devices which are based on B2↔R transformation.

Chapter 5 Influence of low-temperature aging on the superelasticity of NiTi alloys with different grain sizes

5.1 Introduction

Superelasticity is one of the most extensively used functional properties, and a lot of applications of the NiTi alloys are based on superelasticity [11]. On one hand, the previous studies [48, 49] point out that, LTA remarkably varies the superelasticity of CG NiTi alloys. On the other hand, as per the results of chapter 2 and 3, it is known that the LTA presents different influences on superelasticity of the NC and CG NiTi alloys. Therefore, it is necessary to study the influence of LTA on the superelasticity of the NiTi alloys with different grain sizes.

During superelastic deformation, NiTi alloys may sometimes be unloaded within plateau deformation stage and sometimes within the post-plateau stage, which depends on specific service conditions. As pointed out in the previous studies, whether the NiTi alloys experience post-plateau deformation stage substantially influenced superelasticity. For NiTi alloys, the maximum applied strains of 3% and 9% representatively correspond to the unloading within plateau deformation stage and post-plateau deformation stage. Therefore, this chapter studies the influence of LTA on superelasticity of the NiTi alloys with different grain sizes by using the maximum applied strains of 3% and 9%, which is used to investigate the

individual influence of post-plateau deformation stage on superelasticity of the NiTi alloys with different LTA time and grain sizes.

5.2 Effect of grain size on superelasticity before LTA

As pointed out from the previous studies [44-46, 129], even without LTA, grain size itself affects the superelasticity of NiTi alloys. Thus, to investigate the individual effect of grain size on superelasticity before LTA is the basis of the study of the influence of LTA on superelasticity of NiTi alloys with different grain sizes.

5.2.1 Superelasticity under the maximum applied strain of 3%

before LTA

Before LTA, the superelastic stress-strain curves of the NiTi alloys with grain size of 34-8021 nm under the maximum applied strain of 3% are shown in **Fig. 5.1**. All of the NiTi alloys present typical superelasticity and unload within the plateau deformation stage. With the grain size increasing from 34 nm to 8021 nm, loading and unloading plateau stress decrease, residual strain increases, and the initial elastic modulus increases. For the NC and UFG NiTi alloys, the B2 \leftrightarrow R transformation related deformation involves, and the grain boundary volume fraction is larger than that of the CG NiTi alloys. Thus, the initial elastic deformation consists of stress-induced B2 \leftrightarrow R transformation, R-phase reorientation, and the elastic deformations of R-phase and grain boundaries. As can be seen from **Fig. 5.1**, when the grain size increases to above 523 nm, further increasing grain size hardly increases the elastic modulus, which is attributed to

the disappearance of B2 \leftrightarrow R transformation with the increasing grain size. This result is consistent with the corresponding phase transformation variations as analyzed in chapter 4.

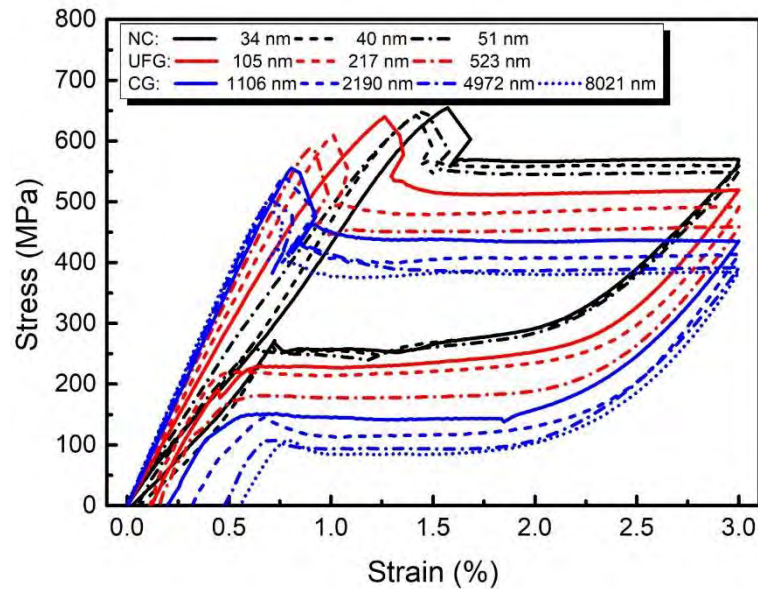


Fig. 5.1 Superelastic stress-strain curves of the NiTi alloys with different grain sizes under the maximum applied strain of 3% before LTA

5.2.2 Superelasticity under the maximum applied strain of 9% before LTA

According to the previous study [215], even unloaded within post-plateau deformation stage, the NC NiTi alloys still present excellent superelasticity, and the recoverable strain and damping ability are improved. This reflects the advantages of NC NiTi alloys over CG NiTi alloys. Therefore, this section studies the superelasticity of the NiTi with different grain sizes under the maximum applied strain of 9%, of which the superelastic stress-strain curves are shown in **Fig. 5.2**.

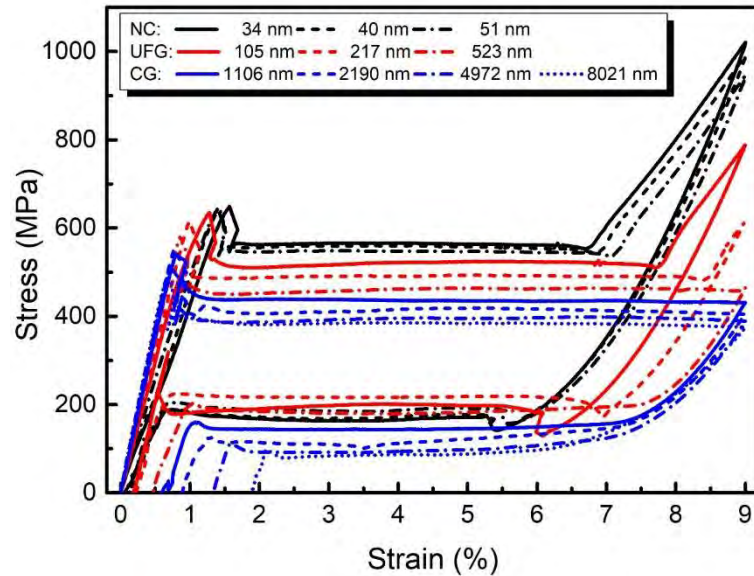


Fig. 5.2 Superelastic stress-strain curves of the NiTi alloys with different grain sizes under the maximum applied strain of 9% before LTA

It can be seen in the figure, under the maximum applied strain of 9%, all of the NiTi alloys still present typical superelasticity. The initial elastic modulus and loading plateau stress are as similar as those under the maximum applied strain of 3%, which is due to the partly same loading paths. However, the unloading paths are different from those under the maximum applied strain of 3%. For the CG NiTi alloys, residual strain obviously increases with the increase of maximum applied strain. For the NC NiTi alloys, the residual strain is still small. Post-plateau deformation stage happens in the NiTi alloys with the grain size less than 217 nm, which further increases the maximum loading stress. Therefore, the B2 austenite phase and R-phase needs to be nucleated in the NiTi matrix of B19' martensite phase, which leads to the stress jumps at the beginning of unloading plateau. With the increasing grain size, unloading plateau stress is first elevated and then decreased, and stress hysteresis first decreases and then increases, of which the grain size of 217 nm is the turning point.

5.2.3 Variations of superelastic indices with grain size before

LTA

Variations of the superelastic indices with grain size under the maximum applied strains of 3% and 9% are shown in **Fig. 5.3**. With the increasing grain size, elastic modulus increases while loading plateau stress decreases. They present nearly the same variations under the maximum applied strains of 3% and 9%, which indicates that these two indices are not affected by the maximum applied strain. Under the maximum applied strain of 3%, the unloading plateau stress increases with grain size. Under the maximum applied strain of 9%, the unloading plateau stress increases from the grain size of 34 nm to 217 nm and decreases from the grain size of 217 nm to 8021 nm.

The variations of stress hysteresis with grain size are shown in **Fig. 5.3(d)**. Under the maximum applied strain of 3%, stress hysteresis decreases with grain size increasing from 34 nm to 217 nm. This is consistent with the results of the previous study [46]. With the increasing grain size, grain boundary volume fraction decreases. Therefore, the energy dissipation of the phase transformation frontiers passing through the grain boundaries decreases, and the grain boundaries volume fraction that involved the accommodation deformation also decreases. These two factors cooperatively decrease the stress hysteresis. With the grain size increasing from 217 nm to 8021 nm, stress hysteresis increases. Under the maximum applied strain of 9%, stress hysteresis also decreases with the grain size increasing from 34 nm to 217 nm, and the decreasing amplitude is larger than that under the maximum applied strain of 3%. This indicates that the post-plateau deformation, besides the grain boundary volume fraction, also increases the stress hysteresis.

With grain size further increasing from 217 nm to 8021 nm, stress hysteresis also increases, which is of the same increase amplitude as that under the maximum applied strain of 3%. Such increase is due to the dislocation slip.

The variations of residual strain with grain size are shown in **Fig. 5.3(e)**. Residual strain increased with grain size no matter under 3% or the maximum applied strain of 9%. The amplitude of increase under the maximum applied strain of 9% is higher than that under the maximum applied strain of 3%. When the grain size increases to above 217 nm, residual strain increases more prominent. This is due to the fact that 200 nm is critical grain size for dislocation slip in NiTi alloys [199]. If the grain size is smaller than 200 nm, dislocation slip seldom happen. If the grain size is larger than 200 nm, the dislocation slip increases with grain size. Thus, residual strain increases with grain size more remarkably when grain size is larger than 217 nm. The increasing dislocation slip activities also enhance the energy dissipation during phase transformation. This thus explains why the stress hysteresis increases with grain size after the grain size increasing to above 217 nm.

The variations of plateau strain with grain size are shown in **Fig. 5.3(f)**. As shown in **Fig. 5.2** that, under the maximum applied strain of 9%, the NiTi alloys with grain size of 34-217 nm finish the plateau deformation, which is shown by the circled data points in **Fig. 5.3(f)**. The other data points reflect the strains from the plateau beginning to the maximum applied strain. It can be seen that the plateau strain increases with grain size.

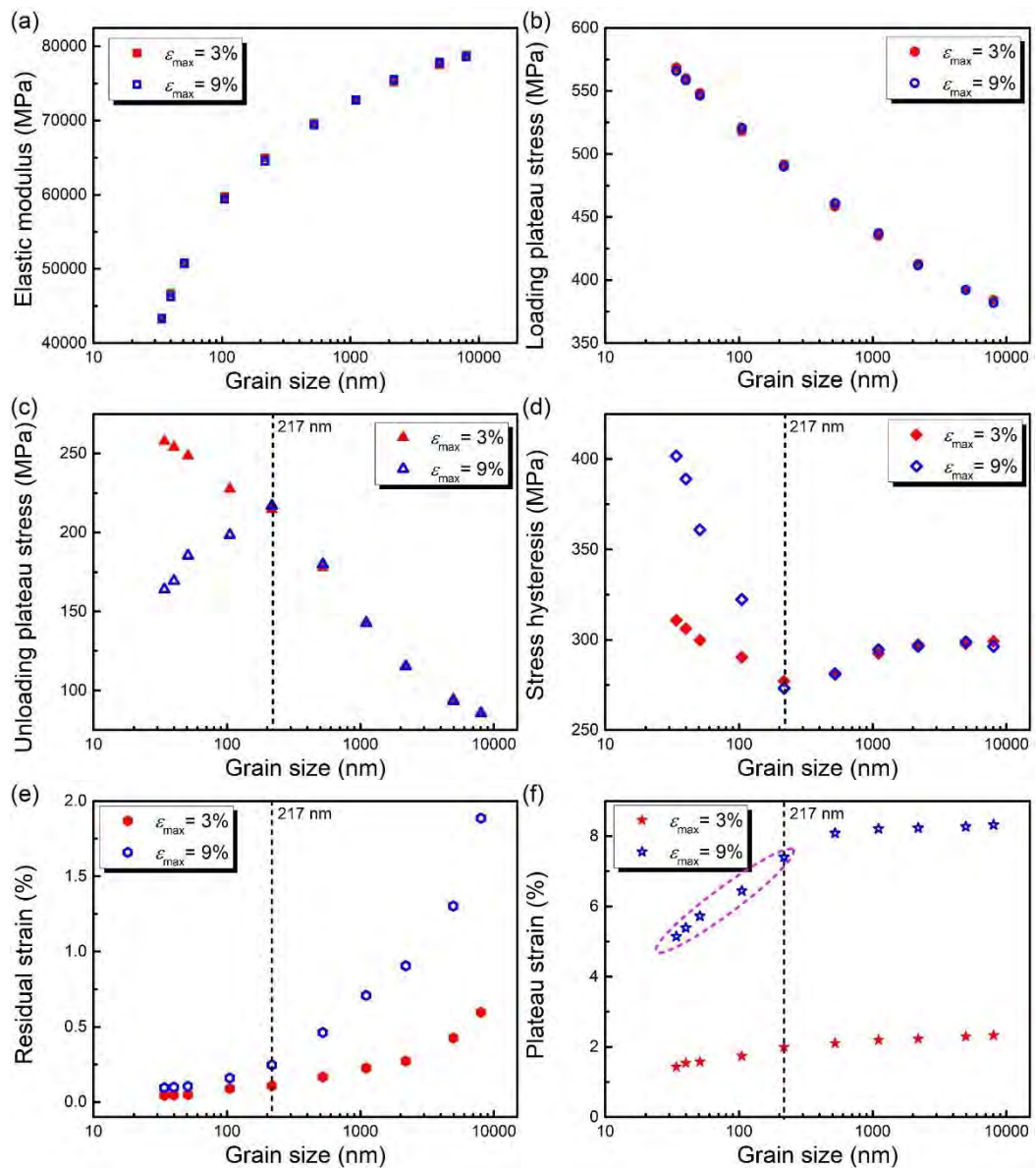
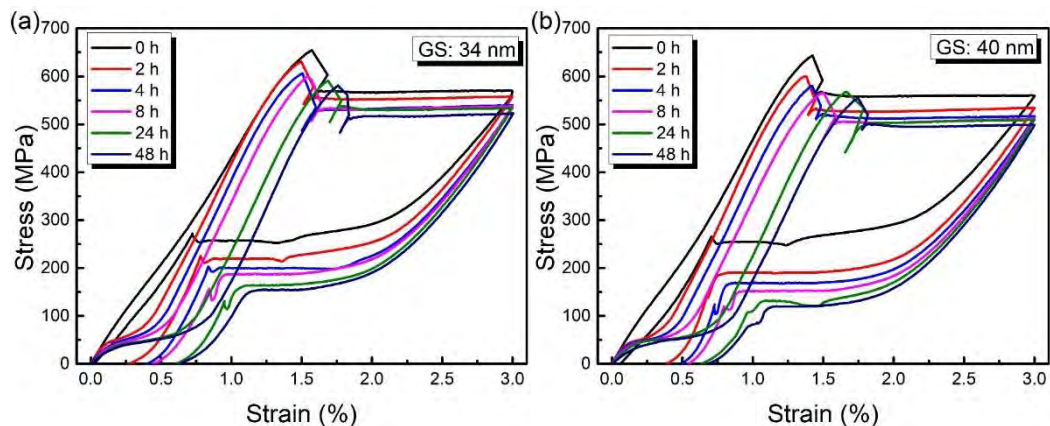


Fig. 5.3 Variations of superelastic indices with grain size before LTA: (a) elastic modulus; (b) loading plateau stress; (c) unloading plateau stress; (d) stress hysteresis; (e) residual strain; and (f) plateau strain (the data points circled by dash line were obtained when plateau deformation stage was finished).

5.3 Effect of LTA on the superelasticity of the NiTi alloys with different grain sizes

5.3.1 Superelasticity under the maximum applied strain of 3% after LTA

After LTA, under the maximum applied strain of 3%, the variations of superelastic stress-strain curves of the NiTi alloys with different LTA time and grain sizes are shown in Fig. 5.4. All of the NiTi alloys present typical superelasticity and obvious initial B2 \leftrightarrow R transformation related deformation. With the increasing LTA time, the plateau stress of B2 \leftrightarrow R transformation decreases, while its plateau strain increases. This is because that the plateau stress and strain of stress-induced B2 \leftrightarrow R transformation depend on its B2 \leftrightarrow R transformation temperature [189, 216]: the higher B2 \rightarrow R transformation temperature leads to lower plateau stress and larger plateau strain. As known from Chapter 4, B2 \rightarrow R transformation temperature of the NiTi alloys increases with LTA time, which is consistent with the above mentioned B2 \leftrightarrow R transformation related deformation in this chapter. When the B2 \rightarrow R transformation plateaus are finished, the elastic modulus of the R-phase seldom changes with LTA time and grain size.



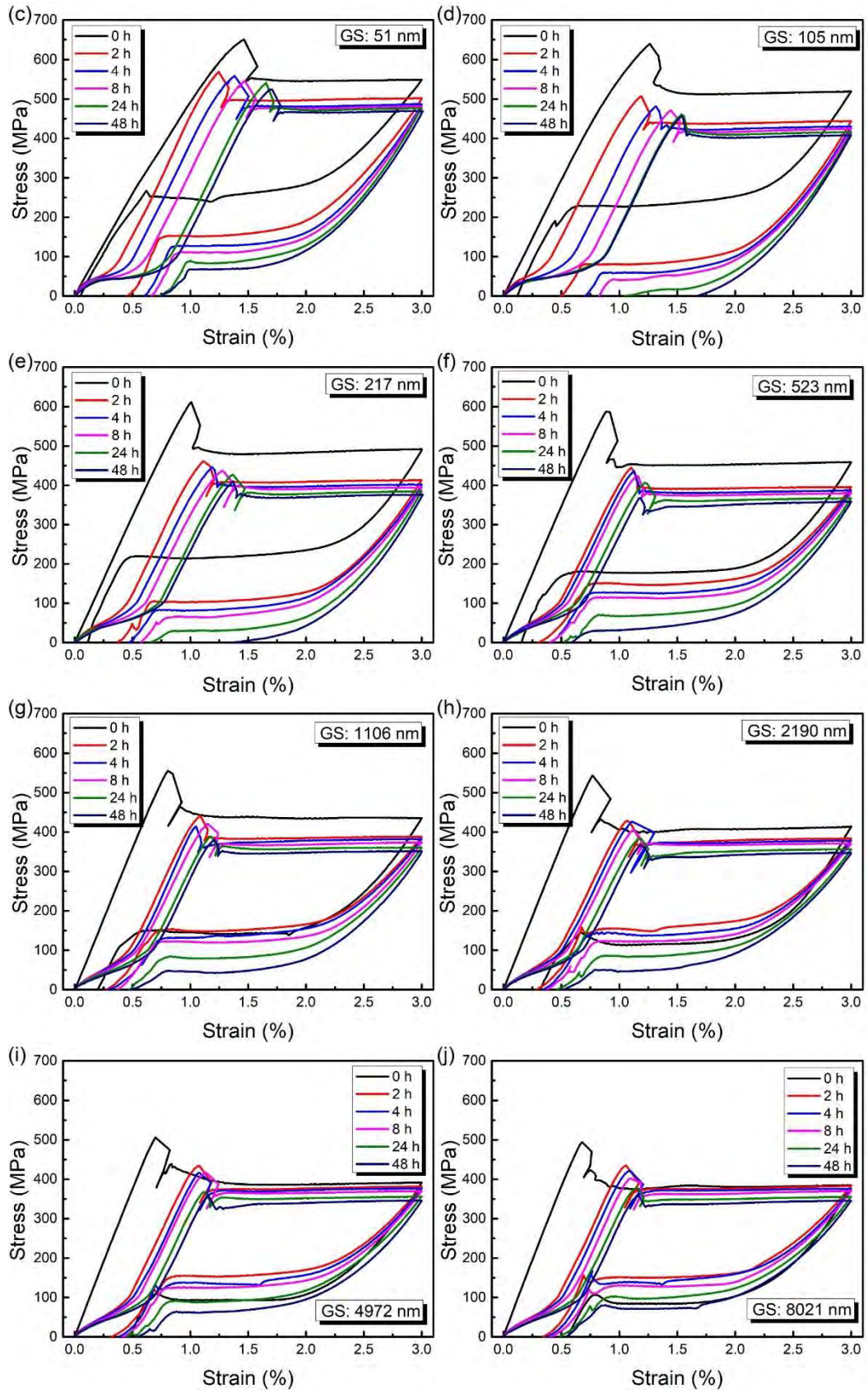
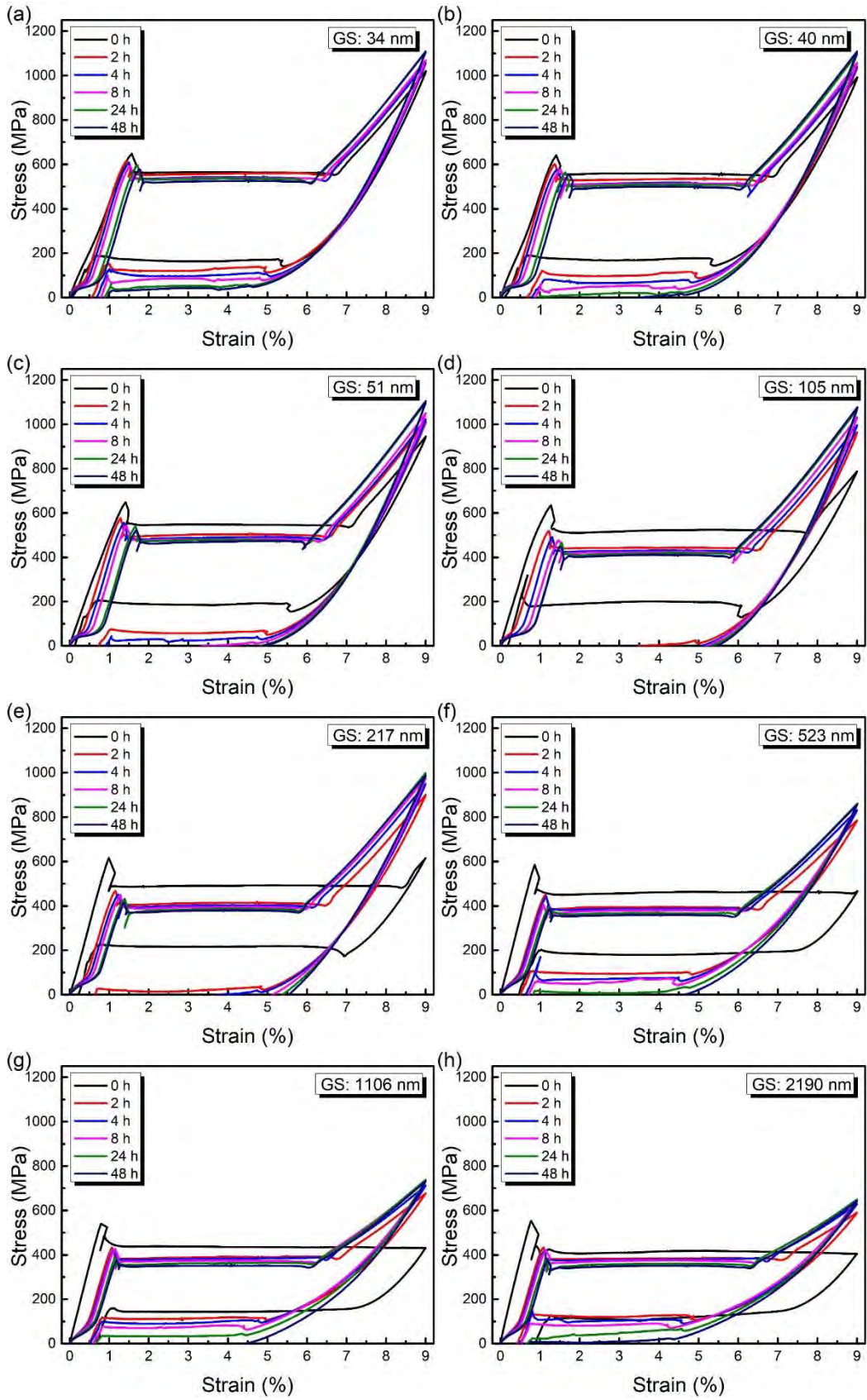


Fig. 5.4 Under the maximum applied strain of 3%, the variations of superelastic stress-strain curves with LTA time of 0-48 h and grain size of (a) 34 nm; (b) 40

nm; (c) 51 nm; (d) 105 nm; (e) 217 nm; (f) 523 nm; (g) 1106 nm; (h) 2190 nm;
(i) 4972 nm; and (j) 8021 nm.

5.3.2 Superelasticity under the maximum applied strain of 9% after LTA

After LTA, under the maximum applied strain of 9%, the variations of superelastic stress-strain curves of the NiTi alloys with different LTA time and grain sizes are shown in **Fig. 5.5**. Some of them present typical superelasticity, which experience loading and unloading plateau deformation stages, respectively. The others do not experience unloading plateau deformation stage even when the applied stress decreases to 0 MPa. After LTA, under the maximum applied strain of 9%, all of the curves finish plateau deformation stage and enter post-plateau deformation stage, and the maximum loading stress thus increases. Under the maximum applied strain of 3%, however, the maximum loading stress should be the plateau stress, if the stress jump induces by the start of Lüders-like deformation is neglected. Under the maximum applied strain of 9%, the stress-strain relationships within B2 \leftrightarrow R transformation related deformation stage and plateau deformation stage are the same as those under the maximum applied strain of 3%, which indicates that the two deformation stages are independent of the maximum applied strain.



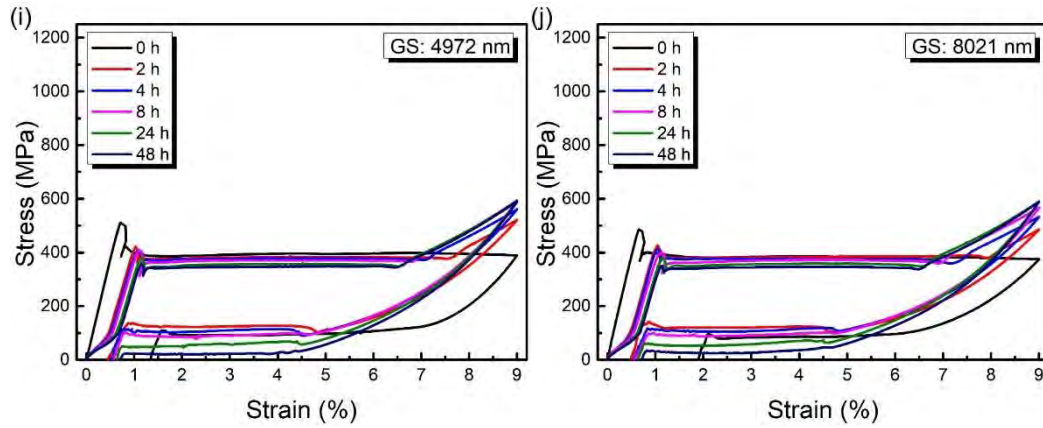


Fig. 5.5 Under the maximum applied strain of 9%, variations of superelastic stress-strain curves with LTA time of 0-48 h and grain size of (a) 34 nm; (b) 40 nm; (c) 51 nm; (d) 105 nm; (e) 217 nm; (f) 523 nm; (g) 1106 nm; (h) 2190 nm; (i) 4972 nm; and (j) 8021 nm.

Plateau strain, the elastic modulus of post-plateau deformation, unloading plateau stress, and residual strain under the maximum applied strain of 9% are different with those under the maximum applied strain of 3%. Under the maximum applied strain of 9%, plateau strain decreases with LTA time. The elastic modulus of post-plateau deformation decreases with grain size while it generally does not change with LTA time. Unloading plateau stress decreases with the increasing LTA time, and the decrease is more remarkable than that under the maximum applied strain of 3%. After the LTA of 48 h, the NiTi alloys with grain size of 40-2190 nm do not finish the unloading plateau deformation, and larger residual strains are left. For the other NiTi alloys, even if the unloading plateau deformation is finished, the residual strains are still higher than those under the maximum applied strain of 3%.

5.3.3 Variations of superelasticity indices with LTA time and grain size

Since the superelasticity indices are important in practical applications for different functional usages, this section discusses the variations of the indices with grain size and LTA time.

5.3.3.1 Loading plateau stress

As shown in **Fig. 5.6**, the loading plateau stress decreases with grain size regardless of the variation of LTA time. Before LTA, the decrease is slight with the increasing grain size. After the LTA of 2 h, the loading plateau stress decreases drastically with the grain size increasing from 34 nm to 1106 nm, while it decreases slightly with the grain size increasing from 1106 nm to 8021 nm. After LTA of 4-48 h, the variations of loading plateau stress with grain size are similar to that after the LTA of 2 h.

As shown in **Fig. 5.6(b)**, the loading plateau stress decreases with LTA time regardless of the variations of grain size. The variation within grain size of 105-1106 nm and LTA time of 0-2 h are most remarkable.

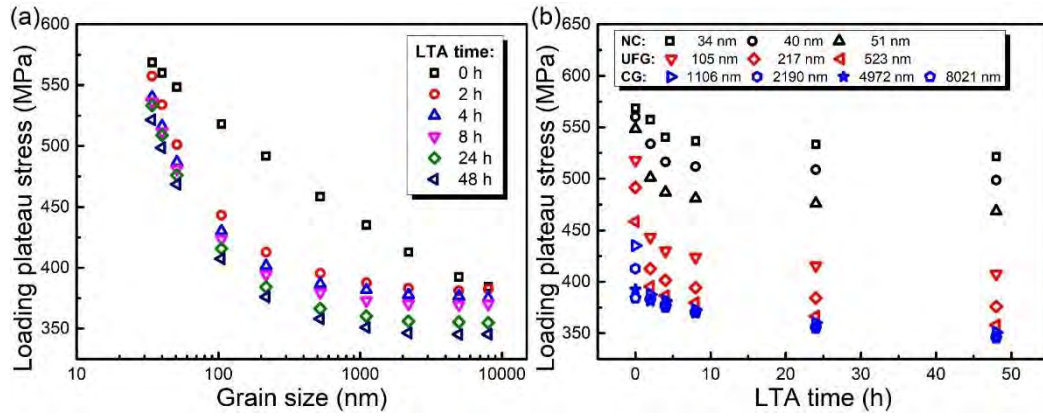


Fig. 5.6 Variations of loading plateau stress with (a) grain size and (b) LTA time.

5.3.3.2 Plateau strain

After LTA, all the NiTi alloys finish the plateau deformation stage under the maximum applied strain of 9%, whilst that is not the case under the maximum applied strain of 3%. Thus, the data under the maximum applied strain of 9% is used to discuss the plateau strain, as shown in **Fig. 5.7**. It is noteworthy that, before LTA, the NiTi alloys with grain size of 1106-8021 nm do not finish the plateau deformation stage. Thus, larger applied strains are used to obtain the plateau strain, which is also shown in **Fig. 5.7**.

As shown in **Fig. 5.7(a)**, before LTA, the plateau strain increases from 5.2% to 10.3 % with the grain size increasing from 34 nm to 8021 nm. After LTA, plateau strains obviously decrease than those before LTA. Within grain size of 34-217 nm, plateau strain slightly decreases with the increasing grain size and is generally maintained within 4%-5.5%. Within grain size of 217-8021 nm, it increases with grain size. The smallest plateau strain emerges within grain size of 105-217 nm.

As shown in **Fig. 5.7(b)**, the plateau strain decreases with the increasing LTA time. The amplitude of decrease is obvious within 0-8 h, whilst it becomes gentle within 8-48 h. This decrease is more remarkable in UFG and CG NiTi alloys.

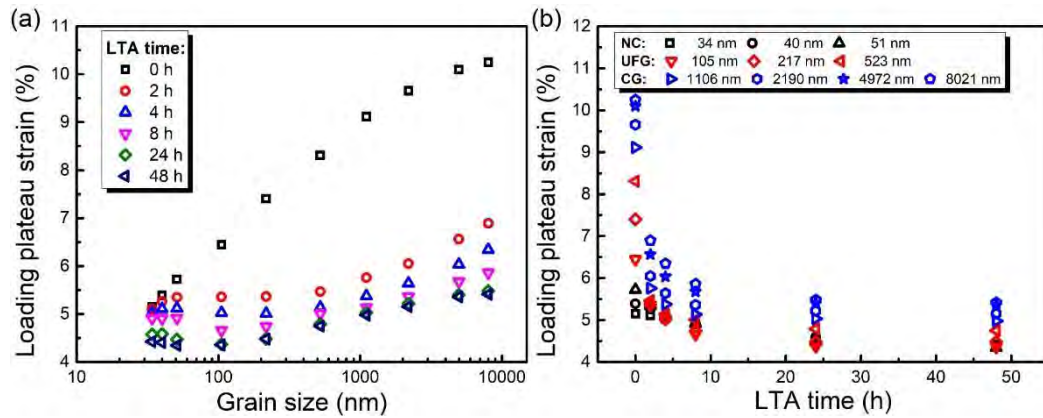


Fig. 5.7 Variations of plateau strain with (a) grain size and (b) LTA time.

5.3.3.3 Unloading plateau stress

Since the unloading stress-strain paths are different between the maximum applied strains of 3% and 9%, the variations of unloading plateau stress with grain size and LTA time under the two maximum applied strains are respectively shown in **Fig. 5.8**.

Under the maximum applied strain of 3%, as shown in **Fig. 5.8(a)**, before LTA, the unloading plateau stress decreases with the increasing grain size. After LTA, the unloading plateau stress decreases with grain size from 34 nm to 105 nm, whilst it increases with grain size from 105 nm to 8021 nm.

As shown in **Fig. 5.8(b)**, within grain size of 34-523 nm, the unloading plateau stress decreases with the increasing LTA time. Within grain size of 1105-8021 nm, the unloading plateau stresses after the LTA of 2 h are higher than those before

LTA. After that, the unloading plateau stress decreases from the LTA of 2 h to 48 h. This decrease is most remarkable in UFG NiTi alloys.

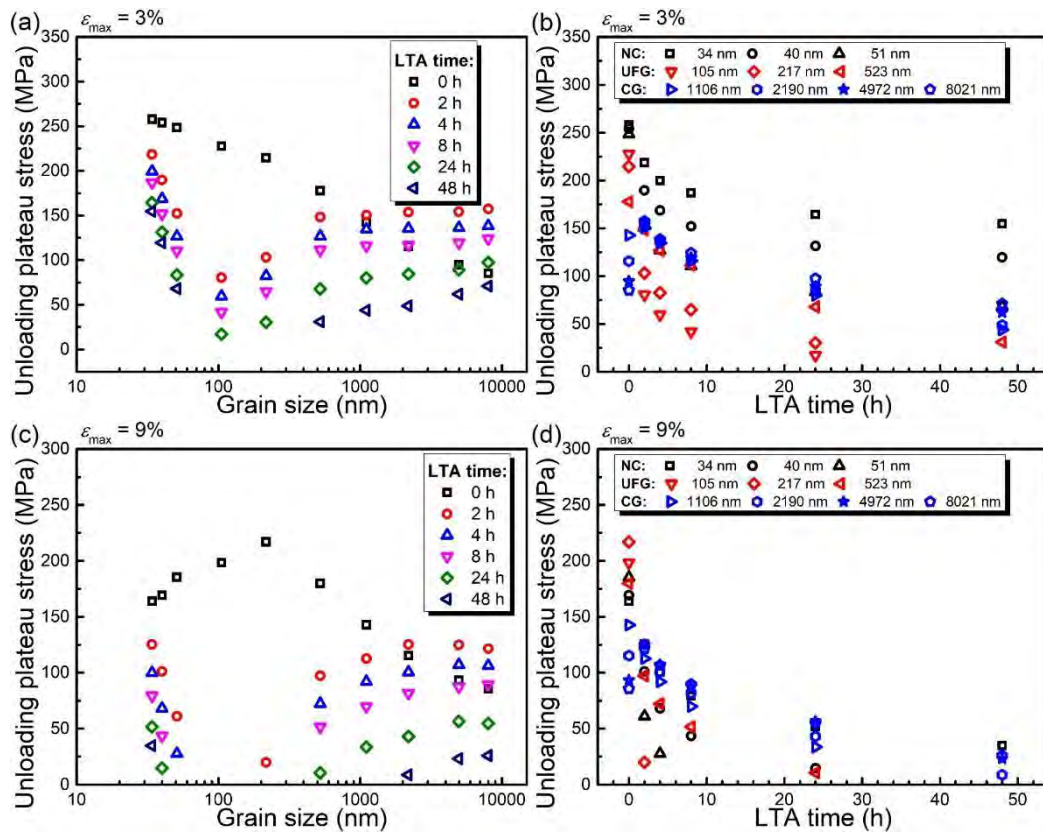


Fig. 5.8 Variations of unloading plateau stress with (a) grain size and (b) LTA time under the maximum applied strain of 3%, and that with (c) grain size and (d) LTA time under the maximum applied strain of 9%.

Under the maximum applied strain of 9%, since a part of the NiTi alloys does not finish the plateau deformation stage, **Fig. 5.8(c)** and (d) only depict the unloading plateau stress of those finished the plateau deformation stage. As shown in **Fig. 5.8(c)**, before LTA, the unloading plateau stress first increases and then decreases, which arrives its maximum at the grain size of 217 nm. After LTA, the variations of unloading plateau stress with grain size are similar to those under the maximum applied strain of 3%.

As shown in **Fig. 5.8(d)**, within grain size of 34-1106 nm, unloading plateau stress decreases with the increasing grain size. Within grain size of 1106-8021 nm, the unloading plateau stress increases after the LTA of 2 h, whilst they decrease with the LTA time further increasing from 2 h to 48 h. Within the UFG grain size scale, the unloading plateau stress decreases most obviously, which is similar to the case under the maximum applied strain of 3%.

5.3.3.4 Stress hysteresis

Since the stress hysteresis variations with grain size and LTA time are different between the maximum applied strains of 3% and 9%, they are respectively discussed as shown in **Fig. 5.9**.

Under the maximum applied strain of 3%, the NiTi alloys are unloaded within the plateau deformation stage, thus their stress hysteresis is independent of the post-plateau deformation. As shown in **Fig. 5.9(a)**, before LTA, stress hysteresis first decreases then increases with the increasing grain size, and it reaches its minimum at grain size of 217 nm. After LTA, the stress hysteresis first increases and then decreases with the increasing grain size, and it reaches its maximum at grain size of 105 nm.

As shown in **Fig. 5.9(b)**, within grain size of 34-217 nm, stress hysteresis increases with LTA time. Within grain size of 523-8021 nm, stress hysteresis first reaches its minimum at the LTA of 2 h, and then increases with the increasing LTA time from 2 h to 48 h.

It is noteworthy that the LTA effectively expands the variation range of stress hysteresis. Before LTA, the variation range of stress hysteresis is relatively small, which is about 275-313 MPa. After LTA, the variation range of stress hysteresis is expanded, which is about 225-400 MPa. That is to say, the variation range is expanded from 38 MPa to 175 MPa, which is increased by 460%. This indicates that the LTA induces the increase of stress hysteresis variation range has the potential to facilitate the applications of NiTi alloys from the damping perspective.

Taking civil engineering as an instance, the vibration of a suspension bridge caused by winds leads to the fatigue of the bridge cable during cyclic loading-unloading deformation [24, 217]; the vibration of an architecture caused by an earthquake may leads to collapse of the whole building if the vibration is not suppressed [26, 27]. By using NiTi alloys as damping material, the stress hysteresis of the alloys is worked as damping, which leads to the energy transformation from kinetic energy to heat. The bridge cable and building were thus protected and strengthened since the vibration energy is absorbed and dissipated. The larger the hysteresis is, and the more is transformed from kinetic energy to heat. In this thesis, the increase of hysteresis adjustment range (from 38 MPa (275-313 MPa) to 175 MPa (225-400 MPa),) can be used to increase the hysteresis from 313 MPa to 400 MPa, which remarkably increases the damping. This will increase the energy absorption and dissipation in civil engineering, i.e. facilitates the engineering application.

As shown in **Fig. 5.9(c)** and (d), the variations of stress hysteresis with grain size and LTA time under the maximum applied strain of 9% are similar to those under

the maximum applied strain of 3%. However, the variations of stress hysteresis under the maximum applied strain of 9% are additionally influenced by post-plateau deformation. Therefore, they are generally higher than those under the maximum applied strain of 3%. As similar to those under the maximum applied strain of 3%, the LTA under the maximum applied strain of 9% still can obviously expand the variation range of stress hysteresis (expanding from 270-405 MPa before LTA to 250-490 MPa after LTA).

Stress hysteresis reaches its minimum after the LTA of 2 h at grain size of 217 nm (under the maximum applied strain of 3%) and 1106 nm (under the maximum applied strain of 9%). This is because the LTA effectively suppresses the dislocation slip and consequently decreases the increase of stress hysteresis induced by dislocation activities.

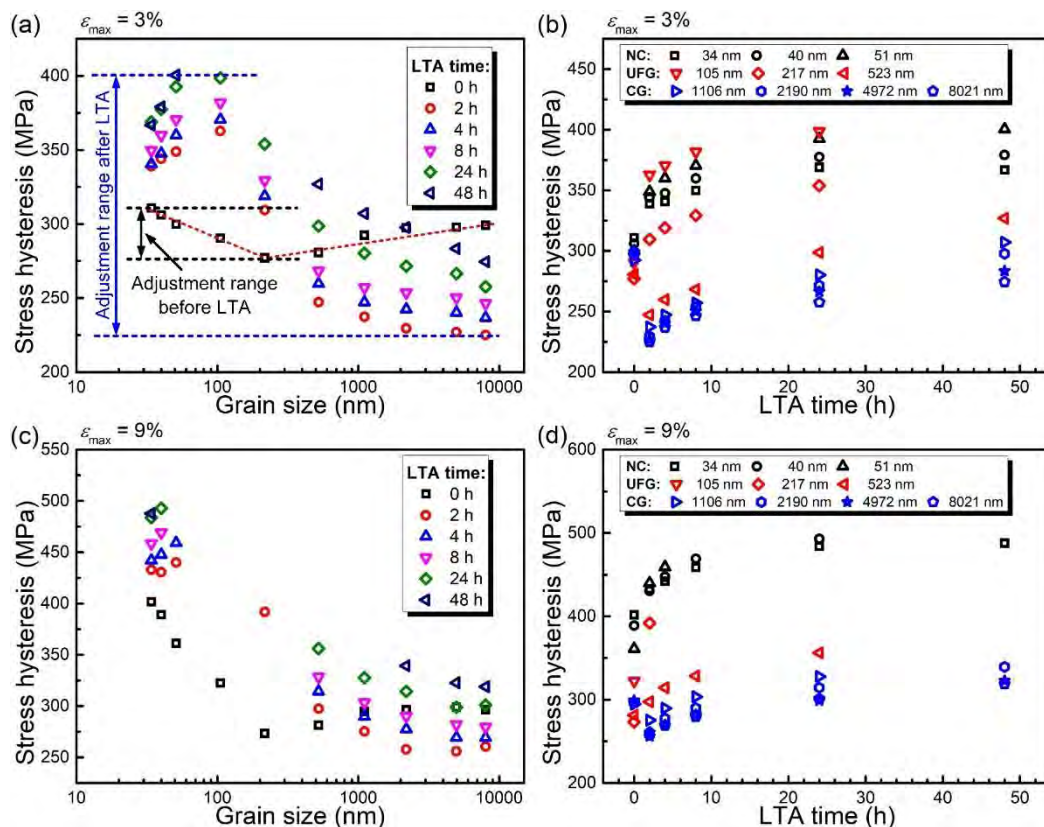


Fig. 5.9 Variations of stress hysteresis with (a) grain size and (b) LTA time under the maximum applied strain of 3%, and that with (c) grain size and (d) LTA time under the maximum applied strain of 9%.

5.3.3.5 Residual strain

The residual strain of NiTi alloys after subjected to loading-unloading deformation usually consists of dislocation slip, R-phase reorientation, incomplete stress-induced R→B2 transformation, incomplete stress-induced B19'→B2(R) transformation. The variations of residual strain with grain size and LTA time under 3% and the maximum applied strain of 9% are shown in **Fig. 5.10**.

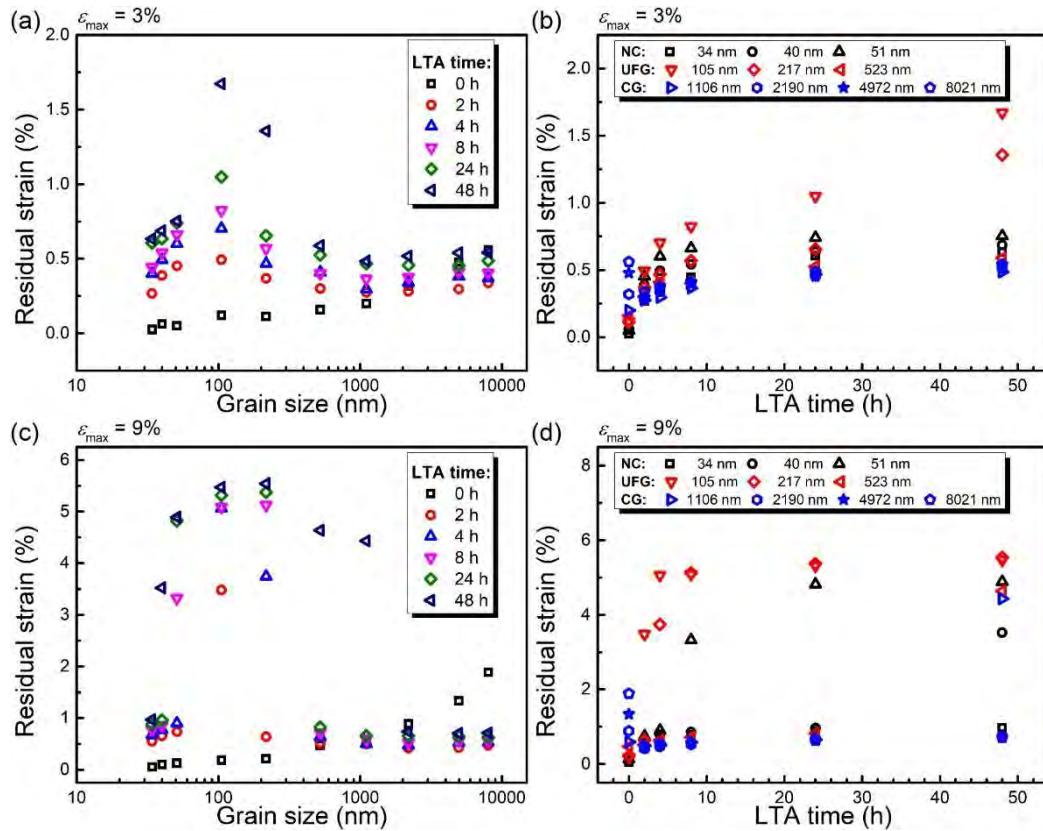


Fig. 5.10 Variations of residual strain with (a) grain size and (b) LTA time under the maximum applied strain of 3%, and that with (c) grain size and (d) LTA time under the maximum applied strain of 9%.

As shown in **Fig. 5.10(a)**, under the maximum applied strain of 3%, before LTA, the residual strain increases with grain size. After LTA, the residual strain of a part of CG NiTi alloys decreases, which is attributed to the suppression of dislocation slip induced by LTA. The rest of the NiTi alloys increases residual strain, which is due to the incomplete stress-induced R→B2 transformation during unloading. The residual strain first increases and then decreases with the increasing grain size, which reaches its maximum within grain size of 105-217 nm. This is because of the incomplete stress-induced B19'→R transformation plateau deformation during unloading. As shown in **Fig. 5.10(b)**, the residual strain increases with LTA time, which is due to the increasing R→B2 transformation temperature with LTA time (The larger R→B2 transformation temperature than the superelasticity testing temperature they present, the less stress-induced R→B2 transformation they proceed during unloading, and consequently the larger residual strain they show).

Under the maximum applied strain of 9%, the NiTi alloys are subjected to post-plateau deformation stage after LTA, and the stress hysteresis consequently remarkably increases. Some of the NiTi alloys do not finish the unloading plateau deformation, thus they present larger residual stains than those under the maximum applied strain of 3%, as shown in **Fig. 5.10(c)**. On the other hand, for the NiTi alloys with the same grain size, residual strain increases with LTA time, as shown in **Fig. 5.10(d)**.

5.3.3.6 Elastic modulus of post-plateau deformation

Under the maximum applied strain of 9%, the NiTi alloys are subjected to post-plateau deformation after LTA, and this deformation can be approximately regarded as linear deformation. Therefore, the stress-strain curves of post-plateau

deformation stage are linearly fitted, and the slope of the linear fitting is regarded as the elastic modulus of post-plateau deformation, as shown in the figure “Schematic plot of superelastic indices” at the beginning of this study.

As shown in **Fig. 5.11(a)** and (b), the elastic modulus of post-plateau deformation is sensitive to grain size whilst insensitive to LTA time. Within grain size of 34-105 nm, the elastic modulus of post-plateau deformation remains at a relatively high level, which is about 21000-22000 MPa. Within grain size of 105-8021 nm, the elastic modulus of post-plateau deformation rapidly decreases with the increasing grain size.

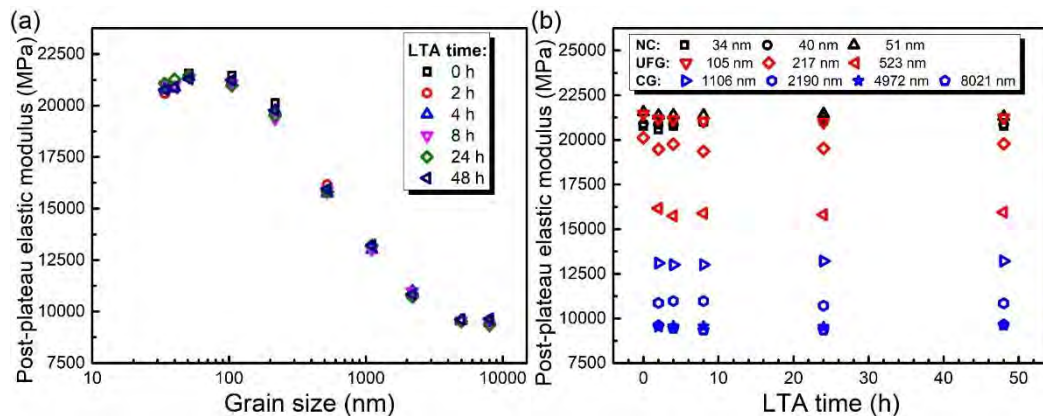


Fig. 5.11 Variation of the elastic modulus of post-plateau deformation with (a) grain size and (b) LTA time.

When grain size is within NC scale, dislocation activities are generally suppressed [199, 218], the post-plateau deformation mainly consists of elastic deformation of grain boundaries and the elastic deformation of B19' martensite phase [46]. The elastic modulus of the elastic deformation of grain boundaries can be referred by the elastic modulus of the amorphous phase, which is about 93000 MPa [35]. Thus, the value is larger than that of B19' martensite phase, which is about 18000 MPa

[219]. Therefore, the combination of the elastic deformation of grain boundaries and B19' martensite phase presented larger elastic modulus than that of the pure B19' martensite phase. As the grain size further increases from NC to UFG and to CG scale, the grain boundary volume fraction drastically decreases, and the influence of the elastic deformation of grain boundaries is consequently weakened. Therefore, the elastic modulus of post-plateau deformation mainly reflects the influence of elastic deformation and reorientation of B19' martensite phase, and the further transformation of residual B2 and R-phase, which leads to the decrease of the elastic modulus of post-plateau deformation with the increasing grain size.

5.4 Mechanisms of the influence of LTA on superelasticity

The LTA presents different influences on the superelasticity of the NiTi alloys of different grain sizes. The underlying mechanisms can be explained by the different microstructural evolutions, as shown in **Fig. 5.12**.

In the NC NiTi alloys, the matrix mainly consists of nanograins. The nanograin size suppresses the Ni_4Ti_3 precipitation during LTA. In the meanwhile, a small portion of ultrafine grains also exists in the NiTi matrix, and Ni_4Ti_3 can precipitate in these UFG grains, as shown in **Fig. 5.12**. As the average grain size increases, the volume fraction of these grains increases, and the suppression of Ni_4Ti_3 precipitation is consequently weakened. The influence of the Ni_4Ti_3 nanoprecipitates on superelasticity gradually increases. In addition, grain boundaries segregation of the solution atoms happen in NiTi alloys [220]. The high grain boundary volume fraction of NC matrix is beneficial for the segregation of

the saturated Ni on the grain boundaries [212]. Therefore, the Ni content increases on the grain boundaries whilst decreases within the grain inners with the increasing LTA time. In the NC NiTi alloys, the grain boundary segregation stabilizes the grain boundaries [212], which increases the energy dissipation when the phase transformation frontiers pass through the grain boundaries. Therefore, the loading plateau stress and plateau strain decrease whilst the stress hysteresis increases with LTA time.

Within the UFG NiTi alloys, it can be obviously observed the Ni_4Ti_3 nanoprecipitates in grains with size above 150 nm, and the corresponding SAED pattern verifies this observation, as shown in **Fig. 4.12**. Therefore, it can be concluded that there is a critical grain size, smaller than 150 nm, which suppresses Ni_4Ti_3 precipitation if grain size is smaller than this value whilst permits Ni_4Ti_3 precipitation if grain size is larger than this value. This further indicates that within the most of UFG grain size scale, LTA can induce Ni_4Ti_3 precipitation. Such precipitation, on one hand, reduces the Ni concentration in the NiTi fraction, and, on the other hand, reduces the volume fraction of transformable material. In the meanwhile, the UFG grain size is preserved after LTA, which leads to that the propagations of phase transformation frontiers are impeded by both the high volume fraction of grain boundary and the densely distributed Ni_4Ti_3 nanoprecipitates within grain inners, and consequently elevate the dissipated energy. The superelasticity of UFG NiTi alloys presents the most remarkable variations after LTA, which presents the largest decrease of loading plateau stress, the smallest plateau strain, and the largest stress hysteresis.

Within the CG NiTi alloys, the density and the volume fraction of grain boundary are the lowest compared with those in NC and UFG NiTi alloys. After LTA, numerous Ni₄Ti₃ nanoprecipitates with size of 7-15 nm emerge in the NiTi matrix. The size of the precipitates does not show an obvious increase, whilst the density of the precipitates increases with LTA time. The nanoprecipitates are always coherent with the NiTi matrix, as shown in **Fig. 4.12**. Such nanoprecipitates can effectively reduce the Ni concentration within NiTi matrix [143], and introduce elastic strain field around the precipitates [144]. This leads to the decrease of loading plateau stress and the variation of stress-induced phase transformation sequence from B2↔B19' to B2↔R↔B19'. Such nanoprecipitates can also effectively elevate the resistance of dislocation activities [48], which leads to the decrease of stress hysteresis and residual strain after LTA. With the increasing LTA time, the density of Ni₄Ti₃ increases, which elevates the energy dissipation during superelastic deformation and consequently leads to the increase of stress hysteresis.

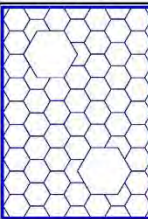
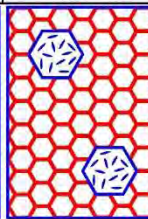
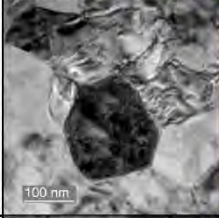
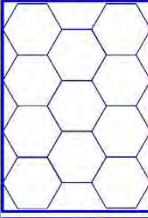
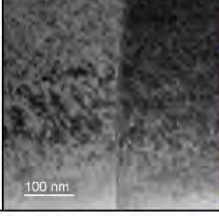
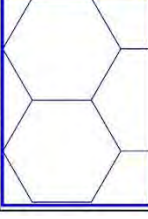
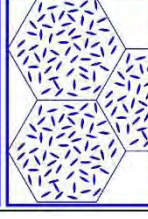
	Microstructure after LTA	Schematic illustration		Mechanisms for the influence of LTA on superelasticity with different grain size
		Before LTA	After LTA	
NC				After LTA, Ni ₄ Ti ₃ precipitation was suppressed in the predominant nanograins but happened in the small number of ultrafine grains in the NC NiTi alloys. Meanwhile, high grain boundary volume fraction facilitated grain boundary segregation further leading to Ni depletion. Thus, loading plateau stress and strain decreased but stress hysteresis increased moderately.
UFG				After LTA, Ni ₄ Ti ₃ precipitation proceeded in the predominant ultrafine grains and numerous Ni ₄ Ti ₃ nanoprecipitates existed within grain inner, which led to Ni depletion in the matrix. In addition, the high grain boundary volume fraction further reduced the volume fraction of transformable material. Thus, loading plateau stress and strain decreased but stress hysteresis increased remarkably.
CG				After LTA, Ni ₄ Ti ₃ precipitation proceeded in the predominant coarse grains leading to Ni depletion in the matrix and the elevation of dislocation resistance. The small grain boundary volume fraction seldom affected the functional properties. Thus, loading plateau stress decreased moderately, plateau strain decreased remarkably, and stress hysteresis first decreased then increased with LTA time.

Fig. 5.12 Comparisons of the mechanisms for the influences of LTA on superelasticity of the NiTi alloys with different grain sizes.

5.5 Increase of the maximum loading stress and stress hysteresis

It can be found from the experimental results that, regardless of grain size or LTA time, the increase of the maximum loading stress inevitably decreases the unloading plateau stress and increases the stress hysteresis, as schematically shown in **Fig. 5.13** (where σ_{ips} is loading plateau stress, σ_{ulps0} is the unloading plateau stress when it unloads within plateau deformation stage, $\sigma_{\text{hysteresis0}}$ is the stress hysteresis when it unloads within plateau deformation stage, σ_{max} is the maximum loading stress). If the unloading happens within the plateau deformation stage, the unloading plateau stress is σ_{ulps0} , then the stress hysteresis keeps

unchanged ($\sigma_{\text{hysteresis0}} = \sigma_{\text{ips}} - \sigma_{\text{ulps0}}$). If the unloading happens within the post-plateau deformation stage, with the maximum loading stress increasing to σ_{max1} , σ_{max2} , and σ_{max3} respectively, the stress hysteresis then correspondingly increases to $\sigma_{\text{hysteresis1}}$, $\sigma_{\text{hysteresis2}}$, and $\sigma_{\text{hysteresis3}}$ respectively. The previous studies [192, 215, 221, 222] also found similar phenomena in NiTi alloys under different grain sizes and aging conditions, which indicates its ubiquity during superelastic deformation.

This study investigates the unloading deformation under 3% and the maximum applied strain of 9%, i.e., unloading within plateau deformation stage and post-plateau deformation stage, respectively, and it covers the grain size from NC to CG scale and LTA time range from 0 h to 48 h. This section analyzes the relationship among the four indices including the maximum loading stress, the loading plateau stress, the unloading plateau stress, and the stress hysteresis. The experimental results show that the increment of the maximum loading stress (the difference between the maximum loading stress σ_{max} and the loading plateau stress σ_{ips}) presents approximate linear relation with the increment of stress hysteresis (the decrease of unloading plateau stress ($\sigma_{\text{ulps0}} - \sigma_{\text{ulps}}$)), as shown in **Fig.**

5.14.

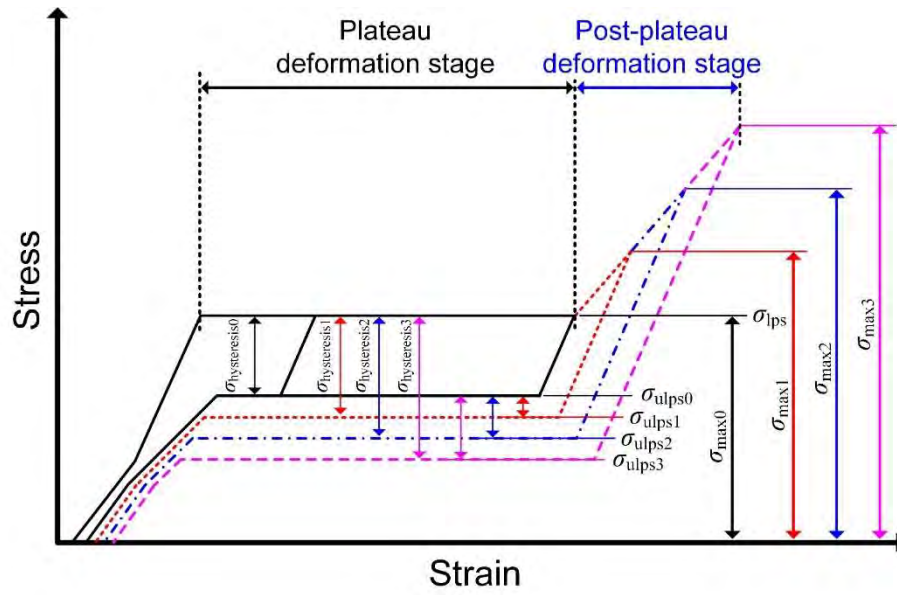


Fig. 5.13 Schematically illustration of the relationship between the increase of the maximum loading stress and the increase of stress hysteresis

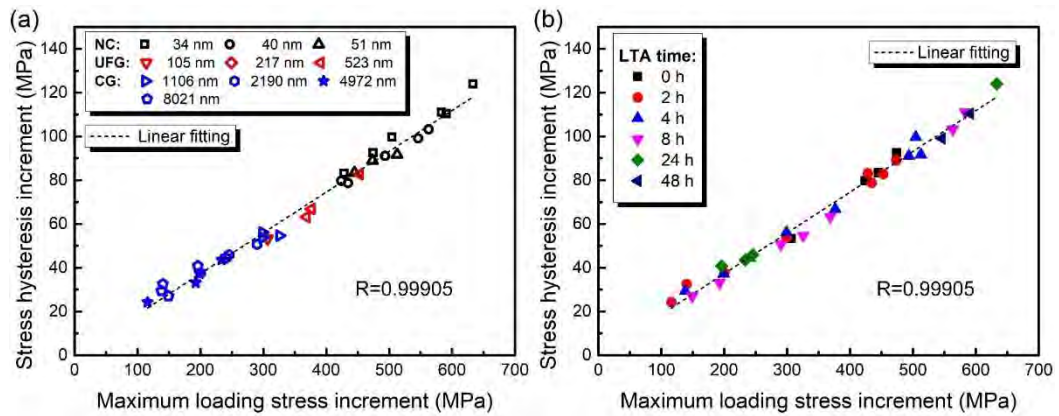


Fig. 5.14 The approximate linear relation between the stress hysteresis increment and the maximum loading stress increment

This approximate linear relation is expressed as Eq. (5.1) of which the correlation coefficient R was 0.99905.

$$\sigma_{ulps} = -0.186 \cdot (\sigma_{max} - \sigma_{lps}) + \sigma_{ulps0} \quad (\varepsilon_{mf} < \varepsilon_{max} \leq 9\%) \quad (5.1)$$

where σ_{ulps} is the unloading plateau stress that unloads within post-plateau deformation stage, σ_{ulps0} is the unloading plateau stress that unloads within

plateau deformation stage, σ_{\max} is the maximum loading stress, σ_{lps} is the loading plateau stress, ε_{\max} is the maximum applied strain, ε_{mf} is the strain at which plateau deformation finished. It is obvious that Eq. (5.1) is fit for the unloading within the post-plateau stage. Based on the current experimental results and those from previous studies [192, 215, 221, 222], if the unloading happens within plateau deformation stage, the unloading plateau stress generally keeps unchanged according to the characteristics of Lüders-like deformation. Therefore, it can be obtained combining with Eq. (5.1) that

$$\sigma_{\text{ulps}} = \begin{cases} -0.186 \cdot (\sigma_{\max} - \sigma_{\text{lps}}) + \sigma_{\text{ulps}0} & (\varepsilon_{\text{mf}} < \varepsilon_{\max} \leq 9\%) \\ \sigma_{\text{ulps}0} & (\varepsilon_{\text{ms}} \leq \varepsilon_{\max} \leq \varepsilon_{\text{mf}}) \end{cases} \quad (5.2)$$

where ε_{ms} is the strain at which the plateau deformation starts. Because stress hysteresis is the difference between loading plateau stress and unloading plateau stress, Eq. (5.2) can thus be obtained as:

$$\sigma_{\text{hysteresis}} = \sigma_{\text{lps}} - \sigma_{\text{ulps}} = \begin{cases} \sigma_{\text{lps}} - \sigma_{\text{ulps}0} + 0.186 \cdot (\sigma_{\max} - \sigma_{\text{lps}}) & (\varepsilon_{\text{mf}} < \varepsilon_{\max} \leq 9\%) \\ \sigma_{\text{lps}} - \sigma_{\text{ulps}0} & (\varepsilon_{\text{ms}} \leq \varepsilon_{\max} \leq \varepsilon_{\text{mf}}) \end{cases} \quad (5.3)$$

Then the relationship between the increment of stress hysteresis and the increment of the maximum loading stress is obtained as follows:

$$\Delta\sigma_{\text{hysteresis}} = \sigma_{\text{hysteresis}} - \sigma_{\text{hysteresis}0} = \begin{cases} 0.186 \cdot (\sigma_{\max} - \sigma_{\text{lps}}) & (\varepsilon_{\text{mf}} < \varepsilon_{\max} \leq 9\%) \\ 0 & (\varepsilon_{\text{ms}} \leq \varepsilon_{\max} \leq \varepsilon_{\text{mf}}) \end{cases} \quad (5.4)$$

Thus, it can be obtained from Eq. (5.2) and (5.4) that, if it unloads within plateau deformation stage, the unloading plateau stress and stress hysteresis keeps unchanged. However, when it unloads within the post-plateau deformation stage, the difference between the maximum loading stress and the loading plateau stress increasing per 1 MPa, then the unloading plateau stress will decrease about 0.186

MPa, and the stress hysteresis will consequently decrease about 0.186 MPa. The function of Eq. (5.2) and (5.4) may facilitate the design and application of NiTi components and parts that based on stress hysteresis.

5.6 Stress hysteresis model considering the effect of LTA time and grain size

The stress hysteresis reflects the energy dissipation during superelastic deformation, which represents the damping capacity of the materials during loading-unloading deformation. This superelastic index is widely used in civil engineering [223, 224]. As shown in **Fig. 5.9**, before LTA, even though the grain size is varied, the corresponding variation of stress hysteresis is within a narrow range. After LTA, however, the stress hysteresis can be adjusted within a much larger range. Under the maximum applied strain of 3%, all the NiTi alloys present complete superelasticity after LTA and unload within the plateau deformation stage. Considering the Lüders-like deformation characteristics, the stress hysteresis generally keeps unchanged as long as the unloading happened within plateau deformation stage. Therefore, the stress hysteresis under the maximum applied strain of 3% can be regarded as the stress hysteresis that after the unloading within plateau deformation stage. Thus, the model of such stress hysteresis considering the effect of grain size and LTA time is to be established as follows:

$$\sigma_{\text{hysteresis}} = f(D, t_{\text{LTA}}) \quad (\varepsilon_{\text{ms}} \leq \varepsilon_{\text{max}} \leq \varepsilon_{\text{mf}}) \quad (5.5)$$

where $\sigma_{\text{hysteresis}}$ is the stress hysteresis unloading within plateau deformation stage,

D is grain size, and t_{LTA} is the LTA time at 573 K.

The data points of stress hysteresis under the maximum applied strain of 3% are divided into two datasets, by random, i.e., the modeling dataset (45 data points) and the verification dataset (15 data points), and the detailed division is shown in **Table 5.1**.

Table 5.1 Division of modeling dataset and verification dataset

LTA time (h)	Grain size (nm)									
	34	40	51	105	217	523	1106	2190	4972	8021
0	○	(3)	○	○	○	(9)	○	○	○	○
2	○	○	○	(7)	○	(10)	○	○	(13)	○
4	(1)	○	○	○	○	○	○	○	(14)	○
8	○	(4)	○	○	(8)	○	○	○	○	(15)
24	(2)	○	(6)	○	○	○	○	(12)	○	○
48	○	(5)	○	○	○	○	(11)	○	○	○

○ Modeling dataset; (1)~(15) Verification dataset

According to the modeling dataset, by using the method described in section 4.6 of chapter 4, based on the superposition principle [214], the model is constructed as follows:

$$\sigma_{\text{hysteresis}} = \begin{cases} a(D) \cdot (t_{\text{LTA}} - 2)^{n(D)} + c(D) & (2 \leq t_{\text{LTA}} \leq 48) \\ k(D) \cdot (t_{\text{LTA}} - 2) + c(D) & (0 \leq t_{\text{LTA}} < 2) \end{cases} \quad (\varepsilon_{\text{ms}} \leq \varepsilon_{\text{max}} \leq \varepsilon_{\text{mf}}) \quad (5.6)$$

where $a(D)$, $n(D)$, $c(D)$, and $k(D)$ are the functions of grain size D , they are respectively as follows:

$$a(D) = \exp(a_1 \cdot \log D + a_2) + a_3 \quad (5.7)$$

$$n(D) = n_1 + n_2 \cdot \log_{10} D + n_3 \log_{10}^2 D \quad (5.8)$$

$$c(D) = \begin{cases} \exp(-c_1 \cdot (\log D - 2.02) + c_2) + c_3 & (105 \leq D \leq 8021 \text{ nm}) \\ c_4 \cdot (\log D - 2.02) + \exp(c_2) + c_3 & (34 \leq D \leq 105 \text{ nm}) \end{cases} \quad (5.9)$$

$$k(D) = \begin{cases} \exp(-k_1 \cdot (\log D - 2.02) + k_2) + k_3 & (105 \leq D \leq 8021 \text{ nm}) \\ k_4 \cdot (\log D - 2.02) + \exp(k_2) + k_3 & (34 \leq D \leq 105 \text{ nm}) \end{cases} \quad (5.10)$$

where $a_1 \sim a_3$, $n_1 \sim n_3$, $c_1 \sim c_4$, and $k_1 \sim k_4$ are the parameters of the model, the values of these parameters are shown in **Table 5.2**.

The surface of the obtained model is shown in **Fig. 5.15(a)**, and the model can depict the variations of the stress hysteresis with the increasing grain size and LTA time. The correlation between the calculated values and the experimental values of the verification dataset is shown in **Fig. 5.15(b)** where the correlation coefficient R is 0.99444 and the AARE(%) is 1.40%. **Fig. 5.16** depicts the comparison of the experimental values and the calculated values of the verification dataset of the stress hysteresis. Within the stress hysteresis range of 226.91 to 392.67 MPa, the maximum absolute error is 12.37 MPa, and the maximum relative error is 3.15%. It thus can be summarized that the obtained model can be used to calculate the stress hysteresis, unloaded within plateau deformation stage, of the NiTi alloys with grain size from 34 nm to 8021 nm and LTA time from 0 h to 48 h

Table 5.2 The values of the parameters of the stress hysteresis model

Parameter	Value	Parameter	Value
a_1	2.14	n_1	-0.30
a_2	-6.35	n_2	0.72
a_3	6.14	n_3	-0.14
c_1	1.86	k_1	1.30
c_2	5.02	k_2	4.47
c_3	216.10	k_3	-48.01
c_4	58.58	k_4	51.04

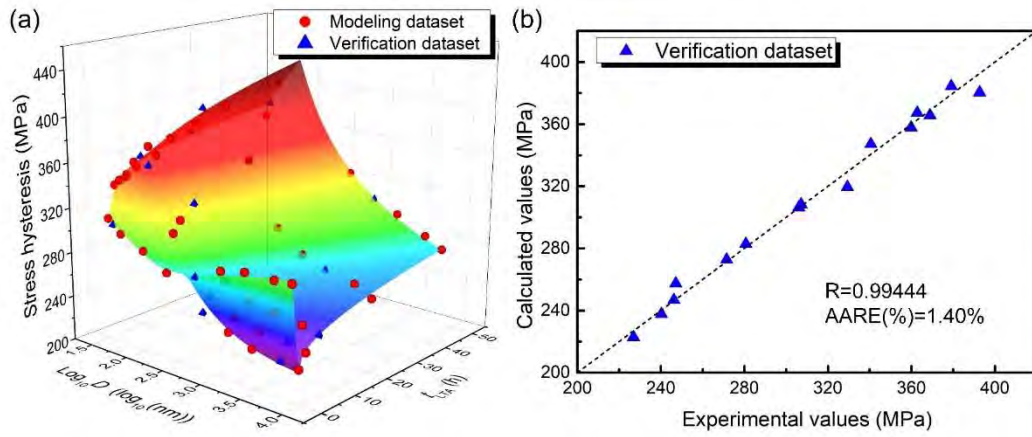


Fig. 5.15 The obtained stress hysteresis model: (a) modeling dataset, verification dataset, and the surface of the stress hysteresis model; (b) the correlation between the calculated values and the experimental values of the verification dataset.

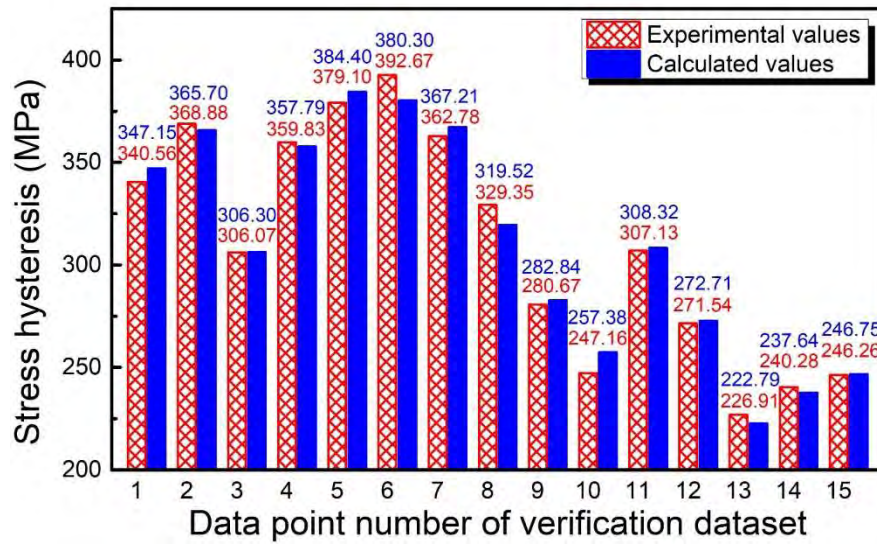


Fig. 5.16 Comparison of the experimental values and the calculated values of the verification dataset of the stress hysteresis

5.7 Summary

This chapter studies the influence of LTA of 0-48 h on the superelasticity of the NiTi with grain size of 34-8021 nm under the maximum applied strain of 3%-9%.

The following concluding remarks can thus be drawn:

- (1) Before LTA, with the increasing grain size, the elastic modulus increases, the loading plateau stress decreases, the residual strain increases, and the stress hysteresis first increases and then decreases of which the critical grain size was 217 nm. The underlying reasons are that, with the increasing grain size, the stress-induced B2→R transformation related deformation disappears, the grain size induced suppression of B2(R)→B19' transformation weakens, and the dislocation activities increase.
- (2) After LTA, under the maximum applied strain of 3%, all the NiTi alloys unload within plateau deformation stage. With the increasing LTA time, the loading and unloading plateau stress decrease, the stress hysteresis increases, the strain of B2→R transformation related deformation increases, and the residual strain increases. These variations are more remarkable within in the UFG NiTi alloys. Under the maximum applied strain of 9%, all the NiTi alloys unload within post-plateau deformation stage. With the increasing LTA time, the loading and unloading plateau stress decrease, the plateau strain decreases, the post-plateau strain increases, which further increases the stress hysteresis and consequently leads to the incomplete unloading plateau deformation of a part of the NiTi alloys. Similarly, these variations are more prominent in the UFG NiTi alloys.

(3) LTA presents different effects on superelasticity of the NiTi alloys with different grain sizes, and the underlying reasons are the different microstructural evolutions. The NC NiTi alloys are mainly influenced by the high grain boundary volume fraction. Ni₄Ti₃ precipitation is suppressed by nanograin size, and the grain boundary segregation is enhanced. Only a few ultrafine grains within the NC matrix can precipitate Ni₄Ti₃. The UFG NiTi alloys are simultaneously influenced by the high grain boundary volume fraction and the densely distributed Ni₄Ti₃ nanoprecipitates with size of 7-15 nm. The volume fraction of transformable material decreases and consequently leads to the shortest plateau strain. The relatively high grain boundary volume fraction and the numerous Ni₄Ti₃ nanoprecipitates remarkably increases the energy dissipation of stress-induced B2(R)↔B19' transformation, which leads to the UFG NiTi alloys presenting highest stress hysteresis. The CG NiTi alloys present lower grain boundary volume fraction, which is mainly influenced by the precipitates. The precipitates suppress dislocation activities within the grain inner and consequently decrease the stress hysteresis and residual strain. As the LTA time increases, the density of the precipitates increase, which increases the energy dissipation during superelastic deformation and consequently the stress hysteresis.

(4) According to the experimental findings, the increment of the maximum loading stress presents approximate linear relation with the increment of stress hysteresis. The function of these two variables is thus obtained. When the NiTi alloys unload within the post-plateau deformation stage, the maximum

loading stress increases per 1 MPa, then the stress hysteresis correspondingly increases 0.186 MPa. This function may facilitate the design and application of the NiTi functional parts and components based on stress hysteresis.

- (5) LTA remarkably expands the adjustment range of stress hysteresis. Unloading within plateau deformation stage, the adjustment range of stress hysteresis increases from 38 MPa (275-313 MPa) to 175 MPa (225-400 MPa), which increases by 460%. This finding may facilitate the engineering application of NiTi alloys from the aspect of damping. Hereby, the stress hysteresis model considering the effects of grain size and LTA time is obtained. The model can be used to calculate the stress hysteresis, unloaded within plateau deformation stage, of the NiTi alloys with grain size of 34-8021 nm under the LTA time of 0-48 h, which may also facilitate the design and application of NiTi parts and components based on stress hysteresis.

Chapter 6 Superelastic stress-strain model considering the effects of LTA and grain size

6.1 Introduction

Based on the results of chapter 5, the superelasticity of the NiTi alloys remarkably varies with LTA time and grain size, and the variations of superelasticity indices are complicated with the two factors. Therefore, based on Graesser superelastic stress-strain model, this chapter is to establish a superelastic stress-strain model that considering the effect of LTA time and grain size. The model is to be used for the calculation of superelastic stress-strain curves of the NiTi alloys with different grain sizes and LTA time, which may facilitate the design and adjustment of the superelastic stress-strain relations of the NiTi parts and components with different grain sizes under LTA.

6.2 Graesser model

Among numerous superelastic stress-strain model, Graesser model is one of the macroscopic phenomenological models with the characteristics of classical viscoplasticity theory [170]. The model is with relative simple mathematical structure, which induces the concept of back stress to describe the Stress-strain hysteresis. The parameters of the model are relatively easy for calibration. It is thus widely used in civil engineering [225, 226]. Some scholars have modified the

model [225, 227-229] and established modified models that described the post-plateau deformation [228], functional degeneration [225], and the effect of strain rate [229], etc. Since the superelastic indices of the NiTi alloys present complicated variations with grain size and LTA time, Graesser model is chosen as the model framework and is used to establish the modified model that can describe superelastic stress-strain relation under certain grain size and LTA time. After that, the parameters of the modified Graesser model are regarded as functions of grain size and LTA time, and they are formulated based on the modeling dataset from the experimental results of chapter 5. Finally, the superelastic stress-strain model that considering the effects of LTA time and grain size is obtained by substituting the parameter functions into the main framework.

6.2.1 Mathematical formulation of the Graesser model

The mathematical structure of Graesser model [170] is as follows:

$$\dot{\sigma} = E_A \left[\dot{\varepsilon} - |\dot{\varepsilon}| \left(\frac{\sigma - \beta}{Y} \right)^n \right] \quad (6.1)$$

where $\dot{\sigma}$ is engineering stress rate, $\dot{\varepsilon}$ is engineering strain rate, E_A is the elastic modulus of austenite phase, β is one dimension back stress, Y is the nominal yield stress (the stress required for activating B2→B19' transformation), and n is a material constant (the value was prescribed as a positive odd number). It is worth noting that, though the Graesser model is written as rate form, this is for calculation but not for the description of the relationship between superelasticity and strain rate [170].

The expression of β in Eq. (6.1) is as follows [170]:

$$\beta = E_A \alpha \left\{ \varepsilon - \frac{\sigma}{E_A} + f_T |\varepsilon|^c \operatorname{erf}(a\varepsilon) [u(-\varepsilon\dot{\varepsilon})] \right\} \quad (6.2)$$

where $\alpha = E_{AM} / (E_A - E_{AM})$, E_{AM} is the modulus of B2(R)→B19' transformation plateau. Thus, when the slope of the plateau is nearly equal to 0 as the case of this study, α can be prescribed as a small positive number representing the small modulus. f_T , c , a are material constants. $\operatorname{erf}(x)$ and $u(x)$ represent the error function and unit step function respectively of which the expressions are as follows:

$$\operatorname{erf}(x) = \frac{2}{\sqrt{\pi}} \int_0^x e^{-t^2} dt \quad (6.3)$$

$$u(x) = \begin{cases} 1 & x \geq 0 \\ 0 & x < 0 \end{cases} \quad (6.4)$$

Besides, it is prescribed the applied stress was 0 when the strain is 0, as shown in Eq. (6.5):

$$\sigma = 0 \Big|_{\varepsilon=0} \quad (6.5)$$

The superelastic stress-strain curve calculated by this model is shown in **Fig. 6.1**. As can be seen in the figure, Graesser can also describe the superelasticity when the strain is negative. According to Eq. (6.1) and (6.2), it can be known that at a given strain increment, the corresponding stress increment is mainly influenced by E_A , σ , and β . The stress-strain hysteresis during loading-unloading is described by the term $f_T |\varepsilon|^c \operatorname{erf}(a\varepsilon) [u(-\varepsilon\dot{\varepsilon})]$ in Eq. (6.2). According to Eq. (6.4), this term equal to 0 during loading, and equal to $f_T |\varepsilon|^c \operatorname{erf}(a\varepsilon)$ during unloading. Therefore, based on Eq. (6.2), the back stress β is larger during unloading than

that during loading, which consequently realizes the description of stress-strain hysteresis during loading-unloading deformation.

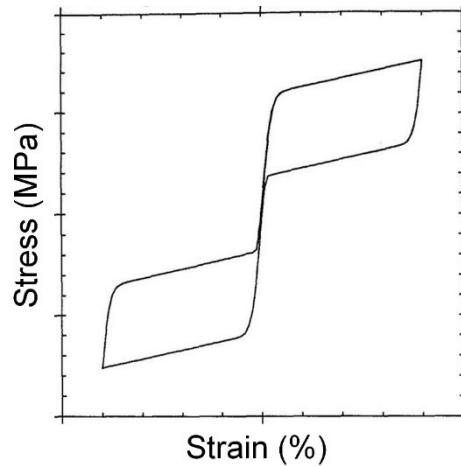


Fig. 6.1 The superelastic stress-strain curves calculated by Graesser model [170].

6.2.2 Influence of the parameters of the Graesser model on superelastic stress-strain curves

The Graesser model includes four main material parameters, which are f_T , n , c , and a respectively. Based on the study of Z.H. Zhang et al [228], the influences of the four parameters on the superelastic stress-strain curve are shown in **Fig. 6.2**. The f_T determines the magnitude of stress hysteresis; the n describes the transition between elastic deformation stage to plateau deformation stage (the smaller the n was; the smoother the transition is, and the faster the calculation speed of this model is); the c determines the unloading plateau stress and the slope of unloading plateau (the larger the c is, the smaller unloading plateau stress and the larger slope of the unloading plateau it is); the a determines the finish of unloading plateau deformation which affects the residual strain after unloading (the larger the a is, the smaller residual strain it is).

Besides, though the influences of other parameters of the Graesser model on superelasticity are not provided here in **Fig. 6.2**, however, according to Eq. (6.1) and (6.2), it is not difficult to know that other parameters also greatly affect the superelasticity. The E_A not only affects the elastic modulus during loading and unloading stage, but it also affects the slopes of loading and unloading plateau. The α not only affects the slopes of the loading and unloading plateau, but it also varies the unloading plateau stress. The Y not only affects the loading plateau stress, but it also affects the unloading plateau stress (the larger the Y is, the larger loading and unloading plateau stresses it is).

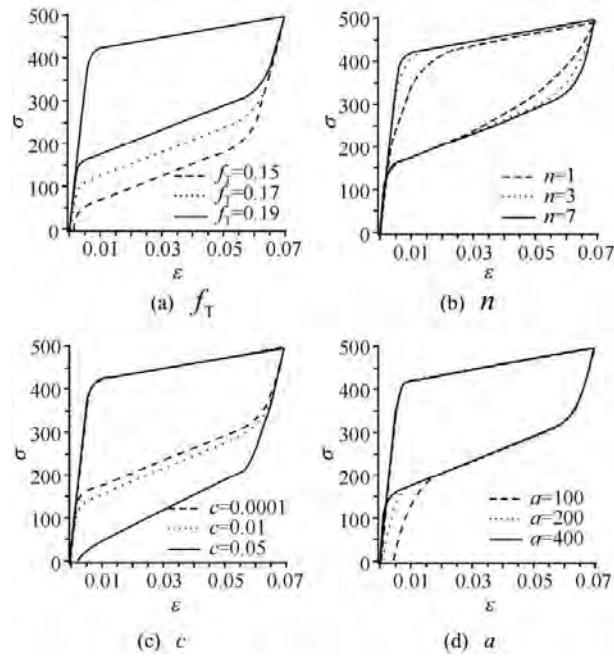


Fig. 6.2 Influence of the parameters on superelastic stress-strain curve [228]: (a)

f_T ; (b) n ; (c) c ; and (d) a .

It can be known from the above analyses that the influences of the parameters, including f_T , n , c , a , E_A , α , and Y , on superelastic stress-strain curves are not

independently, e.g., f_T and c can both affect the unloading plateau stress. Therefore, it is difficult to obtain the one-to-one relationship between the superelastic indices and the parameters.

6.2.3 Limitation of the Graesser model

Though the relative simple mathematical structure and the small number of parameters, the Graesser model exists some limitations:

- (1) The influences of the parameters of the Graesser model on superelastic indices are not independent, which is difficult for the calibration of parameters when an actual superelastic stress-strain is given.
- (2) The Graesser model is only fit for unloading within plateau deformation stage, which cannot describe the loading within the post-plateau deformation and the corresponding unloading, as shown in **Fig. 6.3**.
- (3) The Graesser model is only fit for the superelasticity based on stress-induced $B2 \leftrightarrow B19'$ transformation of which the initial elastic deformation is generally linear. However, in practical scenarios, superelasticity based on $B2 \leftrightarrow R \leftrightarrow B19'$ transformation also exists no matter it is induced by coherent Ni_4Ti_3 precipitates or by nanograin size, as shown in **Fig. 6.3**. The $B2 \leftrightarrow R$ transformation related deformation before reaching $B2(R) \leftrightarrow B19'$ transformation plateau is generally non-linear, which is consequently difficult to be described by the Graesser model.
- (4) The Graesser model cannot describe the influences of grain size and LTA time on superelastic stress-strain curve.

Therefore, this study is to suggest a modified Graesser model which is to avoid the aforementioned disadvantages and finally establishes a superelastic stress-strain model considering the effects of grain size and LTA time.

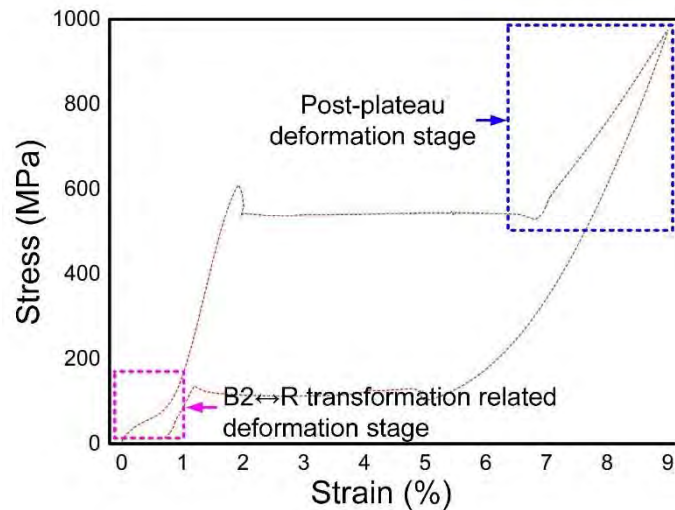


Fig. 6.3 The representative actual superelastic stress-strain curve.

6.3 The modified Graesser model

Based on the Graesser model, a modified model is suggested in this section to describe the superelastic stress-strain curve under certain given LTA time and grain size, which is prepared for the final establishment of the superelastic stress-strain model considering the effects of LTA time and grain size.

6.3.1 Mathematical formulation of the modified Graesser model

To overcome the aforementioned disadvantages, the following improvements are conducted:

- (1) The superelastic deformation is separated into two individual sections, i.e., the loading section and unloading section as referred by the previous study [228].

Additional parameters are used to make each parameter influence the corresponding superelasticity index respectively. This is for the preparation of the final model establishment.

- (2) Using an additional linear function to approximately represent the complicated B2↔R related non-linear deformations before the elastic deformation of B2 or R-phase during loading and after the elastic deformation of B2 or R-phase during unloading.
- (3) Using an additional linear function to approximately represent the loading stress-strain curves of the post-plateau deformation stage, as inspired by the previous study [228].

The detailed modifications are as follows. The loading section is further divided into (1) B2→R transformation related deformation stage, (2) B2 or R phase elastic deformation plus plateau deformation stage, and (3) post-plateau deformation stage. The corresponding mathematic structures are as follows:

- (1) B2→R transformation related deformation stage:

$$\dot{\sigma} = E_{\text{req}} \dot{\varepsilon} \quad (6.6)$$

where $\dot{\sigma}$ is engineering stress rate, $\dot{\varepsilon}$ is engineering strain rate, E_{req} is the effective elastic modulus of B2↔R transformation related deformation (the slope of the approximate linear function). It is noteworthy that the model is modified from Graesser model, thus the rate form expression is only for the ease of calculation, which does not mean that the model can describe the relation between superelastic stress-strain curve and strain rate.

- (2) B2 or R phase elastic deformation plus plateau deformation stage:

$$\dot{\sigma} = E_{\text{pre}} \dot{\varepsilon} \left\{ 1 - \left[\frac{\sigma - E_{\text{pre}} \alpha \left(\varepsilon - \frac{\sigma}{E_{\text{pre}}} \right)}{Y} \right]^n \right\} \quad (6.7)$$

where E_{pre} is the elastic modulus of B2 or R phase, which have experienced the B2 \leftrightarrow R transformation related deformation, σ is engineering stress, ε is engineering strain, α , n , and Y are material constants.

(3) Post-plateau deformation stage:

$$\dot{\sigma} = E_{\text{post}} \dot{\varepsilon} \quad (6.8)$$

where E_{post} is the elastic modulus of post-plateau deformation.

As similar as the loading section, the unloading section is further divided to (1) B19' phase elastic unloading deformation stage plus unloading plateau deformation stage, (2) B2 or R phase elastic unloading deformation stage, and (3) unloading R \rightarrow B2 transformation related deformation stage. The corresponding mathematic structures were as follows:

(1) B19' phase elastic unloading deformation stage plus unloading plateau deformation stage:

$$\dot{\sigma} = E_m \dot{\varepsilon} \left\{ 1 + \left[\frac{\sigma - E_{m0} \alpha \left(\varepsilon - \frac{\sigma}{E_{m0}} + f_T \varepsilon^c \operatorname{erf}(a\varepsilon) \right)}{Y_b} \right]^n \right\} \quad (6.9)$$

where E_m is the elastic modulus of B19' during unloading, E_{m0} , f_T , c , a , and Y_b are material constants.

(2) B2 or R phase elastic unloading deformation stage:

$$\dot{\sigma} = E_{\text{pre}} \dot{\varepsilon} \quad (6.10)$$

(3) unloading R→B2 transformation related deformation stage:

$$\dot{\sigma} = E_{\text{req}} \dot{\varepsilon} \quad (6.11)$$

The unit step function $u(x)$ is adopted to differentiate the loading and unloading sections. Based on Eq. (6.4), $u(\dot{\varepsilon})$ is 1 during loading and 0 during unloading, while $u(-\dot{\varepsilon})$ is 0 during loading and 1 during unloading. As inspired by the previous study [228], the state function U is adopted to differentiate different stages during loading and unloading. Thus, U_1 , U_2 , and U_3 are used to distinguish the three stages during loading, and U_4 , U_5 , and U_6 are used to distinguish the three stages during unloading, which are schematically shown in **Fig. 6.4**.

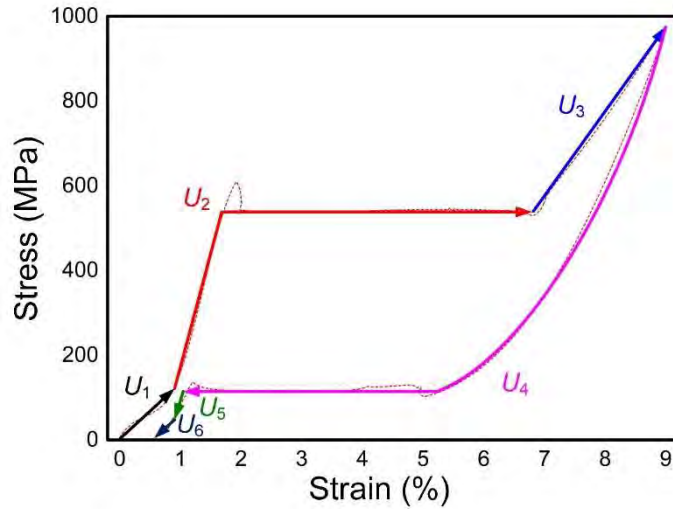


Fig. 6.4 Schematic illustration of the state functions of $U_1 \sim U_6$ and the corresponding superelastic stress-strain curve.

The expressions of U_1 , U_2 , and U_3 are shown in Eq. (6.12):

$$\begin{cases} U_1 + U_2 + U_3 = 1 \\ U_1 = \begin{cases} 1 & (0 \leq \varepsilon \leq \varepsilon_{\text{rf}}) \\ 0 & (\varepsilon_{\text{rf}} < \varepsilon) \end{cases} \\ U_2 = \begin{cases} 1 & (\varepsilon_{\text{rf}} < \varepsilon \leq \varepsilon_{\text{mf}}) \\ 0 & (\varepsilon_{\text{mf}} < \varepsilon \leq \varepsilon_{\text{max}}) \end{cases} \end{cases} \quad (6.12)$$

where ε_{rf} represents the strain at which the B2→R transformation related deformation finished, ε_{mf} is the strain at which B2(R)→B19' transformation plateau is complete, ε_{max} is the maximum applied strain. According to the experimental results of chapter 5, the B2→R transformation plateau stress is smaller than 100 MPa. Since linear function is adopted in this study to approximately represent B2↔R related deformation, 100 MPa is set as the critical stress. Below this critical stress, Eq. (6.6) is used to describe B2→R transformation related deformation; above this critical stress, Eq. (6.7) is used to describe the elastic deformation of B2 and R-phase, thus $\varepsilon_{\text{rf}}=100/E_{\text{req}}$ is obtained.

It can be known from Eq. (6.12) that U_1 is 1 within B2→R transformation related deformation stage, and it is 0 within other deformation stages; U_2 is 1 within B2 or R phase elastic deformation plus plateau deformation stage, and it is 0 within other deformation stages; U_3 is 1 within post-plateau deformation stage, and it is 0 within other deformation stages. Hereby, by combining Eq. (6.12), (6.4), and (6.6)~(6.8), the loading section of the modified model is obtained as follows:

$$\dot{\sigma} = u(\dot{\varepsilon})U_1E_{\text{req}}\dot{\varepsilon} + u(\dot{\varepsilon})U_2E_{\text{pre}}\dot{\varepsilon} \left\{ 1 - \left[\frac{\sigma - E_{\text{pre}}\alpha \left(\varepsilon - \frac{\sigma}{E_{\text{pre}}} \right)^n}{Y} \right] \right\} + u(\dot{\varepsilon})U_3E_{\text{post}}\dot{\varepsilon} \quad (6.13)$$

During unloading, based on the experimental results of chapter 5, if the residual strain is smaller than B2→R transformation strain, it indicates that the proceeding of R→B2 transformation. By contrast, if the residual strain is larger than B2→R transformation strain, it indicates that the R→B2 transformation does not proceed (when the R→B2 transformation temperature is higher than the superelasticity testing temperature, the R-phase cannot transform back to B2 phase after unloading). Thus, the unloading deformation only consists elastic deformation of R-phase other than the R→B2 transformation related deformation. Therefore, the relationship of U_4 , U_5 , and U_6 is determined into two situations:

When $\varepsilon_{\text{risd}} \leq \varepsilon_{\text{rrf}}$,

$$\left\{ \begin{array}{l} U_4 + U_5 + U_6 = 1 \\ U_4 = \left\{ \begin{array}{l} 1 \quad \left(\varepsilon_{\text{rrf}} + \frac{\sigma - \left(1 - \frac{\varepsilon_{\text{risd}}}{\varepsilon_{\text{rrf}}} \right) \cdot 100}{E_{\text{pre}}} \right) \leq \varepsilon \leq \varepsilon_{\text{max}} \\ 0 \quad \varepsilon < \left(\varepsilon_{\text{rrf}} + \frac{\sigma - \left(1 - \frac{\varepsilon_{\text{risd}}}{\varepsilon_{\text{rrf}}} \right) \cdot 100}{E_{\text{pre}}} \right) \end{array} \right. \\ U_5 = \left\{ \begin{array}{l} 1 \quad \varepsilon_{\text{rrf}} \leq \varepsilon \leq \left(\varepsilon_{\text{rrf}} + \frac{\sigma - \left(1 - \frac{\varepsilon_{\text{risd}}}{\varepsilon_{\text{rrf}}} \right) \cdot 100}{E_{\text{pre}}} \right) \\ 0 \quad 0 \leq \varepsilon < \varepsilon_{\text{rrf}} \end{array} \right. \end{array} \right. \quad (6.14)$$

and when $\varepsilon_{\text{risd}} > \varepsilon_{\text{rrf}}$,

$$\left. \begin{array}{l}
U_4 = \begin{cases} 1 & \left(\varepsilon_{\text{risd}} + \frac{\sigma}{E_{\text{pre}}} \right) \leq \varepsilon \leq \varepsilon_{\text{max}} \\
0 & \varepsilon < \left(\varepsilon_{\text{risd}} + \frac{\sigma}{E_{\text{pre}}} \right) \end{cases} \\
U_5 = \begin{cases} 1 & \varepsilon_{\text{risd}} \leq \varepsilon < \left(\varepsilon_{\text{risd}} + \frac{\sigma}{E_{\text{pre}}} \right) \\
0 & \left(\varepsilon_{\text{risd}} + \frac{\sigma}{E_{\text{pre}}} \right) \leq \varepsilon \leq \varepsilon_{\text{max}} \end{cases} \\
U_6 = 0
\end{array} \right\} \quad (6.15)$$

where $\varepsilon_{\text{risd}}$ is residual strain. U_4 is 1 within B19' phase elastic unloading deformation stage plus unloading plateau deformation stage, and it is 0 within other deformation stages; U_5 is 1 within B2 or R phase elastic unloading deformation stage, and it is 0 within other deformation stages; U_6 is 1 within unloading R→B2 transformation related deformation stage, and it is 0 within other deformation stages. Hereby, by combining Eq. (6.14), (6.15), and (6.9)~(6.11), the unloading section of the modified model is obtained as follows:

$$\begin{aligned}
\dot{\sigma} = & u(-\dot{\varepsilon})U_4E_m\dot{\varepsilon} \left\{ 1 + \left[\frac{\sigma - E_{m0}\alpha \left(\varepsilon - \frac{\sigma}{E_{m0}} + ft\varepsilon^c \operatorname{erf}(a\varepsilon) \right)}{Y_b} \right]^n \right\} \\
& + u(-\dot{\varepsilon})U_5E_{\text{pre}}\dot{\varepsilon} + u(-\dot{\varepsilon})U_6E_{\text{req}}\dot{\varepsilon}
\end{aligned} \quad (6.16)$$

Then, by combining Eq. (6.15) and (6.16), the complete modified Graesser model is obtained as shown by Eq. (6.17):

$$\begin{aligned}
\dot{\sigma} = & u(\dot{\varepsilon})U_1E_{\text{req}}\dot{\varepsilon} + u(\dot{\varepsilon})U_2E_{\text{pre}}\dot{\varepsilon} \left\{ 1 - \left[\frac{\sigma - E_{\text{pre}}\alpha \left(\varepsilon - \frac{\sigma}{E_{\text{pre}}} \right)}{Y} \right]^n \right\} + u(\dot{\varepsilon})U_3E_{\text{post}}\dot{\varepsilon} \\
& + u(-\dot{\varepsilon})U_4E_m\dot{\varepsilon} \left\{ 1 + \left[\frac{\sigma - E_{m0}\alpha \left(\varepsilon - \frac{\sigma}{E_{m0}} + ft\varepsilon^c \text{erf}(a\varepsilon) \right)}{Y_b} \right]^n \right\} + u(-\dot{\varepsilon})U_5E_{\text{pre}}\dot{\varepsilon}
\end{aligned} \tag{6.17}$$

where $\text{erf}(x) = \frac{2}{\sqrt{\pi}} \int_0^x e^{-t^2} dt$ and $u(x) = \begin{cases} 1 & x \geq 0 \\ 0 & x < 0 \end{cases}$, which are error function and unit step function, respectively, as shown in Eq. (6.3) and (6.4). The related state functions are Eq. (6.12), (6.14), and (6.15) respectively.

Since the stress is 0 MPa before superelastic deformation, the following initial value is prescribed:

$$\sigma = 0 \Big|_{\varepsilon=0} \tag{6.18}$$

By using the above established modified model to calculate superelastic stress-strain curve via programming in Matlab, a representative superelastic stress-strain curve is obtained as shown in **Fig. 6.5**. This indicates that the obtained model is able to describe the superelastic stress-strain curves considering the B2 \leftrightarrow R transformation related deformation stage and the post-deformation stage, as compared with **Fig. 6.3**.

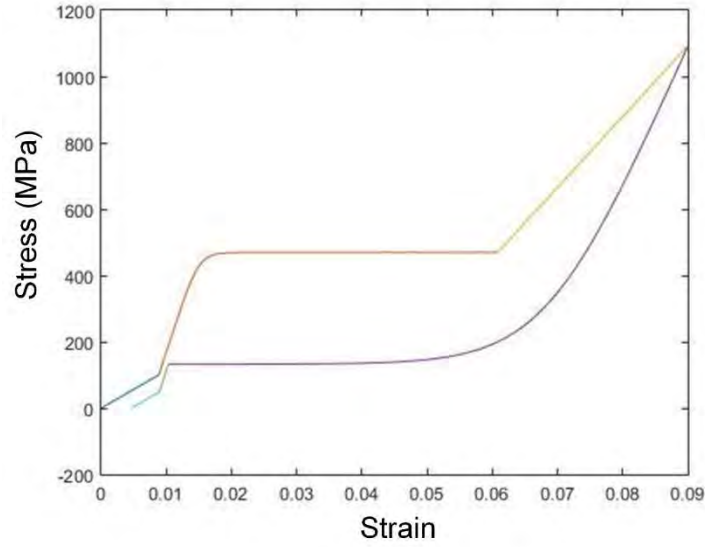


Fig. 6.5 The superelastic stress-strain curve calculated by the modified Graesser model.

6.3.2 Parameters of the modified Graesser model

In the above modified Graesser model, there are some parameters and material constants, which are Y_b , n , a , c , α , E_{m0} , E_{rreq} , E_{pre} , Y , ε_{mf} , E_{post} , E_m , f_T , and ε_{risd} . Among them, Y_b , n , a , c , α , and E_{m0} are material constants of which the values are shown in **Table 6.1**. The E_{rreq} , E_{pre} , Y , ε_{mf} , E_{post} , E_m , f_T , and ε_{risd} are parameters of the model of which the values can independently affect the shape of each section of the superelastic stress-strain curves, and the corresponding relation is shown in **Fig. 6.6**. When the grain size, LTA time, and the maximum applied strain are given, the values of the above model parameters are determined, and consequently the superelastic stress-strain curves.

Table 6.1 The list of the values and the prescribed functions of material constants and parameters of the modified Graesser model

Model constants / parameter	Value / function
Y_b	2000
n	$n = \begin{cases} 11 & (0 \leq \varepsilon_{\max} \leq 0.03) \\ 9 & (0.03 < \varepsilon_{\max} \leq 0.06) \\ 7 & (0.06 < \varepsilon_{\max} \leq 0.09) \end{cases}$
a	2000
c	0.0001 [225]
α	0.0001
E_{m0}	26233.159 [227]
E_{rreq}	$E_{\text{rreq}} = E_{\text{rreq}}(D, t_{\text{LTA}})$
E_{pre}	$E_{\text{pre}} = E_{\text{pre}}(D, t_{\text{LTA}})$
Y	$Y = Y(D, t_{\text{LTA}})$
ε_{mf}	$\varepsilon_{\text{mf}} = \varepsilon_{\text{mf}}(D, t_{\text{LTA}})$
E_{post}	$E_{\text{post}} = E_{\text{post}}(D, t_{\text{LTA}})$
E_m	$E_m = E_m(D, t_{\text{LTA}}, \varepsilon)$
f_t	$f_t = f_t(D, t_{\text{LTA}}, \varepsilon)$
$\varepsilon_{\text{risd}}$	$\varepsilon_{\text{risd}} = \varepsilon_{\text{risd}}(D, t_{\text{LTA}}, \varepsilon)$

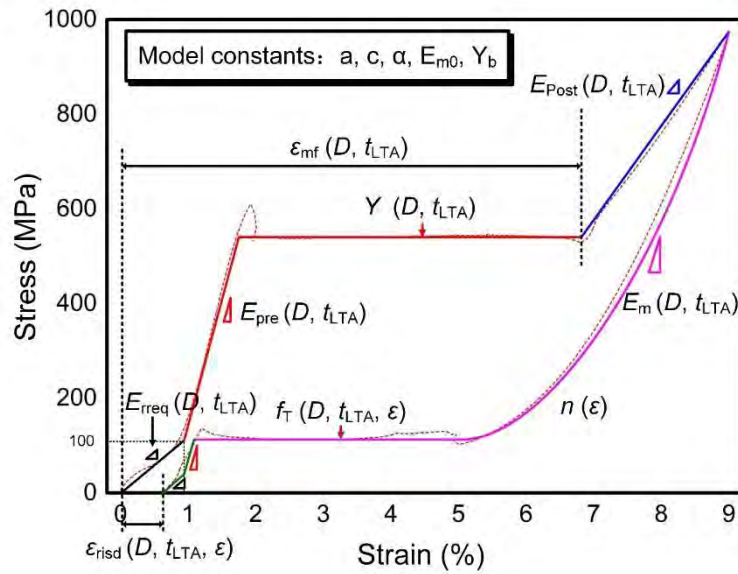


Fig. 6.6 Schematic illustration of the relationship between each section of superelastic stress-strain curves and the corresponding model parameters.

This chapter is to establish the superelastic stress-strain model considering the effect of LTA time and grain size, thus it can be realized by firstly establishing the functions of E_{req} , E_{pre} , Y , ε_{mf} , E_{post} , E_{m} , f_{T} , and $\varepsilon_{\text{risd}}$ about the two variables of LTA time t_{LTA} and Grain size D , as shown in **Table 6.1** (Since the maximum applied strain remarkably affected unloading elastic modulus, stress hysteresis, and residual strain, the parameters of E_{m} , f_{T} , and $\varepsilon_{\text{risd}}$ are not only affected by LTA time and grain size, but they are also influenced by the maximum applied strain. Thus, E_{m} , f_{T} , and $\varepsilon_{\text{risd}}$ are additionally as the functions of strain ε .). Secondly, by substituting these parameter functions into Eq. (6.17), the final superelastic stress-strain model considering the effects of LTA time and grain size can be finally obtained.

6.4 Superelastic stress-strain model considering the effects of LTA time and grain size

Based on the experimental results, the parameter functions (E_{req} , E_{pre} , Y , ε_{mf} , E_{post} , E_{m} , f_{T} , and $\varepsilon_{\text{risd}}$) about LTA time t_{LTA} and grain size D are to be established. There are respectively 60 independent stress-strain curves under the maximum applied strains of 3% and 9%. They are randomly divided into the modeling dataset (45 stress-strain curves under each maximum applied strain) and the verification dataset (15 stress-strain curves under each maximum applied strain). The detailed division of the modeling dataset and verification dataset is shown in **Table 6.2**.

Based on the modeling dataset, the parameter functions of E_{rreq} , E_{pre} , Y , ε_{mf} , E_{post} , E_m , f_T , and ε_{risd} about LTA time, grain size, and strain are respectively established as shown in the following subsections.

Table 6.2 Division of the modeling dataset and the verification dataset

LTA time (h)	Grain size (nm)									
	34	40	51	105	217	523	1106	2190	4972	8021
0	○	(3)	○	○	○	(9)	○	○	○	○
2	○	○	○	(7)	○	(10)	○	○	(13)	○
4	(1)	○	○	○	○	○	○	○	(14)	○
8	○	(4)	○	○	(8)	○	○	○	○	(15)
24	(2)	○	(6)	○	○	○	○	(12)	○	○
48	○	(5)	○	○	○	○	(11)	○	○	○

○ Modeling dataset; (1)–(15) Verification dataset.

6.4.1 E_{rreq} function

The E_{rreq} function about grain size D and LTA time t_{LTA} is to be established, as shown by Eq. (6.19). Based on the superelastic stress-strain curves in chapter 5, the modeling dataset and verification dataset of E_{rreq} are respectively calculated, as shown in **Fig. 6.7(a)**. As per the modeling dataset, based on the superposition principle [214], the function $E_{rreq}(D, t_{LTA})$ is obtained as shown by Eq. (6.20) and (6.21). The values of the parameters of E_{rreq} function are shown in **Table 6.3**. The surface of E_{rreq} function is shown in **Fig. 6.7(a)**. The verification dataset is used to verify the correlation and accuracy of the calculation results from E_{rreq} function. The correlation coefficient R is 0.99928, and the AARE(%) is 1.82%, as shown in **Fig. 6.7(b)**. This indicates that the obtained function can effectively calculate the parameter of E_{rreq} .

$$E_{rreq} = E_{rreq}(D, t_{LTA}) \quad (6.19)$$

$$E_{\text{rreq}}(D, t_{\text{LTA}}) = \begin{cases} \exp(-a(D) \cdot (t_{\text{LTA}} - 2)^{0.7} + b(D)) + c(D) & (t_{\text{LTA}} \geq 2) \\ k(D) \cdot (t_{\text{LTA}} - 2) + \exp(b(D)) + c(D) & (0 \leq t_{\text{LTA}} < 2) \end{cases} \quad (6.20)$$

$$\begin{cases} a(D) = \exp(a_{\text{Erreq1}} (\log_{10} D + a_{\text{Erreq2}})^2 + a_{\text{Erreq3}}) + a_{\text{Erreq4}} \\ b(D) = \exp(b_{\text{Erreq1}} (\log_{10} D + b_{\text{Erreq2}})^2 + b_{\text{Erreq3}}) + b_{\text{Erreq4}} \\ c(D) = \begin{cases} -\exp(c_{\text{Erreq1}} \cdot (\log_{10} D + c_{\text{Erreq2}})) + c_{\text{Erreq3}} & (\log_{10} D \geq c_{\text{Erreq6}}) \\ \left[\exp(c_{\text{Erreq4}} \cdot (\log_{10} D + c_{\text{Erreq5}})) - \exp(c_{\text{Erreq1}} \cdot (c_{\text{Erreq6}} + c_{\text{Erreq2}})) \right. \\ \left. - \exp(c_{\text{Erreq4}} \cdot (c_{\text{Erreq6}} + c_{\text{Erreq5}})) + c_{\text{Erreq3}} \right] & (1.53147 \leq \log_{10} D \leq c_{\text{Erreq6}}) \end{cases} \\ k(D) = \exp(-k_{\text{Erreq1}} \cdot \log_{10}^{k_{\text{Erreq4}}} D + k_{\text{Erreq2}}) + k_{\text{Erreq3}} \end{cases} \quad (6.21)$$

Table 6.3 The values of the parameters of E_{rreq} function

Parameter	Value	Parameter	Value
a_{Erreq1}	-9.95	c_{Erreq2}	-4.45
a_{Erreq2}	-2.01	c_{Erreq3}	13899.74
a_{Erreq3}	-0.98	c_{Erreq4}	0.93
a_{Erreq4}	0.19	c_{Erreq5}	5.65
b_{Erreq1}	-4.66	c_{Erreq6}	2.02
b_{Erreq2}	-1.82	k_{Erreq1}	0.73
b_{Erreq3}	-0.45	k_{Erreq2}	11.12
b_{Erreq4}	8.93	k_{Erreq3}	-30439.73
c_{Erreq1}	-3.22	k_{Erreq4}	1.17

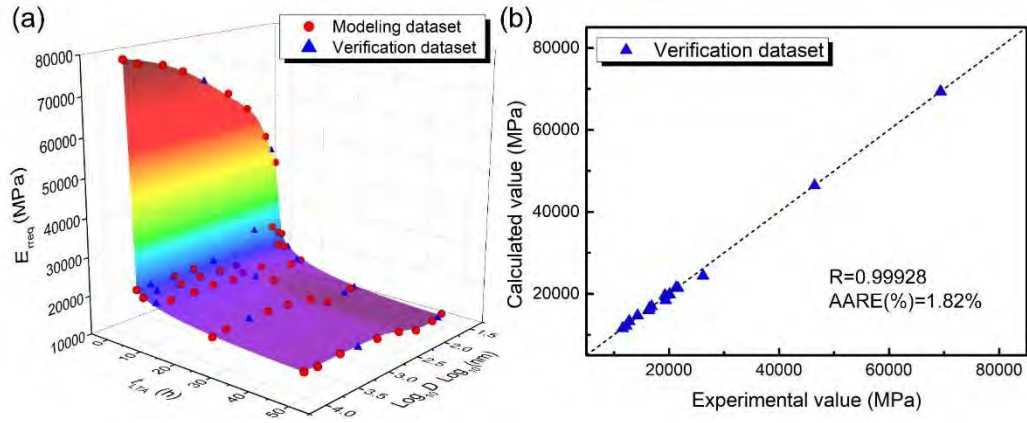


Fig. 6.7 The obtained E_{req} function: (a) modeling dataset, verification dataset, and the surface of E_{req} function; (b) the correlation between the calculated values and the experimental values of the verification dataset.

6.4.2 E_{pre} function

The E_{pre} function about grain size D and LTA time t_{LTA} is to be established, as shown by Eq. (6.22). Based on the superelastic stress-strain curves in chapter 5, the modeling dataset and verification dataset of E_{pre} are respectively calculated, as shown in **Fig. 6.8(a)**. As per the modeling dataset, based on the superposition principle [214], the function $E_{pre}(D, t_{LTA})$ is obtained as shown by Eq. (6.23) and (6.24). The values of the parameters of E_{pre} function are shown in **Table 6.4**. The surface of E_{pre} function is shown in **Fig. 6.8(a)**. The verification dataset is used to verify the correlation and accuracy of the calculation results from E_{pre} function. The correlation coefficient R is 0.99811, and the AARE(%) is 0.30%, as shown in **Fig. 6.8(b)**. This indicates that the obtained function can effectively calculate the parameter of E_{pre} .

$$E_{pre} = E_{pre}(D, t_{LTA}) \quad (6.22)$$

$$E_{pre} = E_{pre}(D, t_{LTA}) = a_{Epre}(D) \cdot \exp(-d_{Epre}(t_{LTA} + b_{Epre})) + c_{Epre} \quad (6.23)$$

$$a_{Epre} = a_{Epre1} \log_{10}(\log_{10} D + a_{Epre2}) + a_{Epre3} \quad (6.24)$$

Table 6.4 The values of the parameters of E_{pre} function

Parameter	Value	Parameter	Value
a_{Epre1}	36240.04	b_{Epre}	1.13
a_{Epre2}	-1.26	c_{Epre}	59970.97
a_{Epre3}	3667.36		

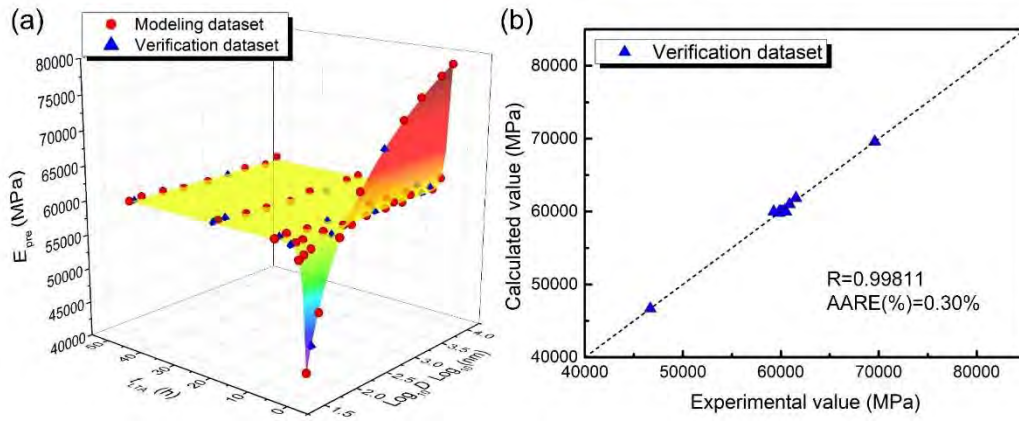


Fig. 6.8 The obtained E_{pre} function: (a) modeling dataset, verification dataset, and the surface of E_{pre} function; (b) the correlation between the calculated values and the experimental values of the verification dataset.

6.4.3 Y function

The Y function about grain size D and LTA time t_{LTA} is to be established, as shown by Eq. (6.25). Based on the loading plateau stress shown in section 5.3.3.1, the modeling dataset and verification dataset of Y are respectively obtained, as shown in Fig. 6.9(a). As per the modeling dataset, based on the superposition principle [214], the function $Y(D, t_{LTA})$ is obtained as shown by Eq. (6.26) and (6.27).

The values of the parameters of Y function are shown in **Table 6.5**. The surface of Y function is shown in **Fig. 6.9(a)**. The verification dataset is used to verify the correlation and accuracy of the calculation results from Y function. The correlation coefficient R is 0.99749, and the AARE(%) is 0.98%, as shown in **Fig. 6.9(b)**. This indicates that the obtained function can effectively calculate the parameter of Y .

$$Y = Y(D, t_{LTA}) \quad (6.25)$$

$$Y(D, t_{LTA}) = a_Y \cdot \exp(-b_Y \cdot \log_{10} D) + c_Y \quad (6.26)$$

$$\begin{cases} a_Y = a_{Y1} \log_{10}(t_{LTA} + a_{Y4}) + \frac{a_{Y2}}{t_{LTA} + a_{Y4}} + a_{Y3} \\ b_Y = b_{Y1} \log_{10}(t_{LTA} + b_{Y4}) + \frac{b_{Y2}}{t_{LTA} + b_{Y4}} + b_{Y3} \\ c_Y = c_{Y1} \log_{10}(t_{LTA} + c_{Y4}) + \frac{c_{Y2}}{t_{LTA} + c_{Y4}} + c_{Y3} \end{cases} \quad (6.27)$$

Table 6.5 The values of the parameters of Y function

Parameter	Value	Parameter	Value
a_{Y1}	-5917.19	b_{Y3}	3.18
a_{Y2}	-31552.83	b_{Y4}	0.75
a_{Y3}	15010.63	c_{Y1}	-35.74
a_{Y4}	2.65	c_{Y2}	-26.58
b_{Y1}	-0.63	c_{Y3}	405.30
b_{Y2}	-2.27	c_{Y4}	0.09

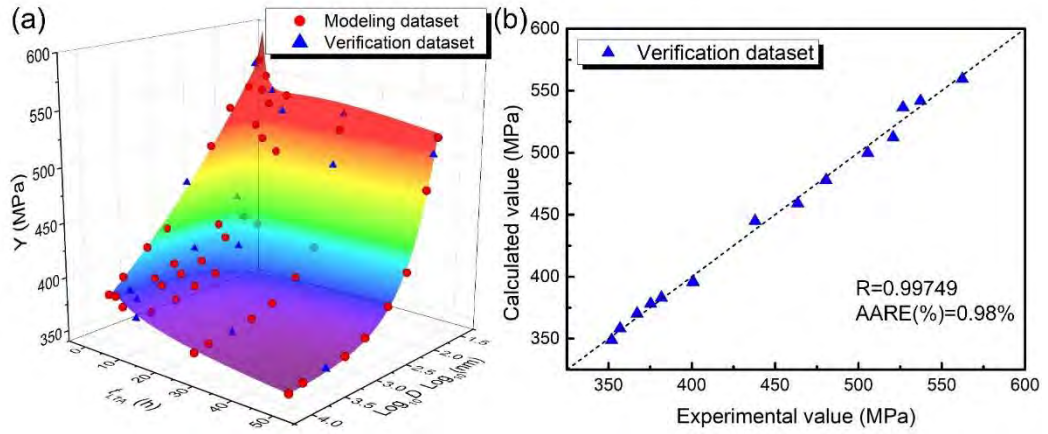


Fig. 6.9 The obtained Y function: (a) modeling dataset, verification dataset, and the surface of Y function; (b) the correlation between the calculated values and the experimental values of the verification dataset.

6.4.4 ε_{mf} function

The ε_{mf} function about grain size D and LTA time t_{LTA} is to be established, as shown by Eq. (6.28). Based on the plateau deformation finishing strain as shown in section 5.3.2, the modeling dataset and verification dataset of ε_{mf} are respectively obtained, as shown in **Fig. 6.10(a)**. As per the modeling dataset, based on the superposition principle [214], the function $\varepsilon_{mf}(D, t_{LTA})$ is obtained as shown by Eq. (6.29). The values of the parameters of ε_{mf} function are shown in **Table 6.6**. The surface of ε_{mf} function is shown in **Fig. 6.10(a)**. The verification dataset is used to verify the correlation and accuracy of the calculation results from ε_{mf} function. The correlation coefficient R is 0.96590, and the AARE(%) is 1.29%, as shown in **Fig. 6.10(b)**. This indicates that the obtained function can effectively calculate the parameter of ε_{mf} .

$$\varepsilon_{mf} = \varepsilon_{mf}(D, t_{LTA}) \quad (6.28)$$

$$\begin{cases} \varepsilon_{mf} = a_{emf} \exp(-b_{emf} \cdot t_{LTA}^{0.5}) + b_{emf} \\ a_{emf} = a_{emf1} \sin[a_{emf2} (\log_{10} D + a_{emf3})] + a_{emf4} \\ b_{emf} = b_{emf1} \sin[b_{emf2} (\log_{10} D + b_{emf3})] + b_{emf4} \\ c_{emf} = c_{emf1} \sin[c_{emf2} (\log_{10} D + c_{emf3})] + c_{emf4} \end{cases} \quad (6.29)$$

Table 6.6 The values of the parameters of ε_{mf} function

Parameter	Value	Parameter	Value
a_{emf1}	-3.42	b_{emf3}	0.57
a_{emf2}	3.15	b_{emf4}	1.38
a_{emf3}	0.97	c_{emf1}	0.35
a_{emf4}	0.66	c_{emf2}	-3.07
b_{emf1}	-0.66	c_{emf3}	6.19
b_{emf2}	0.38	c_{emf4}	1.79

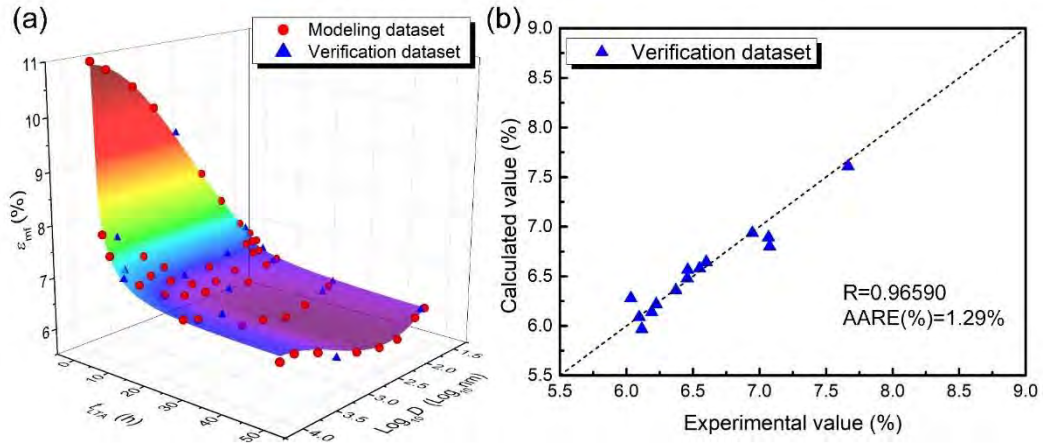


Fig. 6.10 The obtained ε_{mf} function: (a) modeling dataset, verification dataset, and the surface of ε_{mf} function; (b) the correlation between the calculated values and the experimental values of the verification dataset.

6.4.5 E_{post} function

The E_{post} function about grain size D and LTA time t_{LTA} is to be established, as shown by Eq. (6.30). Based on the post-plateau deformation elastic modulus as shown in section 5.3.3.6, the modeling dataset and verification dataset of E_{post} are

respectively measured, as shown in **Fig. 6.11(a)**. As per the modeling dataset, based on the superposition principle [214], the function $E_{\text{post}}(D, t_{\text{LTA}})$ is obtained as shown by Eq. (6.31). The values of the parameters of E_{post} function are shown in **Table 6.7**. The surface of E_{post} function is shown in **Fig. 6.11(a)**. The verification dataset is used to verify the correlation and accuracy of the calculation results from E_{post} function. The correlation coefficient R is 0.99963, and the AARE(%) is 0.76%, as shown in **Fig. 6.11(b)**. This indicates that the obtained function can effectively calculate the parameter of E_{post} .

$$E_{\text{post}} = E_{\text{post}}(D, t_{\text{LTA}}) \quad (6.30)$$

$$E_{\text{post}} = a_{\text{Epost}} \sin \left[d_{\text{Epost}} (\log_{10} D + b_{\text{Epost}}) \right] + c_{\text{Epost}} \quad (6.31)$$

Table 6.7 The values of the parameters of E_{post} function

Parameter	Value	Parameter	Value
a_{Epost}	6005.37	c_{Epost}	15433.88
b_{Epost}	-0.84	d_{Epost}	1.61

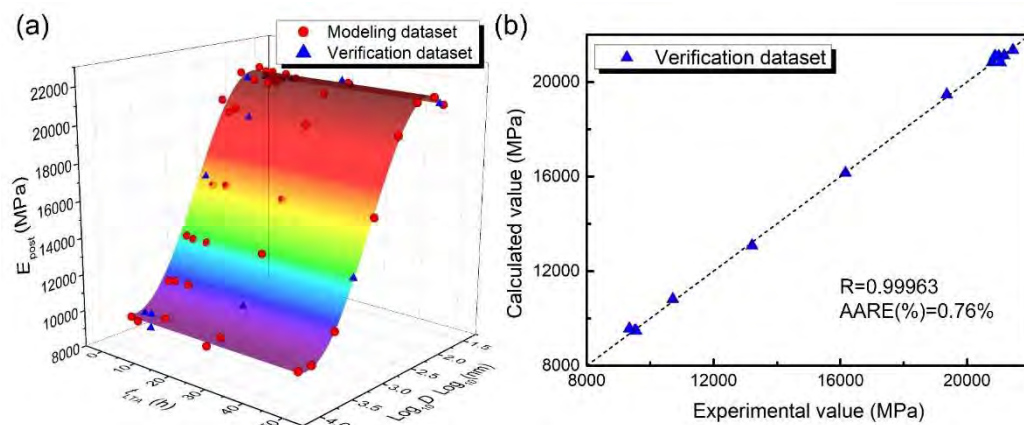


Fig. 6.11 The obtained E_{post} function: (a) modeling dataset, verification dataset, and the surface of E_{post} function; (b) the correlation between the calculated values and the experimental values of the verification dataset.

6.4.6 E_m function

Based on the study [228], the E_m presents linear relation with the maximum applied strain. The smaller the maximum applied strain is, the value of E_m is closer to that of E_{pre} . Therefore, in order to establish E_m function about strain ε , grain size D , and LTA time t_{LTA} , The E_{m0} function (the E_m function under the maximum applied strain of 9% was prescribed as E_{m0}) about grain size D and LTA time t_{LTA} should be first established. Then the E_m function about E_{m0} and ε is established, as shown by Eq. (6.32).

Based on the stress-strain curves under the maximum applied strain of 9% as shown in section 5.3.2, the modeling dataset and verification dataset of E_{m0} are respectively measured, as shown in **Fig. 6.12(a)**. As per the modeling dataset, based on the superposition principle [214], the function $E_{m0}(D, t_{LTA})$ is obtained as shown by Eq. (6.33). The values of the parameters of E_{m0} function are shown in **Table 6.8**. The surface of E_{m0} function is shown in **Fig. 6.12(a)**. The verification dataset is used to verify the correlation and accuracy of the calculation results from E_{m0} function. The correlation coefficient R is 0.99918, and the AARE(%) is 1.05%, as shown in **Fig. 6.12(b)**. This indicates that the obtained function can effectively calculate the parameter of E_{m0} .

$$E_m = E_m(D, t_{LTA}, \varepsilon) = E_m(E_{m0}(D, t_{LTA}), \varepsilon) \quad (6.32)$$

$$\left\{ \begin{array}{l} E_{m0} = \frac{d_{Em}}{1 + \exp(a_{Em} \cdot \log_{10} D + b_{Em})} + c_{Em} \\ a_{Em} = a_{Em1} \cdot t_{LTA} + a_{Em2} \\ b_{Em} = b_{Em1} \cdot t_{LTA} + b_{Em2} \\ c_{Em} = c_{Em1} \cdot t_{LTA} + c_{Em2} \\ d_{Em} = d_{Em1} \cdot t_{LTA} + d_{Em2} \end{array} \right. \quad (6.33)$$

Table 6.8 The values of the parameters of E_{m0} function

Parameter	Value	Parameter	Value
a_{Em1}	-0.03	c_{Em1}	-5.60
a_{Em2}	-2.49	c_{Em2}	44502.68
b_{Em1}	0.08	d_{Em1}	105.66
b_{Em2}	6.67	d_{Em2}	-22673.51

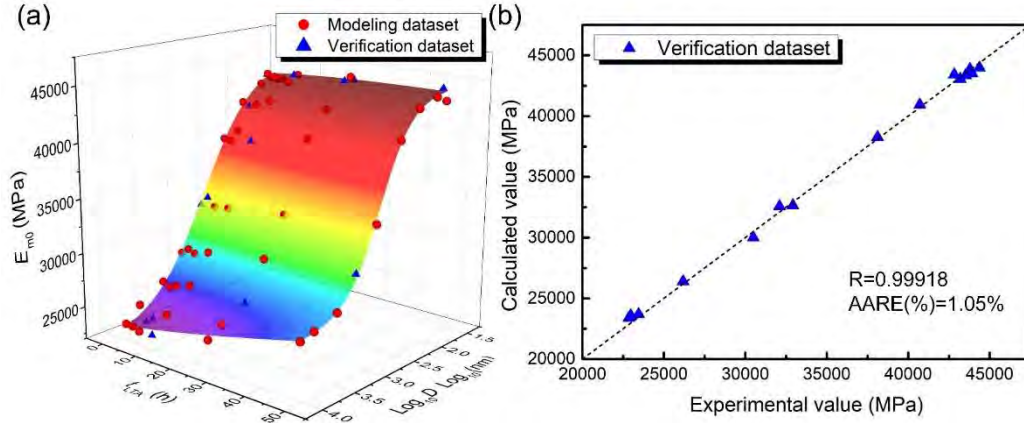


Fig. 6.12 The obtained E_{m0} function: (a) modeling dataset, verification dataset, and the surface of E_{m0} function; (b) the correlation between the calculated values and the experimental values of the verification dataset.

Based on the obtained E_{m0} function, further establish E_m function about E_{m0} and ε . As aforementioned, E_m presents linear relation with the maximum applied strain [228], the E_m is finally obtained as shown in Eq. (6.34):

$$E_m(D, t_{LTA}, \varepsilon) = \frac{E_{m0}(D, t_{LTA}) - E_{pre}(D, t_{LTA})}{0.09} \cdot \varepsilon + E_{pre}(D, t_{LTA}) \quad (6.34)$$

where $E_{m0}(D, t_{LTA})$ and $E_{pre}(D, t_{LTA})$ are respectively shown in Eq. (6.33) and (6.23).

6.4.7 f_T function

6.4.7.1 The relation between f_T and σ_{ulps}

In this model, when the material constants Y_b , α , and c are determined, the f_T can independently control the unloading plateau stress of the superelastic stress-strain curves. It is noteworthy that f_T itself is not the unloading plateau stress σ_{ulps} , but it is a function of σ_{ulps} , as shown in **Fig. 6.13**, and the function is shown by Eq. (6.35):

$$f_T = f_T(\sigma_{ulps}) = k\sigma_{ulps} + b = 0.382 \cdot \sigma_{ulps} + 762.51 \quad (6.35)$$

Therefore, to establish f_T function about ε , D , and t_{LTA} , it first needs to establish σ_{ulps} function about ε , D , and t_{LTA} .

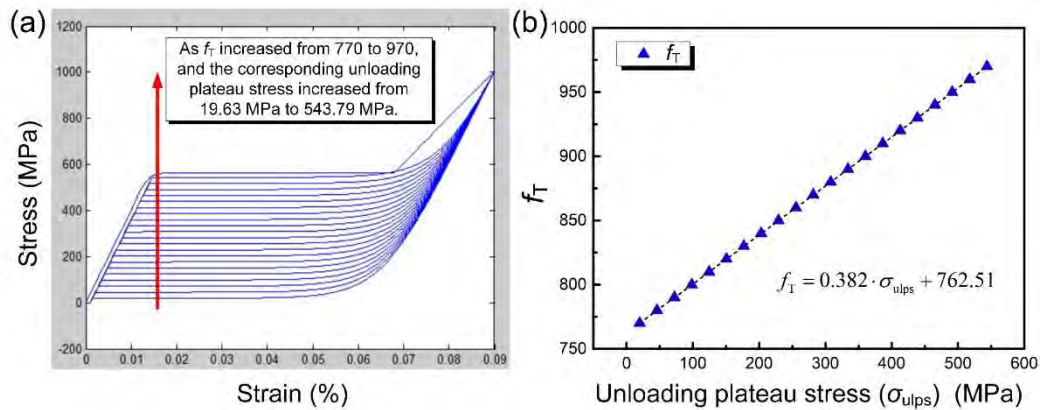


Fig. 6.13 Relation between f_T and σ_{ulps} : (a) σ_{ulps} increased from 19.63 MPa to 543.79 MPa with f_T increasing from 770 to 970; (b) linear relation between f_T and σ_{ulps} .

6.4.7.2 σ_{ulps} function about D , t_{LTA} , and ε

Based on the experimental results of chapter 5 and Eq. (5.2), when the unloading happens within the plateau deformation stage, the unloading plateau stress keeps unchanged with strain; when the unloading happens within the post-plateau

deformation stage, unloading plateau stress decreases with increasing maximum loading stress. After reaching the plateau deformation stage, the maximum loading stress is the function of ε , Y , and E_{post} , as shown by Eq. (6.36):

$$\sigma_{\text{max}} = \begin{cases} Y + E_{\text{post}} \cdot (\varepsilon - \varepsilon_{\text{mf}}) & (\varepsilon_{\text{mf}} < \varepsilon_{\text{max}} \leq 9\%) \\ Y & (\varepsilon_{\text{ms}} \leq \varepsilon \leq \varepsilon_{\text{mf}}) \end{cases} \quad (6.36)$$

where, ε_{ms} is the starting strain of the plateau deformation stage. By combining Eq. (5.2) and (6.36), the following equation can be obtained:

$$\sigma_{\text{ulps}} = \begin{cases} -0.1863 \cdot (E_{\text{post}} \cdot (\varepsilon - \varepsilon_{\text{mf}})) + \sigma_{\text{ulps0}} & (\varepsilon_{\text{mf}} < \varepsilon_{\text{max}} \leq 9\%) \\ \sigma_{\text{ulps0}} & (\varepsilon_{\text{ms}} \leq \varepsilon_{\text{max}} \leq \varepsilon_{\text{mf}}) \end{cases} \quad (6.37)$$

where σ_{ulps0} is the unloading plateau stress unloaded within plateau deformation stage, which is the function of D , t_{LTA} , and ε . Therefore, to establish σ_{ulps} function about ε , D , and t_{LTA} , it first needs to establish σ_{ulps0} function about D , and t_{LTA} , as shown in Eq. (6.38).

$$\sigma_{\text{ulps}}(D, t_{\text{LTA}}, \varepsilon) = \sigma_{\text{ulps}}(\sigma_{\text{ulps0}}(D, t_{\text{LTA}}), \varepsilon) \quad (6.38)$$

According to the unloading plateau stress under the maximum applied strain of 3% (corresponding to unloading within plateau deformation stage) shown in section 5.3.3.3., the modeling dataset and verification dataset of σ_{ulps0} are respectively measured, as shown in **Fig. 6.14(a)**. As per the modeling dataset, based on the superposition principle [214], the function $\sigma_{\text{ulps0}}(D, t_{\text{LTA}})$ is obtained as shown by Eq. (6.39) and (6.40). The values of the parameters of σ_{ulps0} function are shown in **Table 6.9**. The surface of σ_{ulps0} function is shown in **Fig. 6.14(a)**. The verification dataset is used to verify the correlation and accuracy of the calculation results from σ_{ulps0} function. The correlation coefficient R is 0.99831, and the

AARE(%) is 2.27%, as shown in **Fig. 6.14(b)**. This indicates that the obtained function can effectively calculate the parameter of σ_{ulps0} .

$$\sigma_{ulps0}(D, t_{LTA}) = \begin{cases} \exp[-a(D) \cdot (t_{LTA} - 2)^{0.6} + b(D)] + c(D) & (t_{LTA} \geq 2) \\ k(D) \cdot (t_{LTA} - 2) + \exp[b(D)] + c(D) & (0 \leq t_{LTA} < 2) \end{cases} \quad (6.39)$$

$$\begin{cases} a(D) = a_{ft5} \cdot \sin[\exp(-a_{ft1} \cdot (\log_{10} D + a_{ft2})) + a_{ft3}] + a_{ft4} \\ b(D) = \exp[-b_{ft1} \cdot ((\log_{10} D + b_{ft2})^2)^{b_{ft5}} + b_{ft3}] + b_{ft4} \\ c(D) = -\exp[-c_{ft1} \cdot ((\log_{10} D + c_{ft2})^2)^{c_{ft5}} + c_{ft3}] + c_{ft4} \\ k(D) = k_{ft5} \cdot \sin[\exp(-k_{ft1} \cdot (\log_{10} D + k_{ft2})) + k_{ft3}] + k_{ft4} \end{cases} \quad (6.40)$$

Table 6.9 The values of the parameters of σ_{ulps0} function

Parameter	Value	Parameter	Value
a_{ft1}	2.95	c_{ft1}	0.26
a_{ft2}	-1.81	c_{ft2}	-3.02
a_{ft3}	2.06	c_{ft3}	6.45
a_{ft4}	0.13	c_{ft4}	357.95
a_{ft5}	-0.11	c_{ft5}	1.77
b_{ft1}	0.29	k_{ft1}	0.78
b_{ft2}	-3.17	k_{ft2}	-3.68
b_{ft3}	0.81	k_{ft3}	0.97
b_{ft4}	3.81	k_{ft4}	-20.01
b_{ft5}	1.78	k_{ft5}	54.43

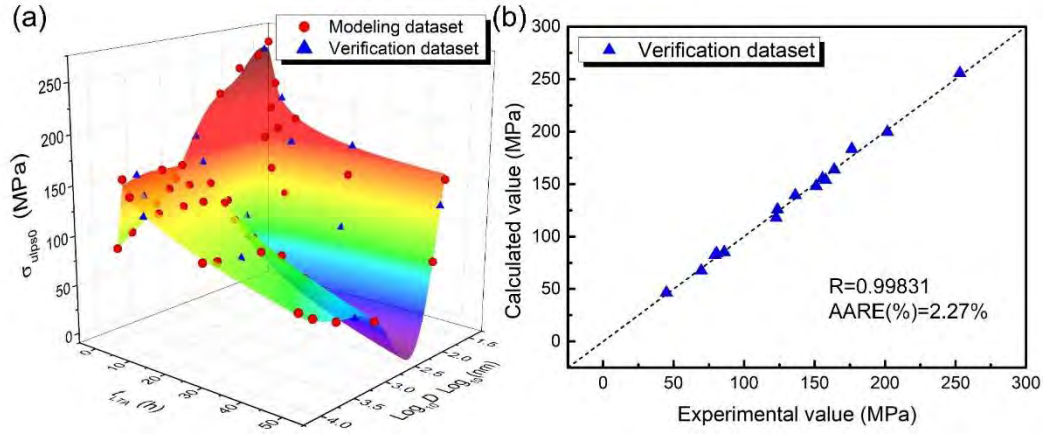


Fig. 6.14 The obtained σ_{ulps0} function: (a) modeling dataset, verification dataset, and the surface of σ_{ulps0} function; (b) the correlation between the calculated values and the experimental values of the verification dataset.

6.4.7.3 f_T function about D , t_{LTA} , and ε

By combining Eq. (6.35), (6.37), (6.39), and (6.40), the f_T function about ε , D and t_{LTA} is obtained as shown by Eq. (6.41):

$$f_t(D, t_{LTA}, \varepsilon) = \begin{cases} \left[0.38156 \cdot \sigma_{ulps0}(D, t_{LTA}) + 762.50979 \right. \\ \left. - 0.071085 \cdot E_{post}(D, t_{LTA}) \cdot (\varepsilon - \varepsilon_{mf}) \right] & (\varepsilon_{mf} < \varepsilon_{max} \leq 9\%) \\ 0.38156 \cdot \sigma_{ulps0}(D, t_{LTA}) + 762.50979 & (\varepsilon_{ms} \leq \varepsilon_{max} \leq \varepsilon_{mf}) \end{cases} \quad (6.41)$$

where $\sigma_{ulps0}(D, t_{LTA})$ is shown by Eq. (6.39) and (6.40), and $E_{post}(D, t_{LTA})$ is shown by Eq. (6.31).

6.4.8 ε_{risd} function

Based on **Fig. 2.14(b)** and related previous studies [215, 222], it is known that the residual strain increases with the maximum applied strain which appropriately presents linear relation. This is because the stress-induced phase transformation of NiTi alloys generally presents Lüders-like deformation behavior [44], thus the

residual strain proportionally increases with the maximum applied strain. Therefore, the $\varepsilon_{\text{risd}}$ as a function of ε and $\varepsilon_{\text{risd0}}$ (the residual strain at the prescribed applied strain of 3%) can be obtained, as shown in Eq. (6.42):

$$\varepsilon_{\text{risd}}(D, t_{\text{LTA}}, \varepsilon) = k_{\text{risd}}(D, t_{\text{LTA}}) \cdot (\varepsilon - 0.03) + \varepsilon_{\text{risd0}}(D, t_{\text{LTA}}) \quad (6.42)$$

where $k_{\text{risd}}(D, t_{\text{LTA}})$ is the slope of $\varepsilon_{\text{risd}}(D, t_{\text{LTA}}, \varepsilon)$, which is a function of D and t_{LTA} but irrelevant to ε ; $\varepsilon_{\text{risd0}}(D, t_{\text{LTA}})$ is the function of D and t_{LTA} and irrelevant to ε . Based on Eq. (6.42), it is necessary to establish $\varepsilon_{\text{risd0}}(D, t_{\text{LTA}})$ and $k_{\text{risd}}(D, t_{\text{LTA}})$ functions firstly in order to finally establish $\varepsilon_{\text{risd}}(D, t_{\text{LTA}}, \varepsilon)$ function.

6.4.8.1 $\varepsilon_{\text{risd0}}$ function under certain maximum applied strain

Based on the residual strain under the maximum applied strain of 3% as shown in section 5.3.3.5, the modeling dataset and verification dataset of $\varepsilon_{\text{risd0}}$ are respectively obtained, as shown in Fig. 6.15(a). As per the modeling dataset, based on the superposition principle [214], the function $\varepsilon_{\text{risd0}}(D, t_{\text{LTA}})$ is obtained as shown by Eq. (6.43) and (6.44). The values of the parameters of $\varepsilon_{\text{risd0}}$ function are shown in **Table 6.10**. The surface of $\varepsilon_{\text{risd0}}$ function is shown in Fig. 6.15 (a). The verification dataset is used to verify the correlation and accuracy of the calculation results from $\varepsilon_{\text{risd0}}$ function. The correlation coefficient R is 0.99747, and the AARE(%) is 3.24%, as shown in Fig. 6.15 (b). This indicates that the obtained function can effectively calculate the parameter of $\varepsilon_{\text{risd0}}$.

$$\varepsilon_{\text{risd0}}(D, t_{\text{LTA}}) = \begin{cases} -\exp[-a(D) \cdot (t_{\text{LTA}} - 2)^{n(D)} + b(D)] + c(D) & (t_{\text{LTA}} \geq 2) \\ k(D) \cdot (t_{\text{LTA}} - 2) - \exp[b(D)] + c(D) & (0 \leq t_{\text{LTA}} < 2) \end{cases} \quad (6.43)$$

$$\left\{ \begin{aligned}
 a(D) &= a_{\text{risd0-1}} \sin(a_{\text{risd0-3}} (\log_{10} D - a_{\text{risd0-2}}) + a_{\text{risd0-4}}) \left\{ \exp \left[- (a_{\text{risd0-3}} (\log_{10} D - a_{\text{risd0-2}}))^2 \right] \right\} \\
 &\quad - a_{\text{risd0-5}} \arctan(a_{\text{risd0-3}} (\log_{10} D - a_{\text{risd0-2}})) + a_{\text{risd0-6}} \\
 b(D) &= b_{\text{risd0-1}} \sin(b_{\text{risd0-3}} (\log_{10} D - b_{\text{risd0-2}}) + b_{\text{risd0-4}}) \left\{ \exp \left[- (b_{\text{risd0-3}} (\log_{10} D - b_{\text{risd0-2}}))^2 \right] \right\} \\
 &\quad - b_{\text{risd0-5}} \arctan(b_{\text{risd0-3}} (\log_{10} D - b_{\text{risd0-2}})) + b_{\text{risd0-6}} \\
 c(D) &= c_{\text{risd0-1}} \sin(c_{\text{risd0-3}} (\log_{10} D - c_{\text{risd0-2}}) + c_{\text{risd0-4}}) \left\{ \exp \left[- (c_{\text{risd0-3}} (\log_{10} D - c_{\text{risd0-2}}))^2 \right] \right\} \\
 &\quad - c_{\text{risd0-5}} \arctan(c_{\text{risd0-3}} (\log_{10} D - c_{\text{risd0-2}})) + c_{\text{risd0-6}} \\
 n(D) &= n_{\text{risd0-1}} \cdot \log_{10} D + n_{\text{risd0-2}} \\
 k(D) &= k_{\text{risd0-4}} \log_{10}^4 D + k_{\text{risd0-3}} \log_{10}^3 D + k_{\text{risd0-2}} \log_{10}^2 D + k_{\text{risd0-1}} \log_{10}^1 D + k_{\text{risd0-5}}
 \end{aligned} \right. \quad (6.44)$$

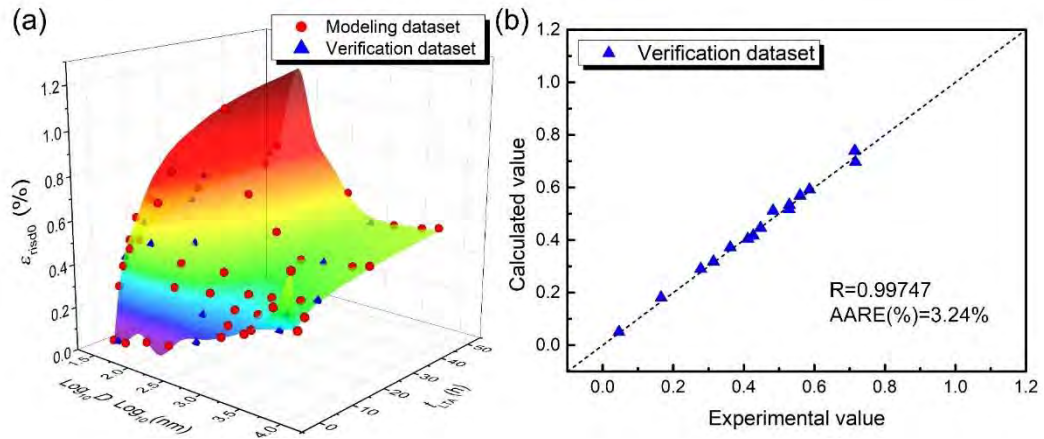


Fig. 6.15 The obtained erisd0 function: (a) modeling dataset, verification dataset, and the surface of erisd0 function; (b) the correlation between the calculated values and the experimental values of the verification dataset.

Table 6.10 The values of the parameters of $\varepsilon_{\text{risd}0}$ function

Parameter	Value	Parameter	Value
$a_{\text{risd}0-1}$	-0.48	$c_{\text{risd}0-2}$	1.85
$a_{\text{risd}0-2}$	1.64	$c_{\text{risd}0-3}$	1.71
$a_{\text{risd}0-3}$	3.05	$c_{\text{risd}0-4}$	5.89
$a_{\text{risd}0-4}$	-2.61	$c_{\text{risd}0-5}$	0.15
$a_{\text{risd}0-5}$	0.03	$c_{\text{risd}0-6}$	1.56
$a_{\text{risd}0-6}$	0.08	$n_{\text{risd}0-1}$	-0.06
$b_{\text{risd}0-1}$	3.11	$n_{\text{risd}0-2}$	0.66
$b_{\text{risd}0-2}$	1.48	$k_{\text{risd}0-1}$	12.12
$b_{\text{risd}0-3}$	2.10	$k_{\text{risd}0-2}$	-6.95
$b_{\text{risd}0-4}$	-2.40	$k_{\text{risd}0-3}$	1.70
$b_{\text{risd}0-5}$	1.21	$k_{\text{risd}0-4}$	-0.15
$b_{\text{risd}0-6}$	1.69	$k_{\text{risd}0-5}$	-7.41
$c_{\text{risd}0-1}$	1.47		

6.4.8.2 k_{risd} function

Based on the residual strain under the maximum applied strains of 3% and 9% as shown in section 5.3.3.5, the modeling dataset and verification dataset of k_{risd} are respectively calculated, as shown in **Fig. 6.16(a)**. As per the modeling dataset, based on the superposition principle [214], the function $k_{\text{risd}}(D, t_{\text{LTA}})$ is obtained as shown by Eq. (6.45) and (6.46). The values of the parameters of k_{risd} function are shown in **Table 6.11**. The surface of k_{risd} function is shown in **Fig. 6.16(a)**. The verification dataset is used to verify the correlation and accuracy of the calculation results from k_{risd} function. The correlation coefficient R is 0.99678, and the AARE(%) is 6.24%, as shown in **Fig. 6.16(b)**. This indicates that the obtained function can effectively calculate the parameter of k_{risd} .

$$k_{\text{risd}}(D, t_{\text{LTA}}) = \begin{cases} -\exp\left[-a_{\text{krisd}} \cdot (t_{\text{LTA}} - 2)^{0.7} + b_{\text{krisd}}\right] + c_{\text{krisd}} & (t_{\text{LTA}} \geq 2) \\ k_{\text{krisd}} \cdot (t_{\text{LTA}} - 2) - \exp(b_{\text{krisd}}) + c_{\text{krisd}} & (0 \leq t_{\text{LTA}} < 2) \end{cases} \quad (6.45)$$

$$\begin{cases} a_{k_{\text{risd}}} = a_{k_{\text{risd}1}} + a_{k_{\text{risd}2}} \cdot \log_{10} D + a_{k_{\text{risd}3}} \cdot \log_{10}^2 D \\ b_{k_{\text{risd}}} = b_{k_{\text{risd}1}} \cdot \sin(b_{k_{\text{risd}2}} \cdot \log_{10} D + b_{k_{\text{risd}3}}) + b_{\text{risd}0-4} \\ c_{k_{\text{risd}}} = c_{k_{\text{risd}1}} \cdot \sin(c_{k_{\text{risd}2}} \cdot \log_{10} D + c_{k_{\text{risd}3}}) + c_{\text{risd}0-4} \\ k_{k_{\text{risd}}} = -\exp(k_{k_{\text{risd}1}} \cdot (\log_{10} D + k_{k_{\text{risd}2}})) + k_{k_{\text{risd}3}} \end{cases} \quad (6.46)$$

Table 6.11 The values of the parameters of k_{risd} function

Parameter	Value	Parameter	Value
$a_{k_{\text{risd}1}}$	-0.06	$c_{k_{\text{risd}1}}$	0.01
$a_{k_{\text{risd}2}}$	0.34	$c_{k_{\text{risd}2}}$	2.30
$a_{k_{\text{risd}3}}$	-0.08	$c_{k_{\text{risd}3}}$	-3.34
$b_{k_{\text{risd}1}}$	-0.58	$c_{k_{\text{risd}4}}$	0.05
$b_{k_{\text{risd}2}}$	3.82	$k_{k_{\text{risd}1}}$	1.10
$b_{k_{\text{risd}3}}$	-3.69	$k_{k_{\text{risd}2}}$	-5.79
$b_{k_{\text{risd}4}}$	-4.49	$k_{k_{\text{risd}3}}$	0.03

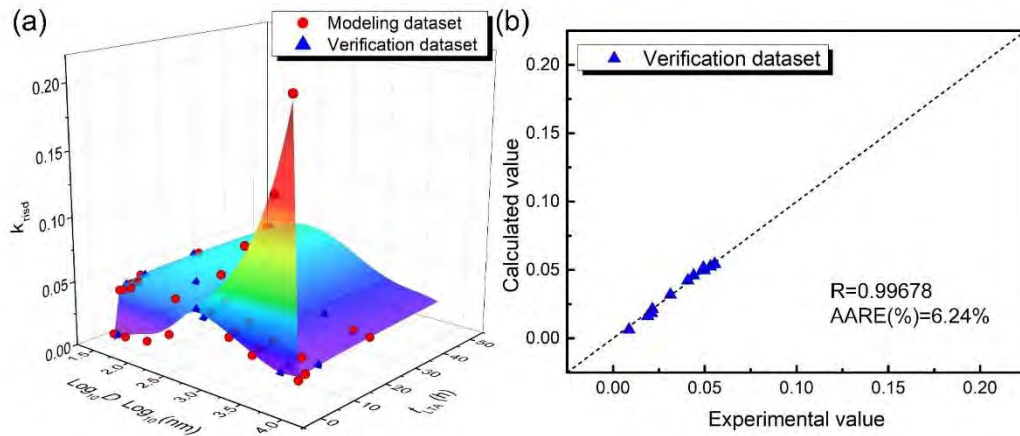


Fig. 6.16 The obtained k_{risd} function: (a) modeling dataset, verification dataset, and the surface of k_{risd} function; (b) the correlation between the calculated values and the experimental values of the verification dataset.

Based on the obtained $\varepsilon_{\text{risd}0}(D, t_{\text{LTA}})$ and $k_{\text{risd}}(D, t_{\text{LTA}})$ functions, the $\varepsilon_{\text{risd}}(D, t_{\text{LTA}}, \varepsilon)$ function is obtained based on Eq. (6.42).

Finally, by substituting the above-obtained functions, including $E_{\text{req}}(D, t_{\text{LTA}})$, $E_{\text{pre}}(D, t_{\text{LTA}})$, $Y(D, t_{\text{LTA}})$, $\varepsilon_{\text{mf}}(D, t_{\text{LTA}})$, $E_{\text{post}}(D, t_{\text{LTA}})$, $E_{\text{m}}(D, t_{\text{LTA}}, \varepsilon)$, $f_{\text{T}}(D, t_{\text{LTA}}, \varepsilon)$, and $\varepsilon_{\text{risd}}(D, t_{\text{LTA}}, \varepsilon)$, into the main model as shown by Eq. (6.17), the superelastic stress-strain model considering the effects of LTA time and grain size is obtained. This model can be used to calculate superelastic stress-strain curves of the NiTi alloys with grain size of 34-8021 nm under LTA of 0-48 h at 573 K and under the maximum applied strains of 3%-9%.

6.5 Model validation and verification

By using Matlab, the established superelastic stress-strain model considering the effects of LTA time and grain size is validated and verified in terms of effectiveness and accuracy respectively.

6.5.1 Effectiveness validation

The following LTA time and grain size conditions are representatively adopted to validate the effectiveness of the suggested model.

- 1) The superelastic stress-strain curves of the NiTi alloys with grain size of 34-8021 nm are calculated, under the maximum applied strain of 3% and before LTA, as shown in **Fig. 6.17(a)**. The corresponding experimental results are shown in **Fig. 5.1**.
- 2) The superelastic stress-strain curves of the NiTi alloys with grain size of 40 nm are calculated, under the maximum applied strain of 9% and after LTA time of 0-48 h, as shown in **Fig. 6.17(b)**. The corresponding experimental results are shown in **Fig. 5.5(b)**.

3) The superelastic stress-strain curves of the NiTi alloys with grain size of 51 nm are calculated, under the maximum applied strains of 3% and 9% and before LTA, as shown in **Fig. 6.17(a)**. The variations of the calculated results are similar to those of **Fig. 2.13**.

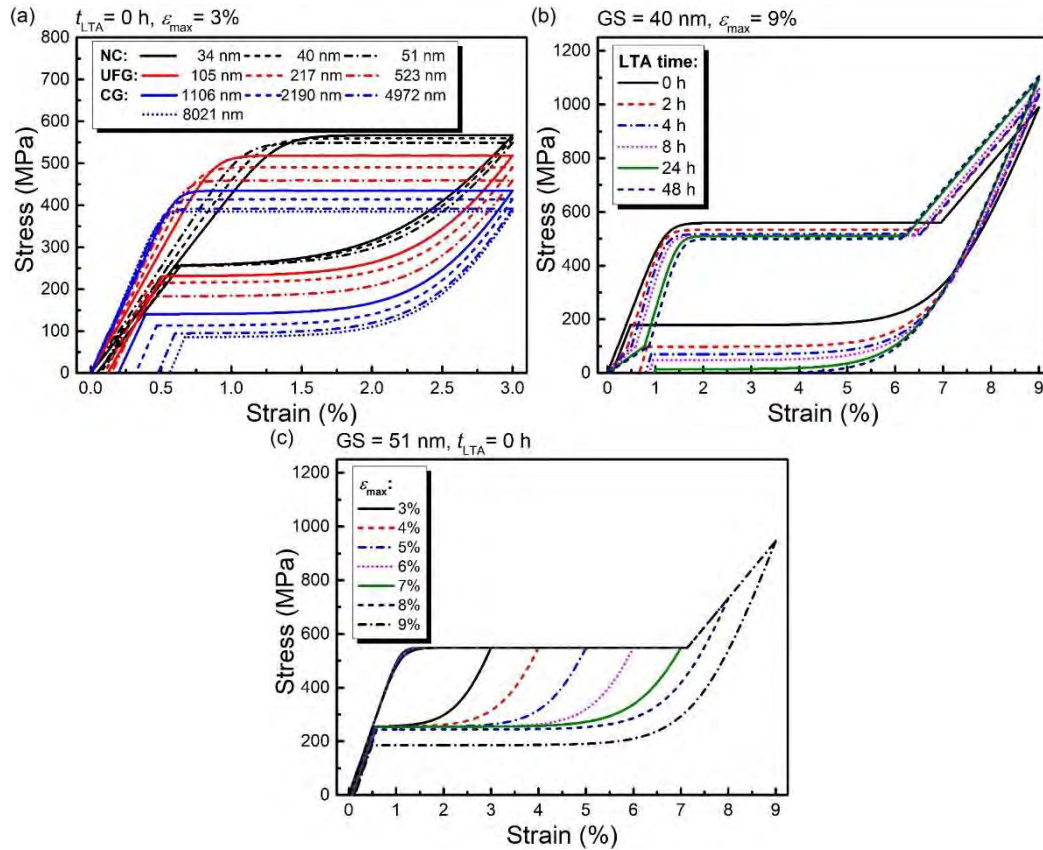


Fig. 6.17 The calculated superelastic stress-strain curves: (a) under the maximum applied strain of 3%, before LTA, within grain size of 34-8021 nm; (b) under the maximum applied strain of 9%, after LTA time of 0-48 h; with grain size of 40 nm; (c) under the maximum applied strains of 3% and 9%, before LTA, with grain size of 51 nm.

As shown in the figures, the model can effectively calculate the superelastic stress-strain curves of the NiTi alloys with different grain sizes, under different LTA time, and under different applied strains. In addition, it can effectively reflect the effects

of grain size, LTA time, and the maximum applied strain on the superelasticity of NiTi alloys, thus the effectiveness of the model was validated.

6.5.2 Accuracy verification

The superelastic stress-strain curves of the verification dataset under the maximum applied strains of 3% and 9% are respectively calculated by the model. The calculated results are compared with the experimental results, as shown in **Fig. 6.18** and **Fig. 6.19**.

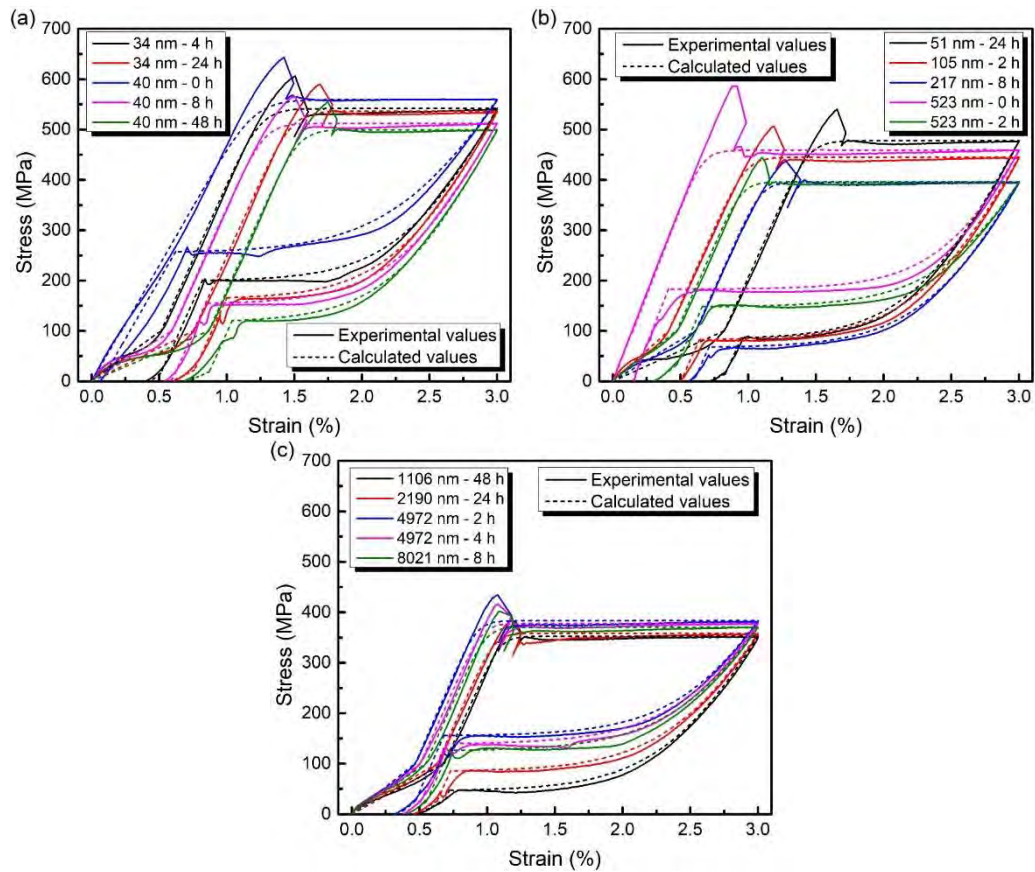


Fig. 6.18 Under the maximum applied strain of 3%, the comparison of the calculated and experimental superelastic stress-strain curves with grain size of:

(a) 34-40 nm; (b) 51-523 nm; (c) 1106-8021 nm.

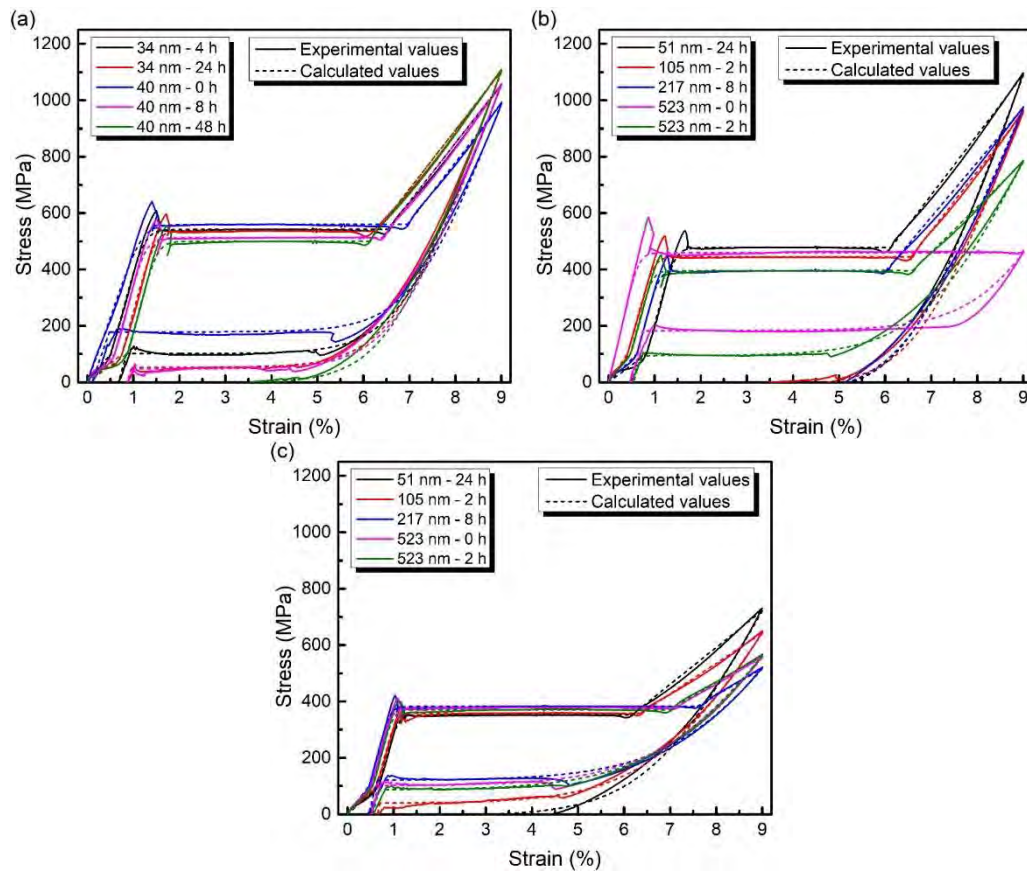


Fig. 6.19 Under the maximum applied strain of 9%, the comparison of the calculated and experimental superelastic stress-strain curves with grain size of:

(a) 34-40 nm; (b) 51-523 nm; (c) 1106-8021 nm.

As shown by the figures, regardless of the maximum applied strain, the calculated results are generally consistent with those of experiment results, which indicates that the suggested model is able to calculate the superelastic stress-strain curves of the verification dataset. At the same time, several details of the comparison indicate the space for further improvements in the future:

- (1) The stress jumps of the start of the loading and unloading plateau are not reflected. Since this factor is not considered in the modeling stage, this deformation behavior is not described and consequently leads to certain errors.
- (2) The transition stage between the elastic unloading deformation of B19' phase and the unloading plateau is not precise enough. This is because the parameter

n can only with values of positive odd number, i.e., 7, 9, 11, ..., thus the description of the transition stage cannot be continuously adjusted, which causes certain errors.

- (3) The approximation of the B2↔R related loading and unloading deformations is with systematic inaccuracy, which is non-linear per experimental results but is approximated by linear function during modeling. This also leads to certain errors.

For further verifying the accuracy of the suggested model quantitatively, the superelastic loading-unloading energy dissipation of the verification dataset, as schematically illustrated in **Fig. 6.20**, is calculated. The calculated results are compared with experimental results, as shown in **Fig. 6.21**.

$$E_{\text{diss}} = \oint \sigma d\varepsilon \quad (6.47)$$

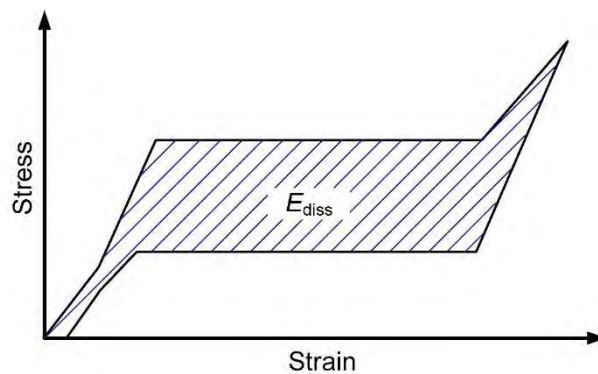


Fig. 6.20 Schematic illustration of superelastic loading-unloading energy dissipation

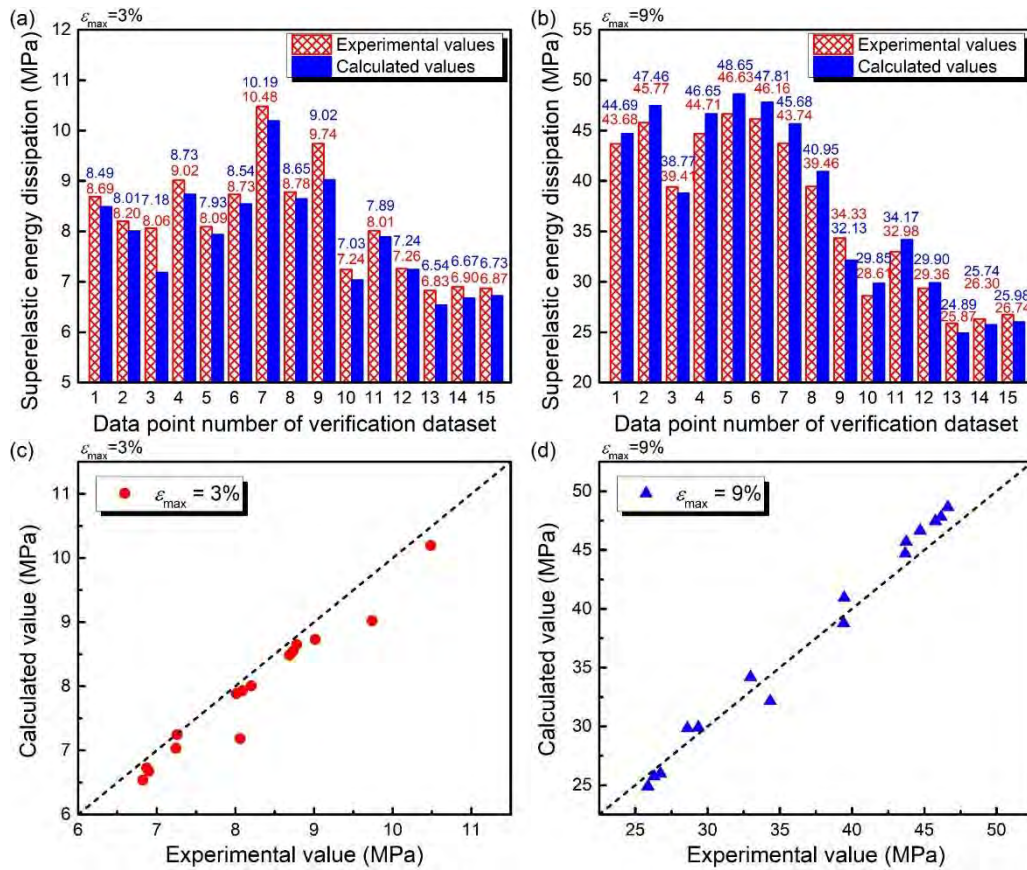


Fig. 6.21 The superelastic loading-unloading energy dissipation of the verification dataset: (a) the comparison of the experimental and calculated values under the maximum applied strain of 3%; (b) the comparison of the experimental and calculated values under the maximum applied strain of 9%; (c) correlation between experimental and calculated values under the maximum applied strain of 3%; and (d) correlation between experimental and calculated values under the maximum applied strain of 9%.

As shown in **Fig. 6.21**, under the maximum applied strain of 3%, the maximum absolute and relative errors are 0.88 MPa and 10.9% respectively, and the corresponding correlation coefficient R is 0.97770 and AARE(%) is 3.26%. Under the maximum applied strain of 9%, the maximum absolute and relative errors are 2.2 MPa and 6.4% respectively, and the corresponding correlation coefficient R is

0.99378 and the AARE(%) is 3.53%. This indicates that the suggested model is able to relatively accurately calculate the superelastic loading-unloading energy dissipation of NiTi alloys with different grain sizes and LTA time.

6.6 Summary

Based on the experimental results of chapter 5 and Graesser superelastic stress-strain model, this chapter establishes the modified Graesser superelastic stress-strain model of NiTi alloys considering the effects of LTA time and grain size.

The following concluding remarks can thus be drawn:

- (1) Graesser model [170] is modified to determine the mathematical framework for the superelastic stress-strain curve under certain given LTA time and grain size. The modified model realizes: 1) the linearly approximate description of B2 \leftrightarrow R transformation related deformation; 2) the linear approximation of the post-plateau deformation. By using this model, superelastic stress-strain relation with B2 \leftrightarrow R transformation related deformation and post-plateau deformation is able to be described, which helps to enlarge the application scope of Graesser model.
- (2) The model is further modified by adding parameters and constants. After the modification, every parameter of the model can independently control the shape of the stress-strain curve of a certain section. This is prepared for the establishment of the final model that considers the effects of LTA time and grain size.

- (3) By establishing the parameter functions about LTA time and grain size of the modified Graesser model, it is further able to describe the effects of LTA time and grain size on superelastic stress-strain curves. Though the model is a phenomenological-empirical model, it simultaneously considers the effects of the two factors, i.e., LTA time and grain size, on superelasticity.
- (4) This study suggests a superelastic stress-strain model considering the effects of LTA time and grain size, which can be used to relatively accurately calculate the superelastic stress-strain curve of Ni_{50.8 at.%}-Ti alloys within grain size of 34-8021 nm, LTA time 0-48 h at 573 K under the maximum applied strain of 3%-9%. This model may facilitate the design and adjustment of the superelasticity of the NiTi parts and components with different grain sizes and under different LTA time.

Chapter 7 Conclusions and suggestions for future research

7.1 Conclusions

The present study preliminarily investigates the influence of low-temperature aging (LTA) on phase transformation characteristics and superelasticity of NiTi alloys with different grain sizes. The variations of the phase transformation characteristics and superelasticity with the increasing LTA time and Grain size are obtained. By observing the corresponding microstructural evolution and hardness variation, the underlying mechanisms for the variations of phase transformation characteristics and superelasticity are understood. Based on the experimental results, the models of transformation temperature, stress hysteresis, and superelastic stress-strain relation are respectively established which consider the effects of LTA time and grain size. This study provides experimental evidences and theoretical references for the functional property tailoring of NiTi alloys via LTA, which are beneficial for realizing functional properties alteration without changing the desired grain size. Based on the present study, some conclusions can be drawn.

- (1) The different influences of LTA on NC and CG NiTi alloys are identified regarding precipitation behavior, phase transformation characteristics, and superelasticity. The feasibility that alteration functional properties without changing grain size is confirmed. It is known from the experimental results

that the LTA of 573 K successfully avoids further grain growth of the NC and CG NiTi alloys and simultaneously changes the phase transformation characteristics and superelasticity. The effect of LTA is different depending on grain size. For NC NiTi alloys, LTA keeps B2→B19' transformation suppressed and elevates B2→R transformation temperature; for CG NiTi alloys, LTA activates B2→R transformation. After LTA, R→B19' transformation stress hysteresis and residual strain increases in NC NiTi alloys but decreases in CG ones. The above difference is due to LTA induced different Ni₄Ti₃ precipitation behavior as well as the grain size and precipitates induced variations of dislocation activates, which indicates that the knowledge of LTA obtained from CG NiTi alloys is not completely fit for the NC ones. In addition, for NC NiTi alloys, thermally induced R→B19' transformation is suppressed while stress-induced R→B19' transformation is able to proceed; for CG NiTi alloys, the thermal hysteresis increases, whilst the stress hysteresis decreases after LTA. These differences between thermally-induced and stress-induced phase transformation further indicates that the judgment of superelasticity cannot only depend on phase transformation characteristics, whilst the microstructural features such as grain size, precipitates, dislocations, etc. should also be considered.

- (2) The influence of direct electrical resistance heat treatment (DERHT) on microstructures, phase transformation characteristics, superelasticity of the NiTi alloy with different grain sizes and aging conditions is studied. The grain size induced suppression of Ni₄Ti₃ precipitation during DERHT is reported. The grain size adjustment models based on DERHT are suggested, which can

be used to rapidly obtain NiTi alloys with grain size from NC to CG scale. As per the experimental results, for the NiTi alloys with 1 mm diameter, DERHT of 12 A can dissolve the previously LTA induced Ni₄Ti₃ nanoprecipitates in 10 s, and that can enlarge grain size from 34 nm to 2 μm in 25 s. DERHT of 8 A can precipitate or enlarge Ni₄Ti₃ to 15-25 nm in size and 15-30 nm in gap in the solution treated or previously LTAed CG NiTi alloys, respectively. By contrast, in NC NiTi alloys, Ni₄Ti₃ precipitates are not observed after the DERHT of 8 A and the nanograin size is well preserved. This proves that nanograin size can induce suppression of Ni₄Ti₃ during DERHT. Based on the grain growth during DERHT, the grain size adjustment models via the alteration of heating time and direct current magnitude are respectively obtained, which can be used for the rapid obtaining of the NiTi alloys with grain size from 34 nm to 8021 nm.

- (3) The variations of phase transformation characteristics with grain size from 34 nm to 8021 nm and LTA time from 0 h to 48 h at 573 K are obtained. Nanograin size induced suppression of Ni₄Ti₃ precipitation during LTA is found with microstructural and hardness evidence. The B2→R transformation temperature model considering the effect of LTA time and grain size is suggested, which may facilitate the design and application of NiTi functional parts and components based on B2↔R transformation. It is known from the experimental results that, before LTA, within grain size of 34-217 nm, B2↔R transformation is activated, R↔B19' transformation is suppressed, and B2↔R transformation temperature decreases with the increasing grain size. Within grain size of 523-8021 nm, B2↔R transformation disappears,

$B2 \leftrightarrow B19'$ transformation is activated, and $B2 \leftrightarrow B19'$ transformation temperature increases with grain size. After LTA, $B2 \leftrightarrow R$ transformation temperature of all the NiTi alloys increases with LTA time. Under the same LTA time, the amplitude of variation of $B2 \leftrightarrow R$ transformation temperature increases with grain size in NC NiTi alloys; $B2 \leftrightarrow R$ transformation temperature decreases with grain size in UFG NiTi alloys; the temperature generally keeps unchanged in CG NiTi alloys. Within grain size of 34-1106 nm, $R \leftrightarrow B19'$ transformation keeps suppressed; within grain size of 2190-8021 nm, $R \leftrightarrow B19'$ transformation temperature increases with LT time. There is a critical grain size (<150 nm) below which Ni_4Ti_3 precipitation is suppressed. Such suppression combining with the effect of grain size on phase transformation characteristics are the fundamental reasons for the LTA induced transformation temperature variations being different regarding different grain sizes. Based on experimental results, $B2 \rightarrow R$ transformation temperature model considering the effects of LTA time and grain size is suggested, which is able to calculate the $B2 \rightarrow R$ transformation temperature of the NiTi alloys with grain size of 34-8021 nm and LTA time of 2-48 h.

- (4) The variations of superelasticity with grain size from 34 nm to 8021 nm and LTA from 0 h to 48 h at 573 K and under the maximum applied strains of 3% and 9% are respectively obtained. LTA can remarkably increase stress hysteresis adjustment range. The function of stress hysteresis increment and maximum loading stress increment during post-plateau deformation is obtained, and the stress hysteresis model considering the effects of LTA time and grain size is suggested, which may facilitate the design and application of

NiTi functional parts and components based on the stress hysteresis of B2(R) \leftrightarrow B19' transformation. As per the experimental results, before LTA, loading plateau stress decreases while stress hysteresis and residual strain increase with the increasing grain size. After LTA, the loading and unloading plateau stress decrease while the stress hysteresis and residual strain increase with LTA time. Among the NiTi alloys, UFG ones vary most remarkably after LTA, because they are simultaneously affected by Ni₄Ti₃ precipitates and the high grain boundary volume fraction; NC ones are mainly affected by the high grain boundary volume fraction, because nanograin size induces suppression of Ni₄Ti₃ precipitation and consequently weakens the influence of the precipitates; CG ones are mainly affected by Ni₄Ti₃ precipitates, because grain size presents limited influence on CG NiTi alloys. Under the maximum applied strain of 3%, unloading happens within plateau deformation stage; under the maximum applied strain of 9%, unloading happens within post-plateau deformation stage. Post-plateau strain increases with LTA time, which leads to the further increase of stress hysteresis. Within post-plateau deformation stage, the increment of stress hysteresis is found of nearly linear relation with the increment of the maximum loading stress regardless of grain size and aging state, thus a function is suggested to describe such relation. As per the function, the maximum loading stress increased per 1 MPa, and the stress hysteresis correspondingly increased 0.186 MPa. LTA is found able to increase stress hysteresis adjustment range: unloading within plateau deformation stage, stress hysteresis adjustment range is expended from 38 MPa (275-313 MPa) to 175 MPa (225-400 MPa), which is enlarged by 460%. Based on this finding, stress hysteresis model considering the effects of LTA

time and grain size was suggested, which can be used to calculate the stress hysteresis with grain size of 34-8021 nm and LTA time of 0-48 h (unloading within plateau deformation stage).

- (5) A superelastic stress-strain model considering the effects of LTA time and grain size is established. The model is able to calculate superelastic stress-strain curves of the NiTi alloys with grain size of 34-8021 nm, after LTA time of 0-48 h at 573 K, and under the maximum applied strain of 3%-9%, which may facilitate the superelasticity design and adjustment of the NiTi alloys with different grain sizes and LTA time. The model is modified from Graesser model: B2 \leftrightarrow R transformation related deformation stage and post-plateau deformation stage are linearly approximated, which expands the application scope of Graesser model; the superelastic deformation is separated to loading and unloading sections; each of the model parameters can independently control the shape of the stress-strain curve of the corresponding section. Furthermore, the functions of the model parameters about LTA time, grain size, and strain are established based on the modeling dataset of the experimental results. These functions are substituting to the main modified Graesser model, then the superelastic stress-strain model considering the effects of LTA time and grain size is consequently obtained. Based on the verification, the model is able to relatively accurately calculate the superelastic stress-strain curves and the superelastic energy dissipation of the NiTi alloys with grain size of 34-8021 nm, after LTA time of 0-48 h at 573 K, and under maximum applied strain of 3%-9%.

7.2 Suggestions for future research

This study preliminary investigates the influence of LTA on the phase transformation characteristics and superelasticity of NiTi alloys with different grain sizes, which provides experimental evidence and theoretical references for the LTA induced functional property adjustment of nanocrystalline and ultrafine-grained NiTi alloys. Some details are suggested to be improved in future studies:

- (1) The LTA induced precipitation behavior of different LTA temperatures is suggested to be further explored. The present study mainly conducts LTA at 573 K. It successfully realizes the alteration of phase transformation characteristics and superelasticity without changing the original grain size of the NiTi alloys with grain size of 34-8021 nm. Nevertheless, 573 K is not the exclusive LTA temperature. Different LTA temperatures leads to different precipitation behaviors, which brings about different influences on the properties of NiTi alloys.
- (2) Effect of LTA on the NiTi alloys with grain size below 34 nm is suggested to be further investigated. The grain size range of this study is 34-8021 nm, while the effect of LTA on the NiTi alloys with grain size under 34 nm deserves to be further studied.
- (3) The effect of LTA on the phase transformation characteristics under external load is suggested to be further studied. The present work studies the phase transformation characteristics by using DSC of which the samples are free of external loads. Future study may investigate the phase transformation

characteristics under external loads by using dynamic thermomechanical analysis, which is beneficial for the further understanding of the effect of LTA on phase transformation characteristics of the NiTi alloys.

- (4) The engineering application of this study is anticipated. This study is in the preliminary stage of the method that using LTA to realize functional property adjustment of NiTi alloys with different grain sizes without changing grain size. The current results provide experimental evidences and theoretical references for the engineering applications of NiTi alloys from the aspect of B2→R transformation, stress hysteresis, and superelastic stress-strain relation. In the future studies, the functions and models suggested in this study are anticipated to be used in engineering applications regarding the application of LTA.

References

- [1] (!!! INVALID CITATION !!! [1-5]).
- [2] E. Wilhelm, C. Richter, B.E. Rapp, Phase change materials in microactuators: Basics, applications and perspectives, *Sensors and Actuators A: Physical*. 271 (2018) 303-47.
- [3] A. Ziólkowski, 2 - Shape memory effects in metallic alloys, In: Ziólkowski A, editor. *Pseudoelasticity of Shape Memory Alloys: Butterworth-Heinemann*; 2015. p. 11-53.
- [4] P. Wollants, J.R. Roos, L. Delaey, Thermally- and stress-induced thermoelastic martensitic transformations in the reference frame of equilibrium thermodynamics, *Prog Mater Sci*. 37 (1993) 227-88.
- [5] S. Jaeger, B. Maaß, J. Frenzel, M. Schmidt, J. Ullrich, S. Seelecke, et al., On the widths of the hysteresis of mechanically and thermally induced martensitic transformations in Ni - Ti-based shape memory alloys, *Int J Mater Res*. 106 (2015) 1029-39.
- [6] J. Frenzel, A. Wiczorek, I. Opahle, B. Maaß, R. Drautz, G. Eggeler, On the effect of alloy composition on martensite start temperatures and latent heats in Ni-Ti-based shape memory alloys, *Acta Mater*. 90 (2015) 213-31.
- [7] P.C. Chang, M.L. Ko, B. Ramachandran, Y.K. Kuo, C. Chien, S.K. Wu, Comparative study of R-phase martensitic transformations in TiNi-based shape memory alloys induced by point defects and precipitates, *Intermetallics*. 84 (2017) 130-5.
- [8] J. Khalil-Allafi, B. Amin-Ahmadi, The effect of chemical composition on enthalpy and entropy changes of martensitic transformations in binary NiTi shape memory alloys, *J Alloy Compd*. 487 (2009) 363-6.
- [9] J. Khalil-Allafi, A. Dlouhy, G. Eggeler, Ni₄Ti₃-precipitation during aging of NiTi shape memory alloys and its influence on martensitic phase transformations, *Acta Mater*. 50 (2002) 4255-74.
- [10] D. Treppmann, E. Hornbogen, The Effect of Dislocation Substructure and Decomposition on the Course of Diffusionless Transformations, *J Phys IV France*. 05 (1995) C2-211-C2-6.
- [11] J. Mohd Jani, M. Leary, A. Subic, M.A. Gibson, A review of shape memory alloy research, applications and opportunities, *Mater Design*. 56 (2014) 1078-113.
- [12] Q. Chen, G.A. Thouas, *Metallic implant biomaterials, Materials Science and Engineering: R: Reports*. 87 (2015) 1-57.
- [13] T. Yoneyama, S. Miyazaki, *Shape memory alloys for biomedical applications: Elsevier*; 2008.
- [14] T. Duerig, A. Pelton, D. Stöckel, An overview of nitinol medical applications, *Materials Science and Engineering: A*. 273-275 (1999) 149-60.
- [15] L.H. Yahia, F. Rayes, A.O. Warrak, 13 - Regulation, orthopedic, dental, endovascular and other applications of Ti-Ni shape memory alloys, In: Yoneyama T, Miyazaki S, editors. *Shape Memory Alloys for Biomedical Applications: Woodhead Publishing*; 2009. p. 306-26.
- [16] S. Kujala, J. Ryhänen, A. Danilov, J. Tuukkanen, Effect of porosity on the osteointegration and bone ingrowth of a weight-bearing nickel-titanium bone graft substitute, *Biomaterials*. 24 (2003) 4691-7.
- [17] T. Ikeda, 11 - The use of shape memory alloys (SMAs) in aerospace engineering, In: Yamauchi K, Ohkata I, Tsuchiya K, Miyazaki S, editors. *Shape Memory and Superelastic Alloys: Woodhead Publishing*; 2011. p. 125-40.
- [18] D. Quan, X. Hai, Shape Memory Alloy in Various Aviation Field, *Procedia Engineering*. 99 (2015) 1241-6.
- [19] A. Concilio, L. Lecce, Chapter 1 - Historical Background and Current Scenario, In: Concilio A, Dimino I, Lecce L, Pecora R, editors. *Morphing Wing Technologies: Butterworth-Heinemann*; 2018. p. 3-84.
- [20] F.T. Calkins, J.H. Mabe, Shape Memory Alloy Based Morphing Aerostructures, *J Mech Design*. 132 (2010) 7.
- [21] N. Choudhary, D. Kaur, Shape memory alloy thin films and heterostructures for MEMS applications: A review, *Sensors and Actuators A: Physical*. 242 (2016) 162-81.
- [22] Y. Bellouard, Shape memory alloys for microsystems: A review from a material research perspective, *Materials Science and Engineering a-Structural Materials Properties Microstructure and Processing*. 481 (2008) 582-9.

- [23] Y. Fu, H. Du, W. Huang, S. Zhang, M. Hu, TiNi-based thin films in MEMS applications: a review, *Sensors and Actuators A: Physical*. 112 (2004) 395-408.
- [24] M.M. Branco, J.M. Kelly, L.M. Guerreiro, An algorithm to simulate the one-dimensional superelastic cyclic behavior of NiTi strings, for civil engineering applications, *Eng Struct*. 33 (2011) 3737-47.
- [25] G. Song, N. Ma, H.N. Li, Applications of shape memory alloys in civil structures, *Eng Struct*. 28 (2006) 1266-74.
- [26] M.S. Speicher, R. DesRoches, R.T. Leon, Investigation of an articulated quadrilateral bracing system utilizing shape memory alloys, *J Constr Steel Res*. 130 (2017) 65-78.
- [27] G. Croci, Strengthening the Basilica of St Francis of Assisi after the September 1997 Earthquake, *Struct Eng Int*. 11 (2001) 207-10.
- [28] Y. Qin, L. Chen, Y. Zhu, L. Zhang, Synthesis and structure of nanocrystalline NiTi alloy, *Journal of Materials Science Letters*. 15 (1996) 1155-7.
- [29] H.-G. Kim, K. Sumiyama, K. Suzuki, Formation and thermal stability of nanocrystalline Cu Ti Ni prepared by mechanical alloying, *J Alloy Compd*. 239 (1996) 88-93.
- [30] J. Koike, D.M. Parkin, M. Nastasi, Crystal-to-amorphous transformation of NiTi induced by cold rolling, *J Mater Res*. 5 (2011) 1414-8.
- [31] T. Waitz, Bulk nanostructured shape memory alloys, *Ciência & Tecnologia dos Materiais*. 20 (2008) 25-9.
- [32] Q. Sun, A. Aslan, M. Li, M. Chen, Effects of grain size on phase transition behavior of nanocrystalline shape memory alloys, *Sci China Technol Sc*. 57 (2014) 671-9.
- [33] J. Frenzel, J.A. Burow, E.J. Payton, S. Rezanka, G. Eggeler, Improvement of NiTi Shape Memory Actuator Performance Through Ultra-Fine Grained and Nanocrystalline Microstructures, *Adv Eng Mater*. 13 (2011) 256-68.
- [34] A.V. Sergueeva, C. Song, R.Z. Valiev, A.K. Mukherjee, Structure and properties of amorphous and nanocrystalline NiTi prepared by severe plastic deformation and annealing, *Materials Science and Engineering: A*. 339 (2003) 159-65.
- [35] K. Tsuchiya, Y. Hada, T. Koyano, K. Nakajima, M. Ohnuma, T. Koike, et al., Production of TiNi amorphous/nanocrystalline wires with high strength and elastic modulus by severe cold drawing, *Scripta Mater*. 60 (2009) 749-52.
- [36] Q.S. Mei, L. Zhang, K. Tsuchiya, H. Gao, T. Ohmura, K. Tsuzaki, Grain size dependence of the elastic modulus in nanostructured NiTi, *Scripta Mater*. 63 (2010) 977-80.
- [37] H. Yin, Y. He, Z. Mounni, Q. Sun, Effects of grain size on tensile fatigue life of nanostructured NiTi shape memory alloy, *Int J Fatigue*. 88 (2016) 166-77.
- [38] X. Zhang, S. Wang, X. Yan, D. Yue, R. Sun, X. Zhou, Probabilistic analysis for the functional and structural fatigue of NiTi wires, *Mater Design*. 102 (2016) 213-24.
- [39] K.T. Liu, J.G. Duh, Grain size effects on the corrosion behavior of Ni_{50.5}Ti_{49.5} and Ni_{45.6}Ti_{49.3}Al_{5.1} films, *J Electroanal Chem*. 618 (2008) 45-52.
- [40] F.L. Nie, Y.F. Zheng, Y. Cheng, S.C. Wei, R.Z. Valiev, In vitro corrosion and cytotoxicity on microcrystalline, nanocrystalline and amorphous NiTi alloy fabricated by high pressure torsion, *Mater Lett*. 64 (2010) 983-6.
- [41] J.E. Schaffer, Structure-Property Relationships in Conventional and Nanocrystalline NiTi Intermetallic Alloy Wire, *J Mater Eng Perform*. 18 (2009) 582-7.
- [42] R.R. Adharapurapu, K.S. Vecchio, Effects of aging and cooling rate on the transformation of nanostructured Ti-50.8Ni, *J Alloy Compd*. 693 (2017) 150-63.
- [43] X. Shi, M. Yu, F. Guo, Z. Liu, D. Jiang, X. Han, et al., Effect of deformation on the stability of stress-induced martensite in nanocrystalline NiTi shape memory alloy, *Mater Lett*. 131 (2014) 233-5.
- [44] X. Yao, Z. Pan, L. Liping, Grain size effect on mechanical performance of nanostructured superelastic NiTi alloy, *Mater Res Express*. 4 (2017) 035702.
- [45] A. Ahadi, Q. Sun, Stress hysteresis and temperature dependence of phase transition stress in nanostructured NiTi—Effects of grain size, *Appl Phys Lett*. 103 (2013) 021902.
- [46] X.B. Shi, F.M. Guo, J.S. Zhang, H.L. Ding, L.S. Cui, Grain size effect on stress hysteresis of nanocrystalline NiTi alloys, *J Alloy Compd*. 688, Part B (2016) 62-8.
- [47] J.I. Kim, Y. Liu, S. Miyazaki, Ageing-induced two-stage R-phase transformation in Ti – 50.9at.%Ni, *Acta Mater*. 52 (2004) 487-99.
- [48] J.I. Kim, S. Miyazaki, Effect of nano-scaled precipitates on shape memory behavior of Ti-50.9at.%Ni alloy, *Acta Mater*. 53 (2005) 4545-54.

- [49] X. Wang, S. Kustov, K. Li, D. Schryvers, B. Verlinden, J. Van Humbeeck, Effect of nanoprecipitates on the transformation behavior and functional properties of a Ti–50.8 at.% Ni alloy with micron-sized grains, *Acta Mater.* 82 (2015) 224-33.
- [50] K. Otsuka, X. Ren, Physical metallurgy of Ti–Ni-based shape memory alloys, *Prog Mater Sci.* 50 (2005) 511-678.
- [51] P. Chowdhury, H. Sehitoglu, Deformation physics of shape memory alloys – Fundamentals at atomistic frontier, *Prog Mater Sci.* 88 (2017) 49-88.
- [52] T. Mineta, Y. Haga, Materials and Processes in Shape Memory Alloy, In: Ghodssi R, Lin P, editors. *MEMS Materials and Processes Handbook*. Boston, MA: Springer US; 2011. p. 355-402.
- [53] V.G. Pushin, V.V. Stolyarov, R.Z. Valiev, T.C. Lowe, Y.T. Zhu, Nanostructured TiNi-based shape memory alloys processed by severe plastic deformation, *Materials Science and Engineering: A.* 410–411 (2005) 386-9.
- [54] K. Otsuka, C.M. Wayman, *Shape memory materials*: Cambridge university press; 1999.
- [55] J. Frenzel, E.P. George, A. Dlouhy, C. Somsen, M.F.X. Wagner, G. Eggeler, Influence of Ni on martensitic phase transformations in NiTi shape memory alloys, *Acta Mater.* 58 (2010) 3444-58.
- [56] M. Zarinejad, Y. Liu, Dependence of Transformation Temperatures of NiTi-based Shape-Memory Alloys on the Number and Concentration of Valence Electrons, *Adv Funct Mater.* 18 (2008) 2789-94.
- [57] M. Nishida, C.M. Wayman, T. Honma, Precipitation processes in near-equiatomic TiNi shape memory alloys, *Metallurgical Transactions A.* 17 (1986) 1505-15.
- [58] X.B. Shi, Z.Y. Ma, J.S. Zhang, H.L. Ding, F.M. Guo, Y. Liu, et al., Grain size effect on the martensitic transformation temperatures of nanocrystalline NiTi alloy, *Smart Materials and Structures.* 24 (2015) 072001.
- [59] T. Waitz, T. Antretter, F.D. Fischer, H.P. Karnthaler, Size effects on martensitic phase transformations in nanocrystalline NiTi shape memory alloys, *Mater Sci Tech-Lond.* 24 (2008) 934-40.
- [60] V.G. Pushin, V.V. Stolyarov, R.Z. Valiev, N.I. Kourov, N.N. Kuranova, E.A. Prokofiev, et al., Features of structure and phase transformations in shape memory TiNi-based alloys after severe plastic deformation, *Annales de Chimie Science des Matériaux.* 27 (2002) 77-88.
- [61] V. Pushin, R. Valiev. The nanostructured TiNi shape-memory alloys: new properties and applications. *Solid state phenomena: Trans Tech Publ*; 2003. p. 13-24.
- [62] C.S. Pande, K.P. Cooper, Nanomechanics of Hall–Petch relationship in nanocrystalline materials, *Prog Mater Sci.* 54 (2009) 689-706.
- [63] T.G. Nieh, J. Wadsworth, Hall-petch relation in nanocrystalline solids, *Scripta Metallurgica et Materialia.* 25 (1991) 955-8.
- [64] C.E. Carlton, P.J. Ferreira, What is behind the inverse Hall–Petch effect in nanocrystalline materials?, *Acta Mater.* 55 (2007) 3749-56.
- [65] C. Koch, D. Morris, K. Lu, A. Inoue, Ductility of nanostructured materials, *Mrs Bull.* 24 (1999) 54-8.
- [66] H.A. Padilla, B.L. Boyce, A Review of Fatigue Behavior in Nanocrystalline Metals, *Exp Mech.* 50 (2010) 5-23.
- [67] C.C. Koch, K.M. Youssef, R.O. Scattergood, K.L. Murty, Breakthroughs in Optimization of Mechanical Properties of Nanostructured Metals and Alloys, *Adv Eng Mater.* 7 (2005) 787-94.
- [68] K.S. Kumar, H. Van Swygenhoven, S. Suresh, Mechanical behavior of nanocrystalline metals and alloys, *Acta Mater.* 51 (2003) 5743-74.
- [69] H. Gleiter, Nanocrystalline materials, *Prog Mater Sci.* 33 (1989) 223-315.
- [70] C. Koch, Top-Down Synthesis Of Nanostructured Materials: Mechanical And Thermal Processing Methods, *Rev Adv Mater Sci.* 5 (2003) 91-9.
- [71] Y. Xun, F.A. Mohamed, Refining efficiency and capability of top-down synthesis of nanocrystalline materials, *Materials Science and Engineering: A.* 528 (2011) 5446-52.
- [72] R.S. Averbach, H. Hahn, H.J. Höfler, J.C. Logas, Processing and properties of nanophase amorphous metallic alloys: Ni - Ti, *Appl Phys Lett.* 57 (1990) 1745-7.
- [73] F. Neves, F.M.B. Fernandes, I. Martins, J.B. Correia, M. Oliveira, E. Gaffet, et al., The transformation behaviour of bulk nanostructured NiTi alloys, *Smart Materials and Structures.* 18 (2009) 115003.

- [74] D. Wu, W.C. Crone, J. Perepezko. Mechanical behavior of Nanostructured melt spun NiTi shape memory alloy. Session on Microstructural Characterization and Processing, Proceedings of the SEM Annual Conference on Experimental Mechanics: Citeseer; 2002.
- [75] V.G. Pushin, N.I. Kourov, T.E. Kuntsevich, Specific features of martensitic transformations, microstructure, and mechanical properties of nanostructured shape memory TiNi-TiFe alloys, *Bulletin of the Russian Academy of Sciences: Physics*. 73 (2009) 1027-9.
- [76] A. Shelyakov, N. Sitnikov, A. Glezer, A. Menushenkov, Nanostructured shape memory alloys of the TiNi-TiCu system, *Bulletin of the Russian Academy of Sciences: Physics*. 74 (2010) 1543-5.
- [77] M.M. Verdian, M. Salehi, K. Raeissi, SYNTHESIS OF AMORPHOUS/NANOCRYSTALLINE Ni-Ti POWDERS BY USING LOW ENERGY MECHANICAL ALLOYING, *Int J Mod Phys B*. 24 (2010) 1261-9.
- [78] M. Ghadimi, A. Shokuhfar, H.R. Rostami, M. Ghaffari, Effects of milling and annealing on formation and structural characterization of nanocrystalline intermetallic compounds from Ni-Ti elemental powders, *Mater Lett*. 80 (2012) 181-3.
- [79] M. Ghadimi, A. Shokuhfar, Effects of Mechanical Alloying on microstructure and microhardness of Nanocrystalline Ni-50at.% Ti Shape Memory Alloy, 2013. 5 (2013) 5.
- [80] M. Karolus, J. Panek, Nanostructured Ni-Ti alloys obtained by mechanical synthesis and heat treatment, *J Alloy Compd*. 658 (2016) 709-15.
- [81] R.Z. Valiev, R.K. Islamgaliev, I.V. Alexandrov, Bulk nanostructured materials from severe plastic deformation, *Prog Mater Sci*. 45 (2000) 103-89.
- [82] R. Valiev, Nanostructuring of metals by severe plastic deformation for advanced properties, *Nat Mater*. 3 (2004) 511-6.
- [83] Y.T. Zhu, T.C. Lowe, T.G. Langdon, Performance and applications of nanostructured materials produced by severe plastic deformation, *Scripta Mater*. 51 (2004) 825-30.
- [84] N.R. Tao, M.L. Sui, J. Lu, K. Lua, Surface nanocrystallization of iron induced by ultrasonic shot peening, *Nanostructured Materials*. 11 (1999) 433-40.
- [85] M. Zehetbauer, R. Grössinger, H. Krenn, M. Krystian, R. Pippan, P. Rogl, et al., Bulk Nanostructured Functional Materials By Severe Plastic Deformation, *Adv Eng Mater*. 12 (2010) 692-700.
- [86] R.V. Sundeev, A.M. Glezer, A.V. Shalimova, Structural and phase transitions in the amorphous and nanocrystalline Ti50Ni25Cu25 alloys upon high-pressure torsion, *Mater Lett*. 133 (2014) 32-4.
- [87] M. Peterlechner, T. Waitz, H.P. Karnthaler, Nanoscale amorphization of severely deformed NiTi shape memory alloys, *Scripta Mater*. 60 (2009) 1137-40.
- [88] D.V. Gunderov, N.N. Kuranova, A.V. Luk'yanov, A.N. Uksusnikov, E.A. Prokof'ev, L.I. Yurchenko, et al., Application of severe plastic deformation by torsion to form amorphous and nanocrystalline states in large-size TiNi alloy sample, *The Physics of Metals and Metallography*. 108 (2009) 131-8.
- [89] I.Y. Khmelevskaya, S.D. Prokoshkin, I.B. Trubitsyna, M.N. Belousov, S.V. Dobatkin, E.V. Tatyannin, et al., Structure and properties of Ti-Ni-based alloys after equal-channel angular pressing and high-pressure torsion, *Materials Science and Engineering: A*. 481-482 (2008) 119-22.
- [90] E.M. Sharifi, F. Karimzadeh, A. Kermanpur, The effect of cold rolling and annealing on microstructure and tensile properties of the nanostructured Ni50Ti50 shape memory alloy, *Materials Science and Engineering: A*. 607 (2014) 33-7.
- [91] Y.-h. Kim, G.-b. Cho, S.-g. Hur, S.-s. Jeong, T.-h. Nam, Nanocrystallization of a Ti-50.0Ni(at.%) alloy by cold working and stress/strain behavior, *Materials Science and Engineering: A*. 438 (2006) 531-5.
- [92] V. Brailovski, S. Prokoshkin, K. Inaekyan, V. Demers, Functional properties of nanocrystalline, submicrocrystalline and polygonized Ti-Ni alloys processed by cold rolling and post-deformation annealing, *J Alloy Compd*. 509 (2011) 2066-75.
- [93] S.D. Prokoshkin, V. Brailovski, A.V. Korotitskiy, K.E. Inaekyan, A.M. Glezer, Specific features of the formation of the microstructure of titanium nickelide upon thermomechanical treatment including cold plastic deformation to degrees from moderate to severe, *The Physics of Metals and Metallography*. 110 (2010) 289-303.
- [94] V. Demers, V. Brailovski, S.D. Prokoshkin, K.E. Inaekyan, Optimization of the cold rolling processing for continuous manufacturing of nanostructured Ti-Ni shape memory alloys, *J Mater Process Tech*. 209 (2009) 3096-105.

- [95] F. Khaleghi, J. Khalil-Allafi, V. Abbasi-Chianeh, S. Noori, Effect of short-time annealing treatment on the superelastic behavior of cold drawn Ni-rich NiTi shape memory wires, *J Alloy Compd.* 554 (2013) 32-8.
- [96] B. Malard, J. Pilch, P. Sittner, R. Delville, C. Curfs, In situ investigation of the fast microstructure evolution during electropulse treatment of cold drawn NiTi wires, *Acta Mater.* 59 (2011) 1542-56.
- [97] C.H. Park, S.H. Han, S.-W. Kim, J.-K. Hong, T.-h. Nam, J.-T. Yeom, An effective approach to produce a nanocrystalline Ni–Ti shape memory alloy without severe plastic deformation, *J Alloy Compd.* 654 (2016) 379-83.
- [98] S. Jiang, L. Hu, Y. Zhang, Y. Liang, Nanocrystallization and amorphization of NiTi shape memory alloy under severe plastic deformation based on local canning compression, *J Non-Cryst Solids.* 367 (2013) 23-9.
- [99] K. Inaekyan, V. Brailovski, S. Prokoshkin, A. Korotitskiy, A. Glezer, Characterization of amorphous and nanocrystalline Ti–Ni-based shape memory alloys, *J Alloy Compd.* 473 (2009) 71-8.
- [100] S. Prokoshkin, V. Brailovski, S. Dubinskiy, K. Inaekyan, A. Kreitchberg, Gradation of Nanostructures in Cold-Rolled and Annealed Ti–Ni Shape Memory Alloys, *Shape Memory and Superelasticity.* 2 (2016) 12-7.
- [101] V. Demers, V. Brailovski, S.D. Prokoshkin, K.E. Inaekyan, Thermomechanical fatigue of nanostructured Ti–Ni shape memory alloys, *Materials Science and Engineering: A.* 513–514 (2009) 185-96.
- [102] A. Kreitchberg, V. Brailovski, S. Prokoshkin, K. Inaekyan, Influence of Thermomechanical Treatment on Structure and Crack Propagation in Nanostructured Ti–50.26 at%Ni Alloy, *Metallography, Microstructure, and Analysis.* 3 (2014) 46-57.
- [103] S. Prokoshkin, V. Brailovski, K. Inaekyan, V. Demers, A. Kreitchberg, Nanostructured Ti–Ni Shape Memory Alloys Produced by Thermomechanical Processing, *Shape Memory and Superelasticity.* 1 (2015) 191-203.
- [104] S. Prokoshkin, I. Khmelevskaya, S.V. Dobatkin, E. Tatyatin, I. Trubitsyna. Studies of severe plastic deformation conditions for amorphous and nanocrystalline structures formation in Ti-Ni based alloys. *Materials Science Forum: Trans Tech Publ;* 2006. p. 481-6.
- [105] S. Prokoshkin, A. Korotitskiy, V. Brailovski, K. Inaekyan. Effect of Nanocrystalline Structure and Polygonized Dislocation Substructure on Ti-Ni Martensite Lattice Parameters and Transformation Lattice Strain. *Materials Science Forum: Trans Tech Publ;* 2008. p. 475-80.
- [106] V. Brailovski, S.D. Prokoshkin, I.Y. Khmelevskaya, K.E. Inaekyan, V. Demers, E. Bastarache, et al., Interrelations between the properties and structure of thermomechanically-treated equiatomic Ti–Ni alloy, *Materials Science and Engineering: A.* 438–440 (2006) 597-601.
- [107] S.D. Prokoshkin, V. Brailovski, K.E. Inaekyan, V. Demers, I.Y. Khmelevskaya, S.V. Dobatkin, et al., Structure and properties of severely cold-rolled and annealed Ti–Ni shape memory alloys, *Materials Science and Engineering: A.* 481–482 (2008) 114-8.
- [108] Y. Facchinello, V. Brailovski, T. Georges, S. Prokoshkin. Functional properties of nanostructured Ti–Ni SMA produced by a combination of cold, warm rolling and annealing. *Advanced Materials Research: Trans Tech Publ;* 2012. p. 615-20.
- [109] Y. Facchinello, V. Brailovski, S.D. Prokoshkin, T. Georges, S.M. Dubinskiy, Manufacturing of nanostructured Ti–Ni shape memory alloys by means of cold/warm rolling and annealing thermal treatment, *J Mater Process Tech.* 212 (2012) 2294-304.
- [110] A. Kreitchberg, V. Brailovski, S. Prokoshkin, Y. Facchinello, K. Inaekyan, S. Dubinskiy, Microstructure and functional fatigue of nanostructured Ti–50.26 at%Ni alloy after thermomechanical treatment with warm rolling and intermediate annealing, *Materials Science and Engineering: A.* 562 (2013) 118-27.
- [111] A.Y. Kreitchberg, S.D. Prokoshkin, V. Brailovski, A.V. Korotitskiy, Role of the structure and texture in the realization of the recovery strain resource of the nanostructured Ti-50.26 at%Ni alloy, *The Physics of Metals and Metallography.* 115 (2014) 926-47.
- [112] V.V. Stolyarov. Nanostructured shape memory TiNi alloy processed by severe electroplastic deformation. *Materials Science Forum: Trans Tech Publ;* 2008. p. 507-12.
- [113] R.F. Zhu, G.Y. Tang, S.Q. Shi, M.W. Fu, Effect of electroplastic rolling on the ductility and superelasticity of TiNi shape memory alloy, *Mater Design.* 44 (2013) 606-11.
- [114] R. Zhu, G. Tang, The improved plasticity of NiTi alloy via electropulsing in rolling, *Mater Sci Tech-Lond.* (2016) 1-6.

- [115] S.D. Prokoshkin, A.V. Korotitskiy, V. Brailovski, K.E. Inaekyan, S.M. Dubinskiy, A comparative study of martensite crystal lattice in nanostructured, quenched and deformed Ti-Ni shape memory alloys. (2009).
- [116] K. Inaekyan, S. Prokoshkin, V. Brailovski, I. Khmelevskaya, V. Demers, S.V. Dobatkin, et al. Substructure and nanocrystalline structure effects in thermomechanically treated Ti-Ni alloys. *Materials Science Forum: Trans Tech Publ*; 2006. p. 597-602.
- [117] V. Pushin, Structures, Properties, and Application of Nanostructured Shape Memory TiNi - Based Alloys, *Nanomaterials by Severe Plastic Deformation*. (2002) 822-8.
- [118] V. Pushin, R. Valiev, L. Yurchenko. Processing of nanostructured TiNi-shape memory alloys: Methods, structures, properties, application. *Journal de Physique IV (Proceedings): EDP sciences*; 2003. p. 659-62.
- [119] T. Waitz, H.P. Karnthaler, Martensitic transformation of NiTi nanocrystals embedded in an amorphous matrix, *Acta Mater.* 52 (2004) 5461-9.
- [120] T. Waitz, V. Kazykhanov, H.P. Karnthaler, Martensitic phase transformations in nanocrystalline NiTi studied by TEM, *Acta Mater.* 52 (2004) 137-47.
- [121] T. Waitz, T. Antretter, F.D. Fischer, N.K. Simha, H.P. Karnthaler, Size effects on the martensitic phase transformation of NiTi nanograins, *J Mech Phys Solids.* 55 (2007) 419-44.
- [122] T. Waitz, M. Peterlechner, H.P. Karnthaler, Phase Transformations of Bulk Nanostructured NiTi Shape Memory Alloys Studied by HRTEM and in-situ TEM, *Microsc Microanal.* 13 (2007) 280-1.
- [123] T. Waitz, W. Pranger, T. Antretter, F.D. Fischer, H.P. Karnthaler, Competing accommodation mechanisms of the martensite in nanocrystalline NiTi shape memory alloys, *Materials Science and Engineering: A.* 481-482 (2008) 479-83.
- [124] G.-B. Cho, Y.-H. Kim, S.-G. Hur, C.-A. Yu, T.-H. Nam, Transformation behavior and mechanical properties of a nanostructured Ti-50.0Ni(at.%) alloy, *Met Mater Int.* 12 (2006) 181.
- [125] H. Zhang, X. Li, X. Zhang, Grain-size-dependent martensitic transformation in bulk nanocrystalline TiNi under tensile deformation, *J Alloy Compd.* 544 (2012) 19-23.
- [126] X. Shi, L. Cui, D. Jiang, C. Yu, F. Guo, M. Yu, et al., Grain size effect on the R-phase transformation of nanocrystalline NiTi shape memory alloys, *J Mater Sci.* 49 (2014) 4643-7.
- [127] Q.P. Sun, Y.J. He, A multiscale continuum model of the grain-size dependence of the stress hysteresis in shape memory alloy polycrystals, *Int J Solids Struct.* 45 (2008) 3868-96.
- [128] A. Amini, Y. He, Q. Sun, Loading rate dependency of maximum nanoindentation depth in nano-grained NiTi shape memory alloy, *Mater Lett.* 65 (2011) 464-6.
- [129] A. Ahadi, Q. Sun, Effects of grain size on the rate-dependent thermomechanical responses of nanostructured superelastic NiTi, *Acta Mater.* 76 (2014) 186-97.
- [130] K.A. Polyakova-Vachiyana, E.P. Ryklina, S.D. Prokoshkin, S.M. Dubinskii, Dependence of the functional characteristics of thermomechanically processed titanium nickelide on the size of the structural elements of austenite, *The Physics of Metals and Metallography.* 117 (2016) 817-27.
- [131] T. Tadaki, C.M. Wayman, Crystal structure and microstructure of a cold worked TiNi alloy with unusual elastic behavior, *Scripta Metallurgica.* 14 (1980) 911-4.
- [132] Y.F. Zheng, B.M. Huang, J.X. Zhang, L.C. Zhao, The microstructure and linear superelasticity of cold-drawn TiNi alloy, *Materials Science and Engineering: A.* 279 (2000) 25-35.
- [133] R. Valiev, D. Gunderov, E. Prokofiev, V. Pushin, Y. Zhu, Nanostructuring of TiNi Alloy by SPD Processing for Advanced Properties, *Mater Trans.* 49 (2008) 97-101.
- [134] V.S. Afonina, R.M. Gizatullin, D.V. Gunderov, V.S. Kalashnikov, V.V. Koledov, V.G. Shavrov, et al., Study of nanostructured NiTi shape memory alloy's structure and functional properties. (2009).
- [135] M. Nishida, T. Honma, Effect of heat treatment on the all-round shape memory effect in Ti-51at%Ni, *Scripta Metallurgica.* 18 (1984) 1299-302.
- [136] M. Nishida, C.M. Wayman, T. Honma, Electron microscopy studies of the all-around shape memory effect in a Ti-51.0 at. %Ni alloy, *Scripta Metallurgica.* 18 (1984) 1389-94.
- [137] M. Nishida, T. Honma, All-round shape memory effect in Ni-rich TiNi alloys generated by constrained aging, *Scripta Metallurgica.* 18 (1984) 1293-8.

- [138] T. Tadaki, Y. Nakata, K. Shimizu, rsquo, ichi, K. Otsuka, Crystal Structure, Composition and Morphology of a Precipitate in an Aged Ti-51 at%Ni Shape Memory Alloy, *Transactions of the Japan Institute of Metals*. 27 (1986) 731-40.
- [139] J. Khalil Allafi, X. Ren, G. Eggeler, The mechanism of multistage martensitic transformations in aged Ni-rich NiTi shape memory alloys, *Acta Mater*. 50 (2002) 793-803.
- [140] K. Gall, H.J. Maier, Cyclic deformation mechanisms in precipitated NiTi shape memory alloys, *Acta Mater*. 50 (2002) 4643-57.
- [141] J. Michutta, C. Somsen, A. Yawny, A. Dlouhy, G. Eggeler, Elementary martensitic transformation processes in Ni-rich NiTi single crystals with Ni₄Ti₃ precipitates, *Acta Mater*. 54 (2006) 3525-42.
- [142] E.A. Prokofiev, J.A. Burow, E.J. Payton, R. Zarnetta, J. Frenzel, D.V. Gunderov, et al., Suppression of Ni₄Ti₃ Precipitation by Grain Size Refinement in Ni-Rich NiTi Shape Memory Alloys, *Adv Eng Mater*. 12 (2010) 747-53.
- [143] D. Schryvers, W. Tirry, Z.Q. Yang, Measuring strain fields and concentration gradients around Ni₄Ti₃ precipitates, *Materials Science and Engineering: A*. 438–440 (2006) 485-8.
- [144] W. Tirry, D. Schryvers, Linking a completely three-dimensional nanostrain to a structural transformation eigenstrain, *Nat Mater*. 8 (2009) 752-7.
- [145] M.L. Young, M. Frotscher, H. Bei, T. Simon, E.P. George, G. Eggeler, Nanoindentation of pseudoelastic NiTi containing Ni₄Ti₃ precipitates, *Int J Mater Res*. 103 (2012) 1434-9.
- [146] K. Otsuka, X. Ren, Recent developments in the research of shape memory alloys, *Intermetallics*. 7 (1999) 511-28.
- [147] Z. Yang, W. Tirry, D. Schryvers, Analytical TEM investigations on concentration gradients surrounding Ni₄Ti₃ precipitates in Ni–Ti shape memory material, *Scripta Mater*. 52 (2005) 1129-34.
- [148] D.Y. Cong, G. Saha, M.R. Barnett, Thermomechanical properties of Ni–Ti shape memory wires containing nanoscale precipitates induced by stress-assisted ageing, *Acta Biomater*. 10 (2014) 5178-92.
- [149] K. Kazemi-Choobi, J. Khalil-Allafi, V. Abbasi-Chianeh, Influence of recrystallization and subsequent aging treatment on superelastic behavior and martensitic transformation of Ni_{50.9}Ti wires, *J Alloy Compd*. 582 (2014) 348-54.
- [150] B. Karbakhsh Ravari, S. Farjami, M. Nishida, Effects of Ni concentration and aging conditions on multistage martensitic transformation in aged Ni-rich Ti–Ni alloys, *Acta Mater*. 69 (2014) 17-29.
- [151] B. Karbakhsh Ravari, M. Nishida, In situ SEM studies of the transformation sequence of multistage martensitic transformations in aged Ti-50.8 at.% Ni alloys, *Philos Mag*. 93 (2013) 2279-96.
- [152] V. Abbasi-Chianeh, J. Khalil-Allafi, K. Kazemi-choobi, The effect of post-deformation aging on superelastic properties of Ni_{50.9}Ti thin wires attaining micro and nano-substructure, *J Alloy Compd*. 563 (2013) 44-50.
- [153] E. Ryklina, S. Prokoshkin, A. Chernavina. Shape memory behavior of nanostructured Ti-Ni alloy. *European Symposium on Martensitic Transformations: EDP Sciences; 2009*. p. 05025.
- [154] E. Prokofiev, J. Burow, J. Frenzel, D. Gunderov, G. Eggeler, R. Valiev. Phase transformations and functional properties of NiTi alloy with ultrafine-grained structure. *Materials Science Forum: Trans Tech Publ; 2011*. p. 1059-64.
- [155] J. Kim, S. Miyazaki. Effect of low-temperature aging on the R-phase transformation of a Ti-50.9 at% Ni alloy. *Materials Science Forum: Trans Tech Publ; 2002*. p. 225-8.
- [156] Y. Zhou, J. Zhang, G. Fan, X. Ding, J. Sun, X. Ren, et al., Origin of 2-stage R-phase transformation in low-temperature aged Ni-rich Ti–Ni alloys, *Acta Mater*. 53 (2005) 5365-77.
- [157] G. Fan, W. Chen, S. Yang, J. Zhu, X. Ren, K. Otsuka, Origin of abnormal multi-stage martensitic transformation behavior in aged Ni-rich Ti–Ni shape memory alloys, *Acta Mater*. 52 (2004) 4351-62.
- [158] S.-y. Jiang, Y.-n. Zhao, Y.-q. Zhang, L. Hu, Y.-l. Liang, Effect of solution treatment and aging on microstructural evolution and mechanical behavior of NiTi shape memory alloy, *T Nonferr Metal Soc*. 23 (2013) 3658-67.
- [159] X. Wang, K. Li, D. Schryvers, B. Verlinden, J. Van Humbeeck, R-phase transition and related mechanical properties controlled by low-temperature aging treatment in a Ti–50.8 at.% Ni thin wire, *Scripta Mater*. 72–73 (2014) 21-4.

- [160] P. Zeng, H. Du, Research progress on constitutive models and finite element analysis of NiTi shape memory alloy, *Forging & Stamping Technology*. 36 (2011) 1-6.
- [161] L. Qiao, R. Radovitzky, Computational modeling of size-dependent superelasticity of shape memory alloys, *J Mech Phys Solids*. 93 (2016) 93-117.
- [162] D.C. Lagoudas, *Shape Memory Alloys: Modeling and Engineering Applications*. (2008).
- [163] K. Tanaka, S. Kobayashi, Y. Sato, Thermomechanics of transformation pseudoelasticity and shape memory effect in alloys, *Int J Plasticity*. 2 (1986) 59-72.
- [164] C. Liang, C.A. Rogers, One-Dimensional Thermomechanical Constitutive Relations for Shape Memory Materials, *J Intel Mat Syst Str*. 1 (1990) 207-34.
- [165] L.C. Brinson, One-Dimensional Constitutive Behavior of Shape Memory Alloys: Thermomechanical Derivation with Non-Constant Material Functions and Redefined Martensite Internal Variable, *J Intel Mat Syst Str*. 4 (1993) 229-42.
- [166] B. Raniecki, C. Lexcelent, K. Tanaka, Thermodynamic models of pseudoelastic behaviour of shape memory alloys, *Arch Mech*. 44 (2001) 261-84.
- [167] R. Abeyaratne, C. Chu, R.D. James, Kinetics of materials with wiggly energies: Theory and application to the evolution of twinning microstructures in a Cu-Al-Ni shape memory alloy, *Philosophical Magazine A*. 73 (1996) 457-97.
- [168] F. Auricchio, R.L. Taylor, Shape-memory alloys: modelling and numerical simulations of the finite-strain superelastic behavior, *Comput Method Appl M*. 143 (1997) 175-94.
- [169] F. Auricchio, R.L. Taylor, J. Lubliner, Shape-memory alloys: macromodelling and numerical simulations of the superelastic behavior, *Comput Method Appl M*. 146 (1997) 281-312.
- [170] E.J. Graesser, Shape-Memory Alloys as New Materials for Aseismic Isolation, *J Eng Mech*. 117 (1991) 2590-608.
- [171] E. Patoor, A. Eberhardt, M. Berveiller, Micromechanical Modelling of Superelasticity in Shape Memory Alloys, *J Phys IV France*. 06 (1996) C1-277-C1-92.
- [172] F. Falk, Model free energy, mechanics, and thermodynamics of shape memory alloys, *Acta Metallurgica*. 28 (1980) 1773-80.
- [173] B. Peultier, T. Ben Zineb, E. Patoor, Macroscopic constitutive law of shape memory alloy thermomechanical behaviour. Application to structure computation by FEM, *Mech Mater*. 38 (2006) 510-24.
- [174] C. Yu, G. Kang, Q. Kan, D. Song, A micromechanical constitutive model based on crystal plasticity for thermo-mechanical cyclic deformation of NiTi shape memory alloys, *Int J Plasticity*. 44 (2013) 161-91.
- [175] C. Yu, G. Kang, D. Song, Q. Kan, Micromechanical constitutive model considering plasticity for super-elastic NiTi shape memory alloy, *Comp Mater Sci*. 56 (2012) 1-5.
- [176] C. Yu, G. Kang, Q. Kan, Crystal plasticity based constitutive model of NiTi shape memory alloy considering different mechanisms of inelastic deformation, *Int J Plasticity*. 54 (2014) 132-62.
- [177] C. Yu, G. Kang, Q. Kan, A micromechanical constitutive model for anisotropic cyclic deformation of super-elastic NiTi shape memory alloy single crystals, *J Mech Phys Solids*. 82 (2015) 97-136.
- [178] C. Yu, G. Kang, Q. Kan, A micromechanical constitutive model for grain size dependent thermo-mechanically coupled inelastic deformation of super-elastic NiTi shape memory alloy, *Int J Plasticity*. 105 (2018) 99-127.
- [179] C. Yu, G. Kang, Q. Kan, An equivalent local constitutive model for grain size dependent deformation of NiTi polycrystalline shape memory alloys, *Int J Mech Sci*. 138-139 (2018) 34-41.
- [180] C. Yu, G. Kang, Q. Kan, Y. Zhu, Rate-dependent cyclic deformation of super-elastic NiTi shape memory alloy: Thermo-mechanical coupled and physical mechanism-based constitutive model, *Int J Plasticity*. 72 (2015) 60-90.
- [181] M.P. Li, Q.P. Sun, Nanoscale phase transition behavior of shape memory alloys — closed form solution of 1D effective modelling, *J Mech Phys Solids*. 110 (2018) 21-37.
- [182] L. Qiao, J.J. Rimoli, Y. Chen, C.A. Schuh, R. Radovitzky, Nonlocal Superelastic Model of Size-Dependent Hardening and Dissipation in Single Crystal Cu-Al-Ni Shape Memory Alloys, *Phys Rev Lett*. 106 (2011) 085504.
- [183] A.S.f. Testing, Materials. ASTM E112-96 (2004) e2: Standard Test Methods for Determining Average Grain Size. ASTM; 2004.
- [184] W.F.H. Günther Höhne, H.-J. Flammersheim, *Differential Scanning Calorimetry*: Springer-Verlag Berlin Heidelberg; 2003.

- [185] R.F. Hamilton, H. Sehitoglu, Y. Chumlyakov, H.J. Maier, Stress dependence of the hysteresis in single crystal NiTi alloys, *Acta Mater.* 52 (2004) 3383-402.
- [186] X. Wang, S. Kustov, B. Verlinden, J. Humbeeck, Fundamental Development on Utilizing the R-phase Transformation in NiTi Shape Memory Alloys, *Shape Memory and Superelasticity.* 1 (2015) 231-9.
- [187] D. Xue, Y. Zhou, X. Ren, The effect of aging on the B2-R transformation behaviors in Ti-51at%Ni alloy, *Intermetallics.* 19 (2011) 1752-8.
- [188] P. Šittner, M. Landa, P. Lukáš, V. Novák, R-phase transformation phenomena in thermomechanically loaded NiTi polycrystals, *Mech Mater.* 38 (2006) 475-92.
- [189] S. Miyazaki, K. Otsuka, Deformation and transition behavior associated with the R-phase in Ti-Ni alloys, *Metallurgical Transactions A.* 17 (1986) 53-63.
- [190] X. Wang, B. Verlinden. Deformation behavior after stress-induced martensite transformation in a Ti-50.8 at.% Ni alloy. *MATEC Web of Conferences: EDP Sciences;* 2015.
- [191] P. Chowdhury, L. Patriarca, G. Ren, H. Sehitoglu, Molecular dynamics modeling of NiTi superelasticity in presence of nanoprecipitates, *Int J Plasticity.* 81 (2016) 152-67.
- [192] Y.-x. Tong, J.-t. Liu, F. Chen, C.-q. Liang, B. Tian, L. Li, et al., Effect of aging on martensitic transformation and superelasticity of TiNiCr shape memory alloy, *T Nonferr Metal Soc.* 24 (2014) 2598-605.
- [193] F. Jiang, Y. Liu, H. Yang, L. Li, Y. Zheng, Effect of ageing treatment on the deformation behaviour of Ti-50.9 at.% Ni, *Acta Mater.* 57 (2009) 4773-81.
- [194] G. Tan, Y. Liu, P. Sittner, M. Saunders, Lüders-like deformation associated with stress-induced martensitic transformation in NiTi, *Scripta Mater.* 50 (2004) 193-8.
- [195] L. Zheng, Y. He, Z. Moumni, Effects of Lüders-like bands on NiTi fatigue behaviors, *Int J Solids Struct.* 83 (2016) 28-44.
- [196] S. Jiang, Y. Zhang, L. Zhao, Y. Zheng, Influence of annealing on NiTi shape memory alloy subjected to severe plastic deformation, *Intermetallics.* 32 (2013) 344-51.
- [197] N.N. Kuranova, D.V. Gunderov, A.N. Uksusnikov, A.V. Luk'yanov, L.I. Yurchenko, E.A. Prokof'ev, et al., Effect of heat treatment on the structural and phase transformations and mechanical properties of TiNi alloy subjected to severe plastic deformation by torsion, *The Physics of Metals and Metallography.* 108 (2009) 556.
- [198] F. Miura, M. Mogi, Y. Ohura, Japanese NiTi alloy wire: use of the direct electric resistance heat treatment method, *The European Journal of Orthodontics.* 10 (1988) 187-91.
- [199] R. Delville, B. Malard, J. Pilch, P. Sittner, D. Schryvers, Transmission electron microscopy investigation of dislocation slip during superelastic cycling of Ni-Ti wires, *Int J Plasticity.* 27 (2011) 282-97.
- [200] Q. Meng, H. Yang, Y. Liu, T.-h. Nam, D. Favier, Ti-50.8 at.% Ni wire with variable mechanical properties created by spatial electrical resistance over-ageing, *J Alloy Compd.* 577, Supplement 1 (2013) S245-S50.
- [201] R. Delville, B. Malard, J. Pilch, P. Sittner, D. Schryvers, Microstructure changes during non-conventional heat treatment of thin Ni-Ti wires by pulsed electric current studied by transmission electron microscopy, *Acta Mater.* 58 (2010) 4503-15.
- [202] V. Delobelle, G. Chagnon, D. Favier, T. Alonso, Study of electropulse heat treatment of cold worked NiTi wire: From uniform to localised tensile behaviour, *J Mater Process Tech.* 227 (2016) 244-50.
- [203] M. Kurumada, Y. Kimura, H. Suzuki, O. Kido, Y. Saito, C. Kaito, TEM study of early Ni₄Ti₃ precipitation and R-phase in Ni-rich NiTi nanoparticles, *Scripta Mater.* 50 (2004) 1413-6.
- [204] N.A. Gershenfeld, N. Gershenfeld, *The nature of mathematical modeling: Cambridge university press;* 1999.
- [205] S.H. Chang, S.K. Wu, G.H. Chang, Grain size effect on multiple-stage transformations of a cold-rolled and annealed equiatomic TiNi alloy, *Scripta Mater.* 52 (2005) 1341-6.
- [206] T.W. Duerig, K. Bhattacharya, The Influence of the R-Phase on the Superelastic Behavior of NiTi, *Shape Memory and Superelasticity.* 1 (2015) 153-61.
- [207] J. Uchil, K.K. Ganesh, K.K. Mahesh. Simple thermal actuator using R-phase transformation of Nitinol. 2002. p. 435-42.
- [208] Y. Luo, T. Takagi, S. Maruyama, M. Yamada, A Shape Memory Alloy Actuator Using Peltier Modules and R-Phase Transition, *J Intel Mat Syst Str.* 11 (2000) 503-11.
- [209] L. Bataillard, J.E. Bidaux, R. Gotthardt, Interaction between microstructure and multiple-step transformation in binary NiTi alloys using in-situ transmission electron microscopy observations, *Philosophical Magazine A.* 78 (1998) 327-44.

- [210] L. Hu, S. Jiang, Y. Zhang, Role of Severe Plastic Deformation in Suppressing Formation of R Phase and Ni₄Ti₃ Precipitate of NiTi Shape Memory Alloy, *Metals-Basel*. 7 (2017) 145.
- [211] P. Lejcek, Grain boundary segregation in metals: Springer Science & Business Media; 2010.
- [212] J. Hu, Y.N. Shi, X. Sauvage, G. Sha, K. Lu, Grain boundary stability governs hardening and softening in extremely fine nanograined metals, *Science*. 355 (2017) 1292-6.
- [213] N. Hansen, Hall–Petch relation and boundary strengthening, *Scripta Mater*. 51 (2004) 801-6.
- [214] R. Haberman, Applied partial differential equations with Fourier series and boundary value problems: Pearson Higher Ed; 2012.
- [215] X.B. Shi, L.S. Cui, D.Q. Jiang, F.M. Guo, M.Y. Yu, Nanocrystalline NiTi shape memory alloys with huge superelasticity and high mechanical damping, *Materials Research Innovations*. 18 (2014) S4-578-S4-83.
- [216] X.B. Wang, B. Verlinden, J. Van Humbeeck, R-phase transformation in NiTi alloys, *Mater Sci Tech-Lond*. 30 (2014) 1517-29.
- [217] M. Liu, H. Li, G. Song, J. Ou, Investigation of vibration mitigation of stay cables incorporated with superelastic shape memory alloy dampers, *Smart Materials and Structures*. 16 (2007) 2202-13.
- [218] X.B. Shi, Z.C. Hu, X.W. Hu, J.S. Zhang, L.S. Cui, Effect of plastic deformation on stress-induced martensitic transformation of nanocrystalline NiTi alloy, *Mater Charact*. 128 (2017) 184-8.
- [219] Y. Liu, H. Xiang, Apparent modulus of elasticity of near-equiatomic NiTi, *J Alloy Compd*. 270 (1998) 154-9.
- [220] D. Liu, M. Peterlechner, J. Fiebig, S. Trubel, M. Wegner, Y. Du, et al., Grain boundary diffusion and precipitates in B2 Ti–50.2 at.% Ni alloy, *Intermetallics*. 61 (2015) 30-7.
- [221] Y. Liu, I. Houver, H. Xiang, L. Bataillard, S. Miyazaki, Strain dependence of pseudoelastic hysteresis of NiTi, *Metallurgical and Materials Transactions A*. 30 (1999) 1275-82.
- [222] X. Huang, Y. Liu, Effect of annealing on the transformation behavior and superelasticity of NiTi shape memory alloy, *Scripta Mater*. 45 (2001) 153-60.
- [223] G. Helbert, L. Dieng, S. Arbab Chirani, L. Saint-Sulpice, T. Lecompte, S. Calloch, et al., Investigation of NiTi based damper effects in bridge cables vibration response: Damping capacity and stiffness changes, *Eng Struct*. 165 (2018) 184-97.
- [224] V. Torra, C. Auguet, A. Isalgue, G. Carreras, P. Terriault, F.C. Lovey, Built in dampers for stayed cables in bridges via SMA. The SMARTeR-ESF project: A mesoscopic and macroscopic experimental analysis with numerical simulations, *Eng Struct*. 49 (2013) 43-57.
- [225] Q. Yang, Q. Kan, G. Kang, C. Yu, S. Dong, Constitutive model on cyclic transformation included plasticity of superelastic NiTi alloy, *Journal of Functional Materials*. 46 (2015) 5.
- [226] K. Wilde, P. Gardoni, Y. Fujino, Base isolation system with shape memory alloy device for elevated highway bridges, *Eng Struct*. 22 (2000) 222-9.
- [227] Q. Kan, Constitutive model study and its finite element application of superelastic NiTi alloys, [Doctor degree dissertation]: Southwest Jiaotong University; 2009.
- [228] Z. Zhang, P. Sheng, Q. Wang, L. Wang, Simulation of pseudo-elasticity behaviors of shape memory alloy, *Chinese Journal of Applied Mechanics*. 33 (2016) 7.
- [229] H. Zhao, S. Yan, W. Wang, One-dimensional Continuous Pseudo-elastic Hysteretic Model of Shape Memory Alloys, *Journal of Huazhong University of Science and Technology(Urban Science Edition)*. 25 (2008) 4.